XUV Photoabsorption Studies of Calcium and the Neon Isoelectronic Sequence

A Thesis for the Degree of
Doctor of Philosophy.

By

Andrew Gray, B.Sc.

Centre for Laser Plasma Research
School of Physical Sciences
Dublin City University

Research Supervisor

Prof. E. T. Kennedy, B.Sc. Ph.D. C.Phys. F.Inst.P.

August 1999

I hereby certify that this material, which I now submit for assessment on the program of study leading to the award of Doctor of Philosophy is entirely my own work and has not been taken from the work of others save and to the extent that such work has been cited and acknowledged within the text of my work.

Signed : _____ I.D. No. : 93701331

Candidate

Date : 10/9/99

You see things; and say 'Why?' But I dream things that never were and say 'Why not?'

- George Bernard Shaw

I have seen waves crash along the shore
Planets round stars, but I want more
I long for the knowledge to see and hear
To understand, and not to fear.

To my parents

Acknowledgements

'It was the best of times, it was the worst of times ...'

- A Tale of two cities by Charles Dickens.

To those who I am about to leave out (unintentionally), I ask forgiveness ...

I would like to thank Professor Eugene Kennedy, who, burdened with the weighty responsibility of department head, found the time to be my supervisor. His contributions and financial assistance are very much appreciated.

To Doctors Jean-Paul Mosnier, John Costello, Tony Cafolla and Enda McGlynn, I offer thanks, not only for unselfishly sharing their imaginations and knowledge, but also for being my friends.

To Dr. Colm McGinley, Dr. William Whitty and soon to be 'Dr', Oonagh Meighan, I owe my sanity. Many times have they pulled me from the precipice of despair. To Mohamed, John H., Paul, Cormac, Chris, Lee, Barry and all the other members of the group and the 'greater' faculty, both past and present, I also say an unreserved thankyou.

Shane, Derek, Dara, Damian, Sean and Joanne, what can I say?

Finally, I'd like to thank my family, John, Patricia, Sarah and David, who have shown me the true meaning of sacrifice and love. All that I am, I owe to them.

Abstract

Using the dual laser plasma photoabsorption technique, the 3p region of Ca^0, Ca^+ and Ca^{2+} and the 2s and 2p regions of Ne^0, Na^+, Mg^{2+}, Al^{3+} and Si^{4+}, have been investigated. High quality spectra have been obtained by paying careful attention to instrumental effects and plasma opacity. For Ca^+, the DLP data has been correlated with previously measured photoion results to obtain improved absolute cross sections. By using spatio-temporal maps, excellent ion stage separation for members of the calcium isonuclear sequence has been achieved. Comparison of the DLP data with independent Hartree-Fock calculations and data from other experimental and theoretical studies has revealed, for the first time, 4 features arising from the $Ca^0 3p^6 4s3d$ excited state and 18 features arising from the $Ca^+ 3p^6 3d$ excited state. New lines of Ca^+ $3p^6 4s$ ground state origin have also been resolved.

In the first systematic experimental study of the neon isoelectronic sequence, higher members of the $2s^2 2p^6 \rightarrow 2s^2 2p^5 ns,nd$ series, not previously resolved, have been measured. Independent $^2P_{3/2,1/2}$ thresholds have been established. The $2s^2 2p^6 \rightarrow 2s2p^6 np$ ^1P inner shell series has also been measured. For the first time, Fano parameters for low lying members of the series in Na^+ through to Si^{4+}, have been extracted. The Si^{4+} $2s2p^6 3p$ ^1P resonance has been found to lie 1.3eV below the $^2P_{3/2,1/2}$ limits. Its profile is asymmetric which strongly suggests forced autoionisation. This is the first observation of this phenomenon in a laser produced plasma. Further evidence to support this assertion is presented. The near threshold photoionisation cross section for members of the neon isoelectronic sequence was recently calculated by Chakraborty et al using the Relativistic Random Phase Approximation (RRPA). The threshold photoionisation cross section for Si^{4+} was shown to be anomalous as a result of the downward movement, with increasing Z, of the $2s2p^6 3p$ ^1P resonance below threshold. The predicted anomalous near threshold behaviour for Si^{4+} is supported by our experimental results. It is suggested that the phenomenon should also occur for higher members of the sequence as higher $2s2p^6 np$ ^1P series members successively move below threshold and that it is a general phenomenon expected to occur in any isoelectronic sequence where the outermost subshell is other than l=0.

Table of Contents


Introduction

Experimental studies of the interaction of light with matter have provided the genesis and expansion of a vast pool of knowledge concerning the properties of the atom and the dynamics of excitation and de-excitation. The spectroscopic techniques employed for the analysis of the by-products of this interaction have seen much growth since spectroscopy's conception by Newton some 300 years ago. The advent of quantum mechanics, circa 1900, synchrotron radiation in 1947 and the laser in 1960 each ushered in new eras of understanding and today many experimental methods are utilised enjoying the benefits derived from a quantum mechanical treatment of atoms on a microscopic scale, an increase in the brightness obtained from highly polarised, broadband synchrotron radiation sources via wiggler and undulator insertion devices and the ever increasing power delivered by both pulsed and continuous wave lasers. Studies pertaining to all regions of the electromagnetic spectrum have seen the benefits of these breakthroughs, the XUV/EUV region being no exception.

Of particular relevance to many astrophysical and plasma phenomena, the XUV region is rich in inner-shell and multiple electron excitations which exhibit important many body effects, a comprehension of which is crucial to the accuracy of any theoretical model. Recent developments in optical components suitable for the XUV region such as layered synthetic microstructures, toroidal and aspheric optics and efficient photoelectric detection have given impetus to research in this region. The arrival of the laser produced plasma in the 1960's, which when created from a high Z target produces an intense, broadband XUV continuum, heralded the dawn of low cost, high quality spectroscopic studies in the XUV region using hot, dense plasmas as both source and absorbing medium. Spectroscopy is now no longer confined to large scale facilities and is readily accessible by way of essentially 'Table-top' sized experimental arrangements. One such arrangement is the 2.2m multichannel XUV spectrometer system in operation at Dublin City University. The system utilises a Dual Laser Plasma (DLP) technique which allows photoabsorption processes to be studied with a relative ease and reproducibility not easily matched by other more complex systems.

In this thesis, we have applied the DLP technique to the study of the first three members of the calcium isonuclear sequence and the first five members of the neon isoelectronic sequence. Both are of considerable astrophysical interest and fundamental importance

for insight into electron-electron correlations. Chapter 1 introduces the theory required for an understanding of what follows in subsequent chapters. The topics discussed include the importance of photoabsorption studies in the study of the light/matter interaction, laser produced plasmas, autoionisation and plasma opacity. Chapter 2 deals almost exclusively with the DLP system, describing its operation and characterising its performance in the measurement of quality photoabsorption spectra. Chapter 3 presents DLP photoabsorption spectra for the calcium isonuclear sequence, the purity of the spectra demonstrating the system's strengths regarding the spectroscopic separation of ion stages. This chapter also details a method for obtaining improved cross sectional data for Ca^{+} in the 3p region and demonstrates, through the first observation of many Ca^{0} $3p^{6}4s3d$ and $Ca^{+}3p^{6}3d$ excited state transitions, how with this system excited states can be populated. Chapter 4 concerns the neon isoelectronic sequence, where we present photoabsorption spectra of the 2s and 2p regions of excitation for Ne^{0} through to Si^{4+}. We have measured the excitation energies for many members of the inner shell $2s2p^{6}np$ ^{1}P series and have extracted, for the first time, their asymmetric Fano parameters. In pushing the system to its limits to obtain sufficient quantities of Si^{4+} ions and through analysing systematic trends within the sequence with the aid of Hartree-Fock and Relativistic Random Phase Approximation (RRPA) calculations, we have also shown how the $Si^{4+}2s2p^{6}3p$ ^{1}P resonance profile is strongly indicative of forced autoionisation and how the near threshold photoionisation cross section of Si^{4+} exhibits anomalous behaviour in contrast to neighbouring members of the sequence. We conclude the thesis with a brief summary of our results and a discussion on how they may be improved upon.

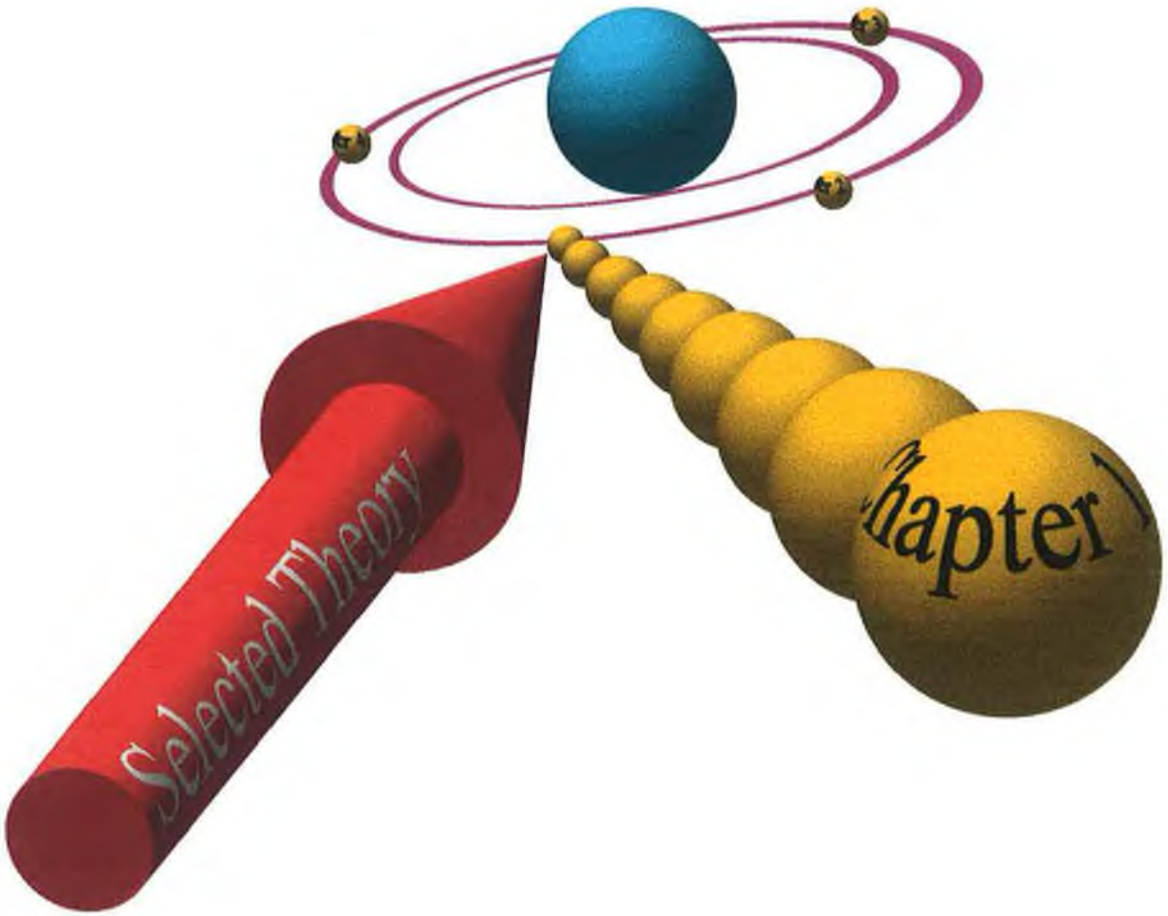
Selected Theory
hapter

Introduction

In this chapter some of the basic concepts relating to the variety of well established spectroscopic techniques, which each access fundamental atomic processes to varying degrees, are presented. Chief amongst these techniques are those involving photoabsorption, photoion and photoelectron measurements. We discuss selected examples of experimental arrangements and highlight some significant examples of the application of these techniques to both atoms and ions which serve to illustrate their respective strengths and weaknesses. Next, the properties and dynamics of laser plasmas are explored within the context of their role as a spectroscopic tool. Only a brief introduction to this vast field is given, most of the fundamentals having been established in the 60's and 70's but which are still quite valid today. Particular emphasis is placed on the atomic processes which take place within the plasma, the plasma's formation and evolution and the various models which allow the plasma and the species within it to be described in terms of electron densities and temperatures. This discussion serves as a foundation for the more specific Dual laser plasma technique introduced in chapter 2. We then highlight the unique characteristics of the process of autoionisation. Its principles are outlined and methods for achieving an experimental interpretation of its asymmetric manifestation in XUV absorption spectra are reviewed in preparation for its importance in relation to our neon isoelectronic sequence results presented in chapter 4. Finally, plasma opacity is discussed, its effect on absorption spectra demanding particular attention especially with relation to the calcium spectra presented in chapter 3. The differences between an optically thick and an optically thin plasma are discussed with emphasis on how the two regimes may be distinguished spectroscopically.

1.1 Spectroscopic techniques for the XUV

1.1.1 Photoabsorption measurements

Perhaps the simplest and most well established technique is a method for obtaining total absorption cross sections $\sigma_t(\lambda)$ which involves measuring the attenuation of a photon beam of wavelength λ as it passes through a sample of thickness d and target density n. The well known Lambert-Beer law

$$I(\lambda) = I_0(\lambda)e^{-\sigma_t(\lambda)nd} \qquad [1.1]$$

formulates the relationship between the incident photon beam $I_0(\lambda)$ and the transmitted beam $I(\lambda)$ upon passage through the absorbing medium. Using this fundamental relationship, extensive absorption studies have been carried out throughout the past thirty years. The principles have remained the same but improved instrumentation has allowed dramatic increases in resolving power and photon flux. Various sources have been used as alternatives to costly synchrotron radiation including Ballofet-Romand-Vodar (BRV) type vacuum spark sources (Ballofet 1961), exploding wires (Martinson 1989 and therein) and laser plasmas (Costello et al 1991), all being particularly favourable for study of highly ionized metals and gases (Martinson 1989 and therein). Techniques such as Resonant Laser Driven Ionization (RLDI) have been successful in ionizing metal vapour columns by tuning a dye laser to a known resonance of the target vapour. Ionisation efficiencies of up to 100% have been obtained (Lucatorto and McIlrath 1976) but the lack of suitable dyes, difficulties in attaining sufficiently high atomic vapour densities and the need for multiple lasers makes RLDI impractical for study of highly ionized species.

With the DLP system, it is the attenuation and measurement of light emitted from a background source plasma and absorbed by a fore-plasma, which potentially allows $\sigma_t(\lambda)$'s to be measured. However, this is subject to a knowledge of the density/length product ($n.d$) within the absorbing plasma and this number is not, in general, known with sufficient accuracy in DLP experiments to allow definitive measurements of $\sigma_t(\lambda)$. Despite this drawback the relative cross section of spectroscopic features can be observed and this allows for measurement of resonance energies and calculation of

binding energies. Comparison with results from other spectroscopic techniques and theoretical predictions is also readily facilitated.

Assuming that n can be measured, we can calculate $\sigma_t(\lambda)$ via equation [1.1] for typical one and two electron processes such as

$$A + h\nu \rightarrow A^{+} + e^{-} \qquad [1.2]$$

and

$$A + h\nu \rightarrow A^{++} + e^{-} + e^{-} \qquad [1.3]$$

but in both of these cases it is only the photon energy $h\nu$ which is being monitored. This means that because

$$\sigma_t = \sum_q \sigma_{ion}(A^q)\frac{N(A^q)}{N_{Total}} \qquad [1.4]$$

(where N corresponds to the number of ions) we may see contributions from other ion stages contributing to the cross section measurement and possibly affecting both total and relative absorption cross sections. It is for this reason that ion stage separation and isolation is a crucial objective in any DLP experiment. So, while photoabsorption studies measuring light attenuation provide us with a broad oversight of the strength and position of excitations, it is the measurement and study of the ions and electrons produced during the photon/atom interaction that provide the deepest insight. These techniques are respectively known as photoion and electron spectroscopy.

1.1.2. Photoion measurements

By application of the well known principles of mass spectrometry, the ions produced by photon/atom interactions can be mass-charge selected and their cross section $\sigma_{ion}(A^q)$ measured. A number of variations concerning *e/m* analysis have been applied (Schmidt 1992 and therein) including magnetic mass analysers, quadrupole mass filters and time of flight (TOF) analysers. Of these, magnetic mass analysis was implemented in the first successful photon-ion merged beam experiment utilising synchrotron radiation (Lyon et al 1986).

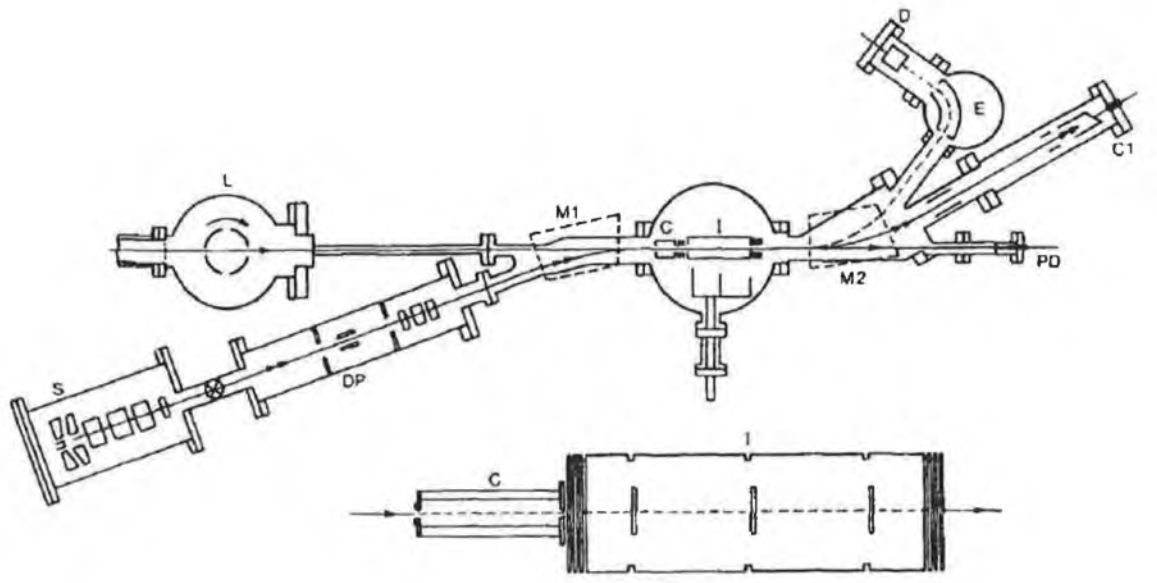

Figure 1.1 : The experimental setup for photoion spectrometry first used by Lyon et al(1986) to successfully merge synchrotron radiation with an ionic beam of Ba^+ ions.

Figure 1.1 shows the experimental apparatus in which Lyon et al (1986), using a surface ionisation source (S), produced ground state Ba^+ ions (~0.1μA, 2keV) which were mass analysed by magnet M1 and fed into the path of a beam of monochromatic synchrotron radiation. Within the interaction zone (I), which was well defined and measured 12.5cm in length, a significant quantity of the Ba^+ ions were photoionised creating Ba^{2+} ions which were accelerated by application of a 600V positive bias. These emerging 2.6keV Ba^{2+} ions were then separated from the slower 2keV Ba^+ ions by a second magnet M2 before collection and detection of both ion beams by a Johnston multiplier (D) and a Faraday cup (C1) respectively. By paying particular attention to beam density overlap, background ionisation levels, monochromator wavelength calibration and photodiode and Johnston multiplier efficiencies, the absolute cross section for Ba^+ within the range 16-30eV was measured to an accuracy of ~15%. The overwhelming success of this technique fueled further application to singly ionised calcium (Lyon et al 1987a), strontium (Lyon et al 1987b), gallium (Peart et al 1987a), zinc (Peart et al 1987a) and potassium (Peart and Lyon 1987).

Collection efficiencies of close to 100% (84% for Ba^{2+} (Lyon et al 1986)) coupled with larger interaction lengths (of the order of cm's) allows photoion spectrometry to unveil

relatively weak features (~1MB) even without the use of photon flux enhancing insertion devices (Wuilleumier 1994). The ability to probe the selected ions without cross contamination combined with inherently low noise levels when compared to photoabsorption measurements, makes photoion spectrometry a powerful diagnostic but it is the strict quantitative analysis of all experimental variables and primarily a knowledge of the ion density which allows $\sigma_{ion}(Aq)$ measurements to be made. Although, clearly a more powerful technique than photoabsorption spectroscopy, it has been limited in recent years by a restriction to neutral and lowly ionised species, as with increasing ionic charge state, the photoionisation cross section decreases. This reduction in cross section allows noise levels to compete vigorously with signal quickly eliminating any possibility for viable cross section measurement. This type of experimentation has also suffered from a lack of adequate resolution due to the large geometrical aberrations which are a consequence of the necessity to operate at grazing incidence in the VUV. Only recently have effective methods of combating these handicaps seen development with the introduction of high quality aspherical mirrors to complement plane grating, fixed exit slit monochromators such as the SX700 (Domke 1991). Improvements in storage ring optics have further boosted performance and resolving powers of up to 10,000 across the 40-900eV energy range are now commonplace in the leading facilities. New developments in ion sources, in particular those based on electron cyclotron resonance (ECR) principles, now allow multi-charged ions to be produced in significant quantities. Enhancement of ECR ion source performance by better magnetic containment and/or the use of multiple discrete microwave radiation for injection has meant an increase in the size of the ECR 'zone' relative to the size of the plasma volume. The creation of a large ECR plasma 'volume' as opposed to the conventional ECR thin 'surface' results in the heating of a much larger electron population to higher energies, the effect of which is to produce higher charge-state distributions and much higher intensities for a particular charge state (Alton and Smithe 1994). Preliminary application of these new ECR ion sources have produced dominant charge states in argon and xenon ion beams of Ar^{8+} and Xe^{8+} respectively, with significant enhancement in the intensity of all other charge states produced in the beams also apparent (Alton et al 1998). Significant enhancements in the production of

O^{7+} (Schlapp et al 1998, Xie 1998) and Ar^{13+}, Ca^{13+}, Fe^{13+}, Co^{14+} and Kr^{18+} ions have also been reported (Xie 1998). Other techniques, employing heavy-ion storage rings - offering long storage times, small effects from collisions with the residual gas, separation of ion production and storage regions and charge-state selectivity - have also been applied and have been found to be particularly favourable for lifetime measurements e.g. C^{2+} (Doerfert et al 1997).

Despite these pros and cons and the continuing advance in technology to optimise instrumental performance, there is a limit to the physical information that can be extracted with Photoion spectrometry. Detection of ions, by whatever means, does not allow differentiation between direct and indirect photoionisation processes nor can the partial cross sections relating to the probabilities of transitions between unique levels be investigated. It is because

$$\sigma(A^+) = \sum_p \sigma_p(A^+) \qquad [1.5]$$

that to measure partial cross sections $\sigma_p(A^+)$ is considered the ultimate in experimental spectroscopic analysis. To do this, we need simply look at equation [1.2] to see that measurement of the kinetic energy of the electrons produced in the photon/atom interaction will provide the means to measure $\sigma_p(A^+)$s and in so doing provide differentiation between direct and indirect (Auger) processes. The ability to investigate other dynamical properties such as the angular distribution parameter β, which describes the angle dependence of electrons ejected from the interaction zone for a fixed photon energy, also becomes a reality. The experimental technique by which this deeper penetration into the realm of atomic processes can be made possible is known as electron spectrometry.

1.1.3. Photoelectron measurements

A typical photoelectron experiment involves an atomic beam being excited or ionised by a monochromatic and polarised photon beam. When both beams intersect in the source volume (typically ~1mm in dimension) of an electron energy analyser, the number, kinetic energy and angular distribution of the outgoing electrons can be determined (Sonntag and Zimmerman 1992). Because of its high photon flux, high brightness, high

degree of polarisation, tunabilty and time structure, synchrotron radiation is ideally suited to photoelectron spectroscopy. Combined with specially designed crucibles which provide high density (~10^{13} atoms cm^{-3}) target vapours by resistive heating or electron bombardment and ultra-high vacuum to reduce background noise levels caused by ion collisions with residual molecules, excellent Auger or direct photoemission spectra can be obtained. By using cylindrical mirror analysers (CMAs), spherical analysers or time of flight analysers, both the kinetic energies of the electrons and partial cross sections σ_p can be determined. However, the accurate determination of these partial cross sections is non-trivial and requires many experimental parameters to be known precisely (Schmidt 1992). However, with careful alignment of the electron spectrometer, its principal axis at 54.7° with respect to the horizontal plane, calculations can be simplified considerably. It is worth mentioning that the angle 54.7° is referred to as the *magic angle* as with this orientation direct angular independent measurement of branching ratios is possible (Jauhiainen et al 1994).

An example of an experimental set-up for angle resolved photoemission studies of gaseous targets is shown in Figure 1.2.

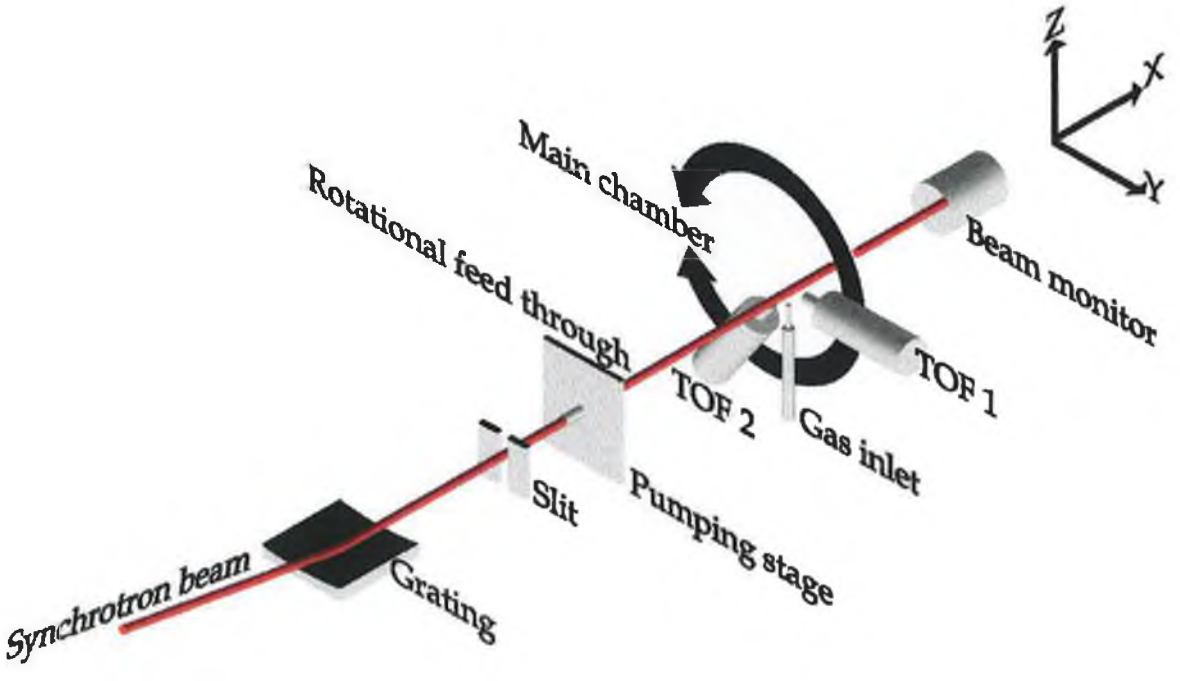

Figure 1.2 : Schematic representation of an angle-resolved gas-phase photoemission experiment using synchrotron radiation excitation and time-of-flight detection (from Becker et al 1989)

Becker et al (1989) have used this set-up to successfully measure angular asymmetry parameters β for neutral xenon, this being made possible by the use of dual TOF analysers mounted on a rotatable vacuum chamber. One of the disadvantages associated with current methods of photoelectron spectroscopy is a lack of sufficient ion current due to interaction lengths typically 1 to 2 orders of magnitude less than those achievable via photoionisation or photoabsorption experimentation. Also of concern is the relatively poor collection efficiencies which are of the order of 0.1 to 1% as compared to possible efficiencies of 100% for ion spectrometry (Wuilleumier 1994). Despite these drawbacks, recent improvements in CMA configurations and the use of ultra-high vacuum have seen great success as in the case of the PISA experiments with the super ACO storage ring where the 'giant' Ca^+ 3d resonance has been measured (Bizau et al 1991, 1992). Of late, the relatively poor resolving power of previous experiments (Bizau et al 1992) has been vastly improved upon by the introduction of third generation synchrotron light sources such as the Advanced Light Source (ALS). So far only neutrals have been studied using this source, high photon flux and high resolution (~18meV) having been effectively employed to measure single and double excitations in atoms such as neon (Langer et al 1997, Wills et al 1998) but the arrival of other newly commissioned 3rd generation sources in the near future augers well for yet another revolution in the means to study the diverse and highly complex nature of the atomic world.

To further emphasise the deeper insight obtainable via photoelectron spectroscopy, let us consider the case of neutral barium. Measured by Lucatorto et al (1981) in conjunction with its isonuclear Ba^+ and Ba^{2+} members, the RLDI technique was put to good use and excellent isolation of Ba, Ba^+ and Ba^{2+} between 80 and 160eV was obtained. Of these three members of the sequence, we show the RLDI results for neutral barium in Figure 1.3(a). We contrast these photoabsorption results with the photoelectron spectrum resulting from ionisation of the 5p subshell (Figure 1.3(b)) and the photoelectron spectrum from ionisation of the 4d subshell (Figure 1.3(c)), taken at fixed photon energies of 93.75eV and 130.2eV respectively (Bizau 1989). The arrows in Figure 1.3 indicate that whilst a single point representing the absolute cross section σ_t is portrayed for photon energies of 93.75eV and 130.2eV respectively in Figure 1.3(a), figures 1.3(b)

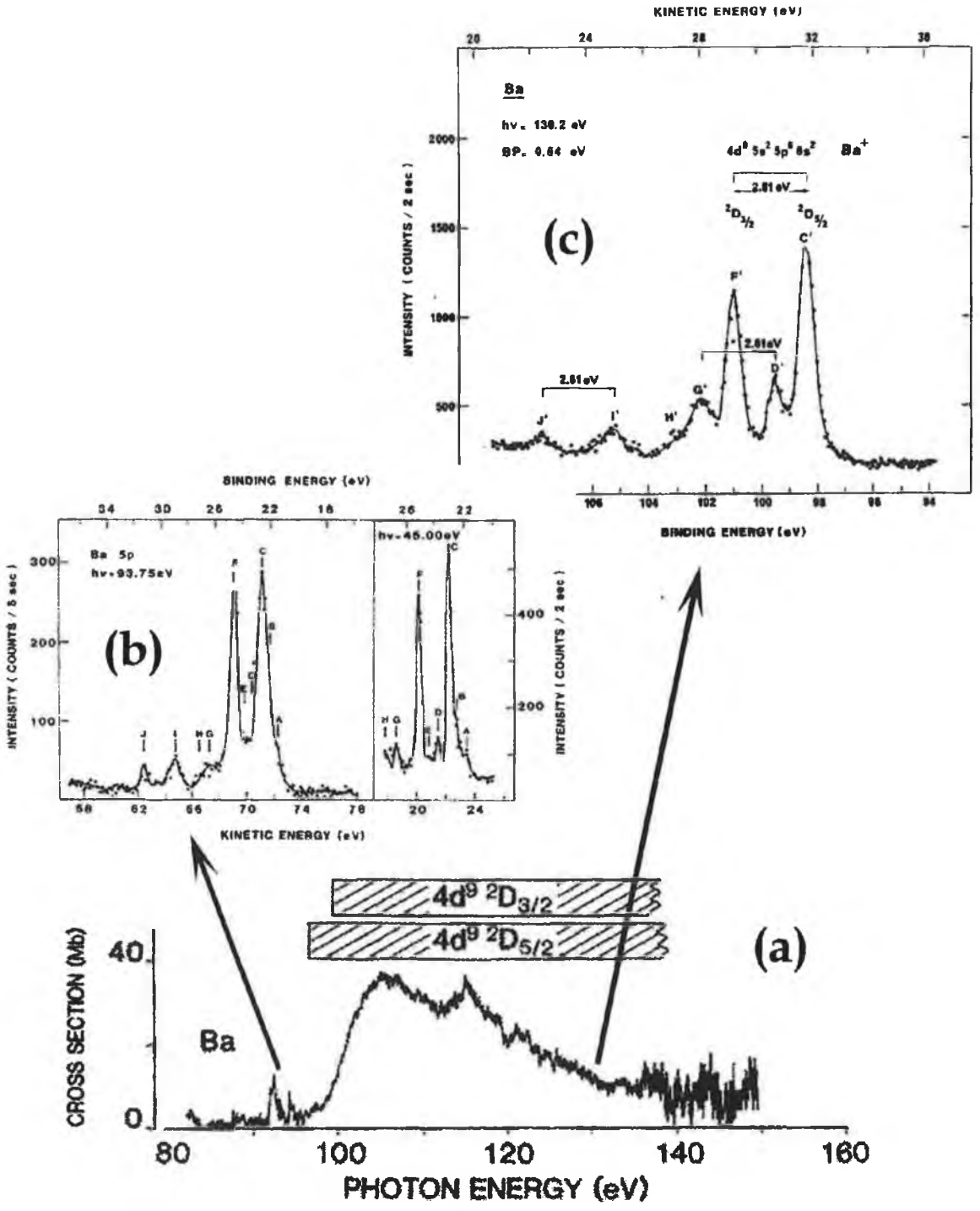

Figure 1.3 : An illustration of the contrast between photoabsorption and photoelectron spectroscopies where (a) is the total absorption cross section for neutral barium as measured by Lucatorto et al 1981 ; (b) is the photoelectron spectrum resulting from ionisation in the 5p subshell of neutral barium recorded for an incident photon energy of 93.75eV (Bizau et al 1989) and (c) is the photoelectron spectrum resulting from ionisation in the 4d subshell recorded at a photon energy of 130.2eV (Bizau et al 1989).

and (c) show how photoelectron spectroscopy can probe the unique partial cross sections or put another way, the *individual* contributions to the absolute cross section. Further scrutiny of figure 1.3 shows how the strength of the photoelectron technique is obvious when measurements of binding energies are considered. From figure 1.3(a), the $4d^9\ ^2D_{5/2,3/2}$ ionisation limits can only be inferred via measurement of discrete series running up to these thresholds. However, examination of figure 1(c) shows an increased intensity for photoelectron peaks corresponding to these limits which allows the limits' *direct* determination. Furthermore, by scanning the incident photon energy, study of the resultant electrons allows observation of an increasing number of atomic energy levels as with increasing photon energy, more and more atomic energy levels are accessed, this being manifested by kinetic energy peaks in the electron spectrum. Indeed, the best of both worlds is there for the taking, total absorption cross sections being easily extracted by summing the partial cross sections for each photon energy. Of course, this process assumes the absence of energy loss by means of photon emission through fluorescence because in the XUV, autoionisation and Auger decay far outweigh fluorescence decay (Sonntag and Zimmermann 1992). Therefore, equation [1.5] holds very well.

Despite the advantages of both the photoelectron and photoion techniques outlined above, photoabsorption studies and in particular photoabsorption by way of dual laser plasma techniques is and will remain competitive for some time into the future due to the ease with which multiply charged ions can be generated and studied. The low photon flux available in one pulse of SR (Wuilleumier 1994) means that probing short-lived plasmas is a difficult business. Not so, with laser plasma sources which are very intense and have lifetimes of the order of the laser pulse itself i.e. nanoseconds. With these advantages in mind, let us now turn to the physics behind laser plasmas as before their use in spectroscopic applications, an understanding of their underlying principles is essential.

1.2 Plasmas

As remarked upon by Hora (1991), many of the basics in laser-plasma physics were established in the 1960's and 70's, following the advent of the laser. As these results are still valid today, it should therefore not be surprising that many of the references given in the following sections relate to the experimental results and theory from the aforementioned era.

1.2.1 Plasma properties

Put simply, plasma is matter in a state of ionisation, either partial or complete. Neutral matter transformation into plasma requires the absorption of energy in order that electrons be stripped from the atoms leaving a residual assembly of ions and electrons. Although now separated, the ions and electrons are assumed to retain overall neutrality such that

$$n_e = \sum_z n_z . z \qquad [1.6]$$

where n_e is the electron density and n_z is the density of ions of charge state z. It is this criterion of ions and electrons, opposite in charge, that allows plasma to possess its unique characteristics. With neutral matter, interactions between neighbouring particles are weak and short ranged. With plasma, Coulomb forces are both strong and long ranged, allowing particle interaction over relatively large distances and giving rise to plasma's signature 'Collective' response to any perturbing influences.

To quantify the concept of 'Collective phenomena', let us define the Debye length λ_D, as the distance over which the electric field of an individual charge extends before it is counterbalanced by surrounding oppositely charged species. It is calculated (in metres), assuming shielding by electrons only, (Bekefi 1976) using,

$$\lambda_D = \left(\frac{\varepsilon_0 T_e}{n_e e}\right)^{\frac{1}{2}} = 7.43x10^3 \left(\frac{T_e}{n_e}\right)^{\frac{1}{2}} \qquad [1.7]$$

where T_e(eV) is the electron temperature and n_e(m^{-3}) is the electron density. Only beyond the Debye length are collective phenomena important and dominating. Hence, in terms of the linear extent of the plasma L it can be stated that

$$L >> \lambda_D \qquad [1.8]$$

is a necessary criterion for a system to meet before it may be regarded as plasma. It must also be assumed that the number of particles within a sphere of radius λ_D must be far greater than unity i.e.

$$N_D = \frac{4}{3}\pi n_e \lambda_D{}^3 = 1.72x10^{12}\frac{[T_e(eV)]^{\frac{3}{2}}}{[n_e(m^{-3})]^{\frac{1}{2}}} >> 1 \qquad [1.9]$$

Another striking property of plasmas is the inherent plasma frequency ω_p, at which either the ions or the electrons oscillate. In this case, let us consider the electrons only.* Thus, it can be stated that

$$\omega_p(Hz) = \left(\frac{n_e e^2}{m_e \varepsilon_0}\right)^{\frac{1}{2}} = 56.4 n_e{}^{\frac{1}{2}} \qquad [1.10]$$

where again n_e is in metres^{-3}. It is this natural frequency which determines the response of the plasma to incident radiation and energy transfer from incident EM waves can be greatly enhanced at these resonant frequencies. Furthermore, it can be shown by application of a dispersion relationship describing EM waves propagating through a plasma, that only for frequencies $\omega > \omega_p$ will the wave propagate, otherwise reflection occurs. The critical density n_c at which this reflection takes place is given by

$$n_c = \frac{\varepsilon_0 m_e \omega_p{}^2}{e^2} = 3.14x10^{-4}\omega_p{}^2 \qquad [1.11]$$

and this threshold is an important parameter in the creation and lifetime of a laser produced plasma as we shall see later.

---

*To obtain the ionic oscillation frequency the electron mass m_e is replaced by the ionic mass m_i of interest.

1.2.2 Atomic processes in plasmas

The emission and absorption of light within a plasma can be attributed to various processes, those of primary concern here being Bound-Bound(BB) transitions, Free-Bound(FB) transitions and Free-Free(FF) transitions. A convenient method of distinguishing the above is by way of an energy level diagram such as that shown in Figure 1.4 (Cooper 1966) and we will discuss the primary processes in terms of the labelling found therein. Because plasmas exhibiting a degree of ionisation in excess of a few percent are dominated by electron-ion collisions, processes due to atom-atom, atom-ion and ion-ion collisions are not dealt with. Using Figure 1.4 as a guide and adopting the nomenclature of Bates, Kingston and McWhirter (1962a,b), the relevant physical processes are as follows, where z is the charge state and p and q denote different levels of S_{z-1}.

(a) Three-body recombination

$$S_z + e + e \rightarrow S_{z-1}(p) + e \qquad \text{(FB)} \qquad [1.12]$$

(b) Collisional ionisation

$$S_{z-1}(p) + e \rightarrow S_z + e + e \qquad \text{(FB)} \qquad [1.13]$$

(c) Dielectronic recombination

$$S_z + e \rightarrow S_{z-1}(p)^{**} \qquad \text{(FB)} \qquad [1.14]$$

(d) Autoionisation

$$S_{z-1}(p)^{**} \rightarrow S_z + e \qquad \text{(FB)} \qquad [1.15]$$

(e) Radiative recombination

$$S_z + e \rightarrow S_{z-1}(p) + h\nu \qquad \text{(FB)} \qquad [1.16]$$

(f) Photo-ionisation

$$S_{z-1}(p) + h\nu \rightarrow S_z + e \qquad \text{(FB)} \qquad [1.17]$$

(g) Collisional de-excitation

$$S_{z-1}(p) + e \rightarrow S_{z-1}(q) + e \qquad \text{(BB)} \qquad [1.18]$$

(h) Collisional excitation

$$S_{z-1}(q) + e \rightarrow S_{z-1}(p) + e \qquad \text{(BB)} \qquad [1.19]$$

(i) Spontaneous and Stimulated emission

$$S_{z-1}(p) \rightarrow S_{z-1}(q) + h\nu \qquad \text{(BB)} \qquad [1.20]$$

(j) Photo-excitation

$$S_{z-1}(q) + h\nu \rightarrow S_{z-1}(p) \qquad \text{(BB)} \qquad [1.21]$$

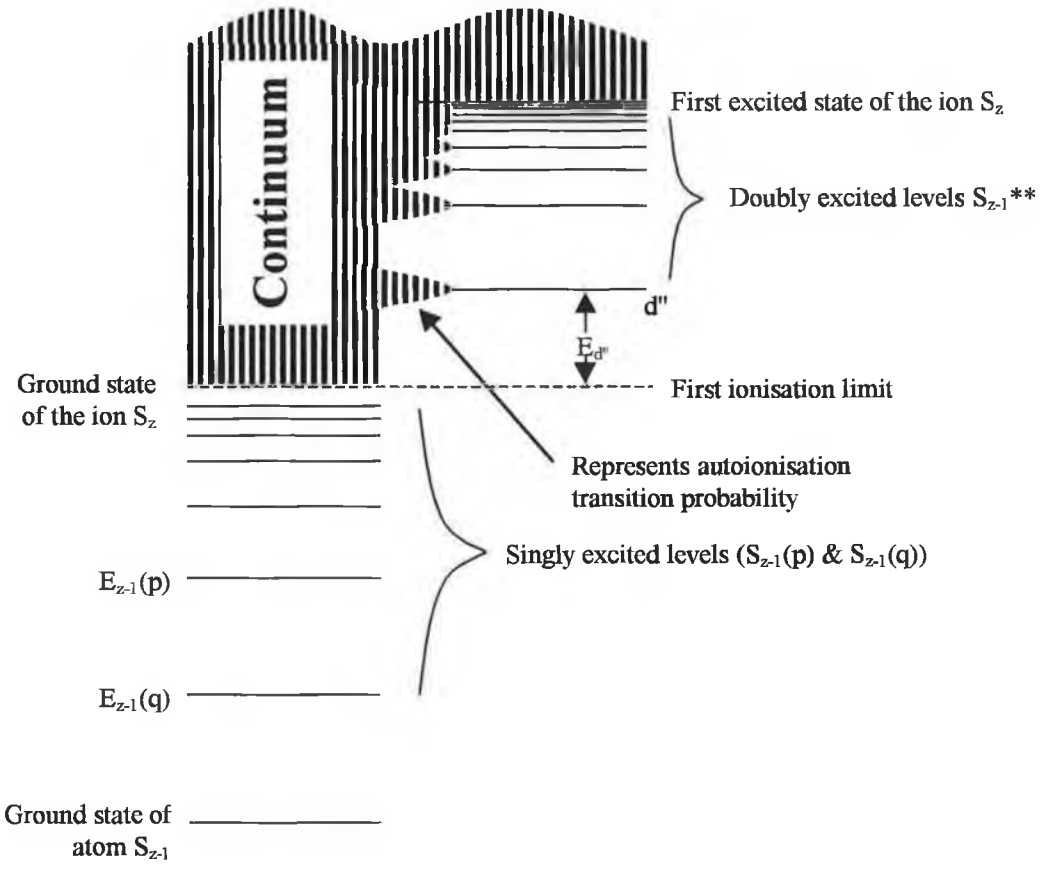

Figure 1.4 : Schematic energy level diagram(after Cooper 1966) for a non-hydrogenic species of charge z-1(S_{z-1}) showing singly and doubly excited states (S_{z-1}(p, q) and S_{z-1}** respectively).

It must be noted that for each recombination process, an inverse ionisation process exists such that in the above list (a) and (b), (c) and (d), (e) and (f), (g) and (h) and (i) and (j) are reciprocal pairs which occur in detailed balance only when the plasma is in complete thermodynamic equilibrium, a state rarely approached in terrestrial plasmas. In the hydrogenic case, only processes (a), (b) and (e) to (j) are important. However, when a non-hydrogenic species is considered, the additional processes of (c) and (d) become active as with more than one electron in the atom there is more than one ionisation stage possible. A special case of process (d) or *autoionisation* is when it occurs from a state that involves a hole in an inner subshell of the core and this is known as the *Auger effect*. The

ejected electron is called an Auger electron. Processes (a) and (e) can produce the recombined atom S_{z-1} directly in the ground state or alternatively they can produce an excited state which can then decay to the ground state by collisional or radiative de-excitation. Although three-body recombination (process(a)) is unimportant for low density plasmas ($n_e < \sim 10^{20} cm^{-3}$ for $T_e > 100eV$) as the rate is proportional to n_e^2, it becomes considerably more probable with increasing electron density whereupon it competes vigorously with radiative recombination. On the other hand, dielectronic recombination necessarily produces an excited state lying above the first ionisation limit, which can then either re-ionise via autoionisation or decay by collision or radiation (Cowan 1981)

So far, we have only considered BB and FB transitions, the bound-bound transitions producing line radiation and the free-bound transitions responsible for a continuous emission spectrum with a fairly sharp low frequency cut-off, this being known as the recombination limit (Hughes 1975). The remaining category of transitions are known as free-free and give rise to what has been termed Bremsstrahlung radiation. It occurs when a free electron collides with another particle and makes a transition to another free state of lower energy with the emission of a photon. The Bremsstrahlung radiation is continuous and the inverse mechanism is known as inverse-Bremsstrahlung. Both of these processes are of particular importance for laser produced plasmas.

1.2.3. Plasma models

Due to the dominant role of electrons in collisional processes, the electron number density n_e and electron temperature T_e are used for meaningful description of species populations and of their respective energy levels. Other plasma properties are often described in terms of n_e and T_e as well (Cooper 1966). In the kinetic theory of gases, the equilibrium velocity distribution of particles is Maxwellian. From this distribution, an electron temperature T_e can be ascertained but in order for the statistics of this process to be valid, the mean free path for particle collisions must be greatly exceeded by the dimensions of the confinement chamber and the time between collisions must be short compared to the times associated with mechanisms such as particle heating. In many laboratory plasmas, including those produced by lasers, these criteria are met to such an

extent that the free electrons can indeed be considered to follow a Maxwellian velocity distribution. This is not the case for ions. Thus, the ion temperature is often of little meaning.

Apart from the kinetic energy of the particles in a plasma, the radiation field energy must be considered. When radiation cannot escape from the plasma due to re-absorption within, the plasma can be deemed to be optically thick (see section 1.4) and a state of complete thermodynamic equilibrium is said to pertain. Within this idealised model the following conditions can be shown to apply :

(a) As mentioned in section 1.2.2., each transition occurs at an equal rate in both directions according to the principle of detailed balance (Hughes 1975).

(b) The ion distribution is given by Saha's equation (McWhirter 1965) i.e.

$$\frac{n_z n_e}{n_{z-1}} = 2\left(\frac{2\pi m_e kT_e}{h^2}\right)^{\frac{3}{2}} \cdot \frac{w_z}{w_{z-1}} \cdot \exp\left(\frac{\chi_{z-1,g}}{kT_e}\right) \qquad [1.22]$$

where n_z and n_{z-1} are ion stage populations, w_z and w_{z-1} are the statistical weights associated with levels within these ion stages and $\chi_{z-1,g}$ is the ionisation potential of the ion of charge $z-1$ in its ground level g.

(c) The population densities of bound levels are given by the Boltzmann equation i.e.

$$\frac{n(p)}{n(q)} = \frac{w(p)}{w(q)} \cdot \exp\left(-\frac{\chi(p,q)}{kT_e}\right) \qquad [1.23]$$

where $n(p)$ and $n(q)$ are the populations of states labelled p and q respectively and $\chi(p,q)$ is the energy difference between levels p and q which could equally be represented by $\hbar w$.

(d) As mentioned previously, the free electron velocity distribution is Maxwellian. Thus, the number of electrons with velocities between v and v+dv is given by (Hughes 1975, McWhirter 1965) :

$$dn_e(v) = 4\pi n_e \left(\frac{m_e}{2\pi kT_e}\right)^{\frac{3}{2}} \cdot \exp\left(\frac{-m_e v^2}{2kT_e}\right) \cdot v^2 dv \qquad [1.24]$$

(e) The intensity distribution as a function of frequency and temperature is given by Planck's law(Carroll and Kennedy 1981).

Unfortunately, complete thermodynamic equilibrium as applies in the ideal case of a blackbody radiator does not obtain in common laboratory plasmas, the very fact that radiation is emitted being testimony to this. Thus, approximations must be made to simplify the situation. The three primary models based on approximations applicable to different electron density regimes are Local Thermodynamic Equilibrium(LTE), Coronal equilibrium and Collisional-Radiative equilibrium.

1.2.3.1 Local Thermodynamic Equilibrium (LTE)

As collisions become more frequent as the plasma density increases, collisional effects become overwhelmingly dominant over radiative effects and one can consider the possibility of detailed balance between collisional processes alone, the collisions occuring so rapidly that the distribution of electron population densities responds instantaneously to any change in the plasma conditions. Thus, the distribution is the same as it would be in a system under complete thermodynamic equilibrium and can be described using conditions (b) to (d) of section 1.2.3. However, the radiative distribution, is no longer suited to description via Planck's law.

Since the electrons possess a greater velocity, they are therefore the most efficient particles in causing collisional transitions and it is the electrons' collision rates that are of interest(McWhirter 1965). To this extent, the electron density and temperature are again the prominent parameters, their significance highlighted by McWhirter in deriving a condition for which LTE may be assumed to hold i.e.

$$n_e \geq 1.6x10^{12}.T_e^{1/2}.\chi(p,q)^3 cm^{-3} \qquad [1.25]$$

where T_e is measured in °K and $\chi(p,q)$ in eV.

1.2.3.2. Coronal equilibrium

In attempting to explain some features found in solar corona spectra, an atomic model was developed which is also applicable to low density laboratory plasmas. This model was appropriately named the Coronal equilibrium model and its prime *raison d'être* is that instead of collision processes being balanced by their inverse actions, as in LTE, it

argues that the balance is now achieved through equalisation of collisional ionisation and radiative recombination. In order for this assumption to qualify, a necessary requisite is that the plasma is optically thin (see section 1.4), radiation escaping it without being re-absorbed such that a balance between excitation via photon absorption and radiative de-excitation is not obtained. Furthermore, if one considers that the rate of collisional ionisation is proportional to n_e and its inverse process, three body recombination, is proportional to n_e^2(as already mentioned in section 1.2.2.), then because the rate of radiative recombination is also proportional to n_e, it follows that it becomes more important as n_e drops. The fact that both collisional ionisation and radiative recombination have an n_e dependence means that the populations of various ion species is independent of n_e, this being shown via the general result of McWhirter (1965) which states that

$$\frac{n_{z-1}}{n_z} \approx 8x10^{-9}.\chi_{z-1,g}^{11/4}.(kT_e)^{-3/4}.\exp\left(\frac{\chi_{z-1,g}}{kT_e}\right) \qquad [1.26]$$

It has been emphasised by McWhirter that in order for the coronal model to describe the emission from plasmas with any degree of accuracy, n_e must be sufficiently low for collisional transitions from an excited state to be slower than radiative decay. As the principal quantum number n increases, the probability of spontaneous radiation falls but the collisional transition probability rises implying that once n exceeds a certain value, the model breaks down. With this in mind and restricting n to 6, McWhirter formulates the following expression for n_e's below which the model is valid for Hydrogen-like ions of charge z.

$$n_e < 5.6x10^8.(z+1)^6.T_e^{1/2}.\exp\left[\frac{1.162*10^3(z+1)^2}{T_e}\right] cm^{-3} \qquad [1.27]$$

where T_e is in $^{\circ}K$.

1.2.3.3. Collisional-Radiative Equilibrium

With the LTE model applying at high electron densities and the Coronal model suited to description of low electron density plasmas, there was a medium density range which defied adequate description until Bates, Kingston and McWhirter (1962a,b) introduced

what they christened the Collisional-Radiative(CR) model. Their CR model modified the Coronal model by taking into account collisional transitions from the higher bound levels and also allowing for three-body recombination. Embracing collisional processes between the upper levels was particularly important as the coronal model assumes all atoms and ions to be in their ground states and only treats collisional excitation from such states. However, as medium electron densities are approached, this assumption of predominant ground state populations is no longer suitable.

Although a thorough treatment of the core essence of the CR model is given by Bates et al (1962a,b) and by McWhirter (1965), we will refine further discussion to the specific treatment of laser produced plasmas as presented by Colombant and Tonon (1973) who assumed CR equilibrium as the ionisation model to describe X-ray emission from both Carbon and Uranium plasmas. They discuss the applicability of the three main ionisation models in terms of n_e and T_e, assuming that the plasma is optically thin to its radiation. Graphically, the applicability of each model is conveniently displayed in Figure 1.5 where it can be seen that the CR model applies, for example, at $n_e = 10^{21}cm^{-3}$ for $T_e \geq 10eV$ and at $n_e \sim 10^{19}cm^{-3}$ for $T_e \sim 3eV$. Figure 1.5 shows how both Nd *and* CO_2 laser generated plasmas might be described within T_e, n_e regimes but we shall only focus on Nd:YAG laser generated plasmas due to their applicability to this work.

For Nd:YAG laser generated plasmas, the following conclusions were drawn :

(a) The LTE model applies for low ionisation stages (z < 10).

(b) The Coronal model applies for high z stages (z > 30).

(c) The CR model generally applies to the z stages covered by both (a) and (b).

In the case of the CR model, the rate equation for any given ionised state can be given (assuming stationary state conditions) as

$$\frac{n_{z+1}}{n_z} = S(z,T_e)/[\alpha_r(z+1,T_e)+n_e\alpha_{3b}(z+1,T_e)] \qquad [1.28]$$

where $S(z, T_e)$ is the collisional ionisation coefficient, given by

$$S = \frac{9x10^{-6}\xi_z(T_e/\chi_z)^{1/2}}{\chi_z^{3/2}(4.88+T_e/\chi_z)}.\exp(-\chi_z/T_e)cm^3s^{-1} \qquad [1.29]$$

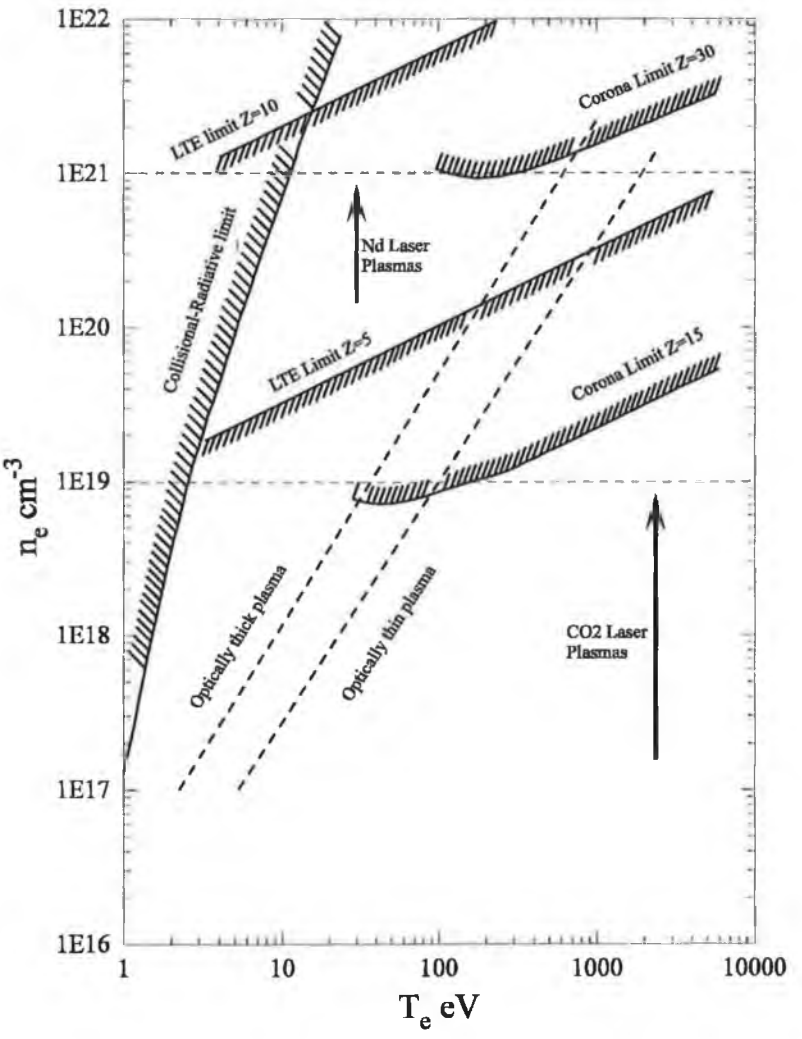

Figure 1.5 : Electron density and temperature requirements for applicability of different ionization models (After Colombant and Tonon 1973).

$\alpha_r(z, T_e)$ is the radiative-recombination coefficient, given by

$$\alpha_r = 5.2x10^{-14}(\chi_z/T_e)^{1/2}.z.\begin{bmatrix}0.429+0.5\log(\chi_z/T_e)\\+0.469(T_e/\chi_z)^{1/2}\end{bmatrix} cm^3 s^{-1} \quad [1.30]$$

and $\alpha_{3b}(z, T_e)$ is the three-body recombination coefficient, given by

$$\alpha_{3b} = \frac{2.97x10^{-27}\xi_z}{T_e\chi_z{}^2(4.88+T_e/\chi_z)} s^{-1} \quad [1.31]$$

It must be noted that χ_z is the ionisation potential and ξ_z is the number of electrons in the outermost shell of the ion of charge state z.

From equation [1.28], the fractional ionic abundance $n_z \Big/ \sum_{k=1}^{z} n_k$ can be calculated as a function of T_e for any chosen n_e. This has been done for Calcium for $n_e = 1\text{x}10^{20}\text{cm}^{-3}$ as can be seen in Figure 1.6.

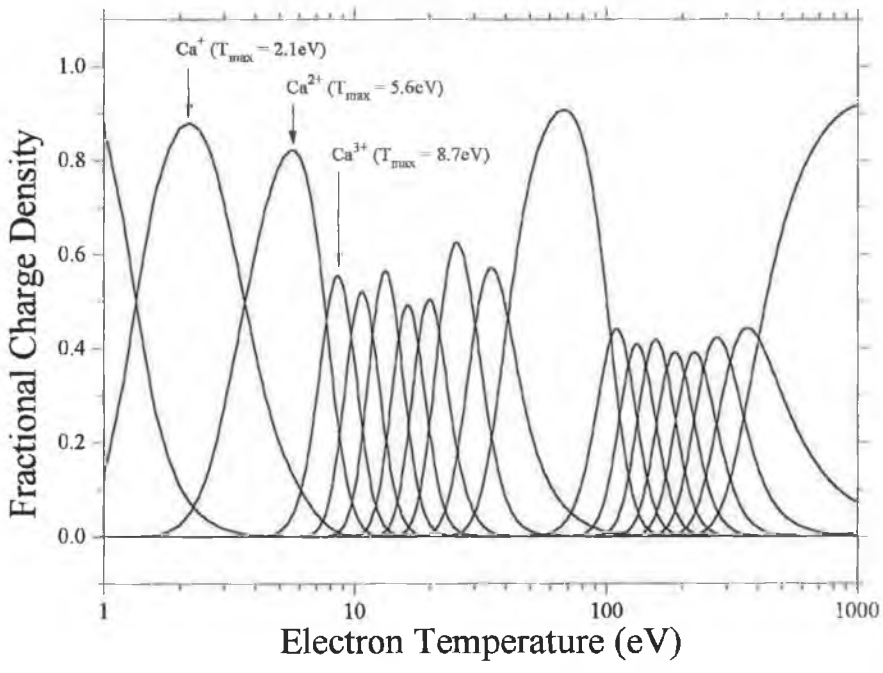

Figure 1.6 : Fractional charge densities as a function of temperature for Calcium with n_e = $1x10^{20}cm^{-3}$, computed using equation [1.28] above.

As we shall see in Chapter 3, for calcium we have only been concerned with ion stages of $z \leq 3$ and this implies that the LTE model is also applicable (see figure 1.5). Using the Saha equation (equation [1.22]) which holds for the LTE model, we have recalculated the fractional ionic abundance for calcium and as expected, for $n_e = 1\text{x}10^{20}\text{cm}^{-3}$, we obtain temperatures of 1.8, 4.5 and 8.0eV for Ca^{+}, Ca^{2+} and Ca^{3+}, respectively, which are very similar to those predicted using the CR model (see figure 1.6). Aside from equation [1.28], which was especially useful in providing insight as to the likelihood of successful ion stage isolation in our experimentation together with reasonable estimates of the n_e and T_e's produced in the plasma, Colombant and Tonon (1973) have provided further simplifications derived from the assumption of stationary states being achieved within the lifetime of the plasma generating laser pulse. For $T_e \geq 30$eV, they have shown that $n_e\alpha_{3b} << \alpha_r$ and thus the relation

$$z \approx \tfrac{2}{3}[AT_e(eV)]^{1/2} \qquad [1.32]$$

holds, where A is the atomic number of the element under consideration. They add as a stipulation that the relation applies better to heavier elements than to lighter ones.

1.2.4. Plasma formation and evolution

When laser light is incident on an opaque solid target, many interesting outcomes, dependent on the irradiance of the light, are seen to occur. The formation of a plasma on or near the target surface is one of such possible outcomes but this is dependent on many parameters including the laser pulse duration and the thermal, optical and mechanical properties of the target material which in their own right exhibit pressure and temperature dependencies. Changes of phase, vaporisation pressure, thermionic emission and shock wave generation all play important roles in an adequate description of the light/matter interaction and the presence of each of these factors must be accounted for within the context of the incident laser irradiance considered.

If one considers low irradiances ($I < 8\text{x}10^{10}\text{Wm}^{-2}$) impinging on a target, it is found that some of the light is reflected and the rest absorbed; the electrons in the target's conduction band being raised to higher energies, these then colliding with other electrons and phonons with the net result being a rise in temperature. The degree by which a temperature increase is felt can be estimated by considering the *Skin depth* of the target material in question. This is the depth to which the EM radiation of the incoming laser light can permeate into the solid and it is given by (Lochte-Holtgreven 1995)

$$\delta = (\pi \nu \mu_0 \sigma)^{-1/2} \qquad [1.33]$$

where μ_0 is the permeability of free space, σ is the electrical conductivity in Mhos m^{-1} or $(\Omega.m)^{-1}$ and ν is the frequency of the laser radiation. As an example if we consider aluminium, its skin depth is found to be ~5nm if one uses the light produced by a Nd:YAG pulsed laser with $\lambda = 1.06\mu m$. As a further demonstration, the conduction of heat over distances not greater than microns has been conveniently plotted by Ready (1965) for the case of a semi-infinite copper target (see Figure 1.7).

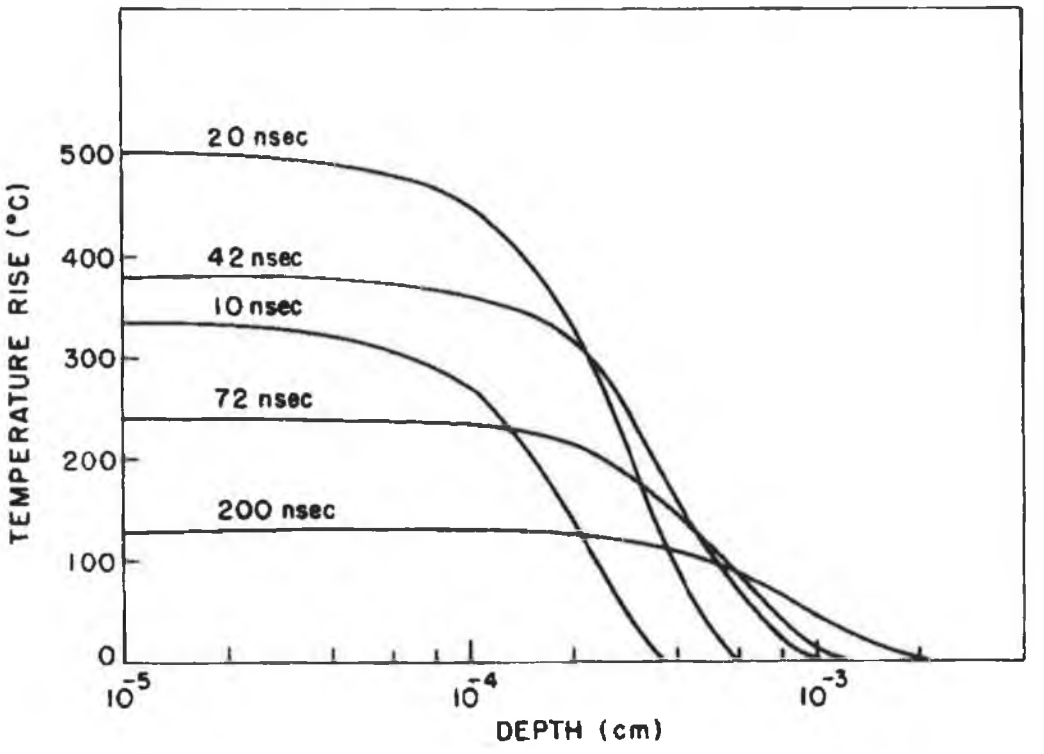

Figure 1.7 : Temperature rise as a function of depth caused by absorption of a Q-switched laser pulse in copper. Note how rapid the rate of cooling is with a reduction in temperature of 75% after 200ns (after Ready 1965).

The next stage in the heating process, provided the incident irradiance is high enough, involves a phase change of the target surface as it enters a melting phase. This region is of particular interest for applications such as laser welding, the subject having been treated in some detail by Ready (1971). However, with regard to plasma production, this transient liquid phase is not of great importance (Hughes 1975) although it has been shown to facilitate a marked increase in the rate of heating due to changes in the material's optical characteristics whereby reflectivity decreases in an almost discontinuous fashion allowing increased coupling of energy into the target surface. This effect has been illustrated in Figure 1.8.

The final phase change a material may undergo during exposure to a high irradiance laser pulse is that of vaporisation. This occurs once the boiling point has been reached. As the boiling point is highly pressure dependent, one must be cautious with

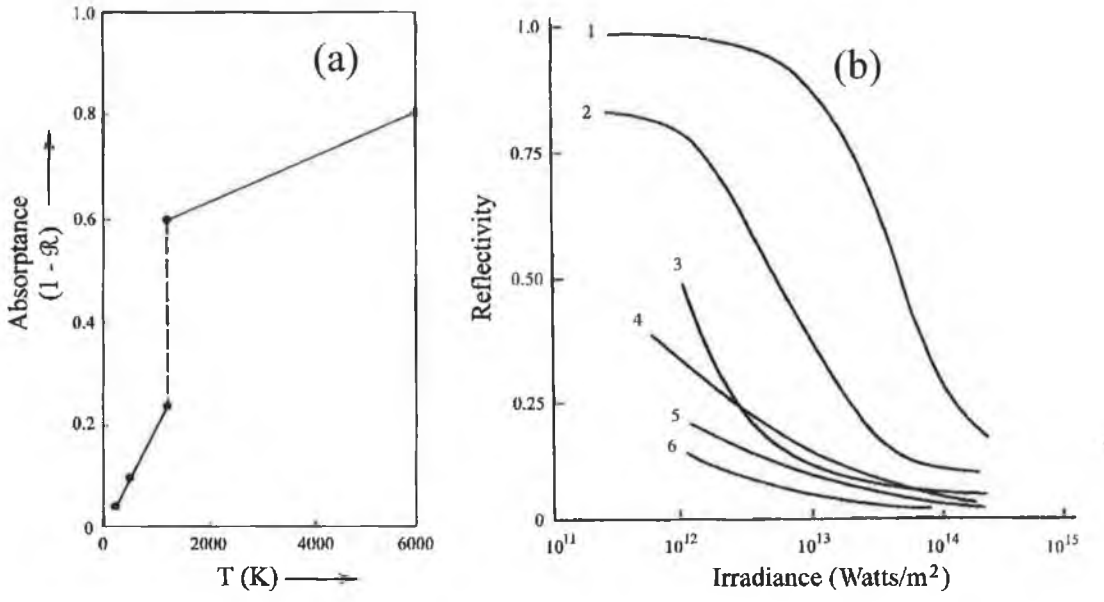

Figure 1.8 :The effect of high power laser pulses on the optical characteristics of surfaces where (a) illustrates the temperature dependence of absorptance of a silver surface (after Hughes 1975) and (b) shows the dependence of reflectivity on the irradiance of a Q-switched laser pulse ; 1=Teflon, 2=Aluminium, 3=Tin, 4=Copper, 5=Ebonite and 6=Carbon (after Ready 1971).

assignment of a specific boiling point temperature without considering both the radiation pressure (P_r) exerted by the incident beam (~300Atm or $3x10^5$mbar for 100MW absorbed over an area of $10^{-4}cm^2$) and the subsequently greater pressures ($>10^4.P_r$) arising due to recoil on the surface from departing particles known as the ablation pressure(P_a) (Hughes 1975).

With the onset of vaporisation, the initial vapour layer, via the few electrons it contains, will begin to absorb the incident light through free-free transitions arising from collisions with neutral atoms, these being the dominant species. As the temperature rises, more and more electrons are stripped from the vapour atoms leaving positive ions, their increasing presence in the vapour enabling us to now label it a plasma. A high density of free electrons now established, the absorption rate of light from the radiation field begins to escalate dramatically, inverse bremsstrahlung through electron-ion collisions soon becoming prevalent.

Pausing momentarily before discussing what happens to the plasma after initiation, let us consider the surface of the metal and how the vaporisation process is affected by the formation of this absorbing plasma shield in front of it. Ready (1971) has provided a schematic illustration of how the vaporisation process proceeds with time in relation to the length of the laser pulse (see Figure 1.9). It is seen that following initial vaporisation and plasma formation, the majority of the incident energy is now absorbed by the plasma, the target surface effectively cut off for a considerable fraction of the laser pulse. However, as the pulse nears the end of its lifetime, the plasma becomes so hot that thermal re-radiation is active. Some of this plasma radiation may reach the surface and cause further vaporisation. Thus, in terms of efficient target vaporisation, it can be said that a given amount of energy deposited at very high power is less effective than the same amount delivered via a longer, lower power pulse.

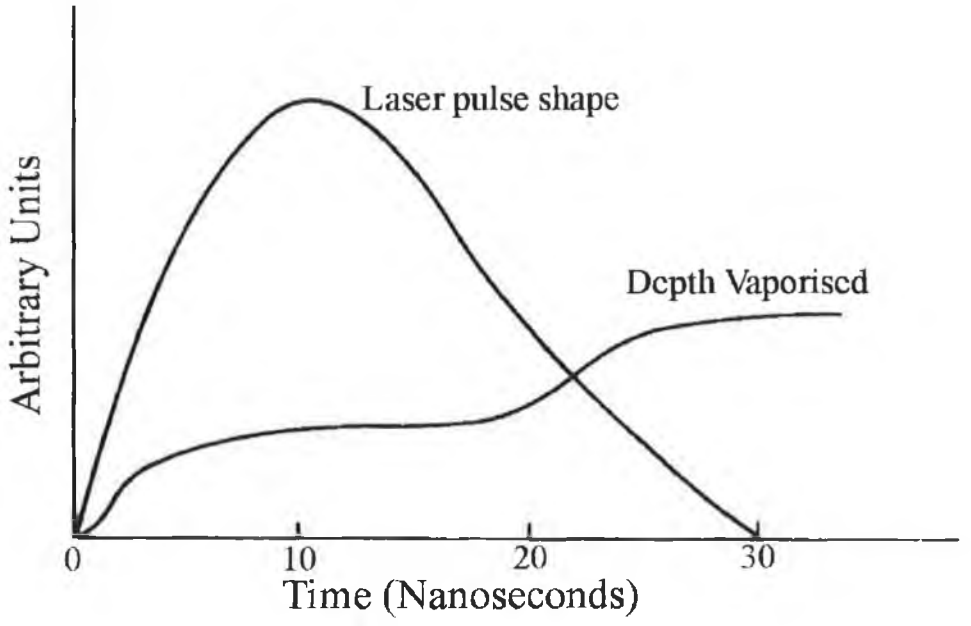

Figure 1.9 : Schematic representation of the depth vaporised in a metal target as a function of time by a high irradiance pulse with indicated pulse length (after Ready 1971).

Returning to a description of events beyond the target surface, we find that the absorption coefficient of the plasma formed by Inverse Bremsstrahlung is given by (Johnston and Dawson 1973)

$$K = 7.8x10^{-9}.\frac{zn_e^{\,2}\ln\Lambda(\nu)}{\nu^2(k_B T_e)^{3/2}}.\frac{1}{\left(1-(\nu_p^{\,2}/\nu^2)\right)^{1/2}}\ (\mathrm{cm}^{-1})\ \ [1.34]$$

where z, $n_e(cm^{-3})$ and T_e have their usual meaning with $k_B T_e$ in eV. ν_p is the plasma frequency given by equation [1.10] where $\omega_p = 2\pi\nu_p$ and Λ is related to the electron-ion collisions with $\ln\Lambda$ usually having a value between 5 and 10 for laser produced plasmas (Carroll and Kennedy 1981). When Inverse Bremsstrahlung is beginning, $\nu >> \nu_p$ and $1/\left(1-(\nu_p^{\,2}/\nu^2)\right)^{1/2}$ may be regarded as unity meaning the absorption is dependent on n_e^2. However, as mentioned earlier, the increasing number of free electrons leads to increased ionization which produces even more electrons until eventually (over a period equivalent to a fraction of the 15-30ns pulse) n_e approaches the critical density n_c. Formed some distance into the plasma, this critical density layer reflects all laser radiation. Once the critically dense layer has formed, the incident radiation can no longer reach the target surface to produce more vapour, but instead, is absorbed in the dense layers preceding the critical front. This rapid absorption heats the plasma, the resulting pressures driving the plasma into vacuum. The expansion of this dense plasma means a rarefaction and the critical layer is no longer sustainable allowing light to again penetrate to the target surface. So this cycle continues throughout the lifetime of the pulse. This general description of the plasma dynamics is consistent with most laser produced plasmas.

It was not uncommon during the course of this work to have irradiances of up to $10^{16}Wm^{-2}$ incident on our targets. Irradiances of this magnitude produce considerable electric fields, the relationship defined by (Carroll and Kennedy 1981)

$$\overline{E} = 19.4\phi^{1/2} \qquad [1.35]$$

where ϕ is the irradiance in Wm^{-2} and $\overline{E}$ the r.m.s electric field strength in Vm^{-1}. With $\phi = 10^{16}Wm^{-2}$ equivalent to a field strength of $2x10^9\ Vm^{-1}$ and the field of a hydrogen nucleus at the Bohr radius equal to $5x10^{11}\ Vm^{-1}$, it is hardly surprising that startling interactions take place at the light/matter interface. Also, of considerable importance in plasma formation is the wavelength of the laser light employed. A direct relationship between it and the critical density has already been established but it has also been shown that the reflectivity at the plasma boundary is also highly laser wavelength dependent.

Assuming a plane wave incident perpendicularly on the plane boundary of an overdense, fully ionised plasma, the plasma to have a uniform temperature and that the plasma density increases monotonically from zero as we move toward the target, Hughes (1975) has shown that

$$\frac{\ln(R_{\omega 1})}{\ln(R_{\omega 2})} = \left(\frac{\omega_1}{\omega_2}\right)^4 = \left(\frac{\lambda_2}{\lambda_1}\right)^4 \qquad [1.36]$$

where $R_{\omega 1}$ is the reflectivity for incident light of frequency ω_1, its equivalent wavelength represented by λ. Using this equation, it is easily seen that comparing Nd:YAG (λ=1.06μm) light to that from a CO_2 laser (λ=10.6μm), we get (via the logarithm property $p.\ln q = \ln q^p$)

$$R_{Nd} = (R_{CO_2})^{10^4} \qquad [1.37]$$

meaning that plasma that is perfectly reflecting for CO_2 light i.e. $R_{CO2} = 0.999$, will hardly reflect any neodynium laser light since R_{Nd} will be $5x10^{-5}$. It can thus be concluded that short wavelength lasers are preferable for plasma heating.

Various models have been proposed which allow a quantitative description of the plasma behaviour. Two such models are illustrated in Figure 1.10. Puell (1970), assuming a self regulating plasma as described above and expanding on earlier models which dealt only with a one dimensional flow of plasma from the target surface, considered a model with three separate regions (see Figure 1.10(a)). Region I was the undisturbed target. Region II was a region of one dimensional flow at high density near the surface in which most of the heating takes place i.e the heating zone, and region III was a region of three dimensional flow which accounted for plasma expansion. Puell (1970) highlighted the finite extent of the focal spot, assumed region II only covered a distance from the target equal to the focal spot radius r_f, allowed for absorption of radiation in passing through less dense regions preceding the critical front and considered the target geometry to be a plane solid. In doing this, he was successful in extracting an expression relating irradiance to electron temperature i.e.

$$T_e \propto r_f^{2/9} \phi^{4/9} \qquad [1.38]$$

Using energy and momentum conservation, Puell also extracted expressions for the expansion energy of the ions and the total particle number in the plasma. The second

model, developed for higher incident irradiance, follows the quantitative analysis of Fauquignon and Floux (1970) for the case of solid deuterium where they consider the creation of a thin high temperature and high density absorbing layer called a deflagration front. According to their model, this deflagration front is responsible for the greater majority of incident radiation field absorption and it moves rapidly toward the target behind a shock wave of even greater velocity. Because the thin deflagration layer has only a small optical thickness, the self-regulating process no longer occurs (Hughes 1975). Figure 1.10(b) shows how the density, temperature and incident/reflected light irradiance varies within the model. Again, setting up equations for conservation of momentum and energy and also for total system particle number, Fauquignon and Floux could establish a relationship between irradiance and plasma temperature (assuming electron-ion temperature equalisation within the time duration of the laser pulse i.e. $T_e = T_i$) and also with the velocities of both deflagration and shock fronts such that

$$v_s = A\phi^{1/3} \qquad [1.39]$$

$$v_f = B\phi^{1/3} \qquad [1.40]$$

and $$T = C\phi^{2/3} \qquad [1.41]$$

where A and B are constants with A>B and C is a constant which depends on the plasma absorption coefficient. They were also able to determine the fraction of energy deposited into the various plasma processes and found that 85% went into the plasma, 10% to the shock wave and 5% into generation of radiation via Bremsstrahlung. Of the 85% of energy input to the plasma, 50% was deemed to be contained in the kinetic energy of expansion and 35% attributable to enthalpic energy which is equal to U + P.V where U=internal energy, P =pressure and V=volume.

A spectroscopic analysis of plasma dynamics has been presented by Boland et al (1968), whereby they studied the spectral intensity of both continua and discrete transitions arising from a polyethylene target exposed to a high power (ϕ = $2.9 \times 10^{15} Wm^{-2}$) laser pulse. Employing spatial resolution along an axis perpendicular to the target surface,

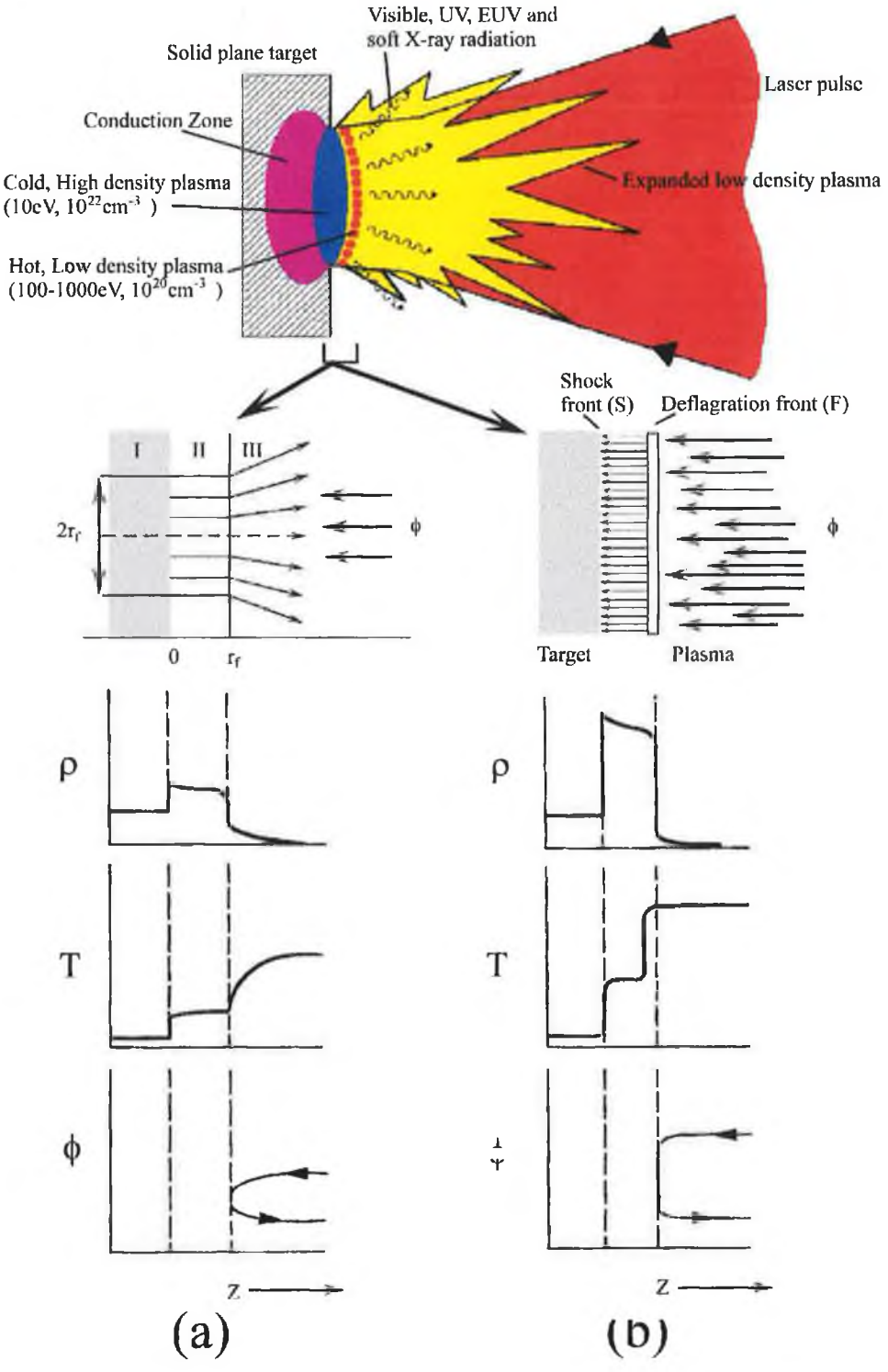

Figure 1.10 : Schematic illustration of plasma formation via high power laser pulse where (a) describes the system according to the model proposed by Puell (1970) and (b) shows the interpretation proposed by Fauquignon and Floux (1970).

they were able to extract electron temperatures as a function of distance from the target via measurement of free-bound C VI and C V continua between 20-35Å. T_e was found to drop rapidly in moving away from the target, decreasing from 90 to 12eV over a distance of only 2mm. Isolating lines representative of each ionic species of carbon, the time duration and time separation of each was recorded, the results suggesting the creation of highly ionised species first, followed by successively lower stages, significant intensities remaining for as long as hundreds of nanoseconds (See Figure 1.11). From their time and space measurements, velocities specific to each ion stage (assuming

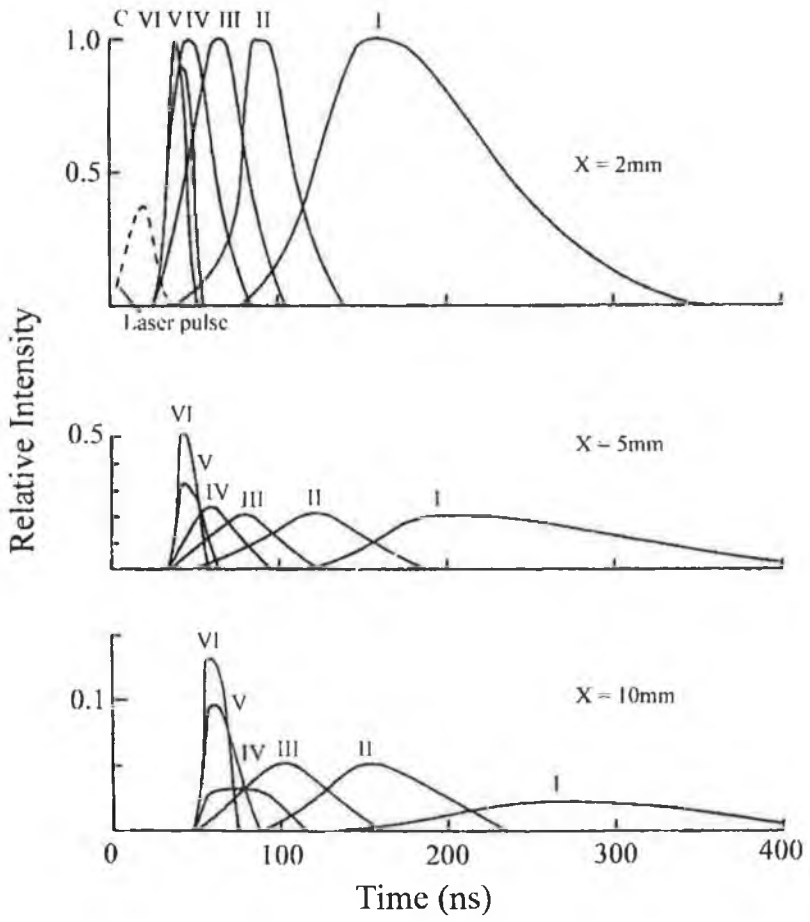

Figure 1.11 : The time and space evolution of C I-VI upon creation via a high power Ruby laser pulse incident on a polyethylene target in vacuum (after Boland et al 1968).

recombination not significantly reducing ion population densities over the duration of measurement) were extracted and ranged from $3.3 \times 10^7 cms^{-1}$ for C^{6+} to $0.7 \times 10^7 cms^{-1}$ for C^+. Further analysis via the Saha equation (equation [1.22]) and line intensity ratios led

to a determination of ion densities (~$10^{17}cm^{-3}$) which facilitated further calculations to infer the total number of carbon ions of all charges (~10^{16}). They also concluded that ~70% of the incident energy was converted to the kinetic velocity of the ions and that only approximately 3 to 6% of all carbon atoms vaporised, by the laser directly, were ionised.

In a continuation of this work, Irons et al (1972) extended the spectroscopic analysis from observations in the preferred direction of expansion (normal to target i.e X direction(see Figure 1.14 for axes definition)) and measured the 'radial' distribution, again via space and time resolved techniques. By observing carbon ion lines from directions normal to the surface and at right-angles to the normal, they were able to calculate the ion velocities via the Doppler shift ($v/c = \Delta\lambda/\lambda$) present in lines observed from the former direction and absent in the latter direction. The results supported the earlier time of flight measurements of Boland et al (1968), ion velocities being of the order of $10^{7}cms^{-1}$. Viewing selected line profiles parallel to the Z axis in the plane Y=0, they could infer radial velocities for the ions and viewing the plasma, again parallel to the Z axis but at different points Y from the X axis, they could determine the radial distribution of ions. Typical results of such scans are shown in Figure 1.12, movement across the Y axis taking place with X fixed at 1.6mm so as to ensure that the underlying continua, in existence near the target surface, did not engulf the line intensities.

Combining these results with a further study, now keeping the time(t) fixed at 45ns and varying the distance X at which movement through Y was monitored (see Figure 1.13), allowed Irons et al to conclude that the highest ion stages appear first, at the front of the plasma, and are followed by successively lower ion stages occupying conical annular regions of successively greater radii which approach the X axis at successively later times(see Figure 1.14). This observation of conical annular structure eliminated earlier speculations of ions forming a sequence of spherical shells. As a final remark, they suggest that this ion separation is inherent in the plasma formation, the decrease in ion charge away from the target normal and back along the normal being related to the decrease of focussed laser flux due to beam divergence/focussing aberrations and preferential absorption in the regions of plasma first encountered by the laser pulse, respectively.

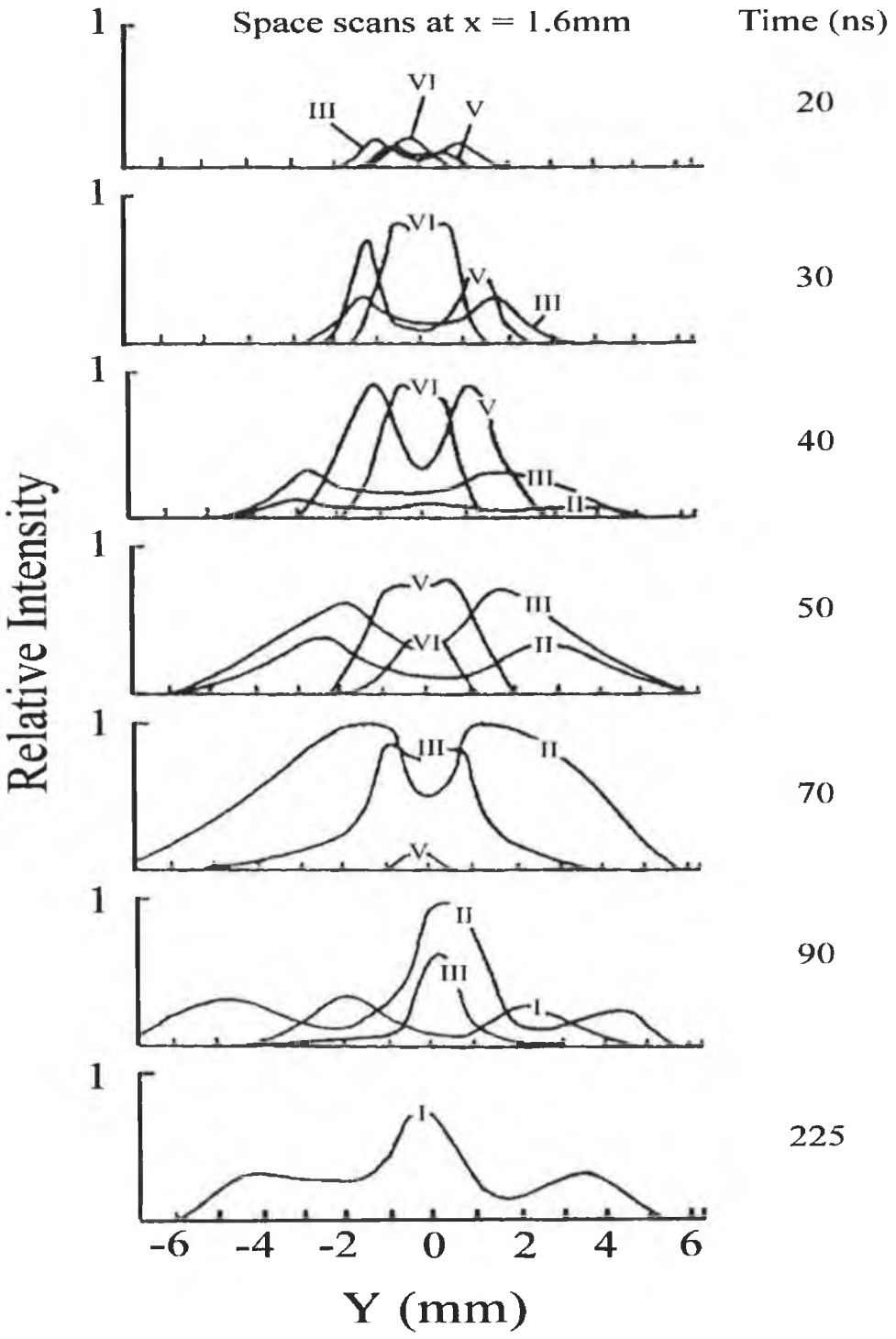

Figure 1.12 : A time sequence showing the spatial distribution development of C I-VI at X = 1.6mm. The peak laser intensity occurs at 20ns (after Irons et al 1972).

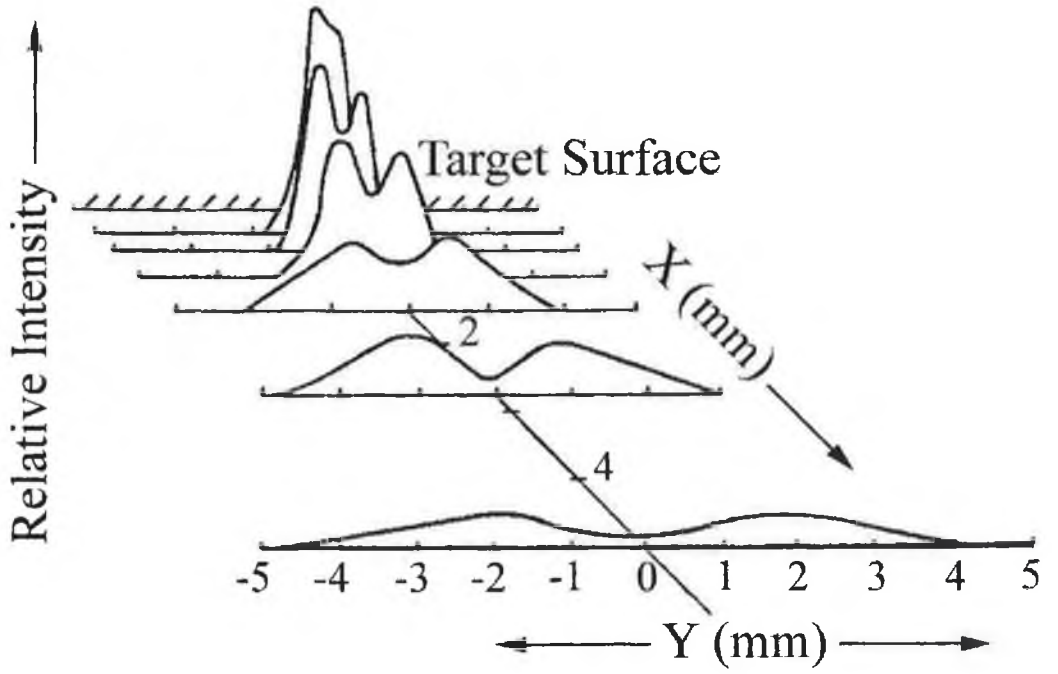

Figure 1.13 : The distribution of C V (obtained via the C V line at 2271Å) in the X, Y plane at t = 45ns (after Irons et al 1972).

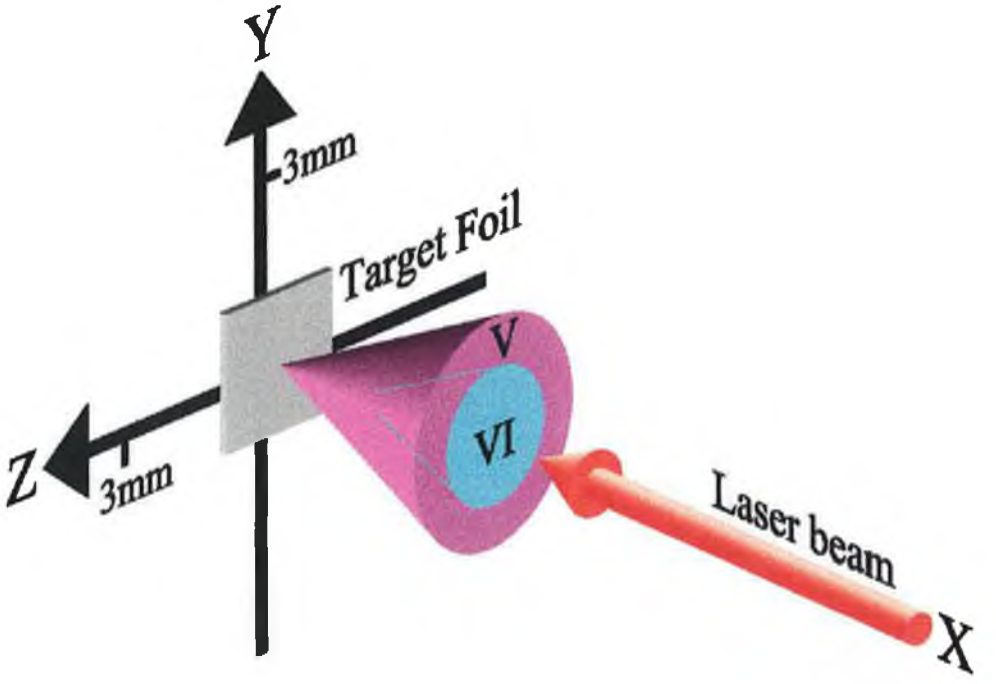

Figure 1.14 : An idealised picture of the spatial distribution of C V and C VI illustrating how the ion stages occupy conical annular regions with lower ion stages having greater expansion radii (after Irons et al 1972).

1.3 Autoionisation

In dealing with the atomic processes active in plasmas (section 1.2.2.), we mentioned the process of Autoionisation. Due to its significance, particularly in the XUV region and more specifically in relation to chapter 4 of this thesis, it is deemed appropriate to dwell for a short time on how this process manifests itself experimentally and also on how an adequate treatment of such phenomena may be undertaken.

1.3.1 A brief theoretical treatment of asymmetric resonances.

First coined by Shenstone in 1931, Autoionisation is the result of mixing, via configuration interaction, between configurations belonging to discrete and continuous spectra and can only occur at energy levels above the first ionisation threshold whereby both discrete and continuous configurations can coincide exactly in energy (Fano 1961). Generally, the resulting resonances can be grouped into two classes, these being, those due to one-electron excitation processes and those due to the simultaneous excitation of two electrons. Examples of each can be clearly seen with the Noble gases where if we consider neon we see that excitations such as $ns^2np^6\ ^1S_0 \rightarrow nsnp^6mp\ ^1P_1$ and $ns^2np^6\ ^1S_0 \rightarrow ns^2np^4mlm'l'$ illustrate the aforementioned classes respectively. Manifesting themselves in continuous absorption spectra as asymmetric peaks, autoionised levels defied suitable quantitative analysis until Fano's seminal publication in 1961, in which he likened their character to an *interference effect*. Fano, building on the implications of earlier applications of quantum scattering theory to nuclear reactions, diagonalised the hamiltonian* by mixing discrete and continuum states. By so doing, a quantum mechanical formalism with direct association to experimentally observed profiles was delivered. Several possible situations under which asymmetric resonances could be produced were treated, these being the interaction of (a) a single discrete state with a

---

*The hamiltonian operator must be diagonalised in order that the associated eigenvalue equation may be solved. See texts such as Bransden and Joachain (1990), Rae (1990) or Cohen-Tannoudji (1977) for detailed accounts of quantum mechanics and its many applications to atomic studies.

single continuum, (b) a single discrete state with two or more continua and (c) a number of discrete states with one continuum.

Concentrating on case (a) and initially using the He 2s2p ^{1}P resonance, measured by Silverman and Lassettre (1964) and later by Madden and Codling (1965), as a test case, it was found that it could be characterised by the formula

$$\sigma(\varepsilon) = \sigma_a\left[(q+\varepsilon)^2/(1+\varepsilon^2)\right] + \sigma_b \qquad [1.42]$$

with $\varepsilon = (E - E_r)/(\Gamma/2)$ being the reduced energy in units of half width which indicates the departure of the incident photon energy E from an idealised resonance energy E_r associated with a discrete autoionising level of the atom. $\sigma(\varepsilon)$ represents the absorption cross section for photons of energy E with σ_a and σ_b representing portions of the cross section which are interacting and non-interacting with the discrete state respectively. Finally, q is the profile index which when negative indicates increased absorption to the low energy side of the resonance; a positive q indicating the opposite. With few other experimental profiles available, Fano was quite successful in reproducing the poorly resolved (instrumental width = 10 x natural width for Silverman and Lassettre (1964) and 17meV for Madden and Codling (1965)) He 2s2p ^{1}P resonance, E_r, q and Γ being 60.1eV, -2.8 and 38meV respectively. However, it was not until 1964 that sufficient experimental data was available to subject the theory to more rigorous testing involving a wide variety of q and Γ parameters. Thus, in a subsequent paper (Fano and Cooper 1965), rare gas spectra between 20 and 100eV were investigated and extensions to the earlier work presented.

In both of Fano's papers (1961, 1965), each discrete autoionising level is assumed to lie, in effect, infinitely far from the others in its particular Rydberg series which allows it to be treated separately although it was pointed out that any thorough analysis must involve taking Rydberg series as whole units. The theory begins by setting up a system of general definitions and formulas such that the ground state wavefunction of any atom, molecule or ion is represented by ψ_0. At energies above the first ionisation threshold, wavefunctions belonging to discrete states are labelled ϕ_n and finally, continuum state wavefunctions orthogonal to the discrete states are referred to with ψ_{jE} where j serves to distinguish other mutually orthogonal continuum states with the same value E of energy. With these few definitions, a number of important formulae may be

written in terms of both dipole transition matrix elements (representing the interaction of the atom with the radiation field) and energy matrix elements (representing mixing between bound and continuum configurations).

The cross section for absorption of photons with energy E far removed from any resonance i.e. $\varepsilon \sim \pm\infty$ is $\sigma_a + \sigma_b$ as seen from equation [1.42]. This can be expressed as

$$\sigma_a + \sigma_b = 4\pi^2 (e^2/\hbar c) E \sum_j \langle \psi_{jE} | z | \psi_0 \rangle^2 \qquad [1.43]$$

where z indicates the component of the atom's electric dipole moment in the direction of photon polarisation and is the sum of the coordinates of all electrons along this axis. The cross section given by equation [1.43] can be partitioned into two terms σ_a and σ_b such that

$$\sigma_a = 4\pi^2 \frac{e^2}{\hbar c} E \frac{\left[\sum_j \langle \phi | H | \psi_{jE} \rangle \langle \psi_{jE} | z | \psi_0 \rangle \right]^2}{\sum_j \langle \phi | H | \psi_{jE} \rangle^2} \qquad [1.44]$$

and

$$\sigma_b = 4\pi^2 \frac{e^2}{\hbar c} E \sum_j \langle \psi_{jE} | z | \psi_0 \rangle^2 - \sigma_a \qquad [1.45]$$

The width of the autoionising resonance can also be expressed in terms of matrix elements so that

$$\Gamma = 2\pi \sum_j \langle \psi_{jE} | H | \phi \rangle^2 \qquad [1.46]$$

Similarly, q takes the form

$$q = \frac{\langle \Phi | z | \psi_0 \rangle}{\pi \sum_j \langle \phi | H | \psi_{jE} \rangle \langle \psi_{jE} | z | \psi_0 \rangle} \qquad [1.47]$$

where Φ indicates the wavefunction ϕ of the discrete state modified by an admixture of states of the continuum. It must be noted that the contribution to q of this admixture is often disregarded in crude estimates of q so that $\langle \Phi | z | \psi_0 \rangle$ can often be written, within our original wavefunction definitions, as simply $\langle \phi | z | \psi_0 \rangle$.

With these expressions, we can now discuss the experimental features of any single autoionising resonance or of the trends which are expected within a Rydberg series.

(a) A single autoionising resonance

From equation [1.42], we see that the cross section has a minimum at ε = -q whereby the cross section reduces to σ_b. This minimum is apparent in spectra as a transmission window, the absorption being reduced in a ratio $\sigma_a/(\sigma_a+\sigma_b)$ with respect to its value away from the resonance (ε~ ±∞). This ratio is often referred to as the squared *correlation index* and is written as ρ^2 where from equation [1.43] and [1.44] we have

$$\rho^2 = \frac{\sigma_a}{\sigma_a+\sigma_b} = \frac{\left[\sum_j \langle\phi|H|\psi_{jE}\rangle\langle\psi_{jE}|z|\psi_0\rangle\right]^2}{\left[\sum_j \langle\phi|H|\psi_{jE}\rangle^2\right]\left[\sum_j \langle\psi_{jE}|z|\psi_0\rangle^2\right]} \qquad [1.48]$$

It is clear from this equation that in the case of only one continuum interacting with the discrete state, there is only one value for j and both the numerator and denominator are equal yielding $\rho^2 = 1$. This means that the autoionisation profile should show zero absorption at its minimum. However, this is seldom the case with experimentally observed profiles due to a lack of instrumental resolution. The influence of both ρ^2 and q on a line profile can quite easily be demonstrated as shown in Figure 1.15.

Fano has also shown that useful atomic information can be extracted from a measurement of either Γ or q. With Γ, and via Heisenberg's uncertainty principle, the autoionisation transition probability rate can be determined since

$$\Gamma = \hbar A^a = 6.582\times10^{-16} A^a(eV) \qquad [1.49]$$

A^a is typically of the order of 10^{14} sec^{-1} for autoionising transitions. With q, a ratio can be obtained which is an estimate of the transition probability to the 'modified' discrete state Φ in terms of the probability of transition to the unperturbed continuum ψ_{jE}. This ratio is given by

$$\frac{1}{2}\pi q^2 = \left[\langle \Phi | z | \psi_0 \rangle\right]^2 / \left[\langle \psi_{jE} | z | \psi_0 \rangle\right]^2 \Gamma \qquad [1.50]$$

By the above formulae, the He 2s2p ^{1}P resonance is seen to possess a decay rate of 6×10^{13} sec^{-1} (taking Γ=0.04eV) and a ratio ($\frac{1}{2}\pi q^2$) of 12.3 (taking q = -2.8).

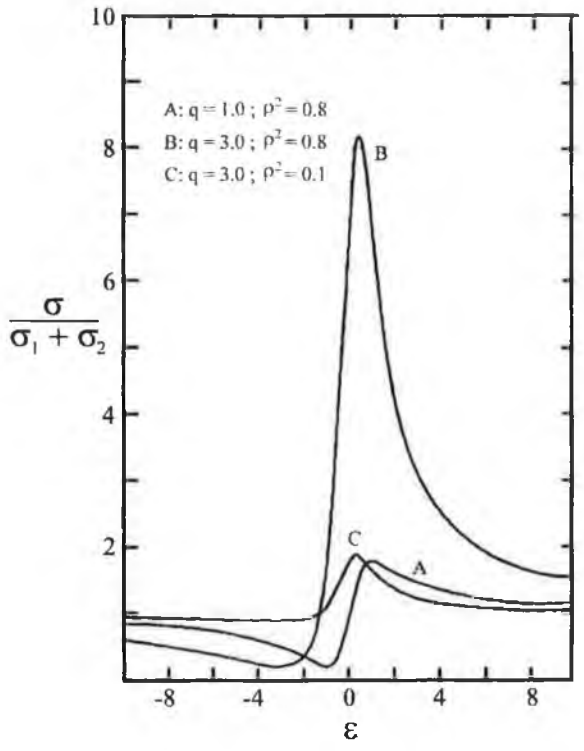

Figure 1.15 : A plot of three theoretical resonance profiles, illustrating the effect on the line shape of both an increase in the profile index q and a decrease in the correlation index ρ^2. The cross section is plotted as a function of the reduced energy variable ε (after Codling et al 1967).

(b) A Rydberg series of autoionising resonances

Should an electron be almost detached from an atom, molecule or ion, we can say that it resides in a region of space outside the rest of the system to such an extent that it may be treated as hydrogenic. Any series of stationary states where the electron is almost detached have energies (E_n) represented by the Rydberg formula

$$E_n = I_p - z^2 R/(n-\delta)^2 \qquad [1.51]$$

where I_p is the series limit which is the energy at which the electron becomes fully detached. z is the spectrum number which depends on the ion stage being examined i.e. 3^+ gives z = 4, or alternatively z is equal to the roman numeral associated with the ion stage. R is the Rydberg constant for the element of concern which can be calculated via (Bransden and Joachain 1990)

$$R_{element} = \frac{\mu}{m} R_{\infty} \qquad [1.52]$$

where R_∞ is the Rydberg constant for an infinitely large nuclear mass (=109737.32cm^{-1} or 13.605697eV) and μ = mM/(m+M) is the reduced mass; m being, as usual, the electron mass and M being the mass of the element's nucleus. n is the principal quantum number, δ the quantum defect and the quantity $n^* = n - \delta$ is known as the effective principal quantum number. Equation [1.51] is an approximation suggesting that the interaction between the outer electron and the rest of the system influences the energy levels through the single parameter δ which is the same for all levels of the series. However, this approximation does not always hold, in which case the equation can be used to define a separate quantum defect $\delta(E_n)$ for each experimental E_n value. This then allows construction of a smooth function $\delta(E)$ by interpolation. In what follows δ is assumed constant or at least to be slowly varying.

If one assumes that the energy differences E_n-$E_{n'}$ are negligible, especially for n and n' >> 1, as compared to the kinetic energies of electrons within the atom's interior, one can say that the corresponding wavefunctions ϕ_n and $\phi_{n'}$ obey Schrödinger equations that practically coincide in the interior of the system. In short, the dependence of the wavefunctions on the coordinates (r, θ, φ) of a single electron can be described by two cases : (a) for values of r relating to the outer portion of the system, ϕ_n and $\phi_{n'}$ differ from one another but are hydrogenic and (b) for r values in the interior, they are not hydrogenic but are equal except for a normalisation factor N_n. Defining N_n in terms of the mean separation of the energy levels adjacent to E_n, we have (Fano and Cooper 1965)

$$N_n^{\,2} = \frac{1}{2}(E_{n+1} - E_{n-1})$$

$$= z^2 R \frac{2(n-\delta)}{\left[(n-\delta)^2 - 1\right]^2} = z^2 R \frac{2n^*}{\left(n^{*2} - 1\right)^2} \qquad [1.53]$$

Case (b) above allows us to define a *reduced wavefunction* $\bar{\phi}$ such that

$$\bar{\phi} = \phi_n / N_n \qquad [1.54]$$

which is nearly independent of n for electron positions in the atom's interior. Reduced wavefunctions are particularly pertinent to values of low n where the processes of excitation and autoionisation take place deeper within the atom e.g. He 2s2p ^{1}P. Using the concept of a reduced wavefunction to express the line shape parameters q, ρ and Γ, it can now be shown that certain trends exist within any particular Rydberg series. Although when a transition occurs from the ground state to a state possessing an almost detached electron, that electron is directly involved, the subsequent autoionisation process does not always require the participation of that same electron. However, here we restrict the possibilities to only include the case of the outer electron fully participating in the process.

Returning to our definition of q (equation [1.47]), assuming that the Rydberg approximation holds and assuming that we are dealing primarily with transitions in the interior of the atom, we obtain, via equation [1.54]

$$q_n = \frac{N_n \langle \bar{\Phi} | z | \psi_0 \rangle}{\pi \sum_j N_n \langle \bar{\phi} | H | \psi_{jE} \rangle \langle \psi_{jE} | z | \psi_0 \rangle}$$

$$= \frac{\langle \bar{\Phi} | z | \psi_0 \rangle}{\pi \sum_j \langle \bar{\phi} | H | \psi_{jE} \rangle \langle \psi_{jE} | z | \psi_0 \rangle} = \bar{q} \qquad [1.55]$$

This essentially implies that q remains the same or $q_n = \bar{q}$ for the entire series. Similarly $\rho_n = \bar{\rho}$ and use of equation [1.54] also uncovers a relationship between the width of successive lines of a series such that

$$\Gamma_n = 2\pi \sum_j \left\langle \phi_n | H | \psi_{jE} \right\rangle^2 = 2\pi N_n^2 \sum_j \left\langle \bar{\phi} | H | \psi_{jE} \right\rangle^2$$

$$= z^2 R \frac{2n^*}{\left(n^{*2} - 1\right)^2} \bar{\Gamma} \qquad [1.56]$$

Provided n* >> 1, equation [1.56] implies that the width of any autoionising resonance is proportional to the inverse cube of its effective principal quantum number. Using this fact and knowing n* for members of a series, a measurement of any one profile width allows an approximate determination of the widths of the others. This is particularly useful as instrumental limitations often prohibit the resolution of profiles associated with higher n. Also inherent in this equation is that $\bar{\Gamma}$ represents the ratio of each line width to the average separation of the adjacent lines; this ratio, called the *reduced linewidth*, being constant for the whole series.

1.3.2 A graphical treatment of experimental profiles

An alternative and closely related parameterisation for absorption cross sections of autoionising lines has been presented by Shore (1967a, b). Invoking scattering theory, both the absorption cross section and refractivity were written, as a function of energy, as

$$\sigma(\varepsilon) = \left[(a\varepsilon + b)/(\varepsilon^2 + 1)\right] + C(\varepsilon) \qquad [1.57]$$

and

$$n(\varepsilon) - 1 = (N\lambda/4\pi)\left[(a - b\varepsilon)/(\varepsilon^2 + 1)\right] + D(\varepsilon) \qquad [1.58]$$

where equation [1.57] bears immediate resemblance to Fano's equivalent parameterisation (equation [1.42]) with $\varepsilon = (E - E_0)/(\Gamma/2)$ as before, a and b being constants, C(ε) and D(ε) being slowly varying backgrounds and N equal to the absorbing atom density. Adopting Shore's parameterisation enables one to graphically determine the standard profile parameters q, Γ and E_0 without computation, providing a convenient, albeit, approximate description of a profile's character.

Given any experimental curve of σ versus ε, we first draw an interpolated background through the resonance profile, this being the function C(ε) or $\sigma_a + \sigma_b$ in Fano's notation. We next measure the maximum excursions of the curve σ(ε) from the background C(ε). These quantities are labelled h (for peak height) and d (for peak depth) as shown in Figure 1.16a, and are related to the constants a and b discussed above by

$$b = h - d \qquad [1.59]$$

and $$a = \pm 2(hd)^{1/2} \qquad [1.60]$$

A measurement of h and d allows a direct determination of $q = \pm(h/d)^{1/2}$, the sign following the conventions discussed earlier. Furthermore, the resonance energy E_0 may be graphically located by drawing a curve parallel to C(ε), a distance h-d above C(ε) (see Figure 1.16a). Of the two resulting intercepts with the curve σ(ε), the resonance energy is the intercept which lies between the energies of maximum and minimum σ. Finally, a value for Γ may be gleaned from a measurement of the energy displacement (ΔE)

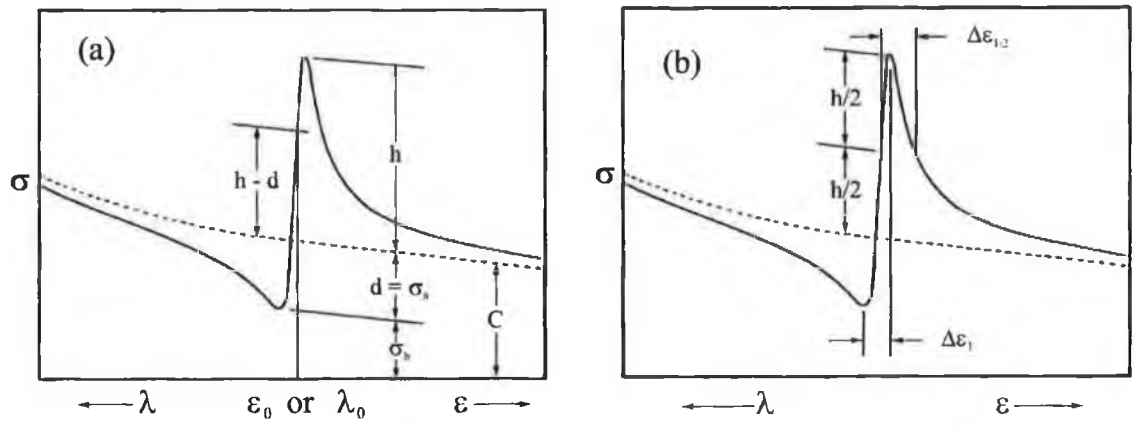

Figure 1.16 : An illustration of (a) a graphical determination of the quantities h, d, ε_0 or λ_0 and the Fano parameters σ_a and σ_b and (b) a graphical definition of $\Delta\varepsilon_1$ and $\Delta\varepsilon_{1/2}$ which are used for determining the resonance width Γ (after Shore 1967b).

between the profile maximum and the profile minimum (see Figure 1.16b) followed by application of the formula

$$\Gamma = \Delta E\left[2\sqrt{hd}/h + d\right] \qquad [1.61]$$

Alternatively, Shore (1967b) has provided a function F such that

$$F(r) = \left[\frac{(1+r^2)^{1/2} + 1}{3(1+r^2)^{1/2} - 1}\right]^{1/2} \qquad [1.62]$$

with $r \equiv a/b$. Thus F(r) can be easily determined for any r and the width Γ quickly ascertained from

$$\Gamma = \Delta E_{1/2} F(r) \qquad [1.63]$$

where $\Delta E_{1/2}$ is the width of the profile peak at half-maximum height (see Figure 1.16b). Although the choice of C(ε) is subjective allowing a degree of error in any evaluation of h and d, the results are surprisingly accurate, a recent application of the graphical method yielding q = -1.57, Γ = 16meV and E_0 = 47.12eV from our experimental DLP measurements of the neon $2s^22p^6\ {}^1S_0 \rightarrow 2s2p^64p\ {}^1P_1$ resonance. Employment of Microcal Origin v3.5© to fit the same profile, via equation [1.42], produced q = -1.55, Γ = 15meV and E_0 = 47.12eV.

1.3.3. Examples of autoionising resonances

(a) Barium and 'forced autoionisation'

Having discussed, in some detail, the characteristics of autoionisation profiles, let us look at some pertinent examples of autoionising lines in absorption spectra. Figure 1.17 shows early spectra of Ba I in the 2300-2500Å region (Garton and Codling 1960, Garton et al 1962, Garton 1966). Figure 1.17(b) shows the photographic absorption spectrum of the Ba I 6snp $^1P_1$ series convergent on its $^2S_{½}$ limit, the spectrum having been taken using a furnace to create the requisite barium vapour. Figure 1.17(a) shows the corresponding densitometer tracing and Figure 1.17(c) shows the same Ba I region taken using a shock-tube to generate the absorbing column. Beyond the $^2S_{½}$ limit, one can immediately identify the asymmetric lineshapes indicative of autoionisation. Indeed, even without photoelectric detection, their appearance on photographic plates is readily distinguished, the 5dnp,nf two electron transitions identified by a region of decreased absorption (white) followed by a region of increased absorption (black) which lies in stark contrast to the 'grey' background continuum. The dramatic difference in symmetry between the 5dnp,nf autoionising resonances and the discrete 6snp $^1P_1$ series is particularly noteworthy but perhaps the most outstanding features of these spectra are the 5d8p $^3P,^3D$ transitions which were interpreted by Garton et al (1962) as the first observation of what he termed 'Forced Autoionisation'. As the 5d8p states lie below the ionisation limit, they are discrete and should possess symmetric profiles. However, by comparing the results from both furnace and shock-tube techniques (Figures 1.17(b) and

(c) respectively), Garton et al concluded that the microfields of the charged particles in the shock heated plasma depress the ionisation potential. This depression drowns out the higher 6snp series members, and in effect produces a pseudo continuum within which the 5d8p states appear to autoionise. Indeed, the presence of further evidence, in

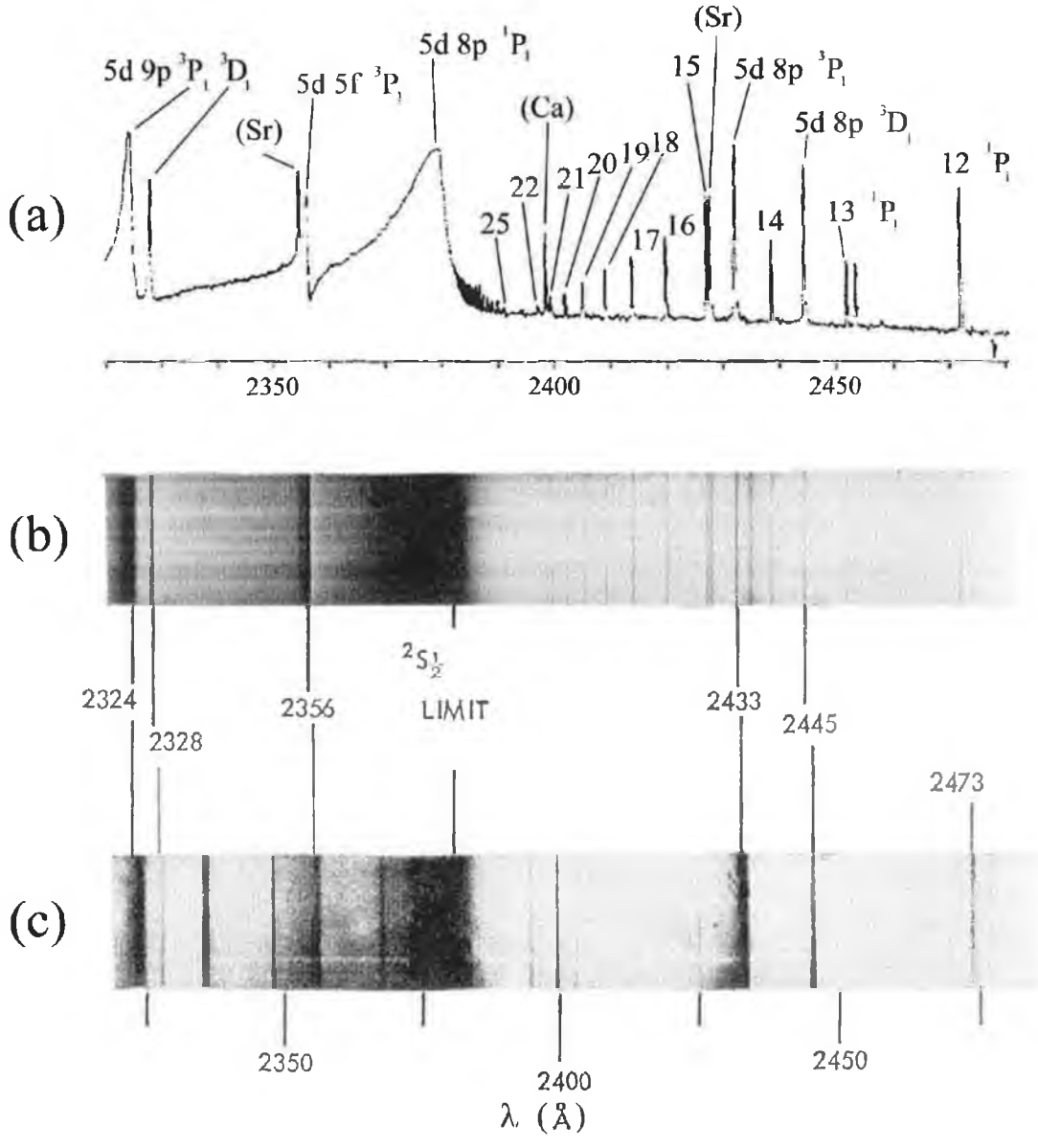

Figure 1.17 : Forced autoionisation in the Ba I absorption spectrum where (a) is the densitometer tracing corresponding to (b), (b) is the furnace absorption spectrum and (c) is the shock-tube spectrum. Plate blackening denotes increased absorption (after Garton 1966).

that the line at 2433Å shows considerable broadening in the case of the shock-tube spectrum, served to enforce Garton's convictions. This interesting hybridisation shall be treated in more detail in relation to the new measurements on Si^{4+} presented in chapter 4.

(b) Double excitations in helium

To end this section, we again return to the He 2s2p $^1P_1$ resonance at 60.1eV. Recorded by Madden and Codling (1965) and the test case for much of Fano's early theory, its observation stood as testament to the, then, state-of-the-art in experimental instrumentation. Initially captured photographically with a resolving power of ~3500 (resolution = 17meV at 60.1eV), Madden and Codling, via Fano's theory, measured the q and Γ to be -2.8 and 38meV respectively (see Figure 1.18). In recent years, a renewed

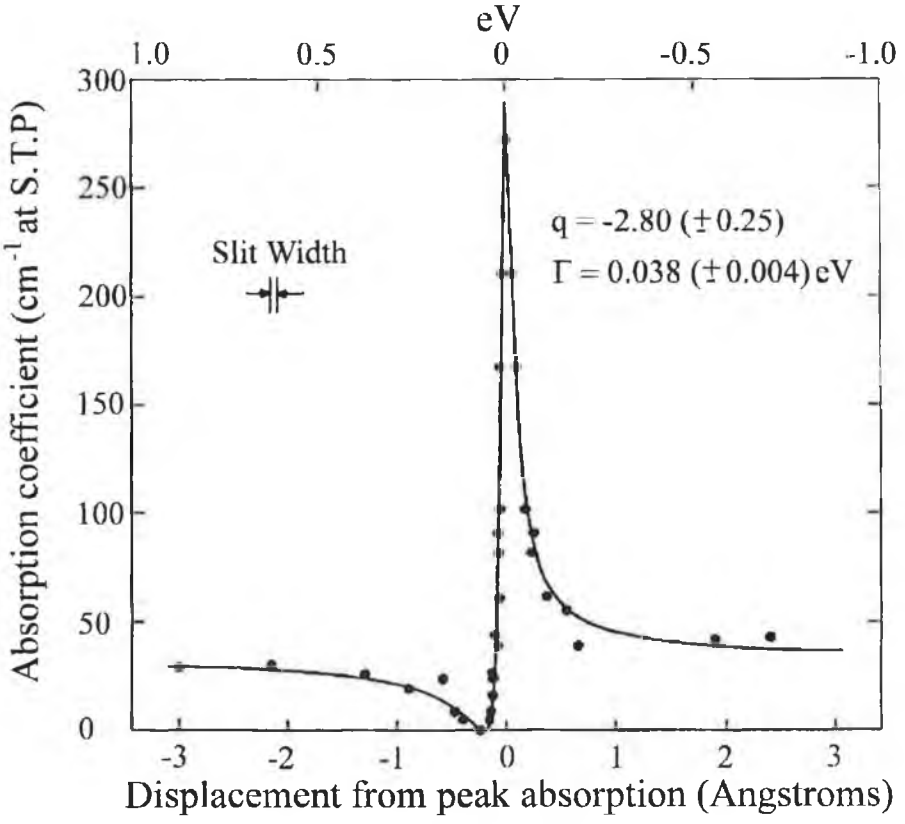

Figure 1.18 : The absorption profile of the autoionising He 2s2p $^1P_1$ two electron excitation state measured with a resolving power of ~3500 (after Madden and Codling 1966).

interest in Helium as the prototype neutral system for the study of electron-electron correlation has seen much reinvestment of effort, this time subjecting the system to close scrutiny via synchrotron radiation (Domke et al 1991, 1992a,b). With only one continuum ($1s\varepsilon p\ ^1P_1$) to interact with, the doubly excited states below the N=2 ionisation threshold of He^+ were captured with a resolving power of ~10,000 (resolution = 6meV at 60.1eV) (Domke et al 1991). Running up to the N=2 threshold, only three doubly excited Rydberg series are allowed under the diplole selection rules. These are $1s^2\ ^1S_0 \rightarrow 2snp\ ^1P_1$, $2pns\ ^1P_1$ and $2pnd\ ^1P_1$, and of these, the first two were observed up to n=16 and n=7 respectively (see Figure 1.19).

Using the classification scheme employed by Madden and Codling (1965) and subsequently used by Domke et al (1991), whereby the intense mixing of the $2pns\ ^1P^o$ and $2snp\ ^1P^o$ states is described by addition ('+' states) and subtraction ('-' states) of the respective wave functions, we note that Fano parameters of $q \sim -2.6$ and $\Gamma = 42.3$meV for 22+, 10meV for 23+ and 2.5meV for 25+ were obtained. The validity of Madden and Codling's earlier measurements was seen to stand the test of time but the beautiful extended Rydbergs now revealed(see Figure 1.19) had been beyond their reach. Indeed, Domke found Fano linewidths Γ for the '+' series to decrease with n to less than 1meV for $n \geq 8$ and with long lifetimes, the '-' states were a serious test of resolution with predicted natural widths of ~ 0.1meV and less for higher members. It is, thus, hardly surprising that the '-' series, having intensities $\approx 1/30$ of that of the '+' states were only seen up to n=7. However, in a subsequent paper, Domke (1992b), with an even better resolving power of ~15,000 (resolution = 4meV at 60.1eV), extended the '+' and '-' series to n=20 and n=11 respectively. Furthermore, this increased resolution enabled the first time observation of the 'missing' $2pnd\ ^1P^o$ series up to n=6 ; a series with even weaker intensity than the '-' series which had led to considerable confusion amongst theoreticians with respect to energies and widths. More recently, improvements in resolution and available photon flux have allowed the study of He Rydberg series converging to N = 3-9 thresholds. With a resolution of 4.1meV at 65eV (resolving power = 16,000), Domke et al (1995) have studied the region of helium double excitation between the N=7 and 9 thresholds where they have observed with great detail the interseries interferences between high-n resonances of series N and the first and second

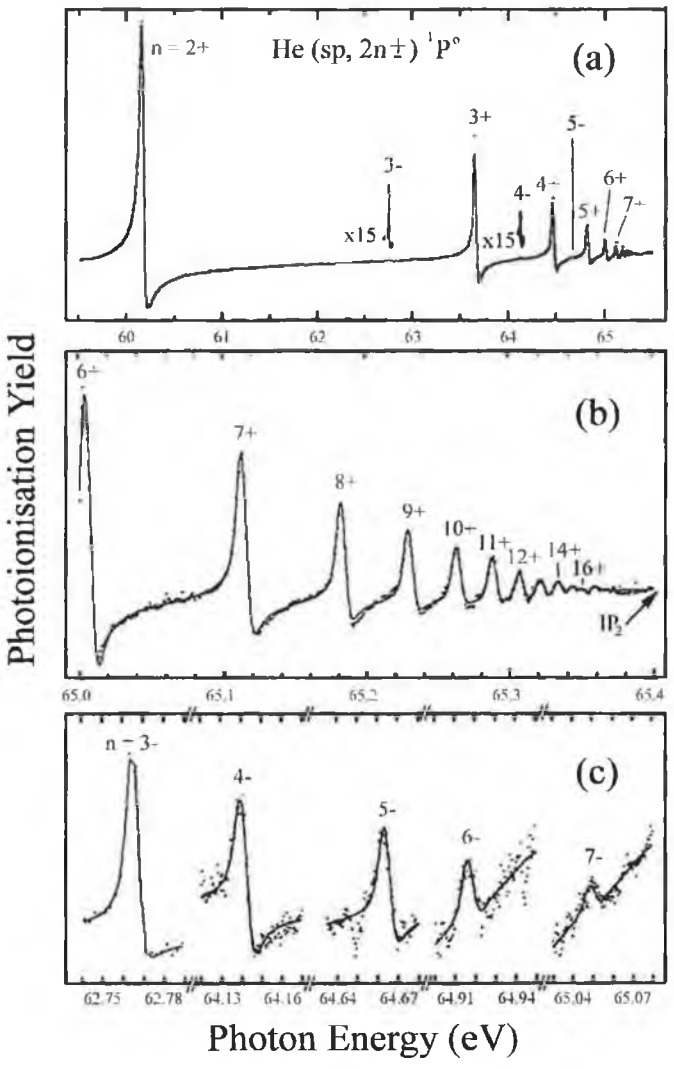

Figure 1.19 : Photoionisation spectra of the N=2 series of autoionising doubly excited states of He i.e $1s^2 \rightarrow (2pns \pm 2snp)$ where (a) is an overview, (b) the expanded high-n region and (c) the '-' states (after Domke et al 1991, 1992a).

members of the (N+1) series. Domke et al (1996) subsequently extended the study up to the N=9 threshold reporting improved measurements of, the three optically allowed Rydberg series below the N=2 ionisation threshold, the two most intense Rydberg series below each of the $3 \leq N \leq 8$ thresholds and one state of a third, previously unobserved, series running up to the N=3 threshold. This was followed with the most highly resolved study to date (Schulz et al 1996) whereby, with a striking resolving power of 64,000 (1.0meV resolution at 64.1eV) and a photon flux a factor of 40 times greater than that available previously (Domke et al 1992b), the advanced light source (ALS), beamline

9.0.1., was used to observe a new Rydberg series below the N=3 threshold of doubly excited helium. Extensions to the series converging to the N=2 threshold were also made where the principal series ('+' states i.e. (sp, 2n+) ^1P) was resolved up to n=26 and the secondary series, (sp, 2n-) ^1P and (2p, nd) ^1P, were resolved up to n=12 and n=7 respectively. Concurrent to these total absorption measurements, partial cross sections and asymmetry parameters (β), for series below the helium N=3,4 and 5 thresholds, have also been measured (Menzel et al 1995, Menzel et al 1996) and recently a review of the experimental and theoretical progress in the study of doubly excited helium has been undertaken (Rost et al 1997).

1.4 Opacity

The optical depth D_ν of a plasma may be defined by (Lochte-Holtgreven 1995)

$$D_\nu = \int k_\nu dx \qquad [1.64]$$

with k_ν being the frequency dependent absorption coefficient per cm and x (in cm), the coordinate along the line of sight. As the radiation emitted from an atom within a plasma may be reabsorbed by others, we say that when this is not seen to occur or is negligible, the plasma is *optically thin* and accordingly, the quantity $\int k_\nu dx$ is found to be small. Likewise, when this reabsorption does occur, radiation trapping results, the quantity $\int k_\nu dx$ is large and the plasma is said to be *optically thick*. For the accurate determination of atomic cross sections or relative cross sections, an optically thick plasma is quite undesirable due to complete absorption of the central region of strong lines obscuring their true intensity relative to weaker 'unsaturated' neighbours. It is therefore of interest to be able to ascertain the optical depth of the plasma, a convenient method of doing so, via examination of absorption spectra line profiles, being the subject of this section.

Much of what follows relates the treatment given by Kirkbright and Sargent (1974), their text being an experimental approach to the earlier theory presented by Mitchell and Zemansky (1934), wherein CGS units were used. Returning to the absorption coefficient k_ν, we find that equation [1.1] can be rewritten as

$$I_\nu = I_\nu^0 e^{-k_\nu L} \qquad [1.65]$$

where $k_\nu = \sigma n$ and d, representing the sample thickness or absorption length, has now been replaced by L. A plot of k_ν against frequency yields the profile of the absorption line of interest but to measure k_ν values directly, a spectrometer must be capable of resolving this profile, its spectral bandpass being considerably less than the line width. As most absorption profiles are narrow, one immediately confronts the problem of insufficient experimental resolution in determining k_ν and it is, thus, more convenient to introduce a more useful quantity K which is the integral, over the extent of the line, of all k_ν with respect to ν. K is independent of frequency and may be written as

$$K = \int k_\nu d\nu = \frac{h\nu_0}{c}\left(B_{ji}N_j - B_{ij}N_i\right) \qquad [1.66]$$

where B_{ji} and B_{ij} are the Einstein coefficients corresponding to absorption and stimulated emission between levels i and j, respectively. N_i and N_j refer to the population of these two levels such that $i > j$ and ν_0 is the frequency at the centre of the line, the small variation of ν throughout the line having been neglected. In many cases, such as that of resonance lines, the population of N_i is small compared to N_j and equation [1.66] may be simplified to

$$K = \frac{h\nu_0}{c} B_{ji} N_j \qquad [1.67]$$

Using the Einstein relationships,

$$A_{ij}/B_{ij} = 8\pi h\nu^3/c^3 \qquad [1.68]$$

$$g_i B_{ij} = g_j B_{ji} \qquad [1.69]$$

and $$A_{ij} = 8\pi^2 e^2 f_{ij} / \lambda^2 mc \qquad [1.70]$$

where A_{ij} is the Einstein coefficient for spontaneous emission, g_i and g_j are the statistical weights for their respective levels and f_{ij} is the oscillator strength or f-value of a transition between the levels i and j, one can rewrite equation [1.67] as

$$K = \frac{\lambda_0^2}{8\pi}\frac{g_i}{g_j} A_{ij} N_j \qquad [1.71]$$

or $$K = \frac{\pi e^2}{mc} f_{ji} N_j \qquad [1.72]$$

Equations [1.71] and [1.72] are of fundamental importance as they show that K has a linear relationship with N_j that is quite independent of whatever physical processes are responsible for the line's formation. Unfortunately, it is difficult to make direct use of this fact to measure atomic populations by absorption as K can only be measured by taking the area under the actual absorption profile and this does not correspond to the absorption measured with a continuum source and a conventional monochromator. It is therefore necessary to employ an alternative measure of how much radiation is absorbed during the experiment. The total absorption factor, A_T, provides one such alternative and may be calculated knowing only the amount of light entering and leaving the absorbing medium. Simply, A_T is given by

$$A_T = \frac{\Delta I}{I_0} \qquad [1.73]$$

where I is the amount of radiation leaving the absorber, I_0 is the incident radiation intensity and $\Delta I = I_0 - I$ is the absorbed radiation intensity. Despite being easy to measure experimentally, it is not as straightforward to relate it to the number of absorbing atoms as it is in the case of k_ν. Thus, it is prudent to express A_T in terms of k_ν. Because A_T is defined in terms of the total light intensity passing through the absorbing medium at a particular spectral line, the intensities used are integrated with respect to the complete absorption line and thus, by definition

$$I_0 = \int I_\nu{}^0 d\nu \qquad [1.74]$$

and

$$I = \int I_\nu d\nu \qquad [1.75]$$

Hence, A_T becomes

$$A_T = \frac{\int I_\nu{}^0 d\nu - \int I_\nu{}^0 e^{-k_\nu L} d\nu}{\int I_\nu{}^0 d\nu} \qquad [1.76]$$

and it is at this point that we must allude to A_T's dependence on both the source emission line (or continuum) and the absorption line in the absorbing medium, and assume that $I_\nu{}^0$ will always possess the same integration limits as k_ν. In other words, we impose the condition that the integration must be made over the source line-width should it be narrower than the absorption line, or over the absorption line-width if it is narrower than the source line. Embracing this assumption, equation [1.76] becomes

$$A_T = \frac{\int I_\nu^0 d\nu \int \left(1 - e^{-k_\nu L}\right) d\nu}{\int I_\nu^0 d\nu} \qquad [1.77]$$

$$\Rightarrow \qquad A_T = \int \left(1 - e^{-k_\nu L}\right) d\nu \qquad [1.78]$$

This general form of A_T can now be tailored to the case of interest. Two possible cases exist, these being (a) the evaluation of A_T for a wide source line and (b) the evaluation of A_T for a sharp line source. Having used a tungsten continuum backlighting source for all our absorption experimentation, we will confine further discussion to the former case only. Thus, with the absorption line much narrower than the continuum, we can say that the total absorbed radiation can be obtained from the integration of equation [1.78] across the entire absorption line i.e from $0 \rightarrow \infty$. This integration can then quite easily be performed for the two further classes of practical interest i.e. optically thin or small $k_\nu L$ and optically thick or large $k_\nu L$.

(a) Optically thin case

In this case, equation [1.78] reduces to (since $[1\text{-}e^{-x}] \rightarrow x$ as $x \rightarrow 0$)

$$A_T = \int_0^\infty k_\nu L d\nu = L \int_0^\infty k_\nu d\nu = LK \qquad [1.79]$$

Hence, from equation [1.72]

$$A_T = \frac{\pi e^2}{mc} f_{ji} N_j L \qquad [1.80]$$

and we see that for an optically thin plasma A_T will increase linearly with N_j (or L).

(b) Optically thick case

With large optical density, the central region of the absorption line shows complete absorption. A further increase in optical density results only in changes at the edges of the line profile, meaning that the form of the k_ν curve is

determined entirely by the edges. Under these conditions, Mitchell and Zemansky (1934) have shown that k_ν can then be represented by†

$$k_\nu = \left[\frac{\Delta\nu_0 \Delta\nu_c}{4\sqrt{\pi}\sqrt{\ln 2}(\nu-\nu_0)^2}\right] k_0' \qquad [1.81]$$

where k_ν and ν_0 have their previously described meanings, k_0' is an ideal quantity representing the peak absorption coefficient which would be obtained with an absorption line broadened only by the Doppler effect and $\Delta\nu_c$ is the sum of half-widths of all Lorentzian type functions¶ like, for example, natural and collisional broadening. Insertion of equation [1.81] into equation [1.78] yields, after integration,

$$A_T = \left[\frac{k_0' \Delta\nu_D^{\,2} a\sqrt{\pi} L}{\ln 2}\right]^{1/2} \qquad [1.82]$$

where $\Delta\nu_D$ is the Doppler half-width and a is a constant. After further substitution for k_0', which Mitchell and Zemansky have shown equal to $\frac{2}{\Delta\nu_D}\sqrt{\frac{\ln 2}{\pi}}\frac{\pi e^2}{mc}N_j f_{ji}$, the final result is

$$A_T = \left[\frac{2\pi e^2 \Delta\nu_D a f_{ji} N_j L}{mc\sqrt{\ln 2}}\right]^{1/2} \qquad [1.83]$$

Thus, for an optically thick plasma, A_T is proportional to the square root of N_j (or L).

The significance of this is that by taking an absorption spectrum for a range of known

---

†The derivation of this expression has not been dealt with here as it would only serve to confuse the salient issues being tackled. For further information, the reader is referred to Mitchell and Zemansky (1934).

¶All line profiles diverge from their lifetime broadening width, their final form due to the combined influence of various other broadening mechanisms such as Doppler broadening (due to the motion of particles) and Stark broadening (due to the presence of electric fields which split the electronic levels of the atom). Other mechanisms are also at play depending on conditions but the effect of all can be catagorised as either Gaussian or Lorentzian in nature.

absorption path lengths (L), A_T can be calculated for the line of interest and plotted as a function of L since from equation [1.78] and equation [1.65]we have

$$A_T = \int_0^{\infty} \left(1 - \frac{I}{I_0}\right) d\nu \qquad \textit{Optically thick} \qquad [1.84]$$

and from equation [1.79] and equation [1.65]we have

$$A_T = \int_0^{\infty} \ln\left(\frac{I_0}{I}\right) d\nu \qquad \textit{Optically thin} \qquad [1.85]$$

Should the A_T values then possess a square root relationship with their corresponding L values, then we can say that the absorption path length is such that the plasma is optically thick (at least for the line being monitored). Alternatively, a linear relationship between A_T and L would signify optically thin conditions prevailing within the plasma. As a final point, it should be mentioned that the above treatment deals with two extreme cases and neglects an optical density of moderate value which would fit neither an optically thin nor an optically thick description. Indeed, many plasmas would be of intermediate opacity but in such a case A_T, N_j and L cannot be simply expressed in analytical terms.

Summary

Dual laser plasma photoabsorption draws together many different fields of which plasma and atomic physics may be considered the most important. Inextricably linked, these two fields represent an enormous body of knowledge and thus, in this chapter, we have only touched upon that which is deemed essential for an understanding of the experimental investigations which follow in subsequent chapters. We have discussed and contrasted the techniques of photoabsorption, photoion and photoelectron spectroscopy. From this brief discussion of their respective strengths and weaknesses, we noted how photoabsorption spectroscopy, especially when carried out using the DLP technique, is particularly suited to the generation and study of highly charged ions. An introduction to plasmas then followed where we discussed their unique properties and the atomic processes which drive them. Various models which have been proposed for the description of plasmas in terms of electron densities and temperatures, were then

introduced and the applicability of the Collisional-Radiative model to the Nd:YAG produced plasmas, used throughout this work, was noted. Following a brief overview of the events surrounding the formation and evolution of a laser produced plasma expanding into vacuum, we then concentrated on the atomic process of autoionisation. Essential to an understanding of the spectroscopic analysis of the neon isoelectronic sequence presented in chapter 4, this treatment examined the significance of the asymmetric spectroscopic profile indicative of the autoionisation process. The parameters by which an autoionising profile is characterised were discussed both in terms of a single isolated resonance and in terms of a Rydberg series of resonances. Finally, plasma opacity was discussed. Here, we concentrated on how an absorbing plasma may be distinguished as being either optically thick or optically thin, purely by applying mathematical relationships descriptive of these regimes, to our absorption spectra. Knowing the opacity regime within which the absorbing plasma may be classed is important so as to avoid saturation. This is paramount to the accurate measurement of photoabsorption spectra, a point emphasised and illustrated in chapters 3 and 4.

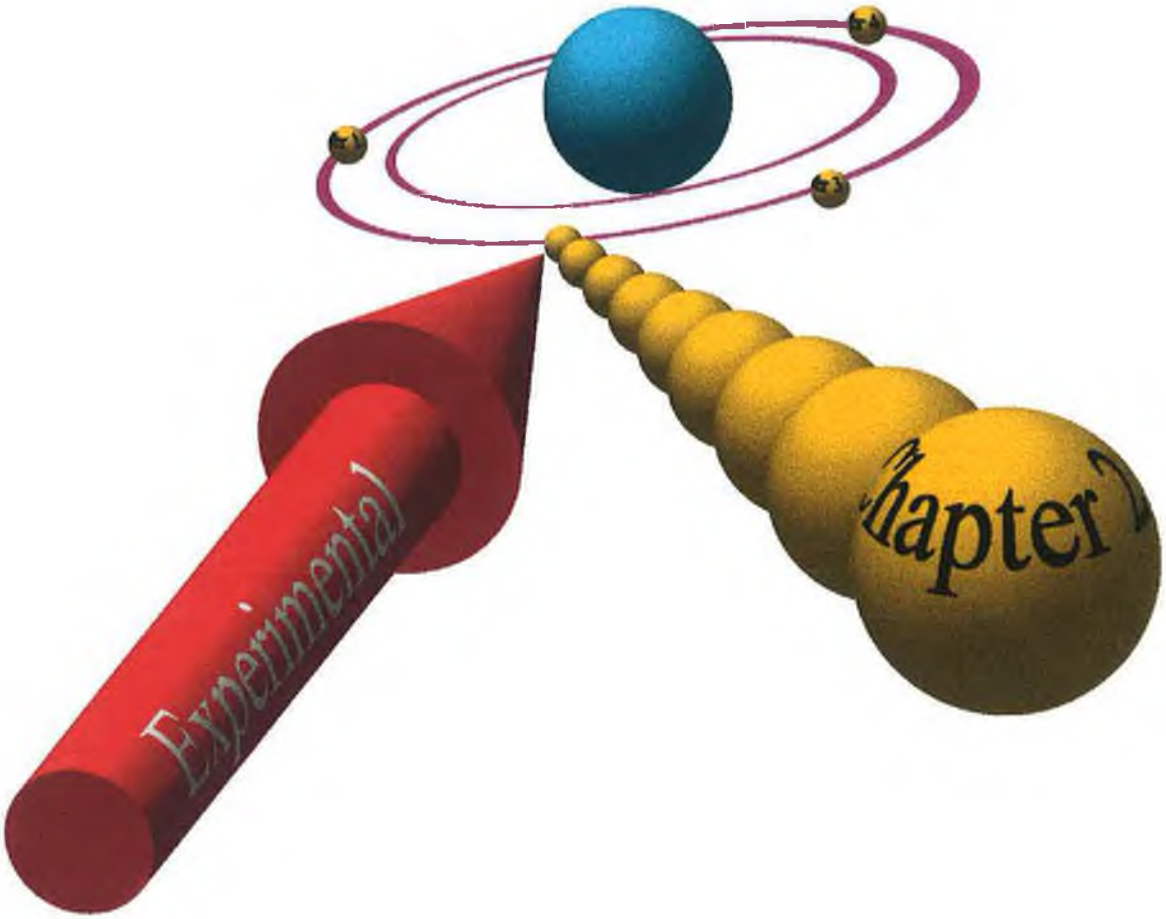
Experimental
hapter

Introduction

This chapter introduces the Dual Laser Plasma (DLP) technique for photoabsorption which has been used throughout this work. A brief historical perspective of the technique is given, followed by a terse description of the DLP system currently in operation at DCU. To emphasise the relative ease with which the DLP system can be used to select and study multiply charged ions and its ability to access excited states of atoms and ions, some selected examples of recent experiments with the system are also discussed. The accurate measurement of photoabsorption spectra being our ultimate goal, we examine the system's characteristics and performance in terms of resolving power, detection efficiency and higher order and stray light contributions. We also describe methods by which the instrument function inherent in the DLP system may be determined.

2.1 Dual Laser Plasma (DLP) Photoabsorption

DLP photoabsorption has been the subject of many experimental papers (see below) and its fundamental principles and methods for its implementation have been described in detail (Costello et al 1991 and references therein). For this reason, only the briefest of synopses, dealing with the DLP technique's timeline from conception to present day use, shall be presented.

The first DLP experiment was carried out by Carillon et al (1970), who, knowing a small number of narrow wavelength intervals ($\leq$1nm) in the aluminium XUV spectrum to be barren of line emission, used these regions to perform a variety of photoabsorption measurements whereby these continuum bands were absorbed by a second aluminium plasma, both plasmas having been created by splitting a single Nd:YAG laser beam. However, with these limited Bremsstrahlung continuum bands, photoabsorption spectroscopy over a broad wavelength range was beyond realisation. Half a decade later, the use of continuum emission from laser plasmas for plasma emission diagnostics was not uncommon (Galanti and Peacock 1975) but this continuum emission was often accompanied by discrete line structure reducing its effectiveness as a source for absorption spectroscopy. However, an earlier study on the laser plasma generated spectra of tungsten, tantalum and uranium by Ehler and Weissler (1966) had shown the predominance of strong and virtually line free continuum emission in the VUV region. Following on this work, Carroll and Kennedy (1977) carried out a DLP experiment on Li^+ where one plasma provided the absorbing species (Li^+) and the other, a tungsten generated continuum source with both plasmas formed by splitting a single Ruby laser pulse. In this DLP experiment, the first to employ a rare earth continuum source, Carroll and Kennedy (1977) successfully photographically captured the doubly excited $1s^2\ ^1S_0 \rightarrow 2snp\ ^1P_1$ series in He-like lithium. This was the first such observation of this series in a He-like ion and because the experimental conditions were such that there was no fore-plasma emission, they were also successful in extracting Fano parameters (see section 1.3) for the $2s2p\ ^1P$ resonance. Soon after Carroll and Kennedy's experiment in the XUV, a DLP technique was developed for the X-ray region, where it was used in a pulsed X-ray shadowgraphy experiment (Key et al 1978). Methods for achieving laser fusion being

of considerable interest at the time, Key et al used the X-ray emission from a brass (Cu+Zn) backlighting source to study the pulsed laser induced implosion of neon-filled glass microballoon targets. Spatially and temporally resolving the imploding neon plasma in the 1.5keV energy region using a pinhole camera and picosecond time delays, the neon plasma's density and temperature were ascertained showing the DLP technique's value as a diagnostic tool.

Continuing to explore the laser plasma generated XUV spectra of the rare earths, Carroll et al (1978) found that the elements from samarium to ytterbium (Z=62-70) all exhibited strong, line free and extensive continuum emission. The prospect of a cheap and compact table-top continuum source, unhampered by line emission in the XUV/VUV, was extremely attractive and Carroll et al (1980, 1983) moved swiftly to consolidate such promise with a series of time-resolved and time-integrated spectroscopic measurements. Subsequent high resolution analysis of the rare earth spectra (Orth et al 1986, Gohil et al 1986) confirmed their continuum nature, the origin of which soon became the focus of attention.

O'Sullivan et al (1983), applying the collisional-radiative model, suggested electron densities of ~$10^{21}cm^{-3}$ and electron temperatures of ~50eV in Ruby laser driven rare earth plasmas and established that, under these conditions, recombination radiation is the dominant source of XUV continuum, with line radiation subdued owing to plasma opacity. However, plasma opacity as a reason for continuum dominance over line radiation was not convincing due to strong lines emanating from plasmas generated via elements both above and below those of the rare earths. Indeed, Carroll and O'Sullivan (1982), examining the occupancy of the 5s, 5p and 4f subshells as a function of both Z and ion stage, discovered that as a result of level crossing, many hundreds of thousands of transitions were possible within the LS coupling framework, an example of this being the $4d^{10}4f^{6} \rightarrow 4d^{9}4f^{7}$ transition array which yields an immense 83,024 possible lines (Carroll and O'Sullivan 1982). Such vast numbers of potential transitions means a distribution of oscillator strength, leaving no one line appreciable in strength. The lines are therefore submerged in the background continuum and even at high resolution cannot be separated providing unresolved transition arrays (UTA's) which are, to all intents and purposes, virtually indistinguishable from true continua.

Ease of production, ease of location, purity, wide spectral coverage, small spatial extent, short pulse duration, synchronisation, insensitivity to ambient pressure, reproducibility and high brightness make the laser plasma an extremely useful backlighting source. More quantitatively, Costello et al (1991) have provided a comparison with rival XUV light sources and concluded that although laser plasmas have a low repetition rate (1-100Hz) as compared to synchrotrons (10-1000MHz), the peak spectral radiance per pulse is ~10^{10} photons cm^{-2} mr^{-2} $Å^{-1}$ implying an average value of 10^{12} photons cm^{-2} mr^{-2} $Å^{-1}$ s^{-1} for a source via a 100Hz laser. Comparing this with the corresponding synchrotron values of 10^{5}-10^{7} photons cm^{-2} mr^{-2} $Å^{-1}$ and an average value of ~10^{14} photons cm^{-2} mr^{-2} $Å^{-1}$ s^{-1}, it can be seen that although the average power difference is three orders of magnitude in favour of the synchrotron, single pulse laser plasma power is four orders of magnitude greater than that of a synchrotron.

With the laser plasma continuum source now well established, the Italian group of Jannitti, Nicolosi and Tondello, further developed the DLP technique during a series of XUV photoabsorption studies involving the light ions i.e. $B^{2+/3+}$ (Jannitti et al 1984a), Be^{2+} (Jannitti et al 1984b), Be^{+} (Jannitti et al 1985, 1987a), B^{+} (Jannitti et al 1986), Be-Be^{3+} (Jannitti et al 1987b) and C^{n+} (Jannitti et al 1988, 1990). A number of improvements were implemented which dramatically increased the capabilities of the now relatively common DLP spectrometer system. The most outstanding of these were the introduction of toroidal mirror optics to increase the coupling of XUV flux into the spectrometer (by now commonly of the Rowland circle mount variety (see Samson 1967)) and the fitting of an XUV optical multichannel analyser (OMA) with a 512 pixel intensified photodiode array. Using a scintillator coated faceplate to convert the XUV to visible light before photodiode detection, allowed this new photoelectric technique to provide direct measurements of relative absorption cross sections with an ease unattainable with traditional photographic techniques.

Concurrent advances were also made in the application of the DLP technique to the X-ray region. One such advance was the introduction of point projection absorption spectroscopy (PPAS). This technique employs an intense, short-lived (ps), quasi-point source of X-rays (which can be continuous, quasi-continuous or discrete depending on the element used) to probe an extended plasma expanding from one side of a foil. The

emergent rays, which pass either side of the foil are then Bragg reflected from a flat crystal onto X-ray film. Absorption and source spectra are recorded simultaneously in two dimensions. This allows spatially resolved measurements of the population density of an absorbing ion species to be deduced for some period in time determined by the backlighter timing and duration. This technique has recently been used to characterise laser-produced aluminium plasmas (Balmer et al 1989, O'Neill et al 1991) and X-ray heated aluminium plasmas (Davidson et al 1988).

Carroll and Costello (1986) further extended the capabilities of the DLP technique in the XUV region with the introduction of a second laser. The use of two independent time synchronised lasers brought the advantages of an increased power density on target and of a widely variable inter-plasma time delay range (0.25→100μs). Electronic sequencing of either Nd:YAG or ruby, Pockels cell, Q-switched lasers was found to possess 100% delay reproducibility. It was also shown that suitable adjustment of target irradiance coupled with long time delays between fore and backlighting plasmas ensured observation of even neutral species. With the laser plasma's inherent ability to produce highly ionised species (even from refractory metals like for example, thorium (mp=1750°C ; bp≈4790°C) (Carroll and Costello 1986)) this new, widely varying, temporal delay introduced a new era in ionic stage separation. Since then, the core elements of the DLP system have remained steadfast with the obvious advances in electronic technology being embraced and assimilated. At Dublin City University (DCU), a multi-laser, multi-channel XUV spectrometer facility based on the DLP technique has been in operation since 1992. All of the data presented in this thesis was taken using this system. In the following sections the system is introduced and its characteristics discussed.

2.2 The 2.2m Dual Laser Plasma system

Constructed and described in detail by Kiernan (1994), the system has seen only minor alterations since its inception. Figure 2.1 depicts all primary components.

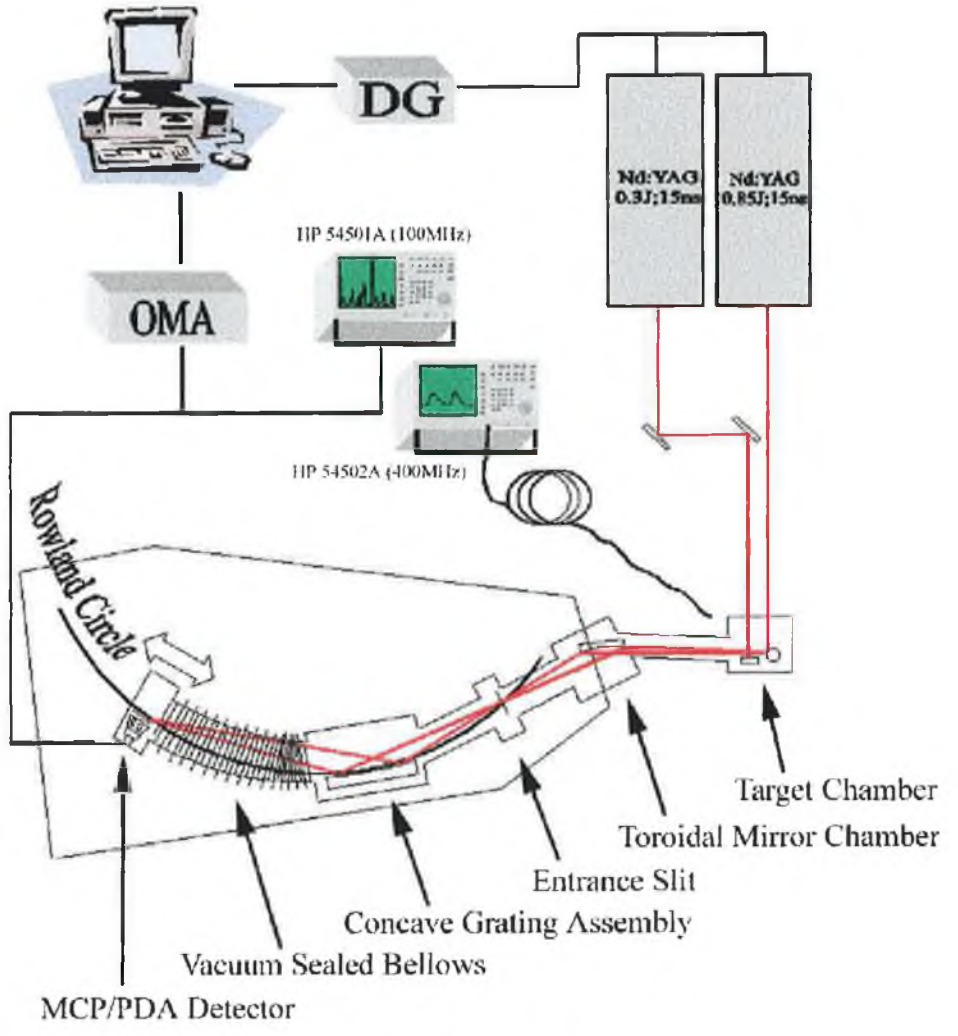

Figure 2.1 : The 2.2m Dual Laser Plasma system in operation at DCU where, OMA indicates the Optical Multichannel Analyser as described in the text and DG indicates the Delay Generator (Stanford DG535) used to set the delay(ΔT) between sample and backlighting plasmas.

2.2.1 Data acquisition

The sequence of events in the data acquisition process is initiated and controlled by a P.C. Using in-house developed software (Shaw 1996), the computer is interfaced to an EG&G PARC 1461 detector interface which houses an EG&G PARC 1462 detector controller. This controller is responsible for the spectral data acquisition from the final link in the chain, an EG&G PARC 1453 silicon photodiode array (PDA), which sits on

the Rowland circle of a McPherson 2.217m grazing incidence spectrometer. Collectively, the interface, controller and detector form what is termed an Optical Multichannel Analyser (OMA), the more intricate details of which are dealt with by Shaw(1996). Using the menu driven software, the user sets a series of parameters such as the number of shots in the firing sequence, the integration time of the detector for each shot and the time delay between each successive shot. Typically, either a single shot or a total of 5,10 or 20 shots constitute a firing sequence, the light from more than one shot, in terms of counts per pixel, being accumulated by the detector and averaged upon return to the PC. The time required to read or reset each pixel is 28μs, so with 1024 pixels on our array the scan time is approximately 30ms. Increased integration times in multiples of 30ms are easily specified but as the average lifetime of the plasma is in the microsecond regime, longer integration times serve to enhance detector noise rather than signal to noise ratio (Shaw 1996). The delay between each shot is usually chosen to be around 3 seconds whereby the detector is scanned 100 times (x30ms) but no signal read out. A three second delay is deemed appropriate in that this prevents laser overheating during long periods of experimentation but shorter delay times allowing 10Hz laser repetition are acceptable for short experimental periods should the user so desire.

2.2.2 Laser synchronisation

For each shot in the firing sequence, the P.C. sends a master (TTL) pulse to the OMA which in turn sends a TTL pulse to the Stanford DG535 delay generator. Upon receipt of the trigger pulse, the delay generator triggers both the Flashlamp and Direct Access inputs (allowing Q-switching) of two Nd:YAG lasers. The first Nd:YAG (0.3J, 15ns) is directed at the sample target of interest whilst at a suitable time delay (ΔT), the second Nd:YAG (0.85J, 15ns) is triggered and the outputted pulse impinges on a tungsten rod to provide the requisite rare-earth backlighting continuum for photoabsorption. The timing diagram is shown in figure 2.2 where the difference between instigation of the two direct access pulses is seen to provide ΔT.

The Stanford DG535 delay generator provides four delay output BNC channels, A, B, C and D. The logic transitions at the outputs of A, B, C and D can be delayed by up to 1000

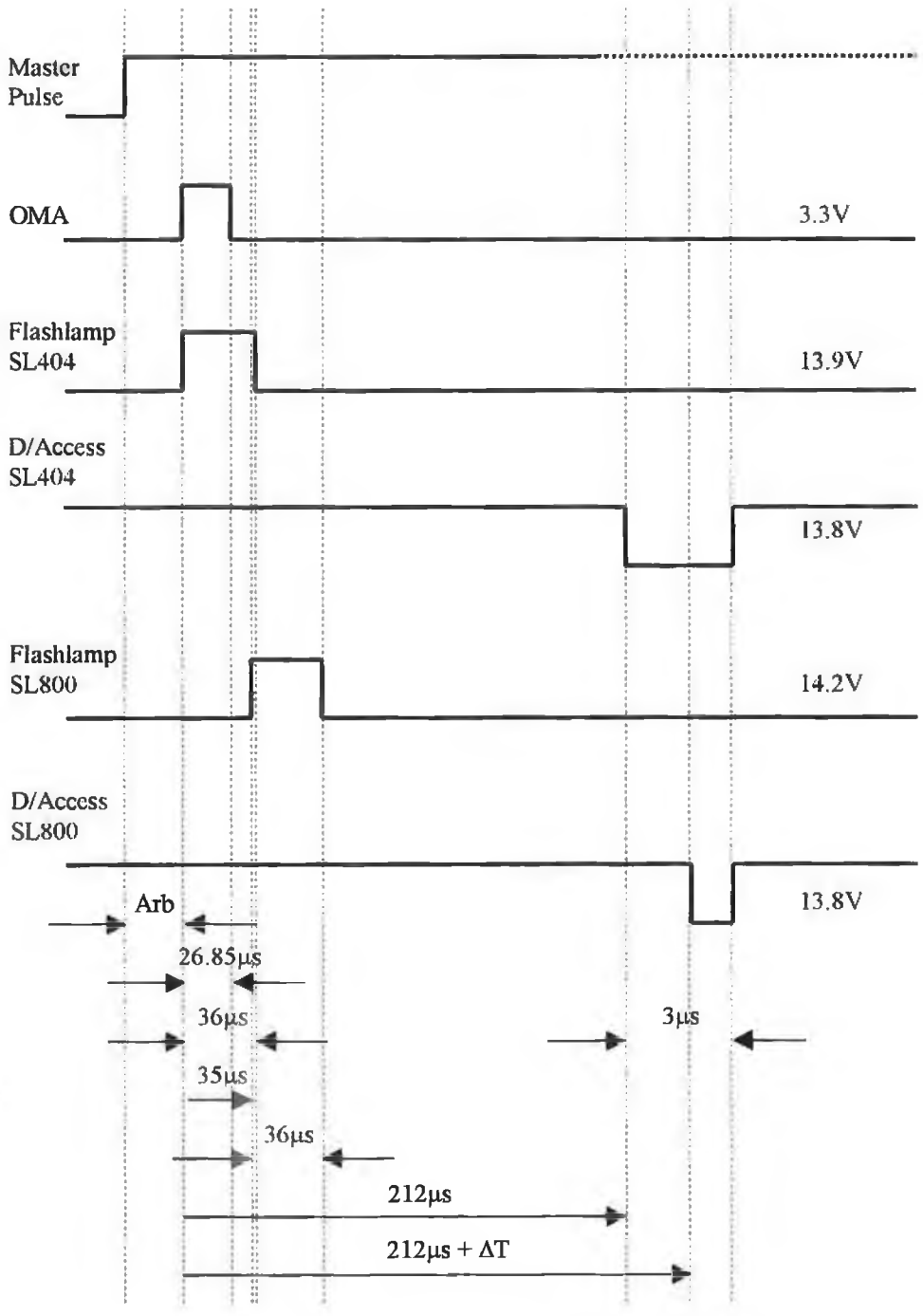

Figure 2.2 : The timing diagram for the Dual Laser Plasma photoabsorption experiments performed during this work where two Nd:YAG lasers, models SL404 (0.3J, 15ns) and SL800 (0.85J, 15ns), were synchronised via a Stanford DG535 delay generator. ΔT is provided by a user defined delay between the SL404 and SL800 direct access inputs. Note that both laser flashlamps do not trigger at the same time, this being due to optimum Q-switched energy being obtained 212µs and 177µs after flashlamp initiation for the SL404 and the SL800 respectively.

seconds in 5ps increments relative to the T_0 pulse. The T_0 pulse, marking the beginning of a timing cycle, is generated in response to an external trigger which in this case is offered by the OMA. Although the pulses generated by the Stanford DG535 have an amplitude limited to between -3 and 4V, the requisite pulse amplitude of ~15V necessary to trigger both the flashlamp and the direct access of the Nd:YAG is provided by external amplification circuitry. These in-house designed amplifiers boost pulse amplitudes to a fraction more than 13.5V which is seen to suffice despite laser manufacturer specifications (Spectron 1991). Also worthy of mention is that the pulse durations of T_0, A, B and C are determined by subtraction of their respective values from the delay value input for D. For example, figure 2.2 corresponds to T_0 = 0sec, A = 35μsec, B = 212μsec, C = 212μsec(for ΔT=0) and D = 215μsec. Thus, the duration of each pulse is 215μsec, 180μsec, 3μsec and 3μsec for T_0, A, B and C respectively. In order to successfully trigger, the Nd:YAG flashlamp must receive a positive going pulse of width 10-100μsec. Likewise, the direct access inputs adhere to similar tolerances, a successful trigger only resulting from a negative going pulse of width 2-100μsec. As can be seen these criteria are met in figure 2.2, the flashlamp triggers being positive going (~14V, 36μsec), the duration fixed by the amplifier circuit and the direct access triggers being negative going (~14V, ~3μsec), their durations being determined by suitable choice of channel B, C and D values. For further information on the Stanford DG535, the reader is referred to http://www.batnet.com/srsys/html/dg535.html.

Although the delay generator has a resolution of 5ps, the Nd:YAG cycles cannot be reproduced to better than ±5ns. This thus provides the upper limit on the system's temporal resolution of ionic species. Experience has shown that YAG to YAG synchronisation is reliable to within this tolerance. However, laser synchronisation and laser pulse reproducibility from shot to shot is continually monitored by fibre optic transport of the laser generated plasma light to a Hewlett Packard 54502A 400MHz digitising scope, a BPX65 fast photodiode acting as the light to voltage transducer.

2.2.3 The target chamber

Drawing attention to figure 2.3, we see that before entering the target chamber, the light from both lasers is focussed such that sufficient incident irradiance on target (typically $10^{15}Wm^{-2}$) for plasma formation is achieved. A spherical lens of 10cm focal length was typically employed for the backlighting plasma with a choice of a 10cm focal length cylindrical or spherical lens available for sample plasma creation. The use of a spherical lens was particularly suited to generating high sample ion stages whereas a cylindrical lens, creating a long, rarefied and cooler *column* of absorbing species was more apt for maximising neutral or low ion stage yields. An added advantage in using a cylindrical lens is that by translating a knife edge across the beam before it's focussed, the absorbing column length may be varied and in so doing, one may therefore alter the plasma's opacity. This fact has been made use of in both chapter 3 and chapter 4 as we shall see later. Indeed, by this technique one may test for plasma homogeneity as only d in equation 1.1 (see section 1.1) is altered. Of course, a true measure of plasma homogeneity must assume that the laser beam in use is uniform in spatial profile and that the target surface is free from non-uniformities.

During any DLP photoabsorption experiment, there are three critical parameters which dictate ion stage selectivity. (1) The target or sample irradiance, (2) the inter-laser time delay (ΔT) between the formation of absorbing and backlighting plasmas and (3) the displacement of the sample target surface from the system's optic axis (ΔX) which, together with the acceptance optics of the spectrometer system, governs the portion of expanding plasma plume contributing to the absorption spectrum. Once the backlighting tungsten plasma is aligned to the optic axis and matched to the source/toroidal mirror distance which allows the mirror to optimally focus the backlighting plasma light into the spectrometer, it is held in constant position. Hereafter, a suitable choice of (2) and (3) enables 'capture' of the desired ions as they flood across the optic axis at velocities determined by their temperature and mass.

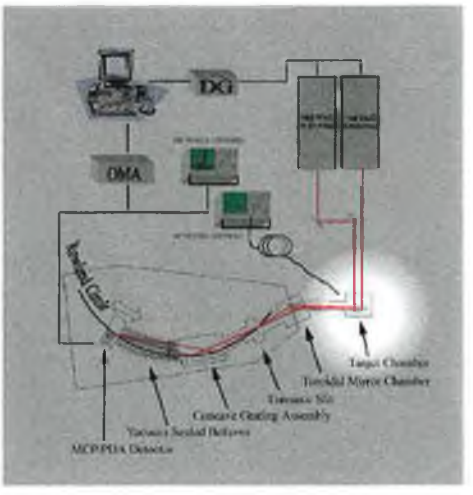

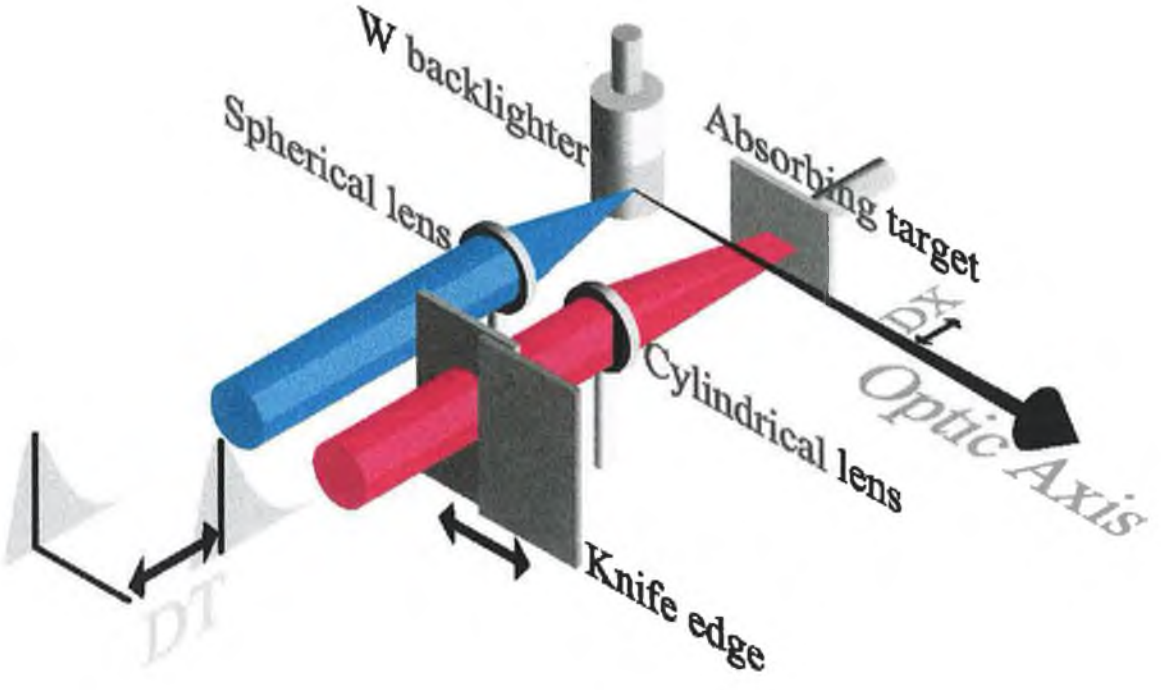

Figure 2.3 : A closer view of the target chamber and entrance optics of the DLP system. The inter-laser time delay is labelled DT and DX denotes the displacement of the sample target surface from the system's optic axis.

2.2.4 The toroidal mirror chamber

Turning to figure 2.4, we now examine the path of the XUV plasma light as it journeys from creation to detection. The backlighting plasma created, its broadband continuum emission passes through the sample plasma plume, absorption taking place therein. The resultant light flux travels down the system's optic axis and moves from pumping stage 1 (i.e. the target chamber at 10^{-5}mbar) into the second pumping stage which, segregated from stage one via a Glass Capillary Array (GCA), contains the toroidal mirror (at ~10^{-6}mbar) . Consisting of tightly packed glass capillaries, the GCA is ideal as a differential pressure barrier, allowing light to pass whilst comfortably withstanding a pressure differential of up to ~1mbar (Lucatorto et al 1979) when, as in this case, pore diameters of 50μm are used. Installation of the GCA also prevented transient pressure fluctuations throughout the system upon plasma generation.

The use of a GCA, to better isolate the mirror and the detector, over other more traditional techniques such as thin-film windows and differentially pumped slits was justified when the thin-film's poor stamina for pressure differentials and limited spectral transmission and the differentially pumped slit's limited spatial aperture, were considered (Lucatorto et al 1979). To protect the GCA from misalignment due to pressure surges and to keep it clean, it is separated from the target chamber by a pneumatic valve. When closed, the valve serves to allow a quick turnaround time for target exchange or replacement, the toroidal mirror chamber, being separately pumped, remaining under vacuum. The valve also stands as sentinel over system integrity as, in the event of a power failure, it closes automatically preventing a breach of vacuum in the mirror chamber.

Upon entering the toroidal mirror chamber via the GCA, the flux impinges on the mirror itself. Gold coated with major and minor radii of 2100mm and 111mm respectively, the mirror has been positioned such that the source (backlighting plasma) distance is 400mm. It is also angled at 8° about the vertical to ensure an incident flux angle of 82°, grazing incidence being required for enhanced reflectance in the XUV (Kiernan 1994). Employed to combat astigmatism, the chief benefit of the mirror is an increase in system speed.† With the above specifications, the mirrors primary focus falls at a distance of

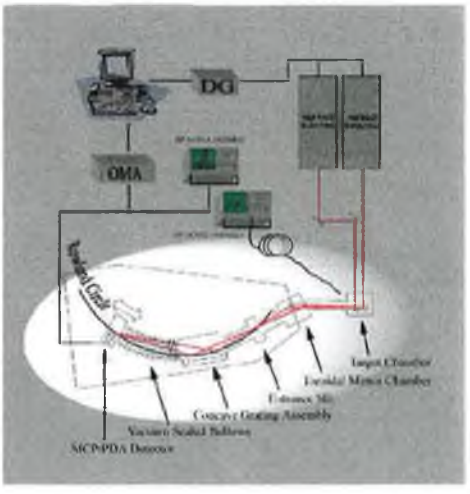

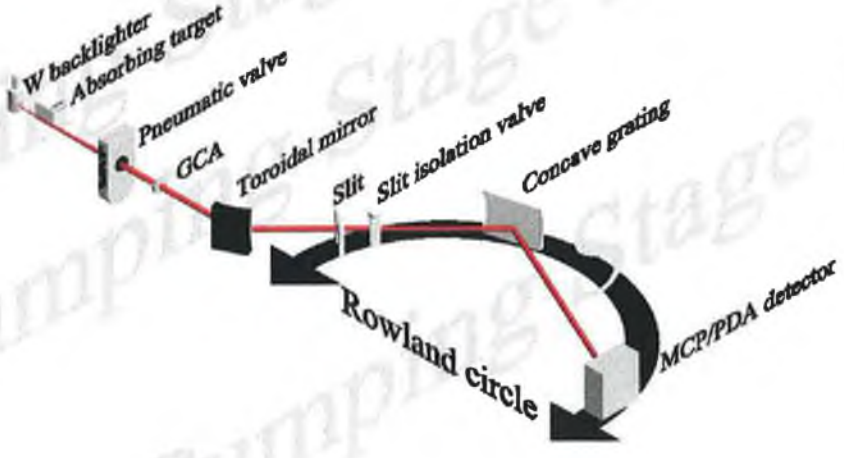

Figure 2.4 : A closer view of the primary components, all under vacuum, of the differentially pumped DLP system. Pumping stage 1 incorporates both targets at a pressure of ~10^{-5}mbar. Pumping stage 2 contains the GCA, the toroidal mirror and the spectrometer entrance slit at a pressure of ~10^{-6}mbar and this is separated from pumping stage 3 by the slit isolation valve, stage 3 containing the grating and detector at ~10^{-7}mbar. Stages 1 and 2 share the same roughing pump but have their own 50l/s turbo-molecular pumps and stage 3 is kept under high vacuum by way of an ion pump with a 240l/s turbo-molecular/rotary pump combination on standby if required.

230mm and it is at this distance that the flux enters the spectrometer through the entrance slit. A choice of either 5,10 or 20μm was available for the entrance slit width, 10μm being the width of preference for most of the experimentation carried out in this thesis. The selection of slit width is dependent on a trade off between the light flux reaching the detector and resolution. With the entrance slit being located on the Rowland circle, the concave grating and the detector must also follow suit to ensure a focussed image of the slit at the detector.

As mentioned above, astigmatism is the main source of image aberration. All concave optics exhibit this handicap, the concave grating being no exception. It is the astigmatism inherent in the grating that forces the implementation of the toroidal mirror. The choice of the above mirror parameters ensures that all diffracted wavelengths are focussed to uniform vertical lines. These image 'lines' are more suitable for detection by PDA. Recently, verification that the system produces focussed lines for each wavelength at the detector has been obtained by ray tracing the entire DLP system using the software package SHADOW (Moloney 1998). Taking five energies ranging from 50 to 150eV, Moloney traced the path of the light from source to detector examining the 'footprint' and effective utilisation of the mirror, the slit and the grating. His conclusions suggested that only approximately 3.4% of the XUV light collected by the mirror reached the detector but that, as intended through the design and installation of the mirror, each wavelength or energy was focussed at the detector to a line of approximately 10mm in height and 0.03mm in width.

2.2.5 The 2.2m grazing incidence spectrometer

Having travelled through the spectrometer entrance slit and into the spectrometer which is maintained at a pressure of ~10^{-7}mbar, the flux is next intercepted by the concave grating.* Again gold coated, the grating used in the DLP system is ruled at 1200 lines per

---

† It should be noted that a detailed analysis of the properties and theory relating to toroidal mirrors, with particular emphasis on their application to DLP systems, can be obtained from Hopkins (1992), Kiernan (1994) and Moloney (1998).

mm and blazed at an angle of 2°4' giving a blaze wavelength (λ_{blaze}) equal to 84.34Å. The grating is fixed at a distance of 231mm from the entrance slit, the angle of incidence between the slit and the grating normal being 84°. Once diffracted by the grating, the wavelengths are dispersed at different angles according to the grating equation

$$\pm m\lambda = (Sin\beta + Sin\alpha)d \qquad [2.1]$$

where m is the spectral order, d is the groove separation and α and β are the angles of incidence and diffraction, respectively. In our case, we take +mλ as we are concerned with the spectrum which lies between the central image (α = β) and the incident beam, this spectrum being referred to as the "inside order" (Samson 1967).

Upon leaving the grating, the diffracted light travels through a vacuum sealed bellows to its final destination, the MCP/PDA detector. Movement of the detector along the Rowland circle, via manual scanning of a precision drive screw and straight edge assembly, expands or contracts the flexible bellows allowing the desired wavelength range to be imaged by the detector. As the detector is moved along the Rowland circle, a mechanical counter indicates (in inches) the chordal distance from the centre of the grating to the approximate centre of the detector. Thus, using the Rowland circle formula

$$r' = RCos\beta \qquad [2.2]$$

with r' equal to the chordal distance in metres, R equal to the diameter of the Rowland circle (=2.2176m) and β equal to the diffraction angle, in combination with equation [2.1] allows the user to approximately determine the centre wavelength imaged by the detector array for any chordal distance. Only one angle of incidence (α=84°) and a single grating (1200lines/mm) were used throughout this work. With the above specifications, the accessible range of the instrument was 60 → 460Å (27→ 207eV) which corresponds to a mechanical counter range of ~14.5 → 30.5".

The MCP/PDA detector has been described elsewhere (Kiernan 1994) but for completeness a brief description shall be given. The diffracted XUV light is incident

---

* Detailed analysis of the properties of concave gratings can be obtained from the seminal works of Beutler (1945) and subsequently Namioka (1959) with their collective theories conveniently provided by Samson (1967).

upon a Microchannel Plate (MCP) which converts the XUV light to electrons with a typical quantum efficiency of ~20%. These newly generated electrons bounce down a channel matrix (a potential of up to -1kV applied between input and output) whereupon secondary emission takes place with a resultant gain in excess of 10^4. The outputted electron bunches are then accelerated across a vacuum gap by a potential difference of ~4kV and proximity focussed upon a visible photon generating phosphor coated fibre optic bundle. The fibre optic bundle tapers from 40 to 25mm (with a resulting demagnification factor of 1.6) in order to match the length of the linear photodiode array (PDA) which possesses a total of 1024 pixels. From an experimental viewpoint, two parameters dictate the response from the detector. The first is the MCP gain which is dependent on the negative voltage applied across the channels. The second is the MCP resolution which depends on the positive potential difference applied across the 0.7mm gap which separates the MCP from the phosphor coated fibre reducer. Typically, the user would supply voltages of +4.2kV and between -790 and -890V for the MCP resolution and gain, respectively. As mentioned previously, the final signal received by the detector is then read to the OMA and subsequently returned to the PC where it is stored in standard ASCII file format. The detected signal/spectrum is also fed, via an OMA video output, to a Hewlett Packard 100MHz scope, this allowing the user a real-time interpretation of the final spectra and on-line monitoring of shot to shot reproducibility.

2.2.6 Energy calibration

As mentioned in section 1.1.1, absorption spectra are generated by application of equation 1.1, whereby the relative difference between the measured background continuum signal in the absence ($I_0(\lambda)$) and presence ($I(\lambda)$) of the absorbing species is calculated. Both $I_0(\lambda)$ and $I(\lambda)$ are stored in separate files, each being the resultant light signal detected by each pixel of the 1024 pixel PDA. The light signal detected at each pixel is translated into the signal at a specific energy or wavelength by the use of low Z elements possessing an abundance of sharp well-defined line transitions in the energy region of interest. To be successful candidates, the calibrating elements must be easily

machined as their location in the system must coincide with the backlighting heavy element i.e. W, used for continuum generation. Thus, as seen in figure 2.3., both the tungsten and the calibrating low Z elements take position on a rod which is easily rotated or translated up and down to provide for fresh target surface in the event of depletion. It has been found that the most suitable elements for calibration in the 60-460Å region are magnesium, aluminium and silicon with oxygen line transitions, although quite broad and being accessed through the presence of an oxide layer on a fresh target surface, often of use. Unfortunately, the crystalline nature of silicon prevents its inclusion in the background rod assembly although, as we shall see in chapter 4, its emission spectra can be used for calibration should silicon be the target of interest for absorption studies. To calibrate an absorption spectrum accurately, the background rod must be vertically translated allowing the Nd:YAG responsible for continuum production to now generate the requisite magnesium or aluminium emission spectrum. It is essential that this procedure be carried out *before* moving to a new region on the Rowland circle as due to mechanical 'slippage' in the drive screw, a return to a previous chordal distance setting fails to consistently guarantee imaging of the previously observed wavelength region by the PDA to better than one pixel. Once captured, the line transitions from either magnesium or aluminium can be identified by way of standard atomic and ionic line reference data tables (Kelly 1987). With each line now having a direct pixel to wavelength correspondence, the mathematical 'best fit' relationship can be established, this usually taking the form of a third order polynomial. It is essential that as many lines as possible are involved in the fit (ideally one line per fifty pixels), as experience has shown that a mere five or six known lines over 1024 pixels provides insufficient accuracy. Furthermore, extrapolation over interpolation as a means of calibration must never be considered, any order polynomial other than first order tending to diverge rapidly external to the reference range. Figure 2.5 illustrates typical spectra obtained from both the low Z calibrating elements and the high Z continuum backlighter. Figure 2.5(a) is the resultant emission spectrum from aluminium whereby five shots have been averaged, the spectrum taken at a chordal distance of 25". Figure 2.5(b) is again an aluminium emission spectrum, also the average of five shots but this time corresponding to a chordal distance of 25.4". Of particular interest is the contrast

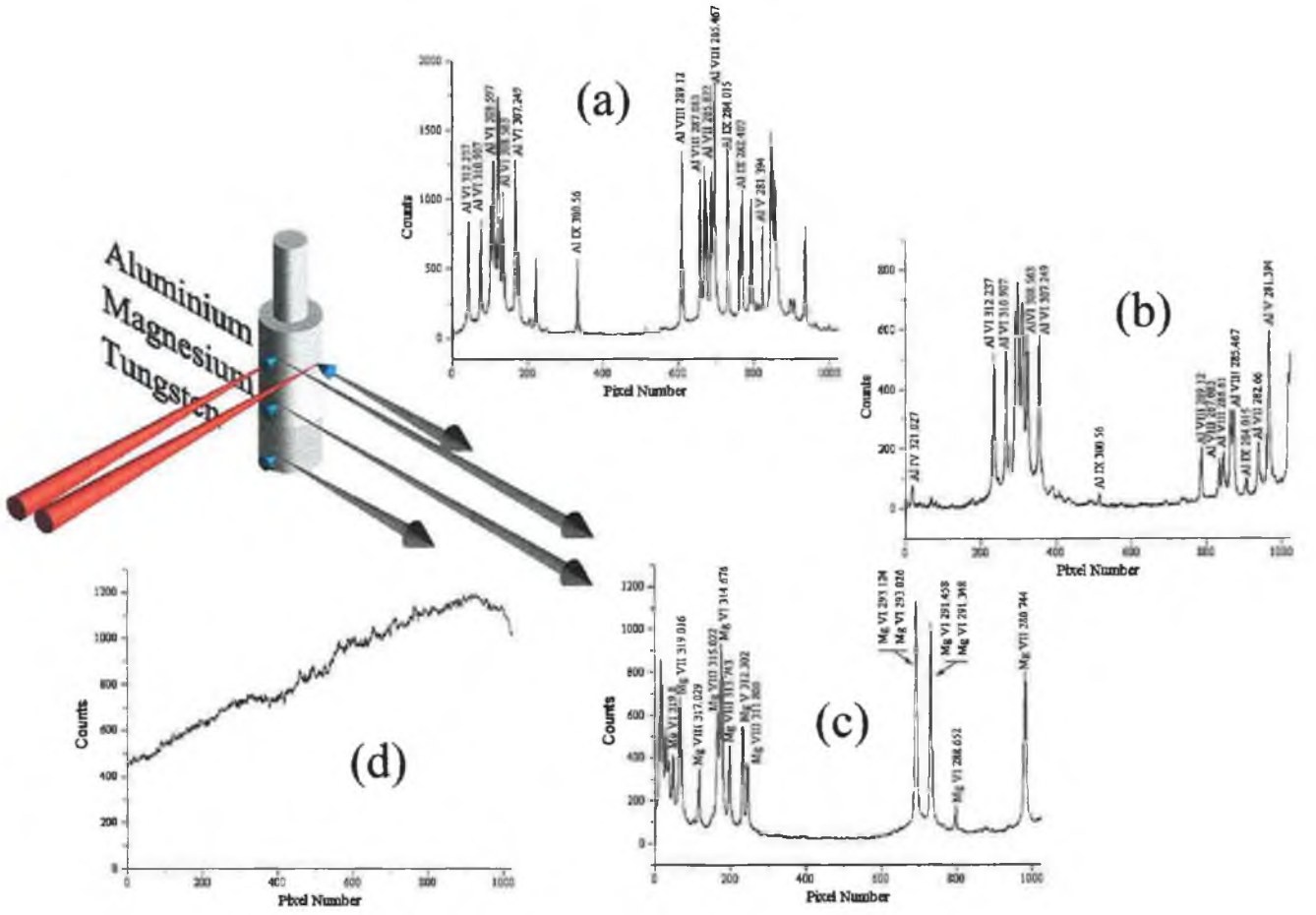

Figure 2.5 : The resulting spectra from various target geometries where (a) illustrates the emission spectrum of aluminium for a chordal distance of 25'', with the hot plasma core being imaged. (b) is again an aluminium emission spectrum, this the result of imaging the cooler regions of the plasma. Here the spectrum corresponds to 25.4''. (c) shows the equivalent magnesium emission for 25.4'' and (d) shows the tungsten continuum again for 25.4''. The red cones indicate the incident focussed Nd:YAG beams. The black cones indicate the optic axis and the blue, the plasma plumes.

between (a) and (b) whereby in (a) the higher aluminium ion stages i.e. Al IX, are favoured over their lower ion stage i.e. Al V,VI and VII, neighbours. In (b), an antithesis is evident, the lower ion stages now very much the dominant species. The promotion of transitions associated with either extreme of ion stage can be, to some extent, controlled by the experimenter as the relative concentration of ions depends both on the target irradiance and the angle at which the laser is impingent on the target. In (a), the geometry is such that the hot plasma core is imaged whereas in (b), with the laser incident normal to the target, the cooler plasma regions are imaged. It is, therefore, immediately obvious that these geometrical considerations allow one to increase the number of available reference lines for use in the spectral calibration procedure. Figure 2.5(c) further demonstrates the benefit derived from the use of multiple elements for calibration. Corresponding to 25.4" as in (b), this magnesium emission spectrum shows how sparse regions of line density in the aluminium spectrum i.e. (b), can be compensated for by the presence of alternate transitions belonging to magnesium. This is particularly evident in the wavelength regions corresponding to pixels 1 to 200 and 600 to 800. Finally, to contrast with the line emission of aluminium and magnesium, we show, in figure 2.5(d), the portion of XUV continuum emitted by tungsten which also corresponds with a chordal distance of 25.4", this spectrum, a typical example of $I_0(\lambda)$ (see equation [1.1]), being the average of 10 shots.

2.2.7 Recent DLP system results

To conclude this section and having discussed the rudiments of the DLP system currently in operation at DCU, it would seem fitting to briefly discuss some of the investigations carried out since the system's launch. A complete list of all the species studied since 1994 is given in Table 2.1 but we will only discuss a few of the resulting publications in what follows. In 1994, the $2p \rightarrow 3s$ excitations to the $2p^5 3s^2 3p$ even parity autoionising states of the isoelectronic species Mg, Al^+ and Si^{2+} were studied allowing the prediction of the kinetic energies of electrons ejected upon autoionisation. These were then compared with previous publications (Pejcev et al 1977) and excellent agreement (<0.02eV) was obtained (Mosnier et al 1994). In this case, it was the relative

Species	Z	Region	Reference
Ground State			
He	2	1s	Kennedy et al 1994
Li	3	1s	Kennedy et al 1996, Kennedy et al 1994, Kiernan et al 1994
Li^+	3	1s	Whitty et al 1998, Kennedy et al 1996, Kennedy et al 1994, Kiernan et al 1994
Ne	10	2s	Chakraborty et al 1999, Kennedy et al 1999
Na^+	11	2s, 2p	Chakraborty et al 1999
		2s	Kennedy et al 1999
Mg	12	2p	Kennedy et al 1996, Kennedy et al 1994
Mg^{2+}	12	2s, 2p	Chakraborty et al 1999
		2s	Kennedy et al 1999
Al	13	2p	Costello et al 1998a
Al^+	13	2p	Kennedy et al 1996, Kennedy et al 1994
Al^{3+}	13	2s, 2p	Chakraborty et al 1999
Si	14	2p	Kennedy et al 1999
Si^+	14	2p	Costello et al 1998a
Si^{2+}	14	2p	Kennedy et al 1996, Sayyad et al 1995, Kennedy et al 1994
Si^{4+}	14	2s, 2p	Chakraborty et al 1999
Ar	18	3s	van Kampen et al 1997
K^+	19	3s	van Kampen et al 1997
		3p	van Kampen et al 1995
Ca^+	20	3p	Kennedy et al 1996
Ca^{2+}	20	3s	van Kampen et al 1997
		3p	Kennedy et al 1996, van Kampen et al 1995
Cr^{2+}	24	3p	Kennedy et al 1999
Zn	30	3p	Kiernan et al 1997
Zn^+	30	3p	Kiernan et al 1997
Zn^{2+}	30	3p	Kiernan et al 1997
Zn^{3+}	30	3p	Kiernan et al 1997
I	53	4d	O'Sullivan et al 1996
I^+	53	4d	O'Sullivan et al 1996
I^{2+}	53	4d	O'Sullivan et al 1996
Ba	56	4d	Kennedy et al 1996
Ba^+	56	4d	Kennedy et al 1996
Ba^{2+}	56	4d	Kennedy et al 1996, Köble et al 1995b
La^{3+}	57	4d	Kennedy et al 1996, Köble et al 1995b
Au	79	5p, 4f	Köble et al 1995a
Th	90	6p	Meighan et al 1999
Excited State			
Mg	12	2p	Kennedy et al 1996, Kennedy et al 1994, Mosnier et al 1994
Al^+	13	2p	Kennedy et al 1996, Kennedy et al 1994, Mosnier et al 1994
Si^+	14	2p	Costello et al 1998b
Si^{2+}	14	2p	Kennedy et al 1996, Kennedy et al 1994, Mosnier et al 1994

Table 2.1 : A summary of the photoabsorption studies in atoms and ions carried out using the DLP system at DCU since 1994.

ease with which samples could be prepared in an excited state which demonstrated the potential of the DLP technique. In close succession followed the first observation of a photon induced triply excited state in atomic lithium (Kiernan et al 1994). Exciting all three electrons into the n=2 subshell leaving the K shell unoccupied meant the creation of a so-called 'Hollow atom' which in the case of lithium represents the ideal system for the study of electron correlation in the context of the fundamental coulombic four body problem. Although previously observed using beam-foil (Bruch et al 1975) and fluorescence (Mannervik et al 1989) techniques, the primary advantage in using the DLP photoabsorption technique was its ability to probe only the photon-atom interaction which, invariably, produces spectra of less complexity being constrained to accessing states optically connected to a known ground state. With the DLP method, Kiernan et al were successful in measuring the $1s^22s(^2S) \rightarrow 2s^22p(^2P)$ transition and extracting its associated Fano parameters (see Section 1.3). A timely observation, Kiernan et al's work

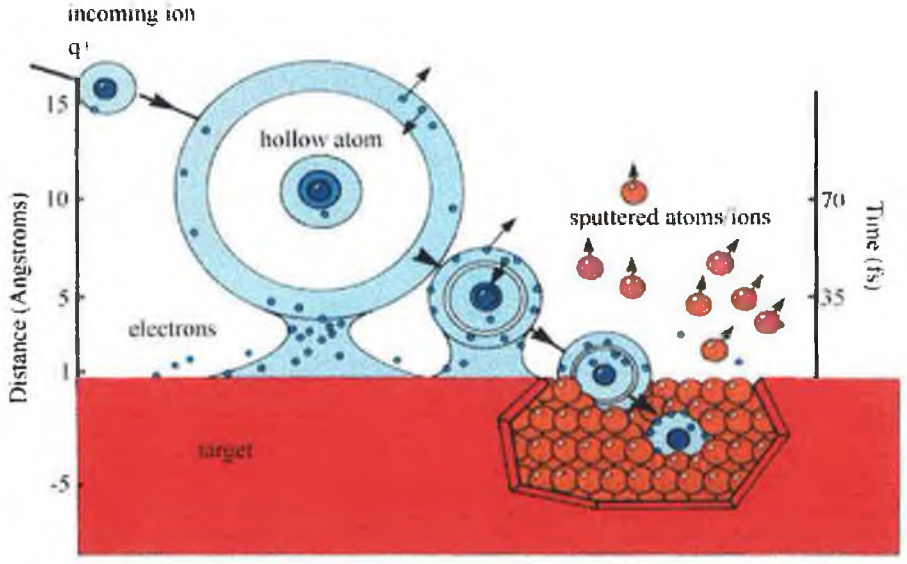

Figure 2.6 : A highly charged ion approaching a surface captures electrons, forming a hollow atom. This highly inverted species begins to decay via a complex cascade of Auger processes, which is interrupted when the ion hits the surface. A localised region of charge depletion may occur causing surface damage on a nanometre scale (after Hughes 1995).

contributed to much sought after insight into the nature of these 'Hollow atoms', their formation and decay as a result of the interaction of multiply charged ions with metal and insulator surfaces being of particular interest (Morgenstern 1997). With lifetimes in the femtosecond domain, these 'Hollow atoms' retain high potential energies on approach toward a solid state surface, the resulting interaction being likened to a firework display, vast numbers of electrons being produced for each incident 'Hollow atom' following its neutralisation period e.g. Th^{71+} ions produce up to 250 electrons per incident ion (Hughes 1995). Speculation has begun in earnest that these hollow atoms may be an appropriate medium for X-ray lasers (Morgenstern 1997) and their role in the impact of highly charged ions with solid state surfaces presents huge potential for nanostructure information storage (see figure 2.6), the controlled impact damage diameters ($\propto$ charge of incident ion) e.g. ~10nm for $Xe^{44+} \rightarrow$ ~40nm for U^{70+} (Hughes 1995), holding promise for a potential increase in storage capability over, say CD's (pits ~$1\mu m^2$) in excess of a factor of 10^4.

In 1995, the DLP system was used to investigate 'Giant resonances' in La^{3+} (Köble et al 1995b). The DLP system's inherent ion stage selectivity coupled with selective power densities on target allowed the successful generation of a sufficiently dense column of these high Z La^{3+}(Z=57) ions. Strong, broad and asymmetric in appearance, giant resonances arise from their multiparticle nature and are, thus, of great interest in the study of many-body effects. Of particular interest was the 4d excitation region of La^{3+}, its equivalent in the Ba Isonuclear sequence having been first observed by Lucatorto et al (1981). Using this experimental data, theorists predicted the gradual collapse of the 4f ^1P orbital in moving along the XeI Isoelectronic sequence from Ba^{2+} to La^{3+}. Indeed, Köble et al were successful in experimentally proving this theoretical supposition, clearly observing the $4d^94f\ ^1P$ giant resonance of La^{3+} at 118.9eV. Supplementing their DLP results with Configuration Interaction Hartree-Fock (CI HF) calculations (see section 2.4), a calculated oscillator strength of 5.0 for the $4d^94f\ ^1P$ transition provided further compelling evidence for orbital collapse in transit along the Isoelectronic sequence, whereby the $4d^94f\ ^1P$ transition demonstrated an unmistakable gain in strength at the expense of the once dominant $4d^{10} \rightarrow 4d^9\varepsilon f$ continuum transitions.

In this same year, the DLP system was used to measure the 5p and 4f excitation regions of atomic Au (Köble et al 1995a). This was followed by Isoelectronic studies on the evolution of 2p photoabsorption in Mg-like ions (Sayyad et al 1995) and the evolution of 3p photoabsorption in Ar-like ions (van Kampen 1995). Subsequent investigations have tackled 2p photoabsorption in Al-like ions (Costello et al 1998a), 3p excitation in the Zinc Isonuclear sequence (Kiernan et al 1997) and 2p excitation from the metastable Si^+ $2p^63s3p^2$ configuration (Costello et al 1998b). Most recently, however, a more quantitative analysis of the relationship between DLP spectra and the dynamics of the plasmas involved therein has been undertaken (Whitty et al 1998). Using spatio-temporal distribution maps of lithium allowed Whitty et al to gain insight into the dynamics of lithium plasma evolution in vacuum and, thus, obtain a high purity of Li^+ plume content. Comparison of their experimental measurements of both discrete $1s^2 \rightarrow 1snp$ (n=4-7) and continuum $1s^2 \rightarrow 1s\varepsilon p$ regions of Li^+, which have known oscillator strengths and cross sections respectively, to synthetic spectra generated using a tailored model followed. The model assumed an atomic frequency response (AFR) (see section 2.3.5.) which is best depicted by a Voigt profile, the profile being a hybrid of both Gaussian Doppler components and Lorentzian Stark components, and implemented a trial value for the number of absorbers, N. A value for the transmission over the energy range of interest was then computed for each line profile/section of continuum and this transmission spectrum convolved with a previously determined instrument function (0.105eV FWHM at 108.85eV). The final result was then compared with the experimental profile. The procedure was iterative in nature, finding conclusion when ultimate correlation was achieved. Using this procedure, Whitty et al were successful in extracting a Li^+ number density estimate of $\sim 9 \times 10^{17} cm^{-3}$ (for a plasma length of 0.3mm) using the discrete Li^+ spectrum and a number density of $\sim 1 \times 10^{18} cm^{-3}$ using measurements for the Li^+ continuum.

Having discussed the present status of the DLP system, let us now examine some system characteristics, each of which is critical to the accurate capture of quality photoabsorption data.

2.3 DLP system characterisation

2.3.1 Resolving Power

Every grating disperses light into its component wavelengths. The degree of dispersion determines the separation of any two wavelengths whereas resolving power may be defined as an instrumental measure of whether that separation can be distinguished. For a concave grating in a Rowland circle mount, the theoretical limit for resolving power ($\Re$) is given by (Samson 1967),

$$\Re = \lambda/\Delta\lambda = W(m/d) = mN \quad \text{for } W \leq W_{opt}/1.18 \qquad [2.3a]$$

$$= 0.92W_{opt}(m/d) \quad \text{for } W = W_{opt} \qquad [2.3b]$$

$$= 0.75W_{opt}(m/d) \quad \text{for } W >> W_{opt} \qquad [2.3c]$$

Here, $\Delta\lambda$ is the minimum wavelength separation which can be resolved, W is the width of the grating illuminated, m is the order number, N is the number of ruled lines within the illuminated grating area, d is the inter-groove spacing and W_{opt} is the optimum width of the grating such that resolving power is maximised for a particular angle of incidence(α), angle of diffraction(β) and wavelength λ. W_{opt} is given by

$$W_{opt} = 2.51\left[\frac{R^3\lambda Cos\alpha Cos\beta}{Sin^2\alpha Cos\beta + Sin^2\beta Cos\alpha}\right]^{\frac{1}{4}} \qquad [2.4]$$

where R is the radius of curvature of the grating (which equals the Rowland circle diameter). In our case, the 1200 lines/mm grating has ruled dimensions of 50mm in width and 30mm in height. However, Moloney(1998) has found, via ray tracing, that only approximately 42mm of the grating's width is illuminated and hence, we can say W = 42mm. Taking λ = 180Å as an example, one can calculate, using equations [2.1] and [2.4], an optimum grating width (W_{opt}) of 25.4mm. Hence, equation [2.3c] is applicable and we obtain a theoretical resolving power of ~23,000 giving a $\Delta\lambda$ of 0.0079Å.

A resolving power of ~23,000 would only be possible were one to use an entrance slit of the order of 1μm. However, the available flux of incident light must be sufficient to overcome drowning of the signal by unwanted noise. To this end, a trade off between spectrometer incident flux and resolving power is a logical inevitability. Indeed, Mack et

al (1932) have established that the minimum wavelength separation that can be resolved ($\Delta\lambda$) is given by

$$\Delta\lambda = \frac{W_s d}{R} \qquad [2.5]$$

where d and R are defined as for equations [2.3c] and [2.4] and W_s is the entrance slit width. Thus, employing a 10μm slit as was the case for all experimentation reported here, we obtain a $\Delta\lambda$ of 0.0376Å. This means that at 432Å, $\Delta\lambda$ corresponds to less than one pixel and at 69.2Å, $\Delta\lambda$ corresponds to ~1.4 pixels. Clearly, this theoretical value for $\Delta\lambda$ is not attained when using the 1024 pixel MCP detector so how may one accurately establish the true $\Delta\lambda$ and its related resolving power? Kiernan (1994) attempted to answer this question by examining the wavelength separation of well known closely spaced lines belonging to the emission spectrum of a laser produced aluminium plasma. The two lines of interest were Al VII 259.207Å and Al VII 259.036Å. The predicted plate factor or reciprocal linear dispersion (Å/mm or nm/mm) at a particular wavelength can be calculated from (Samson 1967)

$$\frac{d\lambda}{dl} = \frac{dCos\beta}{mR}$$

$$= \frac{Cos\beta}{mR(1/d)} \times 10^4 \text{ Å/mm} \qquad [2.6]$$

with d, m, R and β retaining their usual meaning.¶ Hence, with the aluminium lines being separated by 0.171Å and the plate factor (from equation [2.6]) at ~260Å being 0.0397Å/pixel, they were deemed a more than adequate means of assessing the system's resolving power. Initial observations of the doublet proved disappointing, the two lines appearing merged. However, by increasing the positive potential across the MCP/phosphor coated fibre reducer gap (see section 2.2.5) and more significantly moving the detector perpendicularly across the Rowland circle, the resolving power was optimised. Adjustment complete, the two lines were found to be separated by 5 pixels which translates to a resolving power at 260Å of ~1,300. Assuming a minimum of 5

¶ Predictions using this equation are, in fact, very close to the actual plate factors which have been ascertained from our wavelength/energy calibration routines (see section 2.2.6) and have been found to range from 0.026Å per pixel at 69.2Å to 0.048Å per pixel at 432Å.

pixels being required to separate any two features, regardless of the energy/wavelength region under scrutiny, we can then say, using the recently obtained values for plate factors above, that the resolving power varies from ~500 at 69.2Å to ~1,800 at 432Å. However, as a best case scenario, consistent with the well known Nyquist criterion, which states that the minimum number of pixels required to resolve a spectral feature on a PDA is >2, we can say that, at best, 3 pixels will allow a discernible separation of close features and as a result our resolving power is ~900 at 70Å and ~3,000 at 430Å.

Aside from variations in resolving power due to varying grating dispersion as a function of wavelength and a limited number of pixels with which to image the dispersed light, one must also consider the physical limitations imposed by using a flat detector on the curved Rowland circle. Whitty (1998) has examined some of these limitations. By measuring the FWHM of the aluminium $2s^22p^6 \leftarrow 2s^22p^53s$ transition at 160.074Å as a function of being imaged by different pixels on the detector, Whitty has shown how a spectral line is effectively 'smeared' for all pixel positions of the detector that are not tangent to the Rowland circle. By doing this, it has been determined that the detector is tangent to the circle between pixels 500 and 600 and, as such, a line imaged using these pixels is markedly narrower than the same line imaged at either detector extreme. Obviously, such a detector characteristic affects the system's resolving power and measurements made during the course of this work affirm Whitty's findings. Again using the Al VII doublet at ~260Å, it was imaged at thirteen different pixel locations by moving the detector along the Rowland circle in 0.1" steps whilst keeping all other experimental parameters constant. This is shown in figure 2.7(a). In order to measure the relative change in resolving power as a function of detector pixels being used, a modified Rayleigh criterion was employed which states that two lines of equal intensity will be just resolved when the wavelength difference between them is such that the minimum total intensity between the lines is $8/\pi^2$ (= 0.8106) times as great as the total intensity of both at the central maximum of either of the lines (Samson 1967). Measuring the intensity difference between the doublet minimum and the maximum of the slightly weaker component (259.036Å), the relative variation in resolving power could be plotted as shown in figure 2.7(b) where a smaller magnitude on the ordinate axis implies increased resolving power. Clearly, an increase in resolving power is evident between

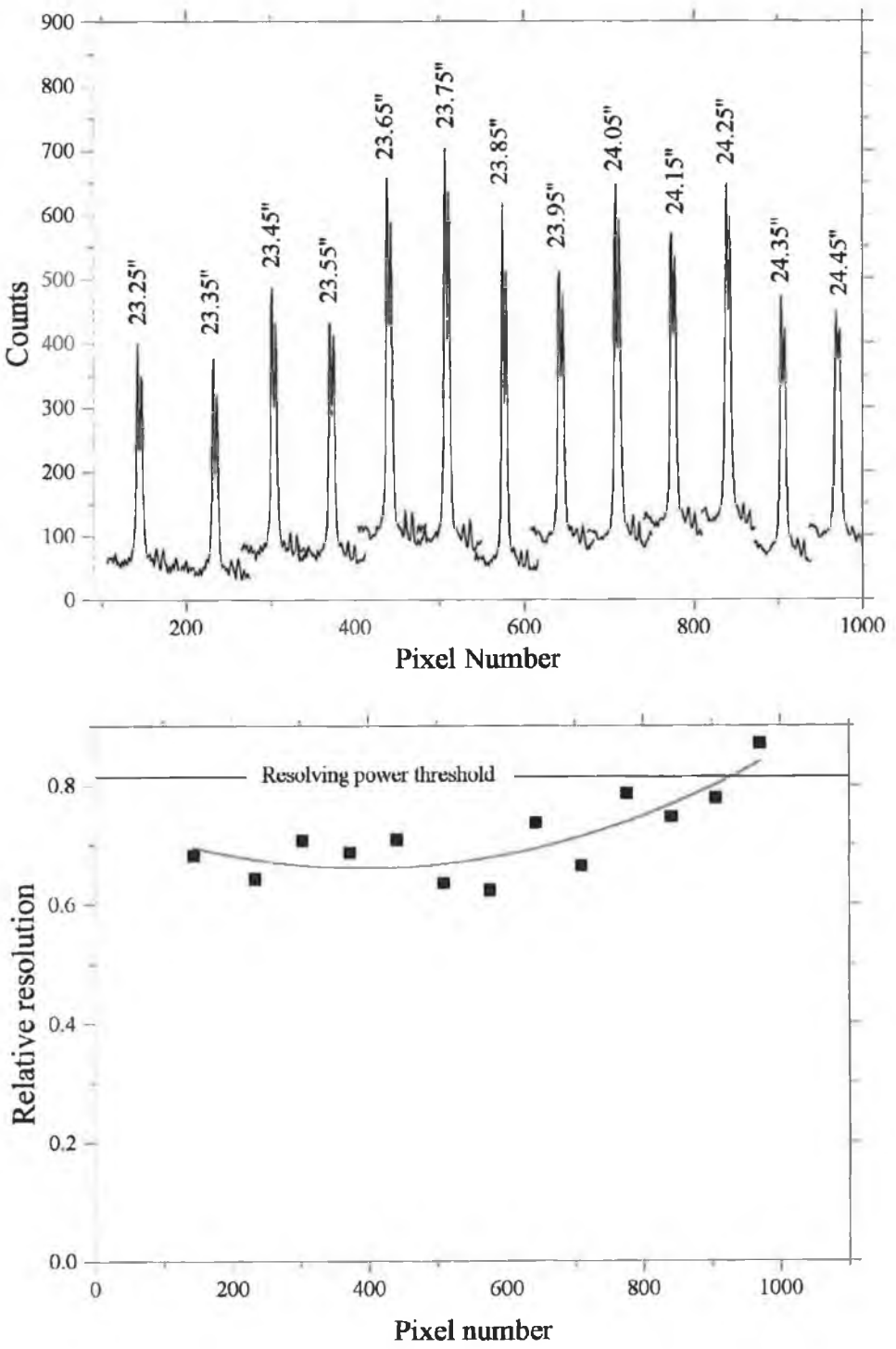

Figure 2.7 : The variation in resolving power across the detector where (a) shows the Al VII doublet at ~260Å imaged at pixel positions corresponding to 13 different chordal distances and (b) shows the associated resolving power of each, measured in accordance with a modified Rayleigh criterion (see text for details).

pixels 500 and 600. Thus, when taking photoabsorption measurements, features of interest should be imaged within this pixel range.

2.3.2 *The spatial gain variation across the detector*

Whitty (1998) has examined the spatial gain variation across the detector due to changes in the penetration depth of the incident radiation into the microchannels as a function of incidence angle (Bridges et al 1986). Using the aluminium $2s^22p^6 \leftarrow 2s^22p^53s$ emission line at 160.074Å, its integrated area for seven different chordal distance settings was obtained. Each different setting allowed the line to be imaged with different sections of

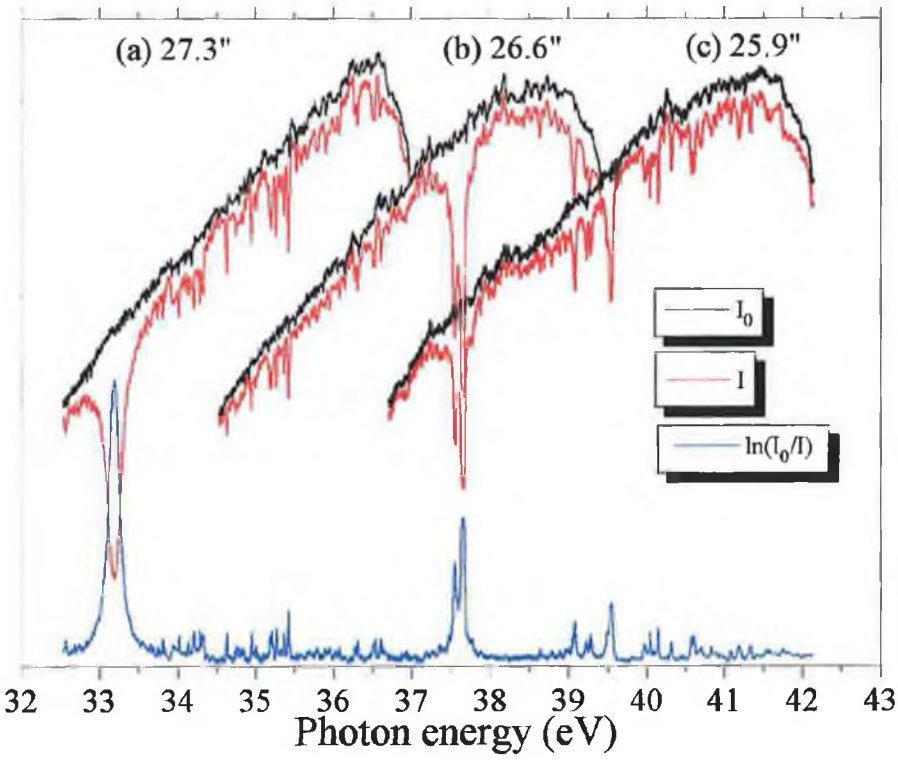

Figure 2.8 : An illustration, using the emission spectrum of tungsten (I_0), of how the detector sensitivity or gain is non-uniform for all 1024 pixels, the sensitivity being particularly poor on the high energy side of the array. As can be seen the effect is more important for emission spectra, all features from the Ca^+ absorption spectrum, shown in blue, retaining the same relative intensities from chordal distance setting to setting, due to the gain variation cancelling out after the $\ln(I_0/I)$ transformation.

the 1024 pixel array in much the same way as was used to examine resolving power in section 2.3.1. Whitty's conclusions supported a notable fall off in detector efficiency at either pixel extreme. To further corroborate this trend, three overlapped tungsten continuum spectra were compared, these corresponding to different detector positions along the Rowland circle. Where intensities should have been equal (all other experimental variables remaining static) for wavelength overlaps, this was clearly not the case, the correlation being particularly poor on the high energy side of the detector. Although this gain variation must be seriously considered when undertaking to capture emission spectra, the effect on absorption spectra is negligible as the gain variation is common to both $I_0(\lambda)$ and $I(\lambda)$ and, thus, cancels. The fall off in detector sensitivity can be easily seen in figure 2.8, where we show adjacent chordal distance settings with large overlaps. Figure 2.8 also illustrates how the gain variation has a negligible effect on absorption ($\ln(I_0/I)$) spectra, the relative intensities of absorption features remaining constant from setting to setting.

2.3.3. Higher order contributions

From the grating equation shown in section 2.2 i.e. equation [2.1], we have, for a given groove density and a given angle of incidence (α) and angle of diffraction (β),

$$m\lambda = \text{constant} \qquad [2.7]$$

This implies that if the diffraction order m is doubled, the wavelength (λ) is halved. Effectively, this means that if a source emits a continuum of wavelengths, then at the physical location of, say, 800Å in first order, wavelengths of 400Å, 266.66Å and 200Å are also present in second, third and fourth orders, respectively (Lerner and Thevenon 1988). To estimate the contribution of higher order light in our 2.2m system which is potentially superimposed upon first order wavelengths, we have used the emission spectrum of lithium (see figure 2.9). As can be seen, the Li^{2+} 1s $\leftarrow$ 2p transition at 135.001Å appears in second order at 270.002Å and third order at 405.003Å. Likewise, the

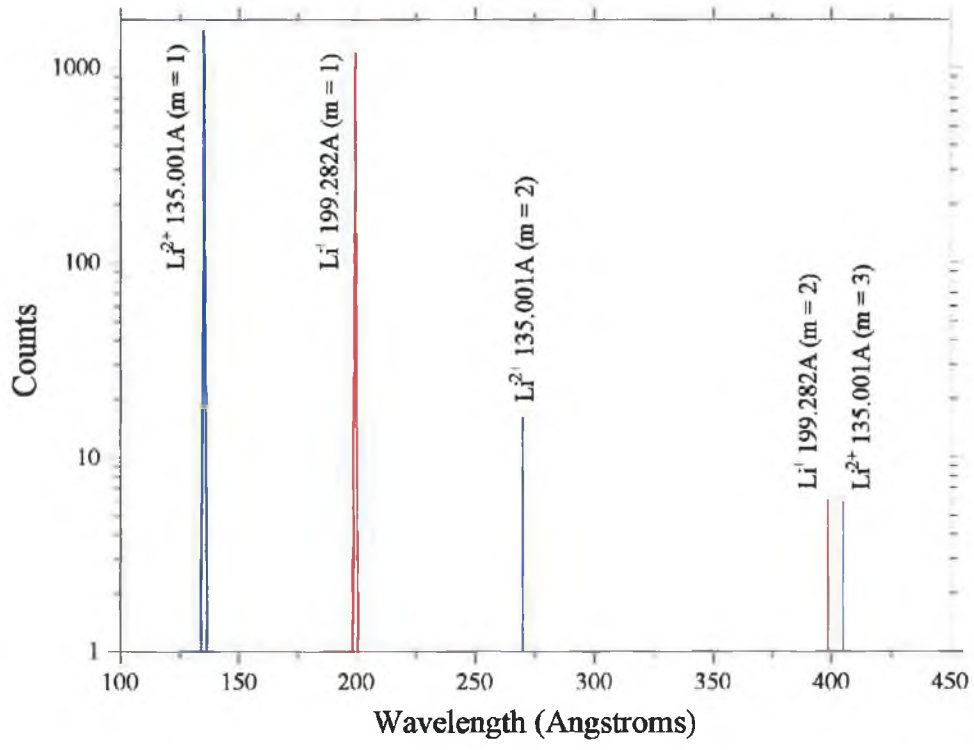

Figure 2.9 : Higher order contributions in the 2.2m system measured using lithium emission lines.

Li^+ $1s^2$ ← 1s2p transition at 199.282Å in first order appears in second order at 398.564Å. From the relative peak heights of first and higher order lines, it is immediately clear that higher orders exhibit intensities ≤ 1% that of their first order counterparts. Thus, higher orders do not have a significant influence on the detected signal and can therefore be ignored.

2.3.4. Stray light

Stray light may be defined as light of other wavelengths which is superimposed upon the useful light i.e. the light the user wishes to detect. Its presence on the detected signal is due to either (a) scattering from any optical surface in the system, or (b) non-periodic errors in the ruling of the grating grooves (Lerner and Thevenon 1988).

It has been shown that the stray light present in the DLP system used here is appreciable for energies >100eV and that it originates from energy regions <100eV (Whitty 1998). Measured DLP photoabsorption spectra with photon energies >100eV must therefore be

corrected to account for stray light contributions. A stray light component can be present on both the I_0 and the I signals. The stray light component on I i.e. I_s, is different for different absorbing plasmas and without known cross sectional values for the energy region of interest of the target element, I_s is difficult to establish. In the absence of an adequate method of determining the stray light associated with the I signal, as was the case for the neon isoelectronic sequence members studied in chapter 4, one may assume that the stray light is the same for both I_0 and I. This simplifies matters somewhat and allows one to follow a stray light treatment in keeping with that subscribed to by Perkampus (1992). Denoting the real transmission, T_{true}, as equal to I_{true}/I_{0true}, one can say that the measured transmission is given by

$$T_{meas} = \frac{I_{true} + I'}{I_{0true} + I'} \qquad [2.8]$$

where I' is the stray light signal. Introducing the proportion of stray light, p, as

$$p = \frac{I'}{I_0 + I'} \qquad [2.9]$$

we obtain,

$$T_{meas} = T_{true}(1 - p) + p \qquad [2.10]$$

and consequently,

$$T_{true} = \frac{T_{meas} - p}{1 - p} \qquad \text{or} \qquad A_{true} = -\ln\left(\frac{T_{meas} - p}{1 - p}\right) \qquad [2.11]$$

where A_{true} is the true absorption.

To calculate p, the transmission from a 0.25μm thin film aluminium filter, purchased from Goodfellow metals, was measured from ~30eV to 190eV. Figure 2.10 shows the recorded transmission over some 20 MCP/PDA chordal distances which go from 16.2" to 29.5" with a 0.7" increment providing a large overlap between settings. The data is compared with other experimental data (Hagemann et al 1974, Powell et al 1990 and Gullikson et al 1994 (plotted via Henke's code¶)). Before discussing the stray light and how p is obtained, it is interesting to note the rather large discrepancy, for energies

¶Henke's computational code (Henke et al 1993) and tables of atomic scattering factors are available from http://www-cxro.lbl.gov/optical_constants

below the L_{III} edge at 72.7eV, between the DLP measured transmission and that of the other authors cited above. Of the three sets of data used in the comparison, the data produced via Henke's code, using optical constants measured by Gullikson et al (1994), is deemed to be the more accurate, all filter thickness values having been determined interferometrically to within ±40Å and the effects of oxidation having been accounted for. Hagemann and Powell, on the other hand, focussed primarily on the energy regions above the L_{III} edge. The mismatch in transmission values may be explained by considering the effects of oxide growth and tungsten deposition via blow-off from the source. Taking the filter to be a little thicker than specified by Goodfellows, but still within tolerance (±20%) at 0.3μm and calculating the composite effect (using Henke's code), on the Henke curve in figure 2.10, of a 150Å Al_2O_3 layer and a 30Å W layer, the theoretical transmission curve was uniquely reconciled with the experimental (see figure 2.11).

Whitty (1998), having used the same Al filter in a similar stray light treatment, also observed a mismatch in theoretical and measured transmission values below the L_{III} edge. In this case the two data sets were reconciled by considering the composite effect of an 80Å Al_2O_3 layer and a 10Å W layer. A reminder of the effects of both plasma deposition (the source having been located ~6cm from the filter) and filter ageing, we note in particular that the data shown in figure 2.10 was taken ~6 months after the measurements of Whitty who had then estimated a filter age of ~1 year. The oxide layer having increased from 80 to 150Å in the intervening period is not beyond the bounds of possibility and indeed this is supported by Powell et al (1990) who has found oxide layers on aluminium filters to reach a thickness of 150Å over a period of about 1.5 to 2 years since manufacture.

Returning to the question of how one may obtain the proportion of stray light, p, we find that if we take the DLP data and compare with the accurately measured Hagemann data for energies beyond the L_{III} edge at 72.7eV, we can say that

$$T_{DLP} - T_{Hagemann} = \frac{I}{I_0} \qquad [2.12]$$

where because in the absence of stray light, I should show zero counts, I is now a direct measure of the stray light signal I' (in counts) i.e. I = I'. Thus, as we already know I_0, it is

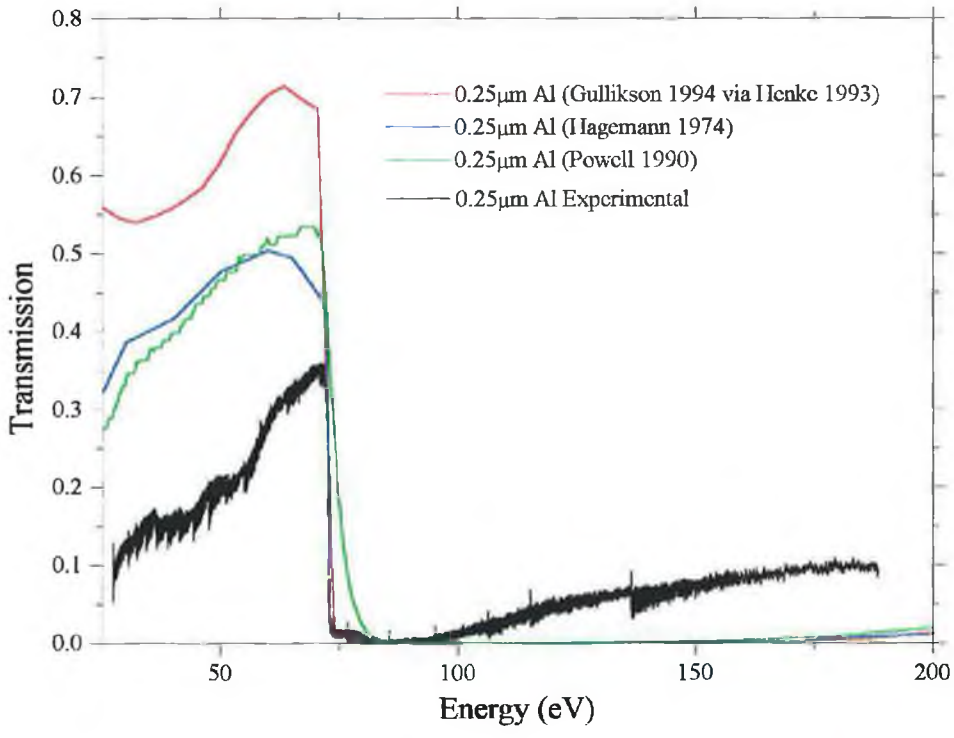

Figure 2.10 : The experimentally measured transmission spectrum of a 0.25μm aluminium thin film. Note the onset of stray light at ~100eV.

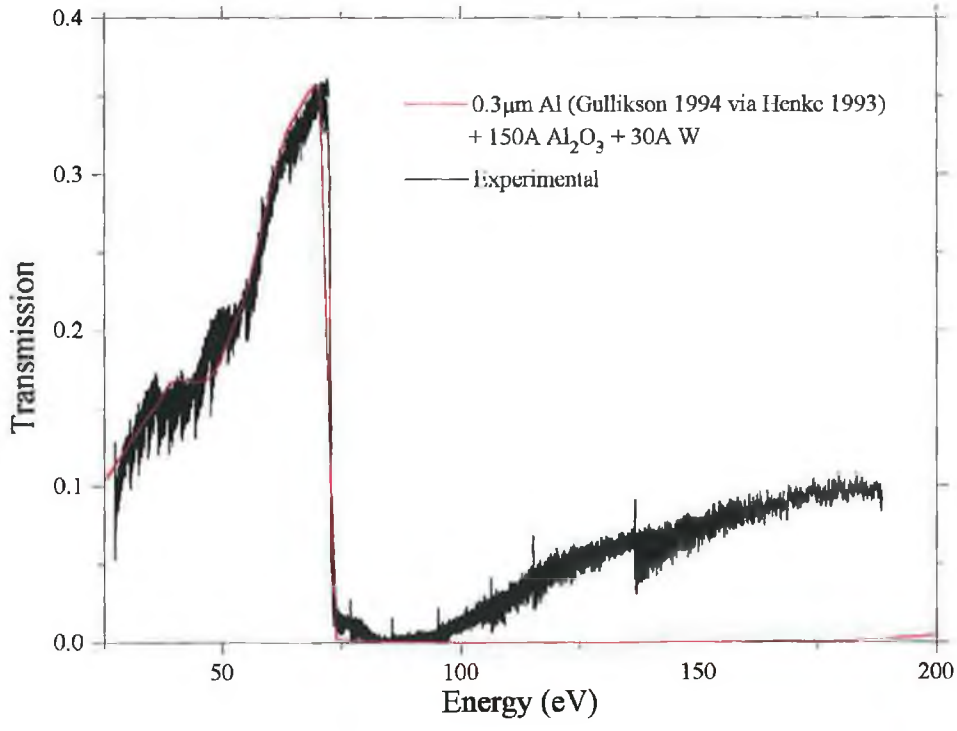

Figure 2.11 : A plot comparing measured and predicted transmission assuming the Al foil is closer to 0.3μm (0.25μm ± 20%) in thickness and has a 150Å layer of Al_2O_3 and a 30Å layer of W.

now a simple matter to calculate p as a function of energy using equation [2.9]. The resultant curve is shown in figure 2.12 and this can be used in conjunction with equation [2.11] to correct any transmission or absorption spectra for their irksome stray light components.

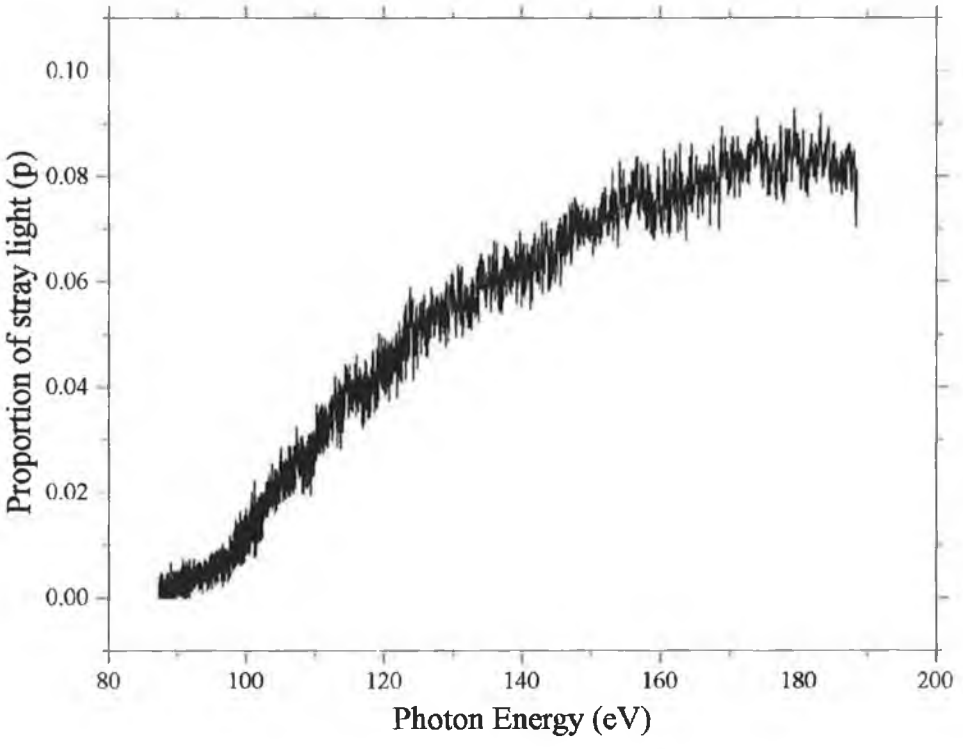

Figure 2.12 : A plot showing the proportion of stray light (p), present in the DLP system, as a function of energy (see text).

As a last point of issue on this subject, it is most important to realise that, as Perkampus (1992) has shown (see figure 2.13), the relative error in absorption or absorbance (=-logT) increases rapidly with the value of absorption/absorbance for a given proportion of stray light, p. Thus, as an example, we see from figure 2.13 that for $0.005 \leq p \leq 0.02$, an absorbance of 0.6 to 0.8 should not be exceeded should one want to keep errors below 10%. In our case, as we can see from figure 2.12, p reaches a maximum of 0.1 on approaching 200eV and thus, from figure 2.13, it is immediately clear that absorption /absorbance values should be kept as low as possible without, of course, succumbing to noise. Without paying special attention to absorption levels, a knowledge of p suggests that any spectra can theoretically be corrected for stray light but it is surely a more

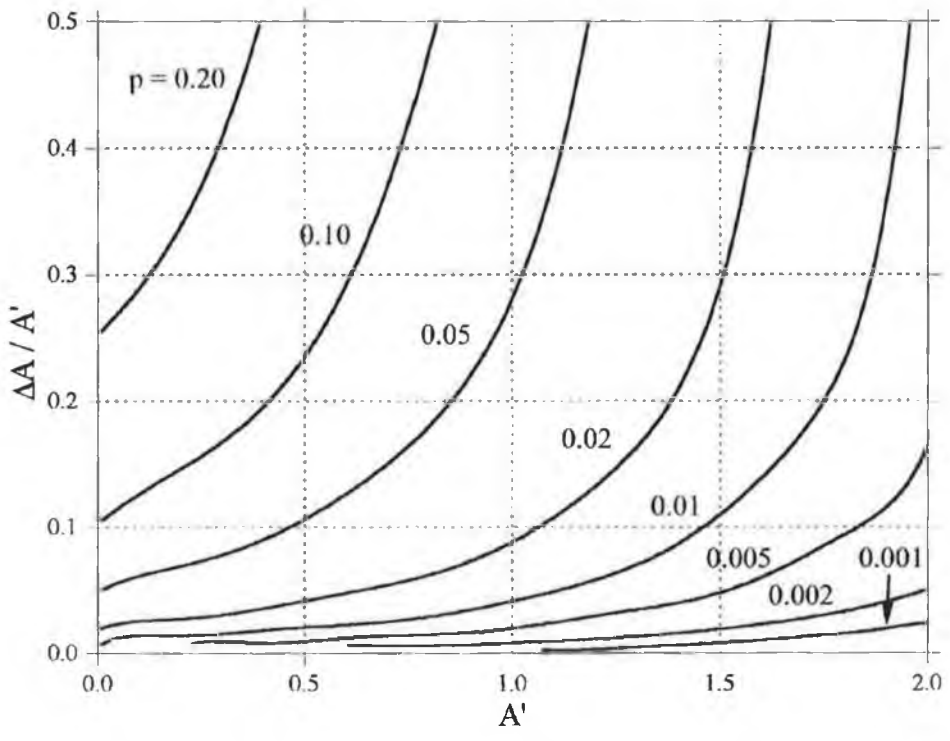

Figure 2.13 : The effect of stray light on the measured (or distorted) absorbance A'. p is the proportion of stray light as defined in the text and ΔA = A' - A is the relative error (after Perkampus 1992).

prudent move to minimise the effects of stray light in the first place by adhering to what may be described as optically thin regimes (section 1.4) and indeed, examples of this will be given in chapter 4.

2.3.5. Instrument function

When using any spectrometer system, the recorded spectrum is effectively the convolution of the real spectrum and the instrumental profile. The shape and width of the instrumental line profile is a function of various parameters including (Lerner and Thevenon 1988),

(a) the width of the entrance slit,

(b) the width of the exit slit or of one pixel in the case of a multichannel detector,

(c) diffraction phenomena,

(d) aberrations,

(e) the quality of the system's components and their alignment.

In order to spectrally restore a recorded spectrum to its original form, one must, therefore, deconvolve it with this 'instrument function' but how is an accurate estimate of the instrument function obtained?

One particular method involves using a spectral line for which atomic parameters are known in some detail. From a measure of these parameters and a knowledge of the conditions existing in the plasma from which the line radiation was emitted, each of the major atomic broadening mechanisms which give a spectral line its intrinsic shape and width can be quantified. Knowing what the line should theoretically look like, we can then deconvolve with the measured profile to obtain the instrument function.

A second and more reliable method is to record a spectral line whose profile parameters have been previously established with high accuracy and which is known to be extremely narrow i.e. beyond the resolving power of our spectrometer. Knowing the line's true shape and width, the shape and width of the instrument function with which it has been convolved to yield the distorted measured profile, can then be established. Details of both determinative methods shall now be outlined.

Method (a)

Many broadening mechanisms can potentially influence the shape and width of a spectral line. Natural broadening, Stark broadening, Doppler broadening, Resonance broadening, Zeeman broadening and Self-absorption broadening represent the greater majority of these mechanisms but within the context of a laser produced plasma, Stark and Doppler broadening are seen to dominate. Before discussing the nature of these mechanisms, one must introduce the concept of the Atomic Frequency Response (AFR) which describes the intrinsic line shape of any spectral line. Normalised, the AFR can be written as

$$\int_{line} \varphi_\nu d\nu = 1 \qquad [2.13]$$

It represents the probability per unit frequency interval for observation of a photon emitted in the interval ν to $\nu + d\nu$ about a central frequency ν_0. All AFR's are either

Gaussian, Lorentzian or Voigt in profile. The Lorentzian profile AFR is written as (Corney 1977),

$$\varphi_{\nu L} = \frac{\Gamma_L/2\pi}{(\nu-\nu_0)^2 + \Gamma_L^{\,2}/4} \qquad [2.14]$$

where ν is the running variable (in this case, frequency), ν_0 is the centre frequency of the profile and Γ_L is the full width at half maximum (FWHM). Alternatively, a Gaussian profile AFR is often related by (Corney 1977),

$$\varphi_{\nu G} = \frac{2}{\sqrt{\pi}\Delta}\exp\left(-4\left(\frac{\nu-\nu_0}{\Delta}\right)^2\right) \qquad [2.15]$$

where ν and ν_0 retain their above definitions and Δ is known as the linewidth parameter which is related to the FWHM (Γ_G) by†

$$\Gamma_G = \Delta\sqrt{\ln 2} \qquad [2.16]$$

Finally, we mention the Voigt profile which takes account of both a Lorentzian and a Gaussian contribution to the AFR. However, as it cannot be expressed in analytic form it has not been used in this work and shall not be discussed further.

Considering only Natural, Doppler and Stark broadening, we find that natural broadening is the result of the finite lifetime of any atom in any excited state. If we know the lifetime Δt then the Heisenberg uncertainty principle,

$$\Delta E \cong \hbar/\Delta t \qquad [2.17]$$

implies an uncertainty in the energy of the state. In principle, this uncertainty must be considered for both the energy levels between which a transition occurs but if one is concerned only with resonance lines then the ground state will have an infinitely large Δt value and the natural broadening will be due to the energy uncertainty in the upper level only. Traditionally, detailed surveys of absorption/emission line atomic parameters list transition probabilities A_{ji}, where the lifetime is given by (Corney 1977),

$$\frac{1}{\Delta t} = \sum_i A_{ji} \quad (s^{-1}) \qquad [2.18]$$

---

† The Gaussian formula used in the software package Origin V3.5 (which has been used extensively throughout this work), is incorrect. The fitted width given therein must be divided by $\sqrt{\ln 2}$ in order to obtain the correct value for FWHM.

In neutral atoms, Δt is no smaller than ~10^{-8}sec (Cowan 1981), which gives natural line widths ΔE_{nat} of the order of 10^{-8}eV. These are negligible in comparison with the widths associated with other broadening effects. However, natural broadening becomes increasingly more important with increasing energy/frequency due to the dependence of A_{ji} on ν_{ji}^3 (see equation [1.68]). The energy/frequency distribution attributable to natural broadening is always described by a Lorentzian AFR.

Doppler broadening is caused by the thermal motion of the emitting or absorbing atoms. If there is a relative velocity v between the observer and an atom emitting light of frequency, ν, the light received by the observer will appear to be of frequency ($\nu + d\nu$) or ($\nu - d\nu$), depending on the direction of motion, where $d\nu = v.\ \nu/c$. As the atoms of a plasma move in a number of directions, the observer will receive light of many slightly different frequencies and thus, the line appears broadened (Kirkbright and Sargent 1974). In the case where the atoms or ions are distributed with a maxwellian velocity distribution at temperature T, then the width (FWHM) of the doppler broadened line is given by

$$\Delta\nu = 7.162x10^{-7}\nu_0\sqrt{T/M} \qquad [2.19]$$

where ν_0 is the central frequency, T is the temperature in Kelvin and M is the atomic weight. Doppler broadening can often be orders of magnitude greater than that of natural broadening and is most pronounced for light elements (Cowan 1981). It is described by a Gaussian AFR.

Stark broadening arises due to radiating particles being perturbed by microscopic electric fields from ambient ions and electrons which lie within a sphere with a radius equal to the Debye length (see equation [1.7]). Two limiting cases of stark broadening exist. The first assumes that the radiating particles are perturbed by ion collisions only. Furthermore, one assumes that the radiating atom/ion is only perturbed during the duration of a collision, t_c, defined by,

$$t_c = \rho/\bar{v} \qquad [2.20]$$

where ρ is the distance of closest approach and $\bar{v}$ is the mean velocity at this point. If the duration of a collision is far greater than the time between collisions, T_c, one may then further say that the line broadening is produced while the perturbing ion moves

only a short distance. Therefore, it is possible to completely ignore the motion of the perturbers and thus we have a criterion for what is known as the *quasi-static approximation*, whereby (Corney 1977)

$$t_c >> T_c \qquad [2.21]$$

The FWHM of any line broadened under this approximation is given (in Å) by (Bekefi 1976)

$$\Delta\lambda_{quasi} = 8.16x10^{-19}\left(1 - 0.7N_D^{-1/3}\right)\lambda_0^{\,2}\left(n_j^{\,2} - n_i^{\,2}\right)\left(\frac{Z_p^{\,1/3}}{Z_e}\right)N^{2/3} \qquad [2.22]$$

with $$N_D = 1.72x10^9\frac{T^{3/2}}{N^{1/2}} \qquad [2.23]$$

where N_D is the number of particles in the Debye sphere, λ_0 is the central wavelength, n_j and n_i are the upper and lower principal quantum numbers associated with the transition of interest, Z_P is the ionic charge, Z_e is the nuclear charge, T is the temperature (in eV) and N is the particle density (in cm^{-3}). From equations [2.20] and [2.21], we can see that the quasi-static approximation is better for high densities ($>10^{18}cm^{-3}$), where T_c is short, and at low temperatures, where $\bar{v}$ is small.

The second case for Stark broadening is known as the *electron impact approximation* whereby line broadening due to collisions from electrons is no longer neglected but on the contrary is now considered to be in the majority. In terms of our previously mentioned criteria i.e. equations [2.20] and [2.21], we now assume that the collision duration is short compared with the time between collisions i.e. $t_c << T_c$. Thus, the impact approximation is better for low pressures or densities ($10^{16} \leq N \leq 10^{18}cm^{-3}$), where T_c is long, and at higher temperatures, where $\bar{v}$ is large (Corney 1977). The FWHM of a stark broadened line under this approximation is given (in Å) by (Griem 1974, Bekefi 1976)

$$\Delta\lambda_{impact} = \underbrace{2W\left(\frac{N}{10^{16}}\right)}_{\text{electron contribution}} + \underbrace{3.5A\left(\frac{N}{10^{16}}\right)^{1/4}\left[1 - \frac{3}{4}N_D^{-1/3}\right]W\left(\frac{N}{10^{16}}\right)}_{\text{ion correction}} \qquad [2.24]$$

where N and N_D retain the same definitions as those given for equations [2.22] and [2.23] and W, A and D are coefficients which are independent of density, N, and which are slowly varying functions of electron temperature T (15% variation for 10,000 ≤ T ≤ 40,000°K). Griem (1974) has tabulated these coefficients for many well known transitions of different atoms ranging from helium to cesium , the values given being specific for N = $1x10^{16}cm^{-3}$. Equation [2.24] is only accurate to within 20 or 30% despite the correction for the relatively unimportant quasi-static ion broadening. Griem (1974) stresses that equation [2.24] is only applicable to lines from neutral atoms. However, the formula may be modified for use with singly ionised ions by simply replacing the 3/4 value by 1.2. Griem imposes further restrictions on equation [2.24]'s use in saying that it is only applicable within the parameter range $N_D \geq 2$ and $0.05 < A\left(N/10^{16}\right)^{1/4} < 0.5$.

In terms of deciding which approximation is more suitable for application to a particular line, apart from the density and temperature considerations mentioned above, Bekefi (1976) has suggested that the quasi-static approximation is more descriptive of hydrogenic lines that do not have a strong central undisplaced component such as Lyman β, Lyman δ, Balmer β etc. On the other hand, Bekefi states that the FWHM of lines like Lyman α and Balmer α etc. are almost completely dominated by electron collisions. These lines are therefore better described by the impact approximation. He further states that neutral atoms and singly ionised non-hydrogenic ions are dominated by electron collisions and so again the impact approximation is more appropriate. Regardless of which approximation is used, Stark broadening is described by a Lorentzian AFR.

As our test case for instrument function extraction, we have chosen the B^{2+} $1s^22s \rightarrow 1s^25p$ transition at 32.942eV. The natural width of this line can be calculated by using the transition probabilities tabulated by Verner (1994) which, via equations [2.17] and [2.18], give a width ΔE_{nat} of $7x10^{-7}$eV. It can thus be concluded that the effect on the line width due to natural broadening is negligible and that the natural width of the line is beyond the resolving power of our 2.2m system. Its measured width is therefore the direct result of instrument function broadening and broadening due to the Stark and Doppler broadening mechanisms discussed above. A low Z element, boron is particularly attractive as a test candidate as it exhibits a sparsity of lines in the VUV and thus any

lines that do reside in this region of the EM spectrum are well isolated and unperturbed by neighbours. Also conducive to its selection is the availability of related atomic parameters.

Having observed the B^{2+} 2s-5p transition in absorption with an averaged total of 45 shots to ensure ample noise suppression, the contributions due to Stark and Doppler broadening were calculated. To calculate the Stark component for B^{2+} 2s-5p, the electron impact line width calculations of Dimitrijevic and Sahal-Bréchot (1996) were used. Unfortunately, independent calculations could not be performed using equation [2.24] as Griem (1974) does not list width and shift parameters (W,A and D) pertaining to the B^{2+} 2s-5p transition. For an electron density of $1x10^{17}cm^{-3}$, Dimitrijevic and Sahal-Bréchot list widths for temperatures of $1x10^4$, $2x10^4$, $5x10^4$, $1x10^5$, $1.5x10^5$ and $3x10^5$°K. To narrow the range of applicable widths, the temperature of B^{2+} ions in a laser produced plasma was estimated using the collisional-radiative model described in section 1.2.3.3. B^{2+} temperatures were calculated for a range of electron densities taking the critical density associated with a Nd:Yag laser, of $1x10^{21}cm^{-3}$ (see equation [1.11]), as the upper limit. The results suggested a temperature ranging from 3.2 to 3.5eV for densities of $1x10^{15}$ to $1x10^{18}cm^{-3}$, respectively. On this basis, the widths given by Dimitrijevic and Sahal-Bréchot of 2.21meV and 1.92meV for temperatures of 1.7eV ($2x10^4$°K) and 4.3eV ($5x10^4$°K) respectively, were most applicable. Inserting these temperatures into equation [2.19], we get Doppler FWHMs of 1 and 1.6meV for T = 1.7 and 4.3eV respectively. Generating Lorentzian AFRs with Stark FWHMs as above and Gaussian AFRs with the relevant Doppler FWHMs, convolving each pair to get the total AFR associated with T = 1.7 and 4.3eV respectively, and then separately deconvolving the two total AFRs from the measured B^{2+}2s-5p profile, we were left with two estimates of the instrument function. As an example, figure 2.14 shows the measured B^{2+}2s-5p profile, the calculated total AFR (for T = 1.7eV) and the resultant deconvolution which is our instrument function estimate. For each of these estimates, both Gaussian and Lorentzian curve fits were performed with the resultant measure of error, in the form of a χ^2 ¶, determining which shape best described the instrument function. The result for T = 1.7eV and 4.3eV was unanimously a lorentzian profile with widths of 19.4 and 20.5meV respectively. Figure 2.15 shows the extracted instrument function for T = 1.7eV, the superior

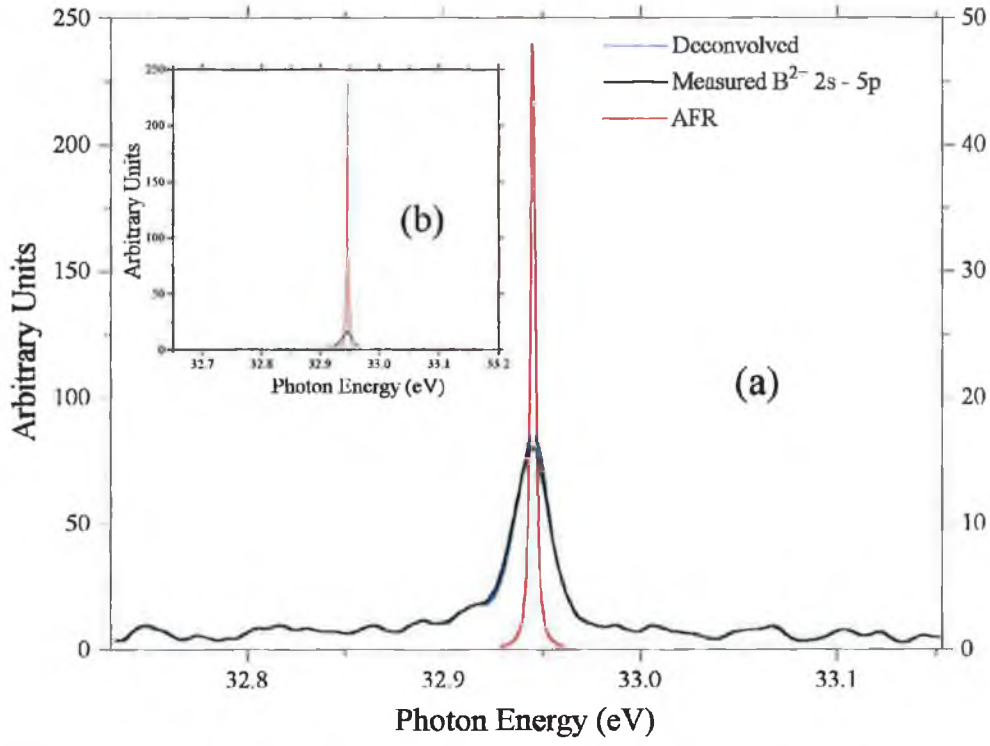

Figure 2.14 : The measured B^{2+} 2s → 5p transition, calculated total AFR (for N = 1x10^{17}cm^{-3} and T = 1.7eV) and extracted instrument function (deconvolved profile) where in (a) the measured and deconvolved profiles are plotted with the same ordinate scale (left scale) and the AFR is on a separate scale(right scale) so that the contrast between the three may be emphasised. In (b), all three profiles are plotted on the same scale, their integrated areas having been normalised to unity for comparison.

correlation with a Lorentzian profile even visibly apparent. Knowing the plate factor at 32.9eV to be 4.2meV per pixel, these values translate to instrument function widths of 4.5 and 4.9 pixels. These results are similar to those obtained by fitting the measured profile directly i.e. a Lorentzian profile of 21meV (5 pixels) FWHM. This is not unexpected as, in cases such as this, where the Stark and Doppler broadening is small compared to the

---

¶ The data processing software Origin V3.5 measures the error in a fit using χ^2 which is defined as $\chi^2 = \frac{\sum_{i=1}^{N}(f(X_i) - Y_i)^2}{N - n}$ where X_i and Y_i are data points, N is the number of data points and n is the number of parameters. It is related to Standard Deviation by S.D. = $\sqrt{\chi^2}$

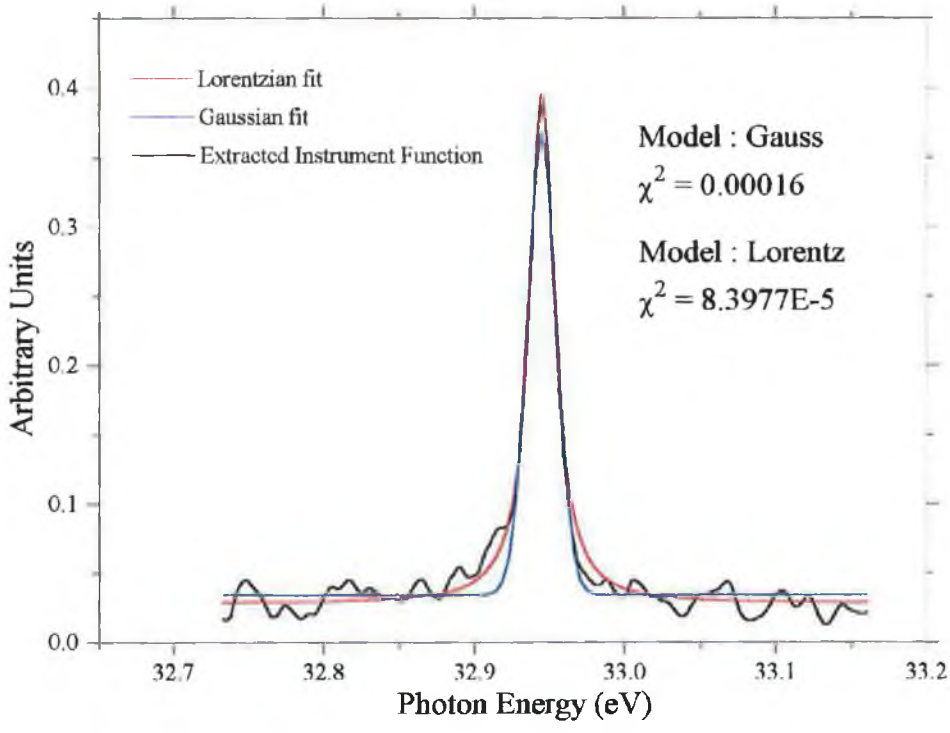

Figure 2.15 : The extracted instrument function which results when the measured B^{2+} 2s→5p transition is deconvolved with the total AFR (for T = 1.7eV). The plot shows the results of both a Gaussian and a Lorentzian curve fit whereby the χ^2 values for both fits clearly indicate that the instrument function is best described by a Lorentzian profile.

width of the measured line, the measured line profile may be considered to be directly representative of the instrument function.

Unfortunately, the results from this method of instrument function calculation are not definitive due to the sensitivity of the calculations involved. Even with a knowledge of plasma temperatures and densities, large discrepancies can arise in the results from different models. This is particularly so for models on Stark broadening. As an example, we direct attention to the work of Seaton (1988), who has calculated thermally averaged collision strengths (Y) for a number of line profiles in lithium like ions assuming an electron impact approximation. These Y parameters allow further calculation of line widths and shifts. Applying Seaton's formulary (Seaton 1988), the Stark width for the B^{2+} 2s → 2p transition can be calculated to be 0.01134Å (FWHM) for a temperature of $2x10^{4}$°K and a density of $1x10^{17}cm^{-3}$. For the same plasma parameters and the same transition, Dimitrijevic and Sahal-Bréchot (1996) obtain a width of 0.0268Å, which differs

from the former by a factor of 2.4. As the above method for instrument function extraction is reliant both on a knowledge of plasma densities and temperatures (quantities which we do not measure directly) and on the choice of model, it is obvious that an alternative, which is model independent and does not require plasma temperatures and densities, would be more accurate. Such a method shall now be described.

Method (b)

In 1967, Codling et al measured the inner shell autoionising resonance Ne I $2s2p^63p\ ^1P_1$ with a resolving power of ~4,500. This allowed an extremely accurate determination of the resonance's associated Fano parameters (see section 1.3). With our 2.2m system possessing a resolving power of ~2,000 in the vicinity of this resonance i.e. 45.546eV (272.22Å), we have followed Codling et al's measurement expecting the resultant profile to be broadened by our system's inherent instrument function. Knowing, from Codling et al (1967), the centre energy (E), the profile index (q) and the FWHM (Γ) of the resonance to be 45.546eV, -1.6 and 0.013eV respectively, we could generate the profile and compare it to our equivalent DLP measurement. This is shown in figure 2.16. When our DLP measured resonance is fitted with equation [1.42], we obtain values for E, q and Γ of 45.546eV, -1.478 and 0.038eV respectively. Convolving Codling's profile with a range of both Gaussian and Lorentzian AFRs which have been generated with FWHMs of 10, 12, 14, 16, 18, 20, 22, 24, 26, 28 and 30meV, we can then curve fit the results to extract E, q and Γ parameters. Using Origin V3.5's χ^2 measure of error, we then fit the DLP measured profile with the parameters extracted from the convolutions being sure to keep the parameters fixed during the fit. The convolved profile which yields the smallest χ^2 value, when fit to the DLP measured resonance, thus leads directly to our instrument function. The E, q and Γ parameters extracted from each Codling 3p resonance/AFR convolution are shown in table 2.2. Also shown is the χ^2 value obtained from the fit to the DLP profile. From table 2.2 we see that the best fit (smallest χ^2) is obtained for a Lorentzian AFR with FWHM of 24meV. The plate factor at 45.546eV is 6meV which implies that the instrument function is Lorentzian in nature and has a FWHM equivalent to 4 PDA pixels.

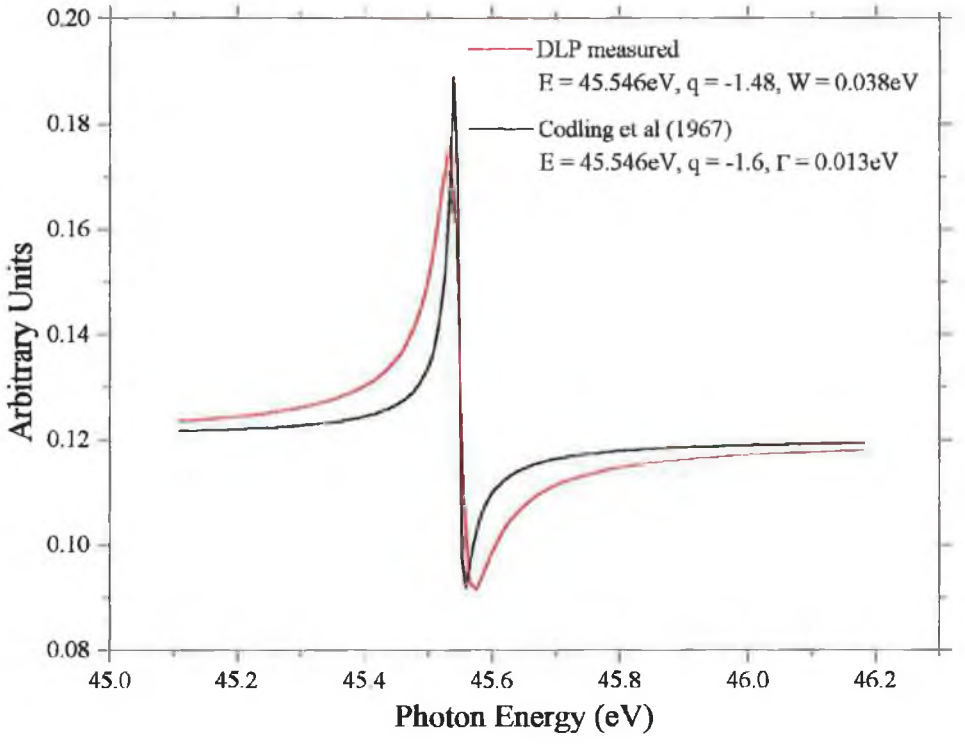

Figure 2.16 : The inner shell autoionising resonance, Ne I $2s2p^63p$. Its profile has been generated from parameters measured by Codling et al (1967) and from parameters measured using the DLP photoabsorption system. Note that the DLP width parameter is denoted, W, as the profile width has been broadened by our instrument function.

Whitty (1998), using a similar technique to that described in method (a), but using the Li^{2+} Lyman β photoabsorption line (113.905Å) and assuming a quasi-static approximation for Stark width determination, obtained an instrument function corresponding to a Lorentzian profile of approximately 3.7 pixels. Having already stated that method (b) above is deemed the more accurate approach, it is thus our assertion that the instrument function has a FWHM of 4 pixels and is Lorentzian in nature. Having discussed, at length, our current methods for obtaining photoabsorption spectra, let us now conclude with an introduction to an important diagnostic tool for interpreting such spectra.

AFR	FWHM(meV)	Fano fit Parameters			χ^2
		E(eV)	q	Γ(eV)	
Gaussian	10	45.546	-1.60	0.017	2.59e-5
	12	45.546	-1.60	0.019	2.19e-5
	14	45.546	-1.60	0.020	1.82e-5
	16	45.545	-1.60	0.021	1.45e-5
	18	45.545	-1.60	0.023	1.16e-5
	20	45.545	-1.61	0.024	9.12e-6
	22	45.546	-1.61	0.026	7.34e-6
	24	45.546	-1.61	0.027	5.58e-6
	26	45.546	-1.61	0.029	4.16e-6
	28	45.545	-1.61	0.030	3.04e-6
	30	45.544	-1.61	0.032	1.72e-6
Lorentzian	10	45.546	-1.60	0.023	1.12e-5
	12	45.546	-1.60	0.025	8.11e-6
	14	45.546	-1.60	0.027	5.69e-6
	16	45.545	-1.60	0.029	3.54e-6
	18	45.545	-1.60	0.031	2.22e-6
	20	45.545	-1.60	0.033	1.34e-6
	22	45.546	-1.60	0.035	1.13e-6
	24	45.546	-1.60	0.037	**9.34e-7**
	26	45.546	-1.60	0.039	1.00e-6
	28	45.546	-1.60	0.041	1.30e-6
	30	45.545	-1.60	0.043	1.34e-6

Table 2.2 : The resulting Fano parameters after the Ne I $2s2p^63p$ profile measured by Codling et al (1967) is convolved with a range of Gaussian and Lorentzian AFRs. The degree to which the DLP measured profile is reproduced is then represented by the magnitude of the χ^2 value where the best fit is the lowest value. As can be seen the best match is obtained for a 24meV FWHM Lorentzian AFR.

2.4 Atomic structure calculations - The Cowan code.

The suite of codes written by Cowan (1968) are perhaps the most widely utilised and available numerical computer codes for atomic structure calculations. The code uses the Hartree-Fock method to obtain approximate solutions to the Schrödinger equation for either single or multiple electronic configurations. Calculating eigenfunctions (ψ_n) and eigenvalues (E_n) for the atomic system under investigation, the code then calculates the values of macroscopic observables such as energy levels and the energies of electronic transitions.

Very briefly, the code can be broken down into three parts which are labelled RCN, RCN2 and RCG. Run in sequence, the first part, RCN, calculates one-electron radial wavefunctions (bound or free) for each of any number of user specified electron configurations. As mentioned earlier, the Hartree-Fock (HF) method or a number of variations of this method such as the Hartree-Slater (HS) or Hartree plus statistical Exchange (HX) methods, are used. The primary output from RCN includes,

(a) the centre-of-gravity energy (E_{av}) for each configuration which, arising in the Slater-Condon theory of atomic structure, refers to the average energy of the configuration and is effectively a statistically weighted sum of the energies of all of the terms within that configuration.

(b) the radial coulomb integrals (F_k and G_k), commonly referred to as the Slater integrals and the spin-orbit integral (ζ) which are required for the calculation of energy levels for that configuration.

Next comes RCN2, which uses the outputted wavefunctions from RCN to calculate the configuration-interaction coulomb integrals (R_k) between each pair of interacting configurations. It also calculates the electric dipole (E^1) and, if desired, the electric quadrupole (E^2) radial integrals between each pair of configurations. In preparing RCN2, the user can specify pre-defined scaling factors which are applied to the coulomb and spin-orbit integrals. This allows improved energy level and wavefunction accuracy and is particularly useful when correlating the codes output to an actual measured spectrum.

Finally, RCG sets up energy matrices for each possible value of the total angular momentum, J, and diagonalises each matrix to get eigenvalues (energy levels) and eigenvectors (under a variety of coupling schemes i.e. LS, jj, jK, or LK). It then computes magnetic and electric dipole radiation spectra giving wavelengths, oscillator strengths, radiative transition probabilities and radiative lifetimes. Should the user so desire, more complex output can be obtained, including, photoionisation cross sections, autoionisation transition probabilities, total lifetimes and autoionisation branching ratios.

For a more complete discussion on the quantum mechanical formalisms upon which the code is based, the reader is referred to the comprehensive volume by Cowan (1981).

Perhaps more conveniently, shorter abbreviated introductions to the Hartree-Fock method, as applied in the code, are provided by McGuinness (1996) and Sayyad (1994), wherein a requisite mathematical discussion is presented. Although the code is freely available for operation on a number of platforms, the PC version, modified by Ralchenko and Kramida (1995), has been the one of choice for this work. It is available (at the time of writing) from ftp://plasma-gate.weizmann.ac.il/pub/software/dos/cowan.

Conclusions

Having introduced the DLP system currently in operation at DCU, we have described its essential components. Through a number of experimental investigations designed to characterise and assess the system's performance capabilities, we have concluded that the system's resolving power varies from ~900 at 70Å (177eV) to ~3,000 at 440Å (28eV). Due to variations in resolving power across the extent of the 1024 pixel PDA detector, we have shown that resolving power is optimised for a spectral feature when that feature is imaged between pixels 500 and 600. Spatial gain variations across the detector have been shown to be important for emission spectra and negligible in the case of absorption spectra. Higher order contributions have been shown to be less than 1% and thus, are deemed to be negligible. The stray light present in the system for energies >100eV has been shown to reach a maximum of ~10% at the upper energy extreme of our measuring capability i.e. ~190eV. Finally, two separate methods of instrument function determination have been detailed, the more reliable of the two suggesting that our instrument function may be described by a Lorentzian profile of 4 pixels FWHM.

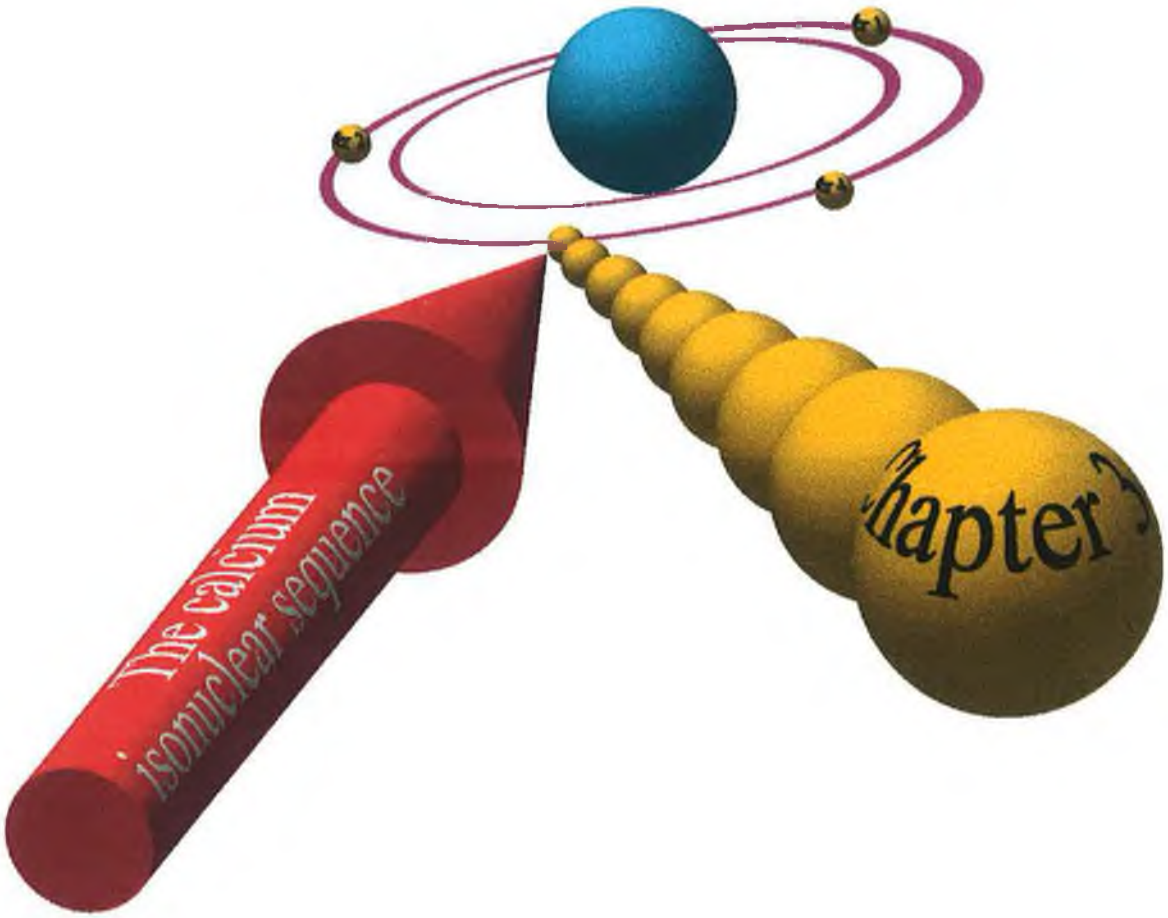
The calcium isonuclear sequence
hapter

Introduction

Calcium[Ar] $4s^2$ (Z=20), is the third member of the alkaline earth series after beryllium and magnesium and its unique position in the periodic table, preceding the occupancy of the 3d subshell in the transition elements (Z=21-30), makes it ideal for study of the effect of 3d wavefunction collapse and electron-electron correlation. Indeed, coupled with its prevalence in interstellar and intergalactic media, whereby its abundance ranks thirteenth of all elements being a factor of ~10^6 less abundant than hydrogen (Shull 1993), it is no surprise that calcium has been extensively investigated over the past two to three decades.

In this chapter, we apply the DLP system to measurement of the 3p region of excitation in the first three members of the calcium isonuclear sequence. By making full use of the DLP system's high resolution capabilities and by careful ion stage selection and consideration of both instrumental effects and plasma opacity, we show how the DLP photoabsorption spectra may be compared with photoion data to derive improved absolute cross sections. We also show how many new Ca^+ ground state features have been resolved, these being assigned where possible and discuss strong experimental and calculational evidence which supports the presence, in our spectra, of both neutral and singly ionised calcium excited state transitions.

3.1 Background

3.1.1. Neutral Calcium

3.1.1.1 3p photoabsorption and the collapse of the 3d wavefunction

In 1977, Mansfield and Newsom published the results of an in-depth survey of the 3p region of excitation where they revealed approximately 125 new photoabsorption lines within the energy region 10 to 41 eV. Through comparison with Hartree-Fock calculations, the overall distribution of intensity was well explained by consideration of $3p^64s^2\ {}^1S_0 \rightarrow 3p^54s^2nd$ and, to a lesser extent, $3p^54s^2ns$ transitions. The first members of the former series showed considerable position and intensity anomalies which were explained in terms of the centrifugal barrier for d electrons and the sensitivity of nd orbitals in $3p^54s^2nd\ {}^1P$ terms to the angular momentum coupling. Hartree-Fock calculations were also successful in the elucidation of transitions due to the simultaneous excitation of the 3p and valence subshells, of which multi-electron excitations of the form $3p^64s^2\ {}^1S_0 \rightarrow 3p^5(3d^2\ {}^1S)ns$, nd were highlighted as the most significant.

In an earlier study (Mansfield 1976), Hartree-Fock calculations had again been invoked for neutral calcium to explain irregular quantum defects and the remarkable strength and breadth of discrete features associated with the more energetic 2p subshell excitation. The anomalous behaviour of, in particular, the $2p^64s^2 \rightarrow 2p^54s^23d$ series, when compared with similar transitions in preceding elements like potassium (Z=19) (Mansfield 1975) and argon (Z=18) (Nakamura 1968) was successfully interpreted through the collapse of the 3d wavefunction. Using much the same theoretical approach, Mansfield and Newsom (1977) treated the general case of $3p \rightarrow 3d$ transitions in the elements Z=18→22 nicely conveying the onset of 3d wavefunction collapse and its ramifications in an instructive manner. Indeed, with a visual approach it is easy to see why with calcium (Z=20), we see a promotion of $3p \rightarrow 3d$ oscillator strength over transitions from the 3p subshell to nd and ns continua, the latter being dominant in pre-calcium elements. In figure 3.1, the effective potentials for 3d electrons in 3p→3d

transitions are shown for Z=18-22, both for the configuration average case and for terms that are particularly sensitive to the angular momentum coupling. The contrast between the two plots for each element shows that for 3p excitation in elements Z=18-20, the appearance of the potential barrier for 3d electrons is strongly term dependent so that, while in the configuration average case there is a very large 3p-3d overlap, a strong potential barrier appears for the important $3p^5 3d\ (^1P)\ 4s^n$ terms (n=0,1,2 for Z=18,19,20) which repels the 3d wavefunction out of the core and prevents the occurrence of a 'giant' 3p→3d resonance.

For argon (Z=18) in figure 3.1a, the potential well is shallow in the configuration average case and the 3d wavefunction is mostly excluded from the core region. For $3p^5 3d\ ^1P_1$, a very strong potential barrier occurs which pushes the 3d wavefunction even farther from the core. The 3d orbital is therefore, kept well out of the core for all terms and thus, 3p→3d transitions in argon are weak with even the 3p→4s transitions being more intense. Here, the greater percentage of 3p→d,s oscillator strength goes into the 3p→εd, εs continua. For potassium (Z=19) in figure 3.1b, the potential well for the configuration average case is far deeper and the 3d wavefunction now enjoys a considerable overlap with the core. However, in the case of $3p^5 3d(^1P)4s\ ^2P$ levels, we again see a barrier which pushes the 3d wavefunction into the outer well. Again, the 3p→εd,εs withhold the majority of oscillator strength. With calcium (Z=20) in figure 3.1c, the potential wells in both configuration average and ^1P term cases have deepened but now the barrier for the ^1P term has weakened substantially so that the 3d wavefunction now has a large overlap with the 3p core wavefunction. Thus, as observed experimentally by Mansfield and Newsom (1977), the $3p^6 4s^2\ ^1S_0 \rightarrow 3p^5 3d 4s^2\ ^1P_1$ transition is by far the strongest discrete feature of the spectrum at the expense of the 3p→εd continua from which it draws oscillator strength. However, the expansion of the 3d orbital due to the presence of the still non-negligible barrier prevents the 3p→3d resonance from attaining true 'giant' resonance status, despite its stature. From figures 3.1d and 3.1e, we see that for scandium (Z=21) and titanium (Z=22), the potential well incrementally deepens and there is no longer a potential barrier dividing the potential well in two for the high lying term. The 3d wavefunction now overlaps substantially with the 3p core for all terms and the 3p→3d transition may now be described as a 'giant' resonance which depletes the

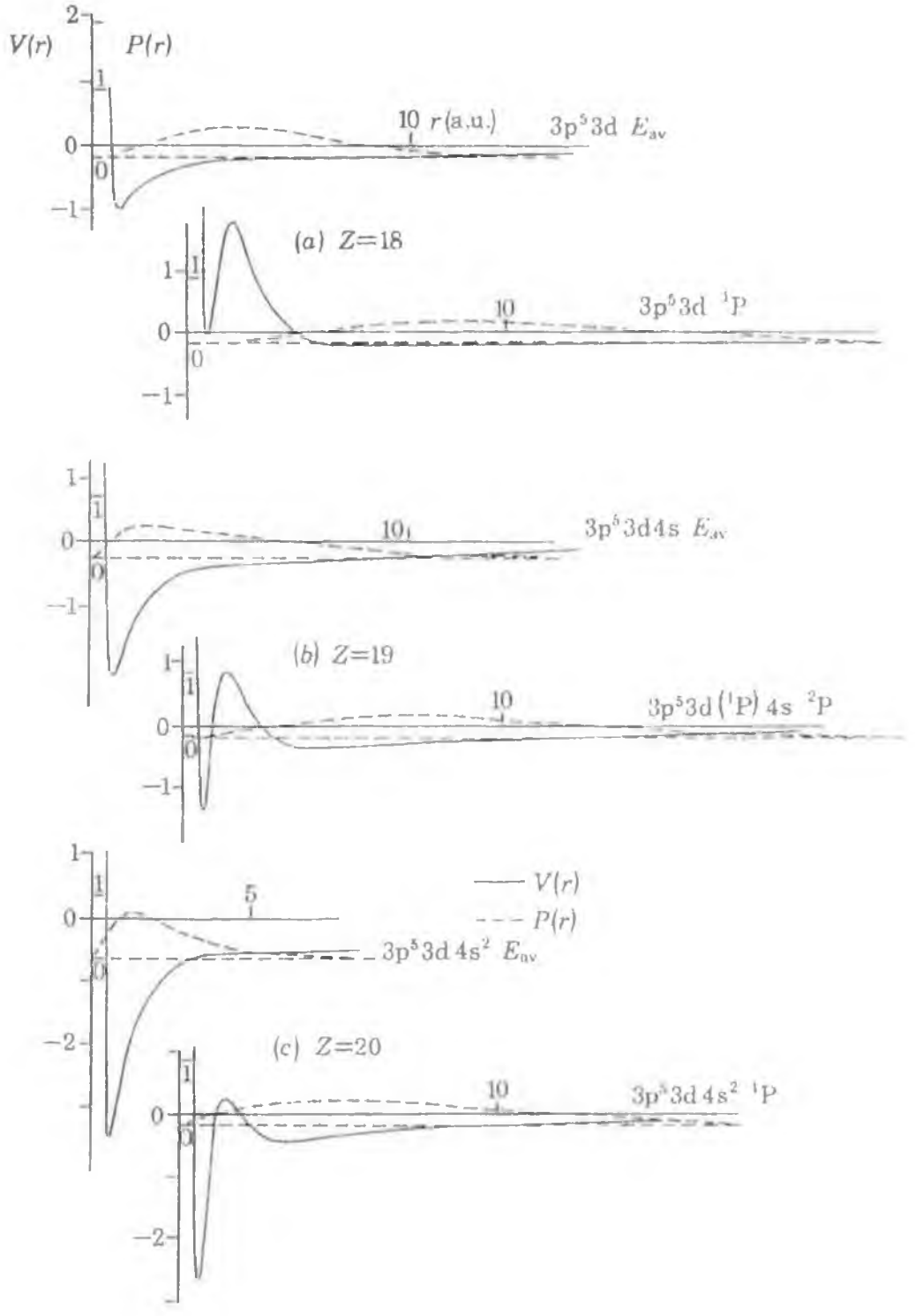

Figure 3.1 : Effective potentials (full curves), V(r), and wavefunctions (dashed curves), $P_{3d}(r)$, for (a) argon (Z=18) $3p^5 3d\ E_{av}$ and $3p^5 3d\ {}^1P$; (b) potassium (Z=19) $3p^5 3d4s\ E_{av}$ and $3p^5 3d({}^1P)4s\ {}^2P$ and (c) calcium (Z=20) $3p^5 3d4s^2\ E_{av}$ and $3p^5 3d4s^2\ {}^1P$ (after Mansfield and Newsom 1977).

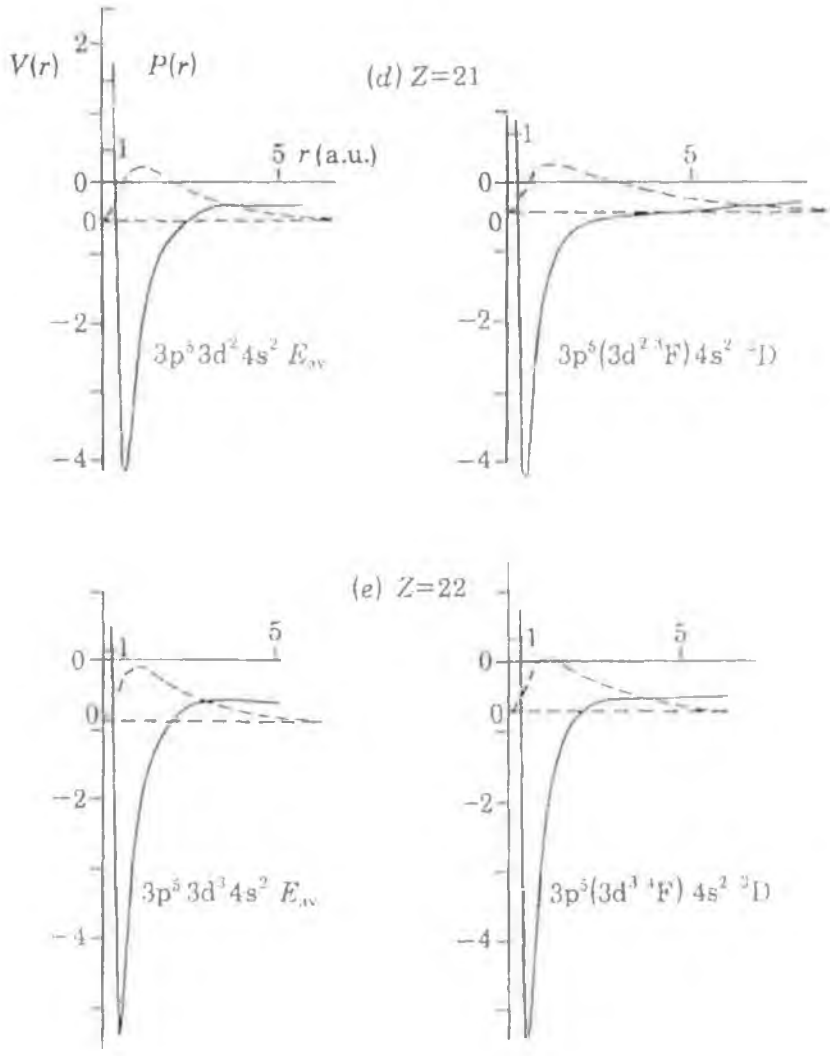

Figure 3.1 (continued) : Effective potentials (full curves), V(r), and wavefunctions (dashed curves), $P_{3d}(r)$, for (d) scandium (Z=21) $3p^5 3d^2 4s^2$ E_{av} and $3p^5(3d^2\ ^3F)\ 4s^2\ ^2D$ and (e) titanium (Z=22) $3p^5 3d^3 4s^2$ E_{av} and $3p^5\ (3d^3\ ^4F)\ 4s^2\ ^3D$ (after Mansfield and Newsom 1977).

3p→εd continuum transitions of nearly all oscillator strength.

As pointed out by Cowan (1981), 3d wavefunction collapse is strikingly apparent when one looks at the effective principal quantum numbers of d electrons as a function of Z in neutral atoms. For ns electrons, the attractive Coulomb potential term $(-2Z/r)$ of the effective potential, V_{eff}, is far greater than the repulsive centrifugal term $(l(l+1)/r^2)$ as for ns electrons, l = 0. This becomes increasingly so for increasing Z, the ns orbitals contracting further towards the nucleus and becoming more non-hydrogenic. Thus, the

binding energy of the ns electrons is greater than the hydrogenic value giving rise to a quantum defect $\delta \equiv n - n^*$, which is always positive. Due to the strength of the penetration by the ns electrons into the core, n* is quite small (δ large). For np electrons, the penetration into the core is smaller due to an increase in the centrifugal term with *l*. Thus, δ decreases or alternatively n* is greater than for ns electrons and is seen to

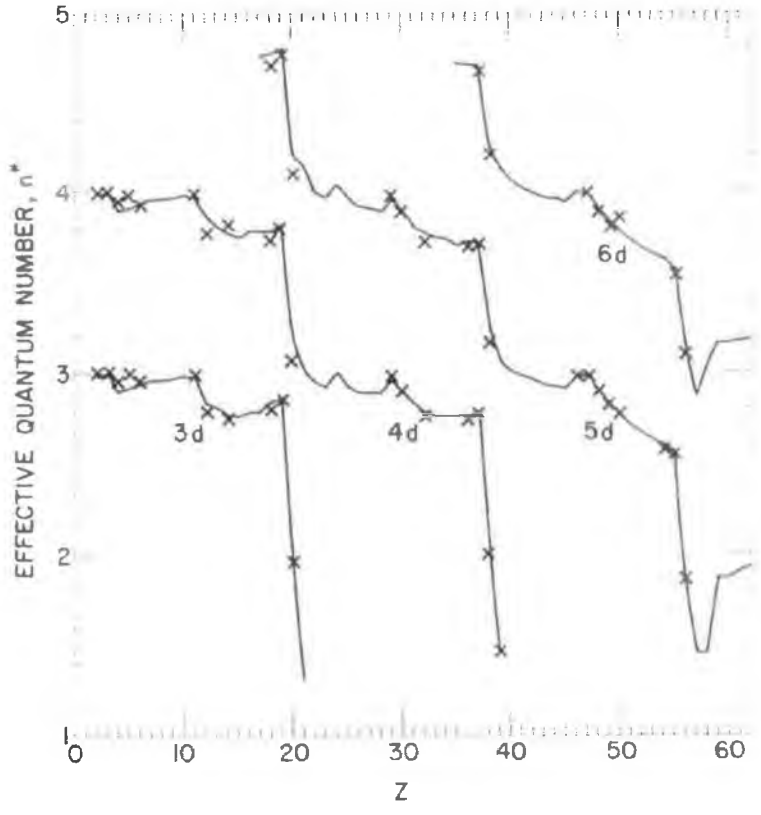

Figure 3.2 : Effective principal quantum numbers, n*, for d electrons in neutral atoms : Experiment (X points) versus Theory (Solid lines) (after Cowan 1981).

approach n. For a d electron, the situation is drastically different, the centrifugal term becoming so important that (at small Z) it keeps the d electron at rather large radii. This means that the electron penetrates only slightly into the core region and sees mainly a hydrogenic potential such that for Z < 20, $n^*_{3d} \cong n_{3d} = 3$. In neutral calcium (Z=20), however, the 3d electron is not completely shielded from the added unit of nuclear charge by the 4s electron and as a result the 3d electron is pulled strongly inward toward the nucleus. The 3d orbital can therefore no longer be described as hydrogenic. Thus, $n^*_{3d} << 3$ and we see wavefunction collapse evidenced through observation of the

effective principal quantum number. This is illustrated in figure 3.2 where the collapse of the 4d, 5d and 6d wavefunctions with increasing Z is also shown. Furthermore, it should be noted that wavefunction collapse is not restricted to nd electrons. In fact, even more dramatic effects, due to higher Z, are observed for 4f wavefunction collapse in lanthanum (Z=57) and 5f wavefunction collapse in actinum/thorium (Z=89/90) (see Mansfield 1987).

3.1.1.2 Ground state investigations in the 3p region

Due to the collapse of the 3d wavefunction in the presence of a core hole, the 4s and 3d levels of neutral calcium are nearly degenerate. This leads to the complex photoabsorption spectrum observed by Mansfield and Newsom (1977) but the resulting strong configuration interactions also produce a rich satellite system of photoelectron lines when the excited Ca I levels decay. In particular, the decay of the $3p^64s^2\ ^1S \rightarrow 3p^54s^23d\ ^1P$ resonance at 31.4eV via $3d \rightarrow 3p$ recombination is controlled by the large 3p-3d overlap which results in the emission of a 4s electron leaving the photoion in the ground state Ca^+3p^64s as the major decay channel. However, due to the abovementioned configuration mixing, a large number of satellites, arising through shake-up and shake-down processes, like $3p^63d$, 4p, 5s, 4d and 5p are also prevalent. Bizau et al (1987) have measured the partial cross sections of the main 4s photoelectron line and the above satellites in the region 26-40eV. By measuring the energies of Auger and photoelectron lines which could be labelled with the aid of Mansfield and Newsom's earlier assignments, Bizau et al could also deduce binding energies for excited singly ionized calcium levels, amongst which was the first measurement of a 3s ionic level. Singly ionised calcium levels are also affected by the perturbation of the 3p core hole on 3d orbitals to such an extent that Ca^+ $3p^54s^2$, $3p^54s3d$ and $3p^53d^2$ levels are nearly degenerate. The core excited Ca states, Ca $3p^54s^2nl$, can therefore decay to both Ca^+ $3p^53d4s$ and Ca^+ $3p^6n'l'$. Sato et al (1985) have studied this process by way of time-of-flight (TOF) mass spectrometry, whereby they have measured the simultaneous photoion yield of Ca^+ and Ca^{2+} ions and examined the ratio $R = Ca^{2+}/Ca^+$ as a function of incident photon excitation energy. They found that below the 3p ionisation limits $3p^54s^2$

$^2P_{3/2,1/2}$ at 34.21 and 34.66eV respectively, the formation of Ca^+ and Ca^{2+} ions is governed by the two step mechanism

$$Ca\ 3p^64s^2\ ^1S_0 + h\nu \rightarrow Ca\ 3p^54s^2nl$$

followed by the autoionisation

$$Ca\ 3p^54s^2nl \rightarrow Ca^+\ 3p^53d4s\ ^2P,^4P + e_1$$

and the subsequent autoionisation

$$Ca^+\ 3p^53d4s\ ^2P,^4P \rightarrow Ca^{2+}\ 3p^6\ ^1S_0 + e_2$$

The Ca^{2+} yield is thus enhanced through the mediation of Ca and Ca^+ 3p hole states such that R ~ 1. Above the 3p thresholds, the Ca^{2+} ions are mainly created through the more direct process

$$Ca\ 3p^64s^2\ ^1S_0 + h\nu \rightarrow Ca^+\ 3p^54s^2\ ^2P + e_1$$

and

$$Ca^+\ 3p^54s^2\ ^2P \rightarrow Ca^{2+}\ 3p^6\ ^1S_0 + e_2$$

and as expected the production of Ca^+ ions falls off due to the Ca 3p hole state no longer contributing, with the result that R $\rightarrow$ ~5.

The 3p region of neutral calcium can also be studied through fluorescence spectroscopy. Altun and Kelly (1985), using Many-body perturbation theory, predicted large cross sections for ionisation and excitation of calcium into the 4p ^2P state of Ca^+ by correlation with excitation of the 3p electrons via the 3p-3d resonance i.e.

$$Ca\ 3p^64s^2\ ^1S_0 + h\nu \rightarrow Ca^*\ 3p^5n\left\{\begin{matrix}s\\d\end{matrix}\right\},nl,\ n'l' \rightarrow Ca^{+*}\ 3p^64p\ ^2P_{3/2} + e$$

$$\rightarrow Ca^+\ 4s\ ^2S_{1/2} + h\nu'\ \ (3933\text{Å})$$

where $h\nu$ is the incident photon and $h\nu'$ the fluorescent photon. Testing this assertion experimentally, Hamdy et al (1991) measured the intensity of fluorescence radiation emitted at λ = 3933Å as a function of incident photon energy in the region 29-35eV and obtained results consistent with those of Mansfield and Newsom (1977), Sato et al (1985) and Bizau et al (1987). In fact, it is no great surprise that the spectra produced by application of photoion yield, photoabsorption and fluorescence techniques closely resemble each other as despite measuring different components in the photoionisation process, the results are all determined by the cross sections of calcium ground state to 3p core excited state transitions. This close correlation between techniques is readily apparent from figure 3.3. where recent DLP photoabsorption measurements are also

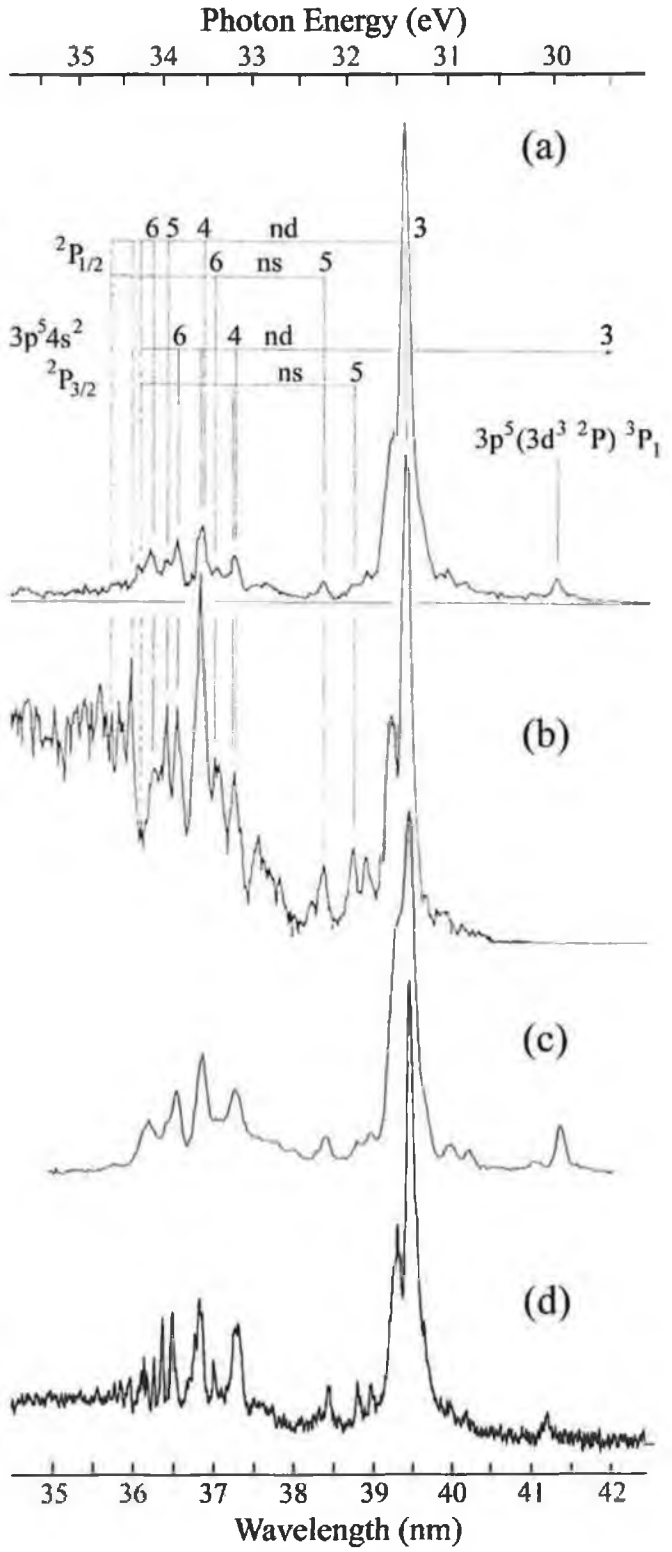

Figure 3.3 : The 3p excitation region of Ca I as seen through (a) Ca^+ photoion yield (Sato et al 1985), (b) Ca^{2+} photoion yield (Sato et al 1985), (c) Fluorescence (Hamdy et al 1991) and (d) DLP photoabsorption measurements (see text for details).

included. The DLP spectrum was taken for $\Delta X = 0.05$mm, $\Delta T = 800$ns and for a line focus of ~10mm on the calcium target.

Over the past decade, a concerted effort has been undertaken, using the Daresbury synchrotron facilities, to move increasingly toward what has been referred to as a 'complete' experiment, in which all the photoionisation parameters are measured. The first step toward this complete photoionisation experiment were taken by Hamdy et al (1991), where apart from measuring fluorescence intensities (as discussed above), the linear polarisation of the fluorescence radiation was also measured. Ueda et al (1993), then applied angle-resolved photoelectron spectroscopy to neutral calcium to measure the relative partial photoionisation cross sections and photoelectron asymmetry parameters (β) for populating the Ca^+4s, 3d and 4p levels in the vicinity of the 3p-3d resonance. With higher photon resolution (50meV) than Bizau et al (1987), the previously unresolved peak at 31.52eV associated with multi-electron excitations (Mansfield and Newsom 1977) could now be observed and branching ratios for both it and the 3p-3d peak at 31.4eV were determined. Of particular note was the decrease in branching ratio to Ca^+4s and the corresponding increase to higher levels in moving only a mere 0.11eV in photon energy from 31.4 to 31.52eV. A short time later, Beyer et al (1995), in the first experiment of its kind, coupled both the above spectroscopic techniques to measure the polarisation of the fluorescent photons, resulting in the decay of excited calcium ions created via the 3p-3d resonance of neutral calcium, in coincidence with the corresponding angle-resolved photoejected electrons. This new approach to the complete photoionisation experiment allowed the extraction of the ratio of the dipole amplitudes for the outgoing waves (only two being possible within the LS coupling approximation) and a determination of their phase difference. However, the sign of the relative phase difference was still indeterminate until West et al (1996) measured the circular dichroism in the polarisation of the fluorescent photons by introducing a degree of left and then right circular polarisation into the incident photon beam. This was yet another important piece of information from the viewpoint of the 'complete' experiment leaving the absolute scale of the dipole amplitudes as the only remaining uncertainty.

The success of these techniques prompted ever more probing measurements. Ueda et al (1996) measured the variation in energy of spectator Auger transitions as they evolve to normal Auger transitions near threshold in the Ca 3p excitation region. The Auger transitions investigated were Ca $3p^5 4s^2 nl \rightarrow Ca^+ 3p^6 n'l + e_{Auger}$ and Ca $3p^5 3d4s nl \rightarrow Ca^+ 3p^6 n'l + e_{Auger}$. Fundamental to this study was the understanding that shake-modified spectator Auger decay¶ occurs such that the *nl* electron is shaken up or down to the *n'l* orbital via Auger decay, where the value of *n'* depends on the degree of overlap between the *nl* and *n'l* radial wavefunctions. Indeed, a relatively simple model based on this fact was used to measure the degree of shake-up for the above decay transitions. Also possible from these measurements was an observation of the Post Collision Interaction (PCI) effect. This was possible due to the fact that for sufficiently high photon energies, the kinetic energy of the Auger electron is independent of the excitation photon energy but when the excitation energy is decreased toward threshold, PCI becomes more probable whereby the slow photoelectron is decelerated by the faster Auger electron which in turn gains energy. More recently, coincidence measurements have been performed of double photoionisation in atomic Ca, again in the region of the 3p-3d resonance, using two spherical sector electron analysers (Ross et al 1997). More pertinent, however, to the previous discussion has been a recent extension of the earlier work on calcium (Ueda et al 1993) again using angle-resolved photoelectron spectroscopy (Ueda et al 1997). Concentrating on the 3p-3d resonance region, improved branching ratios to levels of Ca^+ have been obtained and many more higher *n* levels were resolved than in previous reports. The majority branching ratio (~50%) to the 4s main line contrasted with a ratio of ~4% to the 3d satellite in line with previous observations (Bizau et al 1987). This clearly indicated that the overlap of the 3d and 3p

---

¶ Two dominant decay processes follow inner-shell electron excitation. *Participator (or Normal)* Auger decay involves the excited *nl* electron participating in the transition which leads to the Auger decay. With *Spectator* Auger decay, the excited *nl* electron acts as a spectator during the Auger decay process. In general, especially if *nl* is not the lowest excited level, spectator dominates over participator Auger decay. Furthermore, in spectator Auger decay, the spectator electron may not stay in the initial *nl* level; *n* of the final ionic state may be larger (Shake-up) or smaller (Shake-down) than that of the initial excited state.

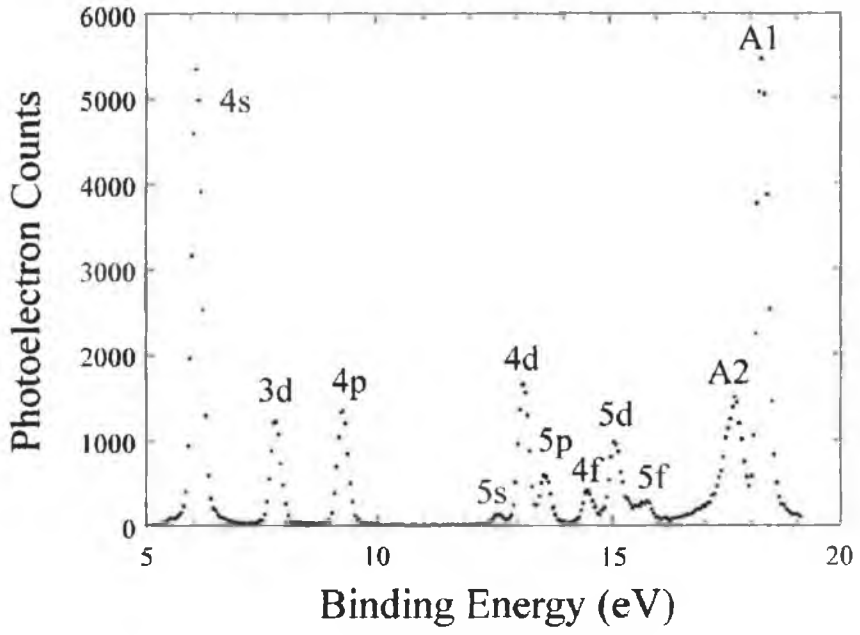

Figure 3.4 : The ejected electron spectrum taken at the peak of the Ca 3p → 3d $^1P_1$ resonance at 31.41eV. A1 is the normal Auger peak corresponding to transitions from $Ca^+3p^53d4s\ ^4P_{1/2,3/2,5/2} \rightarrow Ca^{2+}3p^6\ ^1S_0$ (allowed through mixing of Ca levels) and A2 is an amalgam of spectator Auger transitions $Ca3p^53d4s\ ^2P_{1/2,3/2}$ nd → $Ca^+3p^6\ ^1S_0$ nd' where many levels with n ~ 13 are included (after Ueda et al 1997).

orbitals was substantially larger than that of the 4s and 3p orbitals and showed that for calcium 3p→3d excitation the spectator model broke down. Furthermore, as we can see from figure 3.4, the intensities or branching ratios to the 4d and 5d satellite lines were found to be anomalously large. This was explained through shake-up due to the partially collapsed 3d orbital in the Ca $3p^54s^23d\ ^1P_1$ level having a mean radius (6.38a.u.) very close to that of the Ca^+4d orbital (6.52a.u.). A similar interpretation for shake-up in the participator decay showed that whilst the 4s orbitals in excited and singly ionised calcium have radii that almost coincide (3.54 and 3.59a.u. respectively), the 5s satellite of the ion has a mean radius of 7.62a.u. and thus only marginal shake-up would be expected. This was confirmed by the intensity measurements (see figure 3.4). Autoionisation from the Ca $3p^54s^23d\ ^1P_1$ level to Ca^+nl levels with l = p and f is not

allowed so the anomalously strong populations of 4p, 4f and 5f levels were explained through mixing via ground state correlation of the $4s^2$ level with $4p^2$ and $4f^2$ levels.

3.1.1.3 Excited state investigations in the 3p region

Interest in the 3p region of calcium has not only been restricted to ground state excitation. In fact and particularly in recent years, there has been an upsurge in activity involving the 4s4p $^1P_1$ and 4s4p $^3P_1$ excited states of calcium. In 1973, McIlrath and Carlsten demonstrated how large numbers ($\sim 10^{16}$) of calcium atoms could be placed in the 4s4p ^3P metastable level through optical pumping with a pulsed tunable dye laser (λ = 657.2nm). A fast flash lamp (~4μs) could then be fired to record the absorption spectrum photographically. Their study showed that despite the intercombination line being very weak ($f \sim 5x10^{-5}$), significant numbers of atoms could be excited through this resonant laser pumping process. Using this revelation and motivated by a desire to further probe the characteristics of 3d orbital collapse by producing slight and controlled modifications to the effective potential, Sonntag et al (1986) used the Resonant Laser Driven Ionisation (RLDI - briefly mentioned in section 1.1.1) technique to pump the $Ca4s^2\ ^1S_0 \rightarrow Ca4s4p\ ^3P_1$ transition (which through collisions ionises to $Ca^+4s\ ^2S_{1/2}$) and photoelectrically capture the Ca* 4s4p ^3P and Ca^+ 4s ^2S spectra in the 27-50eV region. They were successful in producing up to 50% ionisation and by measuring the yield of each species through their absorption features as a function of oven temperature and related Ca density, could quite convincingly illustrate the dominant role of collisions in the ionisation process. Attaining their objectives, Sonntag et al (1986) measured dominating 3p→3d resonances for Ca, Ca* and Ca^+ at 31.4, 32.3 and 33.21eV respectively despite suffering varying degrees of success in ion stage separation.

Concentrating on the ionisation process itself, Khan and co-workers have investigated the ionisation of calcium atoms through both pulsed (Khan et al 1990) and continuous-wave (cw) (Khan and Al-Kuhaili 1993) laser pumping of the 4s4p ^3P metastable states. The investigations were carried out under a variety of conditions whereby the ionisation yield was measured as functions of laser power, oven temperature and buffer gas pressure. Results showed that since the creation of electron-ion pairs is the combined

product of laser excitation and subsequent collisional and radiative processes of energy transfer, enhanced magnitude and speed of ionisation is achieved through increases in both laser power and oven temperature. However, increasing the oven temperature and hence the calcium atom density beyond a certain level, where the number of photons available falls short of that needed to excite the available number of Ca atoms, can easily lead to a state of saturation. The influence of the buffer gas (in this case, argon) pressure on ionisation was found to be negligible except for beyond 700mbar where collisional quenching of the laser excited state was thought to become significant.

Further study of the effects of pumping the calcium 4s4p $^3P_1$ metastable state has revealed that the rates of collisional energy transfer in optically prepared atomic metastable states can be considerable when compared with the rate of normal radiative decay. A remarkable consequence of this is a large increase in the effective lifetime of some excited states which lie above the optically prepared state. For example, the 4s3d^{3}D states of calcium exhibit a 1000-fold increase in lifetimes (400ns $\rightarrow$ ~400μs) following pumping of the 4s4p $^3P_1$ state (Khan et al 1994a). A first observation, this lifetime extension of some higher excited states through the processes of quasi-continuous collisional population, radiative and collisional depopulation, and repopulation has been christened 'collisional recycling' and has been interpreted in a subsequent paper (Khan et al 1994b) as arising as a direct result of 3d orbital contraction.

In the presence of an argon buffer gas (which serves to promote rapid mixing of populations in the 4s4p^{3}P multiplet), fluorescence was observed from many excited states located at higher energies than the 4s4p $^3P_1$ laser pumped state. This fluorescence and the anomalously long lifetimes of some states can be understood with the help of figure 3.5. In a first step after laser excitation, the 4s5s ^{3}S and 4s4p ^{1}P states are populated in energy pooling collisions such as

$$Ca4s4p\ ^3P_1 + Ca4s4p\ ^3P_1 \rightarrow Ca4s5s\ ^3S_1 + Ca4s^2\ ^1S_0 + \Delta E$$

where ΔE is the energy defect. Similarly, collisions with superelastically heated free electrons populate the Ca 4snl levels. From these levels, other excited states may be populated through similar means. Above the double broken line in figure 3.5, excited states are strongly mixed by collisions and as a result, the Rydberg spectrum dies out rapidly. Fluorescent transitions involving 4s5s $^3S_1$ were seen to be prominent but those

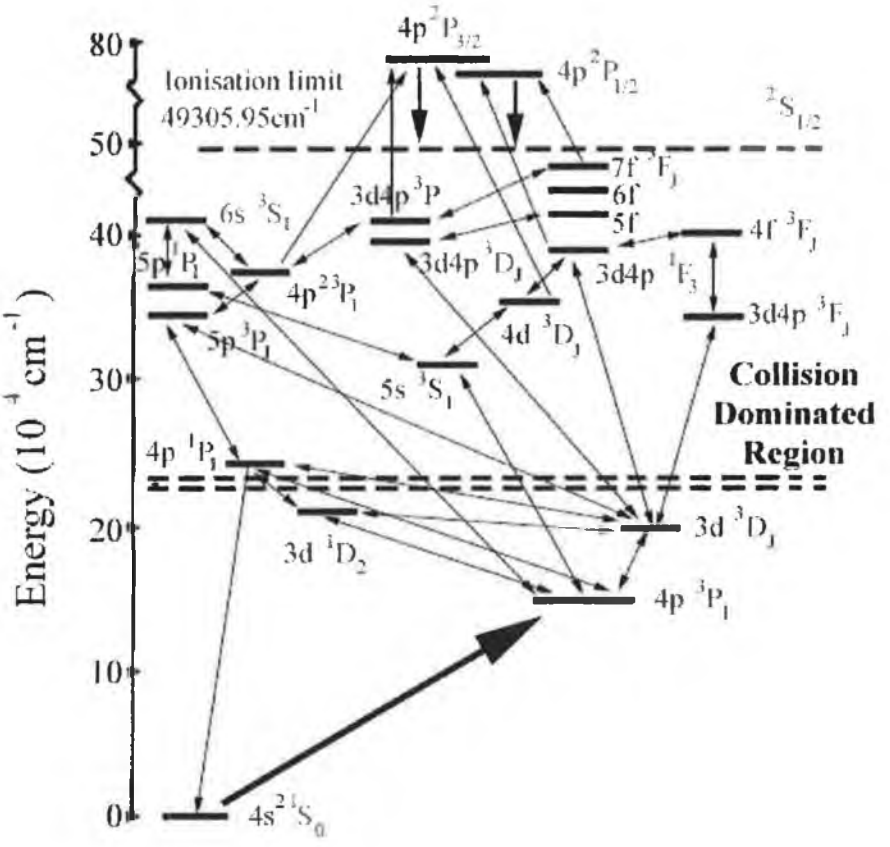

Figure 3.5 : A simplified energy level diagram of Calcium showing the levels of interest for the 'Collisional recycling' process which takes place after laser pumping the $4s^2\ ^1S_0 \rightarrow 4s4p\ ^3P_1$ transition. The collision dominated region is indicated above the double broken line where strong collisional mixing of levels takes place and the Rydberg states are quenched (after Khan et al 1994b).

involving 4sns (n>6) were absent indicating that only states with radii more compact than 4s5s survived. Below the line, although collisions are significant, their effect is less pronounced but because triply excited states are metastable they act as reservoirs, living long enough for substantial probability of the occurrence of further collisions which may either re-excite the atom to states above the line (but below 4s5s) or drive it to the statistically less likely (due to radii differences) ground state. The fact that the 4s3d ^{3}D levels lie below the collision dominated region due to orbital collapse is the reason for their anomalous lifetimes as whilst higher triplet states feed into them, collisions do not occur rapidly enough to quickly depopulate them. This effect is not thought to be unique to calcium but has been predicted (Khan et al 1994b) to accompany wavefunction

collapse in homologous higher Z elements like strontium (Z=38) and Barium (Z=56). Presently, studies of this ilk continue (Khan et al 1997), the potential for population inversion and metal vapour lasers giving much impetus.

Despite having an oscillator strength ~10^5 times that of the $4s^2\ {}^1S_0 \rightarrow 4s4p\ {}^3P_1$ intercombination line, the $4s^2\ {}^1S_0 \rightarrow 4s4p\ {}^1P_1$ resonance transition has only been employed for the study of excited states in calcium of late, as both pulsed and cw dye lasers, capable of lasing at the requisite 422.7nm have only recently been available. One of the first studies pumping this resonance was performed by Baier et al (1992) where they exploited the linear polarisation of both a ring dye laser (λ = 422.7nm) and a VUV synchrotron radiation source. Using the dependence of the photoelectron signal on the polarisation axes of both radiation sources, the symmetry character of the core $3p^53d4s4p$ resonances was determined, having isolated the Ca^+3p^64p, 4s and 3d photolines from the difference of spectra recorded with and without laser pumping. Extending this lead study, Wedowski et al (1997) obtained superior statistics and improved resolution on the photoionisation from the laser-excited aligned $4s4p\ {}^1P_1$ state of calcium, in the 3p-3d region (31.5-34.5eV). Combining measurements from an angle resolving electron spectrometer (ES) with those from an angle integrating cylindrical mirror analyser (CMA) of the type used by Baier et al (1992), Wedowski et al were able to completely characterise the three main diagram lines (4s, 3d and 4p) by six independent parameters : the cross section and five generalised anisotropy parameters including the conventional anisotropy of the photoelectrons from an unpolarised target. In so doing, they demonstrated yet another means of performing a 'complete experiment', the essence of which we mentioned earlier.

3.1.1.4 The 2p region of excitation

Finally, we note that the 2p region of calcium, also dramatically demonstrative of the effects of 3d wavefunction collapse and electron-electron correlation, has also received considerable attention. Most notably, photoelectron spectra due to the decay of the core $2p \rightarrow 4s$ and $2p \rightarrow 3d$ resonances have been recorded in systematic studies of Ar, K and Ca

(Meyer et al 1990, 1994). The results provided further evidence for the breakdown of the spectator model in calcium which leads to final states possessing two 3p holes. More recent studies of this highly energetic 2p region (200 - 1000eV) have determined the Ca 2p ionisation thresholds with an energy bandwidth comparable to the natural width of the photoelectron lines i.e. 150meV < ΔE < 300meV, using a high resolution electron analyser (Wernet et al 1998) and have resolved the multi-resonance structure of the prominent 3d resonances at 348 and 352eV by way of photoion and photoelectron spectroscopy (Obst et al 1999).

3.1.2 Singly ionised calcium

3.1.2.1 Ground state investigations in the 3p region

Early investigations of this astrophysically significant ion and in particular the region corresponding to 3p excitation, were through electron impact experiments which, unfortunately, were limited by low resolution (±1eV) (Peart and Dolder 1975). Concurrent theoretical studies (HF and MCHF - within the context of a broader study of singled ionised alkaline earths) predicted significant Ca^+ autoionisation cross sections involving $3p^53d4s\ ^2P$ terms (Hansen 1975) but it was not until 1978 that significant experimental progress in the study of Ca^+ was achieved when Pejcev et al (1978) successfully captured high resolution (20-25meV) ejected-electron spectra of calcium vapour autoionising levels excited by low energy electron impact. Observing ejected electrons with energies between 12.8 and 28.1eV for incident electron beam energies ranging from 30 to 500eV, Pejcev et al were able to measure 165 lines, the vast majority of which corresponded to decay from Ca excited levels. However, through photoabsorption threshold measurements by Mansfield and Newsom (1977) and through the known high excitation thresholds for Ca^+ (Moore 1949), Pejcev et al were able to ascribe some 32 of their listed lines as being of Ca^+ origin. This ejected electron data was subsequently compared with Hartree-Fock calculations by Mansfield and Ottley (1979) whereby many lines were determined to be of 3d character (primarily $3p^53d4s$), 3d wavefunction collapse in Ca^+ greatly influencing the process

$$e_1 + Ca(3p^64s^2) \rightarrow e_1 + e_2 + Ca^+(3p^54snl) \rightarrow e_1 + e_2 + Ca^{2+}(3p^6) + e_3$$

In total, some 20 lines, observed by Pejcev et al, were identified (albeit in some cases tentatively) by Mansfield and Ottley, all being assigned to $3p^5 3d4s$ levels.

Quite some time elapsed before interest in Ca^+ resumed whereby, as mentioned in section 3.1.1, Sonntag et al (1986) applied the RLDI technique to calcium, probing the resulting population densities with the continuum radiation from a samarium laser plasma source to obtain the Ca^+ 4s photoabsorption spectrum between 27 and 50eV. Unfortunately, the nature of the technique meant that unambiguous ion stage selectivity was unattainable. However, having captured the corresponding Ca photoabsorption spectrum for this energy region, a comparison of both spectra lent itself to the extraction of the most prominent Ca^+ features, these being the $3p^6 4s\ ^2S_{1/2} \rightarrow 3p^5 4s^2\ ^2P_{3/2,1/2}$ and $3p^6 4s\ ^2S_{1/2} \rightarrow 3p^5 4snd$ (n=3-5) transitions. As mentioned in section 1.1.2, the first accurate measurements of bound-free transitions in alkali like Ba^+ ions were carried out by Lyon et al (1986), using merged beams of synchrotron radiation and projectile ions. However, as remarked upon by Lyon at al, barium's high atomic number meant that a theoretical description was difficult. This warranted similar measurements to be performed on kindred lighter and less complex ions such as Ca^+. Combining such motivation with the calcium ion's solar and stellar abundance, saw the first absolute photoionisation cross section measurements for Ca^+ in the 25 to 44eV region (Lyon et al 1987). Despite the Ca^+ cross sections being weaker than for equivalent transitions in Ba^+ and being limited by a resolution ($\Delta\lambda$) ranging from 0.2 to 1.0Å and less available photon flux at the higher photon energies required, Lyon et al were successful in resolving some 30 peaks with an error in peak cross section determination of ±15%. The most outstanding feature by far was the $3p^5 3d4s\ ^2P$ resonance, measured at 33.19eV, possessing a peak cross section of 2200MB which, consistent in domination with the $3p^5 3d4s^2\ ^1P$ resonance in calcium, again bore testament to the influence of 3d wavefunction collapse.

With reliable data now available for comparison, Miecznik et al (1990) used the R-matrix method to calculate the absolute photoionisation cross section of ground state Ca^+ in the 27-44eV energy range. Improving upon earlier calculations (Burke et al (1983), Pindzola et al (1987)), Miecznik et al (1990) included fifteen target states of Ca^{2+} i.e. $3p^6$ and $3p^5 nl$ (nl = 4s, 4p and 3d), and also accounted for 3s shell excited configurations $3s3p^6 nl$ (nl = 4s, 4p and 3d). This allowed 'complete' coupling with continuum electrons of symmetry

s, p, d, f and g. The importance of interference effects through interaction between channels was clearly demonstrated, predicted cross sections varying considerably with the exclusion of especially the d and f waves. In terms of agreement with the data of Lyon et al (1987), the major resonance structures at ~28, 30, 33 and 37eV relating to $3p^54s^2$, $3p^53d^2$, $3p^54s3d$ and $3p^54s4d,5d$ configurations respectively were in good agreement. However, the experimentally observed peak at 28.545eV (Lyon et al 1987) was assigned to the double excitation $3p^5$ ($3d^2$ ^1D) ^2P, in conflict with Mansfield and Newsom (1977) and Lyon at al's (1987) earlier designation of $3p^54s^2$ $^2P_{1/2}$. For the remaining structure seen between 34 and 37eV but unaccounted for by Lyon et al, Miecznik et al predicted many sharp peaks but no attempt at identification was attempted.

In 1991, Bizau et al (1991, 1992) reported the first observation of photoelectron spectra emitted in the photoionisation of a singly charged ion beam with synchrotron radiation. Despite the technical limitations associated with photoelectron studies of ions (see section 1.1.3) i.e. small ion current, interaction region and electron spectrometer collection efficiencies, Ca^+ was chosen for this prototype investigation. In particular, resonant photoionisation of the 4s electron was targeted since in this case, the photoionisation cross section, known from previous work to be 2200MB at $h\nu$ = 33.2eV, is greatly enhanced by the existence of the intermediate $3p^53d4s$ ^2P excited autoionising state. Figure 3.6 shows the resultant photoelectron spectrum obtained by real-time subtraction of an enormous background, the background being due to low energy scattered electrons and collisional ionisation with molecules present in the residual gas. This subtraction procedure also allowed rejection of anomalous signals caused by ion beam variations. With poor resolution (~0.4eV at kinetic energy peak) and weak signal, Bizau et al were still capable of extracting a peak cross section of 3000MB which was within a factor of two of that measured by Lyon et al (1987).

Following on the work of Miecznik et al (1990), Ivanov and West (1993) used a non-relativistic, spin polarised version of the random phase approximation with exchange (SPRPAE) in an attempt to extend the interpretation of the Ca^+ photoionisation spectrum between 27 and 43eV. With particular emphasis placed on oscillator strengths and asymmetry parameters, for which the code is more suited, Ivanov and West were able to

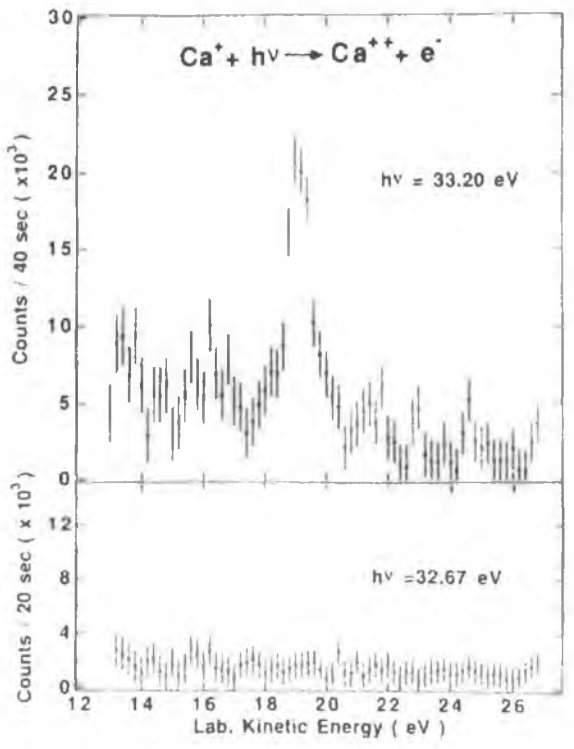

Figure 3.6 : Top : Photoelectron spectrum measured in the photoionisation of a 20keV, 35μA Ca^+ ion beam with 33.2eV(33.17eV in the laboratory frame) photons. With the ionisation energy of Ca^+ being 11.87eV, the kinetic energy of the autoionisation electron should be 21.3eV. However, it appears at 19.2eV due to corrections arising from the ionic current and the CMA contact potentials. Bottom : Same conditions as top spectrum but with the photon energy detuned from the resonance maximum by 0.5eV (after Bizau et al 1991).

corroborate previous identifications of the main one-electron transitions made by other authors (Mansfield and Newsom 1977, Lyon et al 1987, Miecznik et al 1990). More tentatively, as multiple electron transitions were not included in their SPRPAE calculations, they extended the analysis through comparison with Lyon et al's data and by using term averaged energies from standard Hartree Fock calculations, to assign structure centred ~32, 34 and 35eV as belonging to two-electron excitation to $3p^53d^2$, $3p^53d4p$ and $3p^54p^2$ levels respectively.

More recently, Al Moussalami et al (1996) have made advances in photoelectron measurements of Ca^+ whereby they have measured, for the first time in an atomic ion, the angular distribution of electrons emitted in the autoionisation of the Ca^+ $3p^64s\ ^2S \rightarrow 3p^53d(^1P)4s\ ^2P$ resonance. They reduced the large background signal which frustrated

earlier Ca^+ photoelectron work (Bizau et al 1991) by using a high transmission CMA and by attaining ultrahigh vacuum conditions (10^{-9} Torr). By symmetrically deploying eight identical electron multipliers in the focal plane of the CMA, an asymmetry parameter β of 1.89±0.13 at the peak of the resonance was obtained. In fact, very little deviation from this value was seen to occur over the extent of the entire resonance suggesting that, as with the 'giant' 3d resonance in neutral calcium (Ueda et al 1993), LS coupling, for which $\beta = 2$ for an εp wave (see Schmidt 1992), is still a good approximation for the $3p^53d4s\ ^2P$ resonance in Ca^+, despite concerns that β might exhibit strong oscillations due to possible interferences between outgoing waves in continuum channels with different momenta.

3.1.2.2 Excited state investigations in the 3p region

Of particular interest to this work as we shall see in section 3.3, are recent investigations into Ca^+ transitions from the metastable $3p^63d$ level. The lowest lying metastable state in Ca^+ (GS + 1.7eV), the $3p^63d\ ^2D$ state is thought to be present in significant quantities in ion beam experiments such as that performed by Lyon et al (1987). However, transitions from this state had not previously been identified. Thus, Hansen and Quinet (1996) undertook to calculate the energies and gf values of Ca^+ $3p^63d^N \rightarrow 3p^53d^{N+1}$ transitions using the Cowan suite of codes. Transitions between these two levels were of special interest as previous calculations (Quinet and Hansen 1995) on inner shell transitions in the iron group elements had found that for configurations of the type $3p^53d^N$, the influence of core excitations and in particular the $3p^2 \rightarrow 3d^2$ excitation, is important for prediction of both energies and oscillator strengths to the ground configuration $3p^63d^{N-1}$. Ultimately, the conclusion of this earlier study was that while core excitations are important for the description of transitions out of the open 3d shell, they are crucial for transitions out of the closed 3p shell. Indeed, the effect of including core correlations is all too apparent when one considers the differences in the calculated and observed structure of the $3s^23p^53d^2$ configuration in Ni X (see figure 3.7). Thus, to cater for core correlation effects, a total of 26 odd and even configurations were included in the basis set for Hansen and Quinet's Ca^+ calculations. Their results predicted very strong (gf ≈ 3-

4) transitions between 30 and 31eV but with no experimental identifications of metastable transitions, the accuracy of their results was difficult to establish. On the experimental front, Gottwald et al (1997) have recently applied an ion-electron coincidence technique to photoelectron spectroscopy of Ca^+. The technique allowed them to reduce the signal to background ratio from an estimated 1:40 to 1:4. This

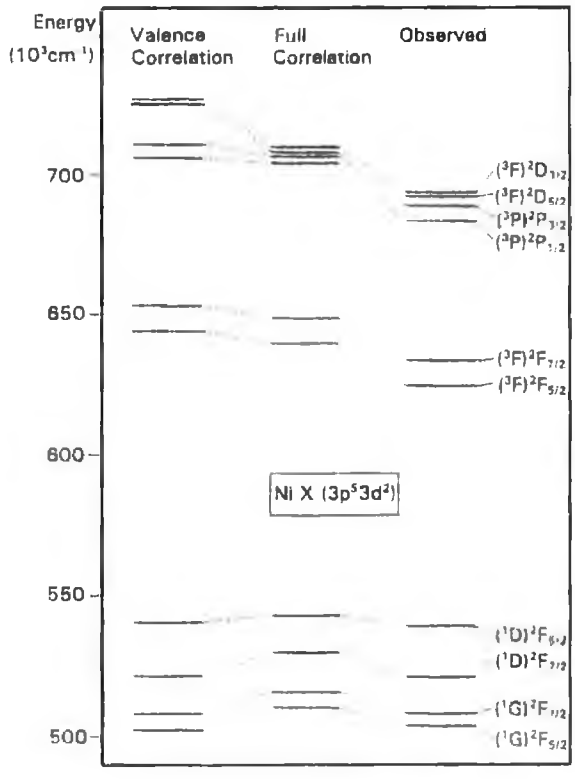

Figure 3.7 : Calculated and observed structure of the $3s^23p^53d^2$ configuration in Ni X. The levels on the left have been calculated by including only correlation in the valence shell, $3d^2$. The centre levels have been calculated by including valence correlation and the most important correlation effects in the $3s^23p^5$ core (called 'Full correlation'). These are compared with observed levels taken from Sugar and Corliss (1985) (after Quinet and Hansen 1995).

enabled them to obtain reasonable statistics for constant ionic state (CIS) spectra corresponding to both Ca^+ $4s^{-1}\varepsilon p$ and Ca^+ $3d^{-1}\varepsilon p$, εf photoemission whereby the monochromator and electron analyser are scanned with a fixed energy difference corresponding to Ca^+4s and Ca^+3d ionisation energies, i.e. 11.9eV and 10.2eV, respectively. In the Ca^+ $4s^{-1}\varepsilon p$ spectra, they clearly observed a peak at 33.2eV which corresponds to the familiar $3p^53d4s$ ^2P resonance. In the Ca^+ $3d^{-1}\varepsilon p$, εf case, they

observed resonances at 31.8, 32.4 and ~32.7eV which they tentatively assigned to members of the $3p^6 3d\ ^2D \rightarrow 3p^5 3d4s\ ^2P,D,F$ multiplet, particularly in light of the fact that the peak at 31.8eV roughly corresponds to the energy one would expect for excitation from $Ca^+ 3d\ ^2D$ to $3p^5 3d4s\ ^2P$ i.e. 33.2 - 1.7 = 31.5eV. These interesting results shall be remarked on further in section 3.3.

3.1.2.3 Lifetime measurements

Finally in this section, we note that the Ca^+ metastable $3d\ ^2D_{3/2,5/2}$ states are of considerable interest as forbidden transitions between the ground state $4s\ ^2S_{1/2}$ and these states serve as calibration lines in astrophysics where they are used to monitor densities and temperatures in stellar atmospheres. For these applications, precise knowledge of lifetimes, quenching and mixing rate constants is necessary (Knoop et al 1995) and thus, there has been much interest, both theoretically and experimentally, in establishing the lifetime of these 3d states. Experimentally, most lifetime measurements have involved ion storage using R.F. ion traps where the Ca^+ ions can be stored over a period of hours. During this time, the metastable levels can be populated by direct diode laser excitation of the forbidden S-D transitions and the lifetimes measured through the subsequent fluorescence decay to the ground state. Using such methodologies, Arbes et al (1993) have measured the average lifetime, τ (3d), of the $3d\ ^2D_{3/2,5/2}$ states to be 1.24 seconds and Knoop et al (1995) have obtained $\tau\ (D_{3/2})$ = 1111ms and $\tau\ (D_{5/2})$ = 994ms. More recently, precise determinations have been made using the 'electron shelving' technique (see figure 3.8) whereby light from a frequency doubled Ti:Sapphire laser at 397nm excites the ions from the ground state to the $4p\ ^2P_{1/2}$ state. From here the ions can either decay back to the ground state or to the $3d\ ^2D_{3/2}$ state. A diode laser at 866.4nm is employed to pump ions from the $3d\ ^2D_{3/2}$ state back to the $4p\ ^2P_{1/2}$ state thereby creating a closed three level system. When another diode laser is added to the fold and tuned to the $3d\ ^2D_{3/2} \rightarrow 4p\ ^2P_{3/2}$ transition at 850nm, population trapping in the $3d\ ^2D_{5/2}$ state occurs as it is the only state to which the $4p\ ^2P_{3/2}$ state may decay. Thus, fluorescence from the $4p\ ^2P_{1/2}$ state drops. When the third laser is turned off, the ions return to the closed three level system by exponential decay of the $3d\ ^2D_{5/2}$ state and accordingly the

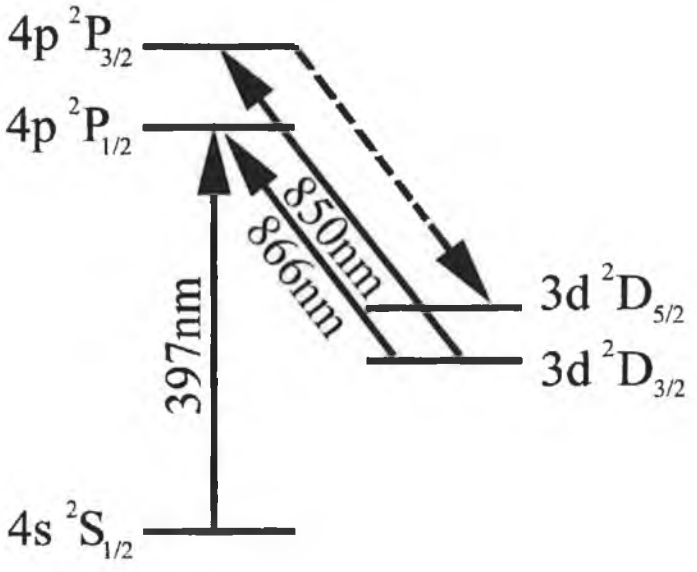

Figure 3.8 : The relevant levels of Ca^+ for measurement of 3d lifetimes via the 'electron shelving' technique(after Ritter and Eichmann 1997). See text for details.

observed fluorescence increases. By measuring the rate of change in fluorescence the lifetime of the 3d $^2D_{5/2}$ state has been measured by Gudjons et al (1996) as 1064ms. While Gudjons et al (1996) trapped an ion cloud of ~10^2 Ca^+ ions, Ritter and Eichmann (1997) have applied the electron shelving technique to a single ion and measured τ ($D_{5/2}$) to be 969ms. Both authors repute errors of <2%. On the theoretical side, Vaeck et al (1992) have calculated τ ($D_{3/2}$) and τ ($D_{5/2}$) values of 1.16 and 1.14 seconds respectively and Liaw (1995) has obtained 1.08 and 1.045 seconds for τ ($D_{3/2}$) and τ ($D_{5/2}$).

3.1.3. Doubly ionised calcium

In contrast to Ca and Ca^+, Ca^{2+} has received relatively little attention over the years. One electron $3p^5nl$ transitions only being possible below the first ionisation limit at 50.91eV, its 3p spectrum is relatively simple. The first observation in the 3p region was made by Anderson (1924) using a vacuum spark. Combining Anderson's measurements between 3 and 5.5eV with his own, Bowen (1928) measured and analysed the spectrum up to 31eV which resulted in the identification of most terms belonging to the $3p^54s$, 5s, 4p, 3d and 4d configurations. Ekefors (1931) subsequently expanded the study up to ~124eV. It

was not until 1968, however, that significant revision and extension of the Ca^{2+} 3p region was performed by Borgström. Publishing two papers (Borgström 1968, 1971) on spectra obtained with a sliding spark, he identified most terms for the $3p^5$6s, 5p, 6d, 7f and 5g configurations. Inner shell transitions were reported through calculations by Hansen et al (1975) for the $3s3p^6$3d configuration and through high voltage spark measurements by Kastner et al (1977) on the $3s3p^64p\ ^1P_1$ and $5p\ ^1P_1$ levels.

More recently, van Kampen et al (1995) has recorded 3p photoabsorption spectra of Ca^{2+} in the 25-55eV region using the dual laser plasma technique. By comparing with similar measurements in the 3p region of K^+, van Kampen et al explored the effects of term dependent wavefunction contraction using the Cowan suite of codes. Again, the influence of 3d wavefunction collapse is paramount, significantly influencing transitions with 3d character. Calculations using centre-of-gravity (COG) wavefunctions were therefore inaccurate for $3p^5$nd ^1P levels. Thus, van Kampen et al performed a separate term dependent calculation in order to extract Slater integrals suitable for the 3d ^1P and 4d ^1P wavefunctions and substituted these for 3d and 4d while using COG values for all other terms. The use of this partially LS term dependent (PLSD) calculation was quite successful permitting, in combination with quantum defect analyses, the identification of ~30 new 3p $\rightarrow$ ns,nd transitions. Finally, we note that van Kampen et al (1997) have also investigated inner shell 3s $\rightarrow$ np resonances, again via the DLP technique. These investigations allowed the first observation of dramatic changes in the Fano parameters of these inner shell resonances in moving up the isoelectronic sequence from Ar to Ca^{2+}. The striking q reversal for 3s $\rightarrow$ np transitions in going from Ar to K^+ and the subsequent change in profile to almost purely symmetrical in moving from K^+ to Ca^{2+} has been interpreted in terms of the proximity to the resonances of the 3s and 3p Cooper minima.

3.2. DLP versus photoion measurements : A comparative study.

In this section, the photoabsorption spectrum of Ca^+ in the region of 3p excitation will be the focus for analysis. In an earlier study, Kiernan (1994) used the dual laser plasma technique to capture the Ca^+ photoabsorption spectrum in the 27-42eV energy region. By

minimising, through a suitable choice of experimental parameters (see section 2.2.), the intensity of the neutral calcium $3p^54s^23d\ ^1P$ 'giant' resonance at 31.4eV relative to the 3p-3d resonance of Ca^+ at 33.2eV, Kiernan was assured of a high degree of ion stage separation. However, upon comparison with the absolute cross section photoion measurements of Lyon et al (1987), a large discrepancy was apparent in the relative intensities of predominant Ca^+ resonances. Most notable was the ratio in peak cross section of the $3p^54s3d$ and 4d resonances. In this work, we have addressed this problem and attempted to reconcile the DLP spectra with the data of Lyon et al (1987). In particular, we have examined the import of plasma opacity and the possibilities for the extraction of improved absolute cross sections through utilisation of the DLP system's superior resolution capabilities.

3.2.1. Opacity considerations

Figure 3.9 shows three Ca^+ spectra corresponding to the region of 3p excitation. Figure 3.9(c) is the resultant photoabsorption for ΔX=6mm and ΔT=700ns, these being the experimental parameters most suited to strong and well isolated Ca^+ ion plasma population. In addition, using a cylindrical lens, an absorbing plasma length of 10.5mm was implemented. Figure 3.9(a) was taken under identical conditions except that here, the absorbing plasma length was 0.5mm. Both DLP spectra were taken using Nd:YAGs, one of which produced 235mJ for creation of the backlighting plasma and the other ~825mJ for creation of the absorbing plasma. Each spectrum is the average result of 90 shots. It is clear by contrast with figure 3.9(b), which shows the photoion results of Lyon et al (1987), that figure 3.9(a) shows better agreement. With no stray light thought to be present in this energy region (see section 2.3.4.) and with a substantially increased absorption level (in particular for the 3p→3d resonance i.e. ~79% at peak), the spectrum illustrated in figure 3.9(c) is thought to be saturated and will thus be referred to as 'optically thick'. Indeed, the evidence for saturation is manifested in the profile of the 3p→3d resonance which appears broader and much reduced in intensity relative to the higher 3p→4d series member, when compared to its equivalent in figure 3.9(b). Hence,

we may conclude that saturation of this resonance was responsible, as it is here, for Kiernan's poor correlation with the photoion data.

We have described the spectrum portrayed in figure 3.9(c) as optically thick and accordingly we shall look upon the regime under which figure 3.9(a) was taken as 'optically thin'. However, one must acknowledge that a feature's opacity is dependent on its cross section so we cannot just label spectra as being within a certain opacity regime (based on whether absorption levels are high or low) without some mathematical criteria for such an assertion. To this end, we have measured the 3p region of Ca^+ for a range of absorbing plasma lengths whilst leaving all other experimental parameters unaltered as above. The absorbing plasma lengths used were 10.5, 7, 5.5, 3.5, 2.5, 1.5 and 0.5mm. This was facilitated by using a translatable knife edge as described previously in section 2.2.

Assuming strong features in the Ca^+ spectrum to be optically thick for absorbing plasma lengths, L, in the 10.5 - 3.5mm range and optically thin for lengths ranging from 2.5 to 0.5mm, we measure the integrated area under the resonances of interest according to equations [1.84] and [1.85] for optically thick $\left(\int (1 - I/I_0) d\nu\right)$ and thin $\left(\int \ln(I_0/I) d\nu\right)$ respectively. Considering only the 3p→3d resonance at 33.2eV and the doublet structure corresponding to 3p→4d centred at ~37.6eV, we should find that the integrated area of each shows a linear relationship with L for optically thin conditions and a square root relationship with L under optically thick conditions. The results are plotted in figure 3.10 where we have fitted each resonance with Lorentzian profiles before extracting the areas in an attempt to reduce the effects of noise. The results show clearly that the integrated resonance area/absorbing plasma length dependence is best described by a linear relationship for L = 0.5→2.5mm, as evidenced by the fit error (χ^2) (see section 2.3.5). For L = 3.5→10.5mm, the results are more ambiguous with the χ^2 error being similar for both square root and linear fits but this in itself, when compared to the obviously superior linear fit for L = 0.5→2.5mm, suggests an approach for L = 3.5→10.5mm to an optically thick regime. The maximum plasma length ultimately being dictated by the Nd:YAG beam diameter (~10.5mm), the modest number of data points in figure 3.10 was unavoidable. However, despite this limitation and not withstanding 'hot spots' in the

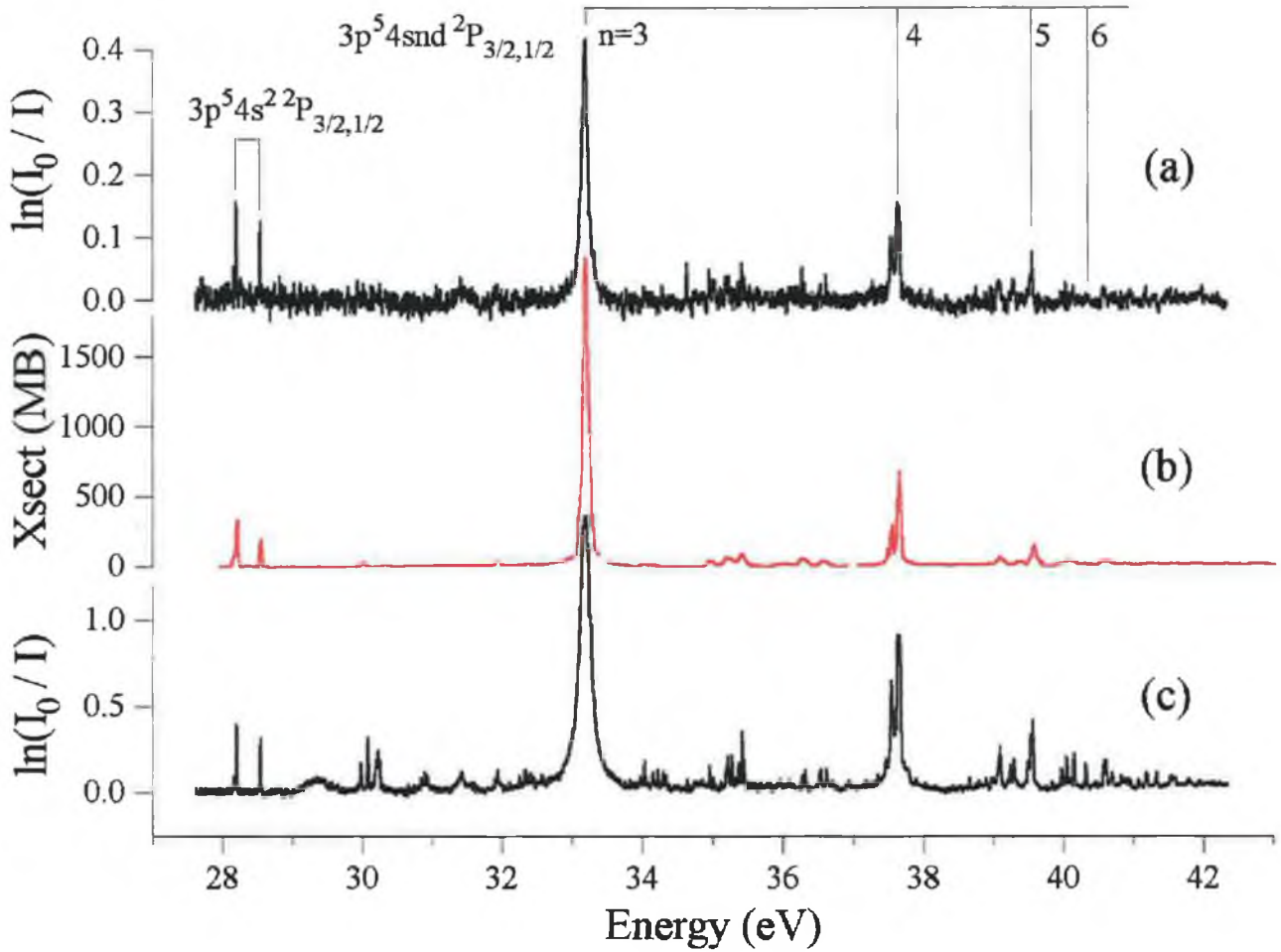

Figure 3.9 : The 3p excitation region of Ca^+ where (a) is a DLP photoabsorption spectrum taken for ΔX=6mm, ΔT=700ns and an absorbing plasma length (L) = 0.5mm (Optically thin), (b) is the photoion measurement of Lyon et al (1987) and (c) is as (a) except L = 10.5mm(Optically thick).

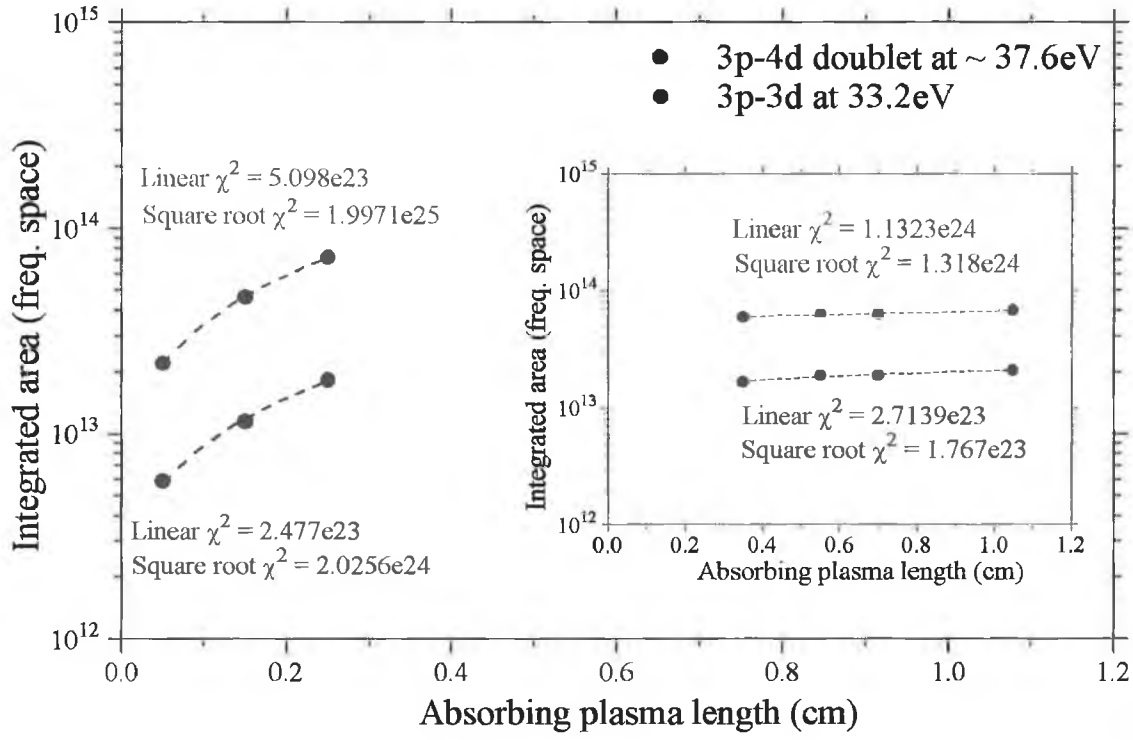

Figure 3.10 : A plot showing how the relationship between the total absorption factor, A_T (see section 1.4) changes with the absorbing plasma length, L. The main part of the figure shows how optically thin conditions pertain for L = 0.5 - 2.5mm whilst the inset shows how for L = 3.5 - 10.5mm, the plasma is more likely optically thick. The best fit for each set of points is shown as a dashed line. See text for further details.

laser beam's spatial profile, the results agree well with theoretical predictions and allow some confidence in considering spectra taken for L = 0.5 and 10.5mm to be optically thin and thick respectively.

To further demonstrate the effect of opacity on our photoabsorption spectra, we show in figure 3.11(a), the ratio of peak heights for the resonances located at 33.2eV and at 37.55 and 37.65eV. With the equivalent ratios from the data of Lyon et al (1987) also indicated, it is clear that the relative height of these dominant features is incorrect by up to a factor of 2 when measured under optically thick conditions. The approach to the data of Lyon et al is clearly evident as one moves into the optically thin domain but still falls somewhat short, even for L = 0.5mm. A possible explanation for this is that the poor resolution of the photoion data would affect the narrower resonances at ~37.6eV more

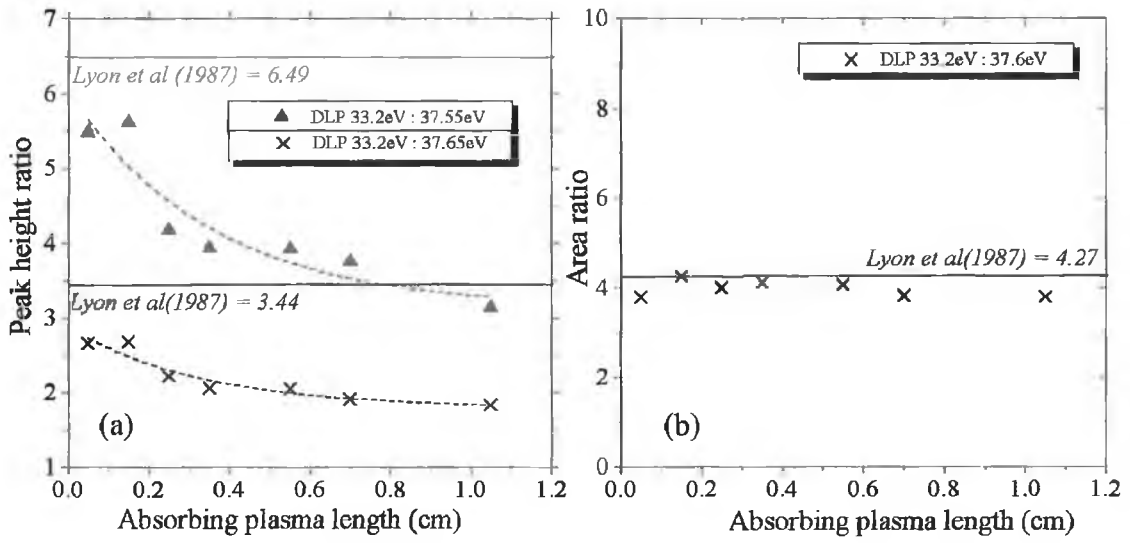

Figure 3.11 : The effect of opacity on the DLP Ca^+ photoabsorption spectrum where (a) examines how the peak height ratio of the 3p-3d resonance at 33.2eV and the 3p-4d doublet ~37.6eV varies as a function of L and (b) examines the integrated area ratio of the same lines except that here we have summed the doublet. The equivalent ratios from the data of Lyon et al(1987) are shown for comparison.

than the broad 3p-3d resonance at 33.2eV. Thus, the relative peak height difference would appear greater than that for the more highly resolved DLP data. Contrasting the relative areas in a similar manner, we find in figure 3.11(b) that excellent agreement between DLP and photoion data is apparent. In this case we have taken the summed area of the doublet at ~37.6eV rather than the area of each component and we note that, as one may expect, the ratio of integrated areas is not altered by the saturation encountered under optically thick conditions.

3.2.2. Absolute cross sections

Plasma densities, both in terms of ions and electrons are traditionally difficult quantities to measure where dual laser plasma photoabsorption spectra are concerned. Without a knowledge of n, the spectra cannot be put on an absolute cross sectional scale and as such DLP spectra are typically limited to the extraction of information on relative cross section behaviour only. However, one may well ask if it is possible to correlate DLP data

with absolute cross section measurements of the same atom or ion, taken via other means. Were it so, the benefits would be seductive in that the DLP system's high resolution would prevent the smearing, broadening and subsequent reduction in intensity inherent in the measurement of resonances under lower resolutions. Indeed, once normalised to the known absolute cross sections, information on cross sections throughout extended energy regions could be obtained.

In this section we discuss a procedure for putting the Ca^+ photoabsorption spectrum in the 28-42eV energy region on an absolute cross sectional scale by correlation with the photoion measurements of Lyon et al (1987). Both the optically thin and optically thick (figure 3.9(a) and (c) respectively) DLP spectra were utilised. The 'thin' spectrum was deemed saturation free and therefore reliable for a measure of the relative intensity of the large 3p→3d and 4d resonances whilst the 'thick' spectrum, with a better signal-to-noise ratio than the 'thin', would be used for a measure of the relative intensities of the weaker multi-electron structures. The photoion data was taken with a resolution which varied from 0.2Å for the larger resonances to 1Å for the weaker structure where resolution was necessarily sacrificed in order to boost the photon flux. As the DLP resolution was better than 0.14Å in the 3p region, the first step in correlating the two sets of data was the convolution of the DLP data with an estimate of the instrument function inherent in the photoion experiment. The narrowest resonance measured by Lyon et al (1987) at 28.545eV had a FWHM of ~44meV. This therefore sets the upper limit on the instrument function estimate. The DLP data was thus, convolved with a range of instrument functions, each Gaussian in profile, with widths of 16, 26, 35 and 44meV. The resultant convolutions were then compared with the photoion data and assessed for correlation using the profiles of the five most prominent Ca^+ resonances. Only five features were included in the correlation as the other peaks were either too weak for reliable profile parameter extraction or of uncertain ground state Ca^+ origin. The correlation was made in terms of relative area, peak height and FWHM. The data is shown in figure 3.12 where (a), (b) and (c) refer to the Ca^+ optically thick spectrum and (d), (e) and (f) to the Ca^+ optically thin spectrum. For each convolution the data was normalised using the peak cross section of the 3p→4d resonance at 37.65eV. The 3p→4d resonance was deemed the most suitable for the nexus between data sets as it was strong

under both opacity regimes meaning good statistics for accurate profile extraction. On the other hand it was not so intense, again under both opacity regimes, as to suffer from saturation. This meant that its relative intensity was consistent in both 'thick' and 'thin' spectra when compared to the next highest Rydberg member, the 3p→5d resonance at ~39.5eV. Examining figure 3.12, we see that in (a), allowing for the effect of noise on the DLP fits, the relative areas are well correlated with the obvious exception of the two lines ~28eV. The lack of agreement here, particularly when contrasted with the equivalent optically thin results in (d) is suggestive of these narrow resonances suffering from Stark broadening, the effect being more pronounced in the larger 10.5mm plasma column. In terms of peak heights, we again see better correlation in the optically thin case (figure 3.12(e)), excellent agreement having been obtained for the peaks at 33.2eV and 28.545eV. For the optically thick peak heights (figure 3.12(b)), we see how saturation leads to a discrepancy in heights for the 3p→3d resonance of almost 53%. The two features ~28eV also correlate poorly for similar reasons as given for figure 3.12(a). The lack of agreement for the 3p→5d resonance at ~39.5eV is due to it being quite weak (~150MB) in the data of Lyon et al (1987). Thus, being more highly resolved and subject to better statistics, the DLP relative measurements of this resonance are thought to be more accurate. For the FWHM measurements, we again note the superior agreement for the optically thin data, our FWHM for the 3p→3d resonance being broader than that of Lyon et al (1987) by only 4meV. In the optically thick case, the discrepancy follows the trend seen in peak heights and is strikingly disparate, the DLP FWHM being almost a factor of two broader. It is clear from the data that the convolution with an instrument function of FWHM equal to 26meV yields the best correlation under both opacity regimes. Normalising to the 3p→4d peak in both 'thick' and 'thin' cases, we can then put the DLP raw data on a cross sectional scale. The final step is the application of spectral restoration through deconvolution of these spectra with the DLP system's instrument function which has been found in section 2.3.5. to be described by a Lorentzian profile with a FWHM of 4 pixels.

Deconvolution was performed in pixel space whereby each of the six chordal distance or CEMA (Channel electron multiplier array) settings, which constitute the Ca^+ spectrum

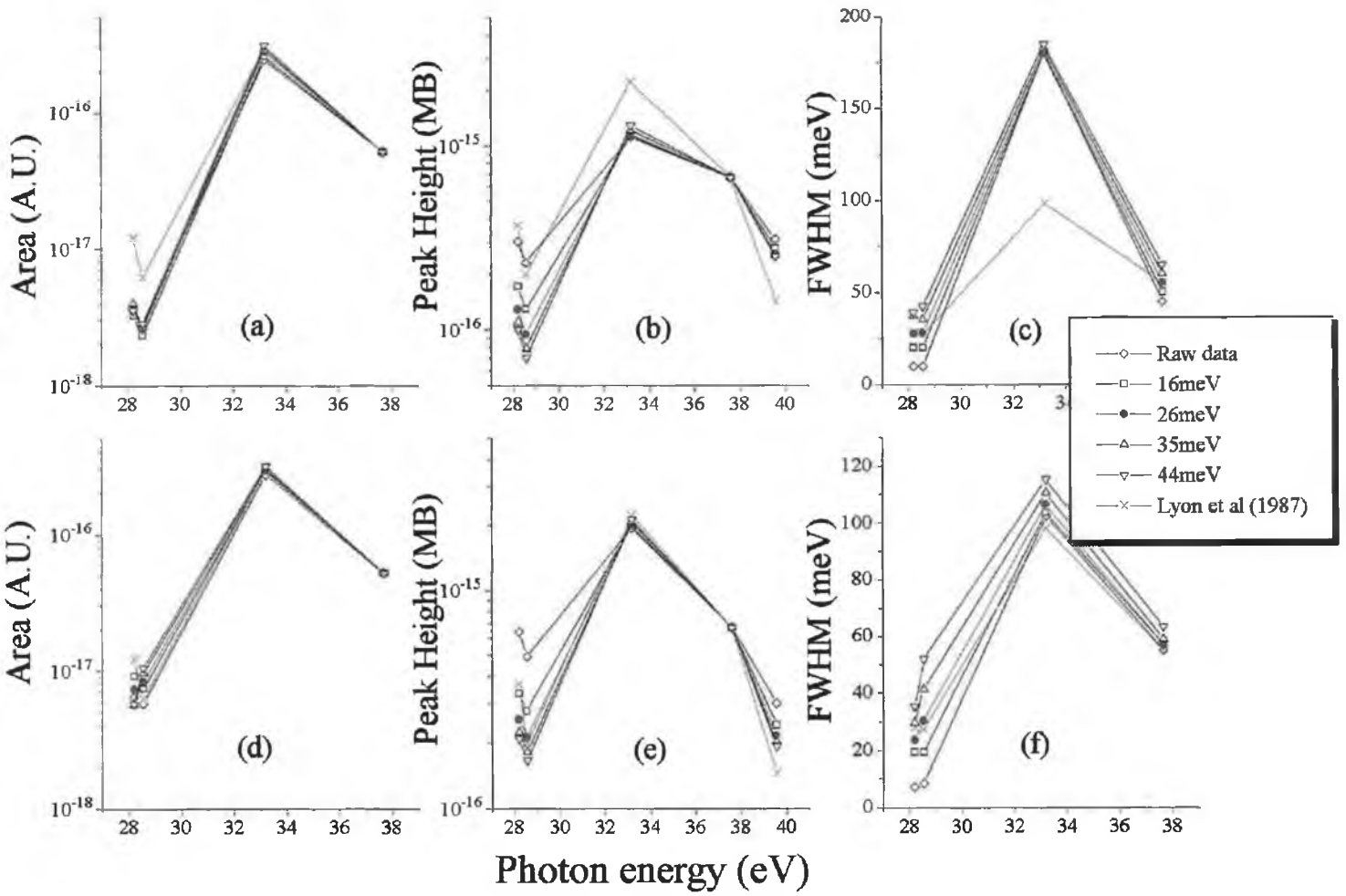

Figure 3.12 : A comparison of Ca^+ features as seen by Lyon at al (1987) and via the DLP photoabsorption technique. Resonances at 28.2, 28.55, 33.19, 37.65 and 39.5eV were correlated in terms of area, peak height and FWHM. The DLP data was convolved with estimates of Lyon et al's instrument function (FWHM = 16, 26, 35 and 44meV) and normalised in both area and peak height to Lyon et al's 3p→4d resonance at 37.65eV. (a), (b) and (c) refer to the DLP optically thick data and (d), (e) and (f) to the optically thin data. See text for more detail

from 27 to 44eV, were deconvolved and then reconnected on the appropriate energy scale. All deconvolutions were carried out using 20 iterations of Varosi's maximum likelihood¶ routine which has been coded for operation through IDL (interactive data language) on the UNIX platform (see Whitty 1998). The results are shown in figures 3.13 and 3.14 where (a), (b), (c) and (d) show, respectively, the photoion data of Lyon et al (1987), the DLP data convolved with the 26meV Gaussian found to best approximate the instrument function of Lyon et al, the DLP raw data and the DLP data deconvolved with a 4 pixel FWHM Lorentzian instrument function. Figure 3.13 shows the results for the optically thick data and figure 3.14, the results for the optically thin data.

The final results become more legible when the deconvolved DLP data is compared to the photoion data in a piecemeal fashion. In figure 3.15 and 3.16, we present the two sets of data in energy windows identical to those shown in Lyon et al's publication. During the following discussion, we will also refer to table 3.1 where all distinct features in the 28 to 42eV region with a final deconvolved cross section in excess of 95MB are shown. In table 3.1, our data is compared with energy measurements for Ca^+ features observed by Bizau et al (1987), Pejcev et al (1978) and Lyon et al (1987) and our derived cross sections compared, where possible, with those of Lyon et al (1987). The associated errors in our energy measurements are deemed to be ±0.02eV, this being roughly three times the plate factor (0.006eV) present at ~42eV where the linear dispersion of our instrument in the Ca^+ 3p region is greatest. This error margin is comparable with that reported by Lyon et al (1987) of between ±0.01eV and ±0.02eV and compares with an accuracy of ±0.04eV and ±0.06eV reported by Bizau et al (1987) and Pejcev et al (1978) respectively. In the data of Lyon et al, the margin of error in the peak cross sections was assessed to be ±15% although they noted that their finite energy resolution may have resulted in errors in excess of this. In an effort to establish the degree of error in our final peak cross section derivations, we have deconvolved our raw data with the upper and lower extremes within which we are certain that our instrument function lies. Hence, we have as our lower limit a Lorentzian profile of FWHM equal to 3 pixels and as our upper limit, a Lorentzian profile of FWHM

¶ The routine is called 'MAX_LIKELIHOOD.PRO' and is available at http://www.astro.washington.edu/deutsch/idl/htmlhelp/slibrary01.html

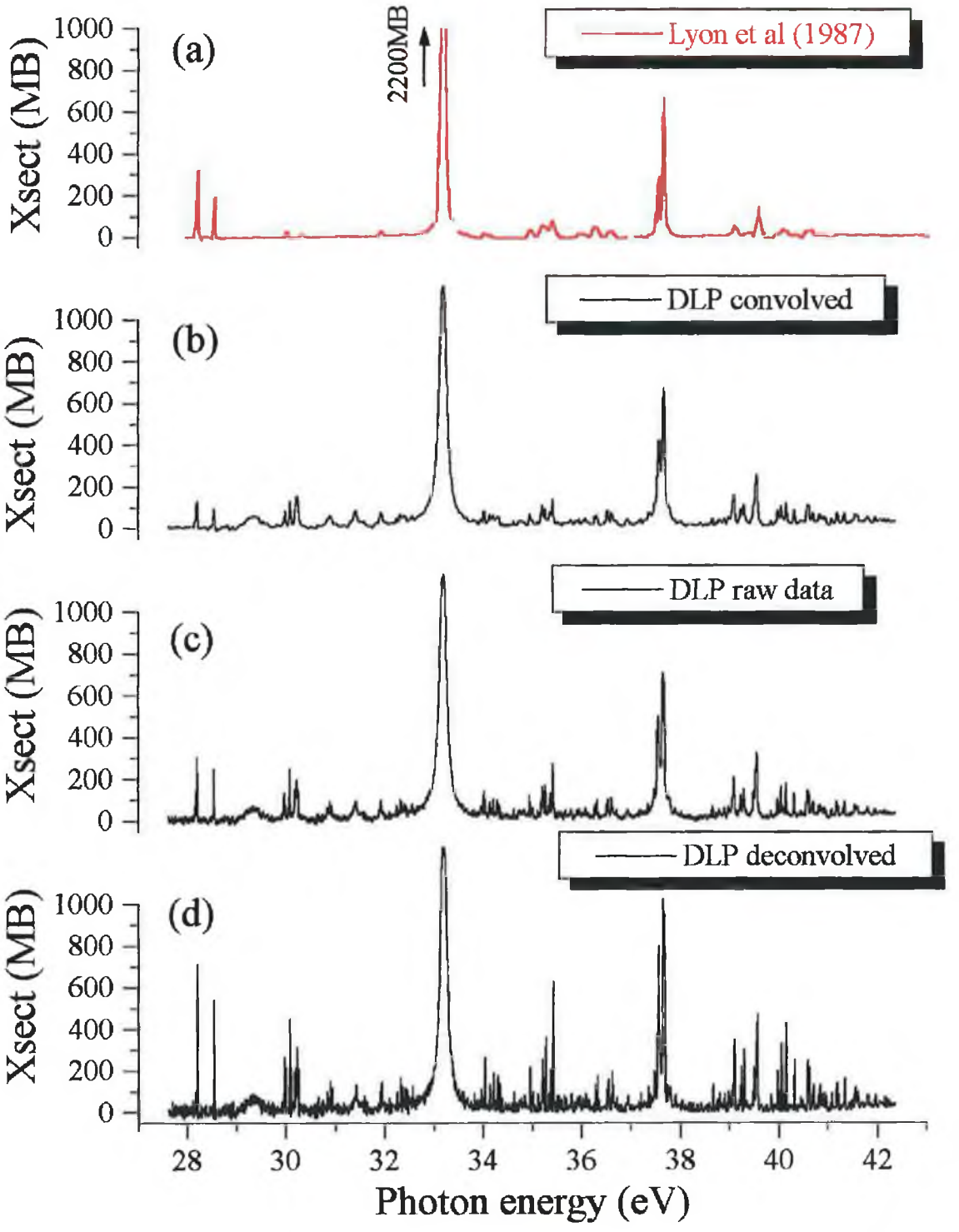

Figure 3.13 : Comparison of DLP optically thick Ca^+ spectra (now on a cross sectional scale) with the data of Lyon et al (1987) where (a) is the photoion data, (b) the DLP raw data convolved with a 26meV FWHM Gaussian, (c) the DLP raw data and (d) the DLP raw data deconvolved with a 4 pixel FWHM Lorentzian.

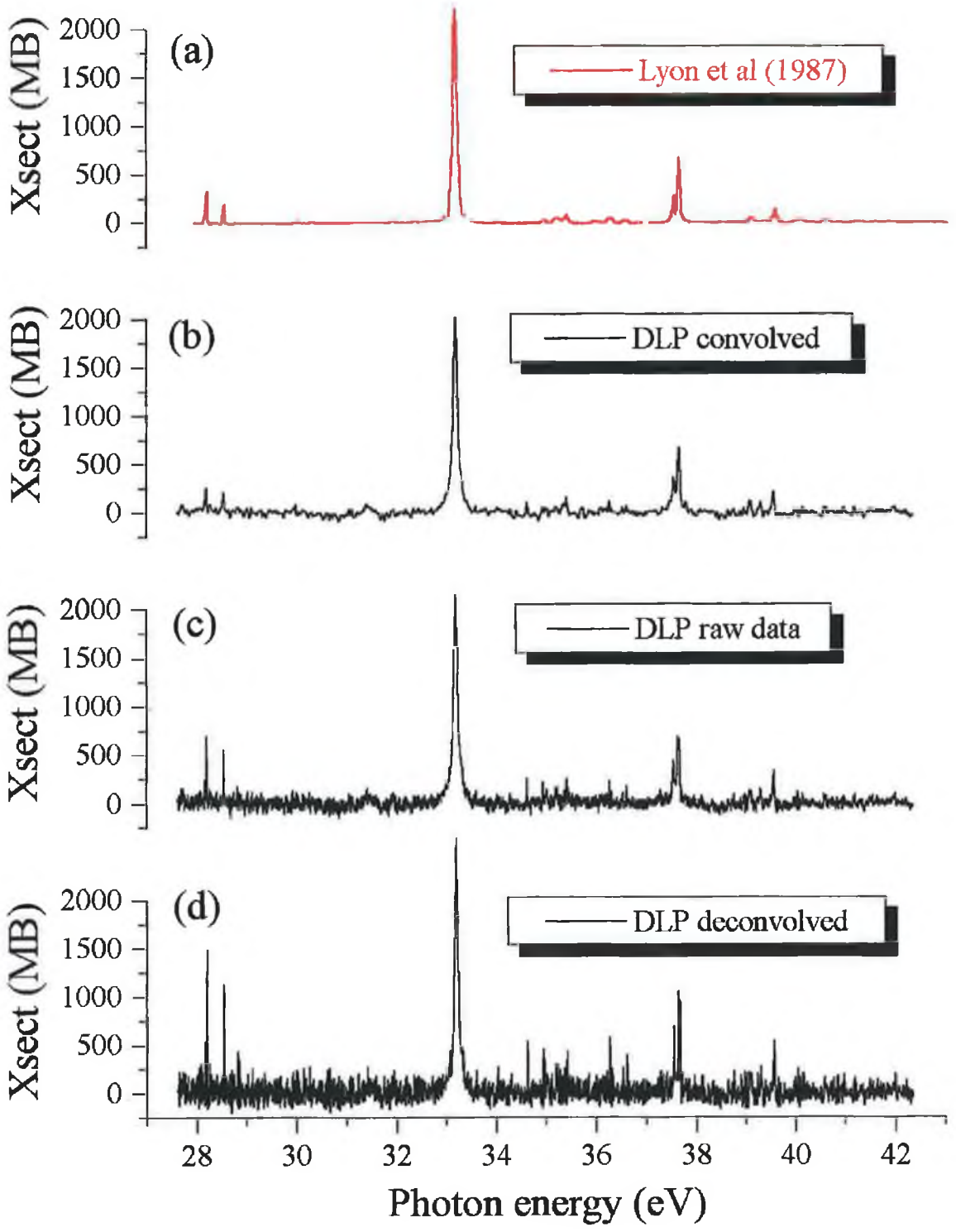

Figure 3.14 : Comparison of DLP optically thin Ca^+ spectra (now on a cross sectional scale) with the data of Lyon et al (1987) where (a) is the photoion data, (b) the DLP raw data convolved with a 26meV FWHM Gaussian, (c) the DLP raw data and (d) the DLP raw data deconvolved with a 4 pixel FWHM Lorentzian.

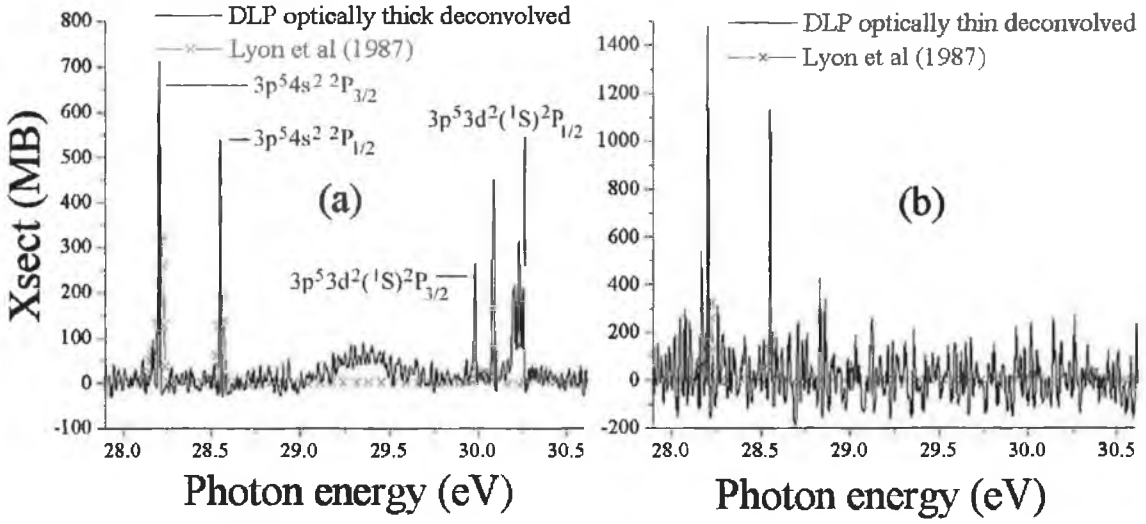

Figure 3.15 : The absolute cross section measurements of Lyon et al (1987) for Ca^+ compared with in (a) the derived cross sections obtained via DLP measurements using an optically thick calcium plasma and (b) the derived cross sections obtained via DLP measurements using an optically thin calcium plasma. Lines are labelled in accordance with table 3.1.

equal to 5 pixels. The resulting departure from the peak cross sections obtained through deconvolution with a 4 pixel FWHM Lorentzian was seen to be no more than ±12%. As the error in the photoion peak height measurements of Lyon et al (1987), about which our cross section extrapolation is based, was ±15%, we therefore quote ±20% as our peak height error.

Figures 3.15 (a) and (b) show the derived cross sections for the $3p^54s^2\ ^2P_{3/2,\ 1/2}$ resonances at 28.2 and 28.55eV respectively. We see the peak heights much reduced in the optically thick case but still in excess of a factor of two greater than those measured by Lyon et al. Even more striking is the optically thin case (figure 3.15(b)), where we reveal the peak cross sections to be, in fact, approximately five times greater than that estimated under Lyon et al's limited resolution. The discrepancy in these derived cross sections between opacity regimes is, as discussed previously, thought to be due to the increased broadening of these narrow resonances¶ within the larger 'optically thick' plasma. Also of note is the absence in the photoion spectrum of an equivalent to the broad feature observed by DLP, centred ~29.35eV. The structure ~30.24eV also has no counterpart in

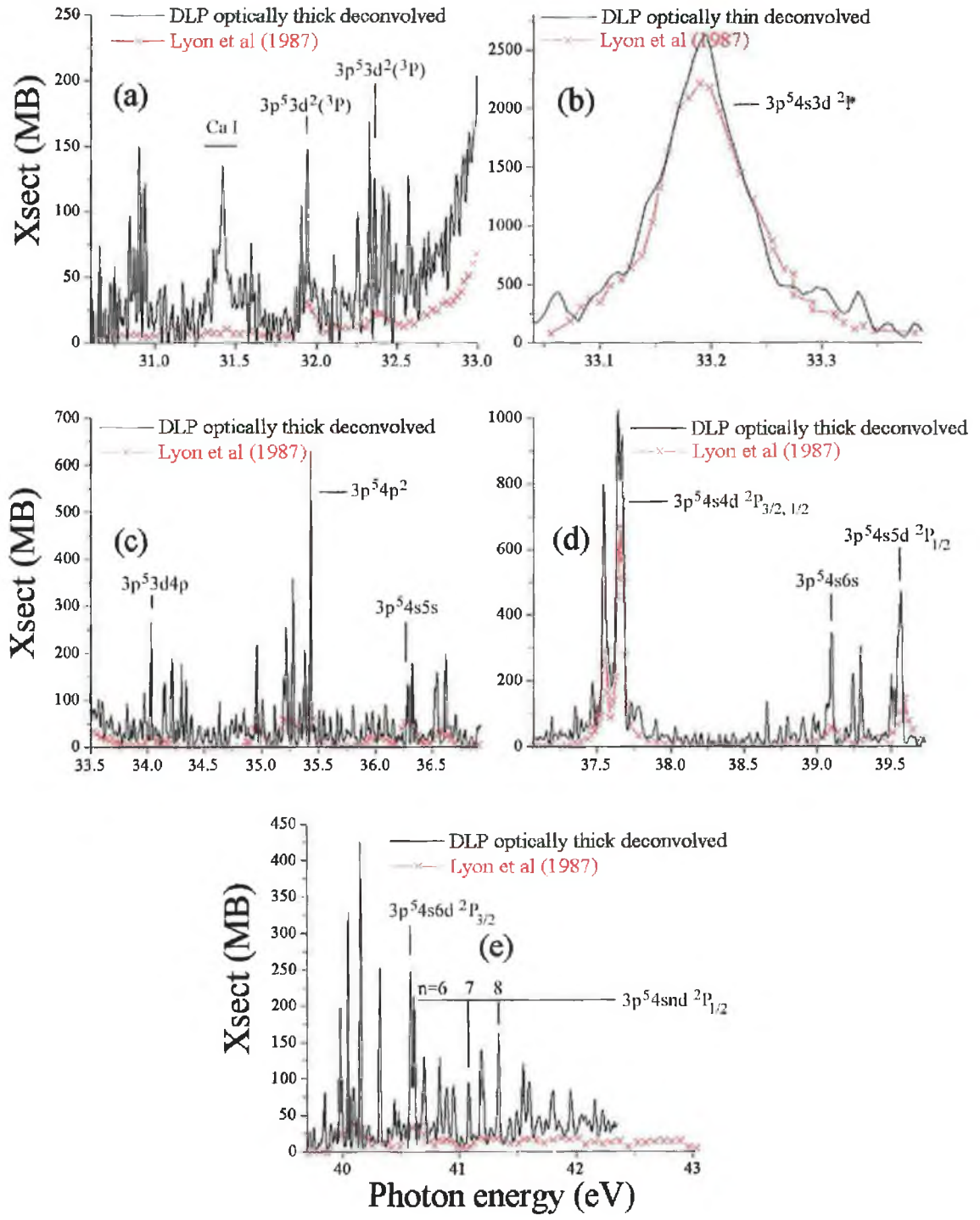

Figure 3.16 : The absolute cross section measurements of Lyon et al (1987) for Ca^+ compared with in (a), (c), (d) and (e) the derived cross sections obtained via DLP measurements using an optically thick calcium plasma and (b) the derived cross sections obtained via DLP measurements using an optically thin calcium plasma. Lines are labelled in accordance with table 3.1.

Photon energy (eV) DLP*	Photon energy (eV) (Lyon et al 1987)	Photon energy (eV) (Bizau et al 1987)	Photon energy (eV) (Pejcev et al 1978)	Peak Xsect. (MB) (Lyon et al 1987)	Peak Xsect. (MB) DLP deconvolved†	Assignment
28.16					98	
28.20	28.205	28.20	28.199	320	1479	$3p^5 4s^2\ ^2P_{3/2}$
28.55	28.545	28.51	28.545	190	1127	$3p^5 4s^2\ ^2P_{1/2}$
30.01	30.00	30.01	30	25	266	$3p^5 3d^2(^1S)\ ^2P_{3/2}$§
30.11			30.14		451	
30.22					218	
30.24					310	
30.27	30.31	30.28	30.27	14	210	$3p^5 3d^2(^1S)^2P_{1/2}$¶
		30.4	30.395			
		30.65	30.605			
30.90			30.91		143	
	31.09	31.1	31.025	12		
		31.64	31.43			
31.90			31.905		104	
31.94	31.933	31.94	31.95	31	147	$3p^5 3d^2(^3P)$¶
32.25			32.21		99	
32.32			32.33		169	
32.36	32.382		32.38	22	126	$3p^5 3d^2(^3P)$ ¶
32.41					119	
32.44					114	
32.56			32.58		127	
33.20	33.19			2200	2642	$3p^5 4s3d\ ^2P$
		33.32	33.38			
		33.68	33.64			
33.81			33.75		91	
34.02	34.025			22	266	$3p^5 3d4p$¶
34.14	34.14		34.17	14	135	
34.21		34.2			189	

Table 3.1 : The peak cross sections for all major features in the Ca^+ 3p region between 28 and 42eV. Only features with a DLP peak cross section >95MB are listed. The measured energies of features obtained through photoelectron (Bizau et al 1987) and electron impact (Pejcev et al 1978) experiments are also shown. Assignments are given where possible (see text for further details).

Photon energy (eV) DLP*	Photon energy (eV) (Lyon et al 1987)	Photon energy (eV) (Bizau et al 1987)	Photon energy (eV) (Pejcev et al 1978)	Peak Xsect. (MB) (Lyon et al 1987)	Peak Xsect. (MB) DLP deconvolved†	Assignment
34.29					176	
34.32			34.39		141	
34.63			34.63		94	
34.95	34.962	34.98		36	218	
35.01					101	
35.19					147	
35.21	35.232			56	255	
35.27			35.28		359	
			35.35			
35.37			35.38		206	
35.42	35.424		35.435	82	630	$3p^5 4p^2$¶
		35.46	35.46			
36.27	36.285		36.27	53	134	$3p^5 4s5s$¶
36.31		36.36	36.32		177	
36.52		36.66			127	
36.54			36.53		157	
36.61	36.586			34	197	
37.56	37.554			289	799	
37.64	37.656			670	1022	$3p^5 4s4d\ ^2P_{3/2}$‡
37.67			37.87		948	$3p^5 4s4d\ ^2P_{1/2}$‡
38.65			38.68		135	
39.09	39.09			57	348	$3p^5 4s6s$¶
39.24					221	
39.29					302	
39.50			39.45		218	
39.56	39.589			144	473	$3p^5 4s5d\ ^2P_{1/2}$‡
39.98					198	
40.05	40.070			40	329	
40.15					425	
40.32					252	

Table 3.1 (continued)

Photon energy (eV) DLP*	Photon energy (eV) (Lyon et al 1987)	Photon energy (eV) (Bizau et al 1987)	Photon energy (eV) (Pejcev et al 1978)	Peak Xsect. (MB) (Lyon et al 1987)	Peak Xsect. (MB) DLP deconvolved†	Assignment
40.58					247	$3p^5 4s6d\ ^2P_{3/2}$ ‡
40.61	40.612			35	213	$3p^5 4s6d\ ^2P_{1/2}$ ‡
40.70					129	
40.84					129	
41.09					95	$3p^5 4s7d\ ^2P_{1/2}$ ‡
41.19					139	
41.33					162	$3p^5 4s8d\ ^2P_{1/2}$ ‡
41.54					121	
41.59					95	

* ±0.02eV
† ±20%
‡ Tentative assignment.
§ Mansfield and Newsom (1977)
¶ Ivanov and West (1993)

Table 3.1 (Continued)

the photoion data and we thus suspect that both of these features are not of ground state Ca^+ origin. Lyon et al(1987), using Mansfield and Newsom's (1977) neutral calcium threshold data, have assigned the peak at 30eV to $3p^53d^2(^1S)\ ^2P_{3/2}$ and we concur, also seeing at this energy a strong sharp feature with a peak cross section of 266MB. Ivanov and West (1993) have suggested that the other feature observed by Lyon et al (1987) at 30.31eV is the spin-orbit (J=1/2) counterpart of this doubly excited resonance, its splitting of 0.3eV consistent with that of the $3p^54s^2\ ^2P$ pair. We observe a line at 30.27eV, which if the $3p^53d^2(^1S)\ ^2P_{1/2}$ resonance, leaves three other strong lines in the immediate vicinity unaccounted for. These will be the subject of further discussion in section 3.3.

Moving to figure 3.16, we see in (a) that the lines observed at ~30.9eV have no analogue in the photoion data and thus, as above, we suspect that they are not the result of transitions from ground state Ca^+. The DLP feature at 31.4eV is the well known Ca I $3p^54s^23d\ ^1P$ resonance, illustrating that we have not been completely successful in the separation of ion stages. By far the most intense resonance in the Ca I 3p region, it appears only very weakly in our Ca^+ spectra so we can be sure that all other Ca I features are of negligible presence. Ivanov and West (1993), using term averaged Hartree-Fock energy calculations, have inferred that the $3p^53d^2$ triplet configuration lies well above the singlet configurations, which as we have mentioned are the most likely assignment for the peaks at 30 and 30.3eV. They have therefore suggested that the photoion peaks at ~31.9eV and 32.4eV be associated with the $3p^53d^2\ (^3P)$ configuration. However, instead of these two peaks, we have observed two strong peaks at ~31.9eV and seven peaks in the immediate vicinity of 32.4eV (see table 3.1). In figure 3.16(b), we see the familiar $3p^54s3d\ ^2P$ resonance, which we have measured at 33.2eV. It is interesting to note that through our deconvolution procedure, we estimate a peak cross section of ~2640MB which is now slightly closer to the value reported by Bizau et al (1991) of 3000MB than to Lyon et al's value of 2200MB. The calculations of Ivanov and West (1993) produce an oscillator strength for this resonance of 3.0 which corresponds to an approximate peak cross section of 3600MB. They suggest that the discrepancy

---

¶ Miecznik et al (1990) and Ivanov and West (1993) have calculated the FWHM of the $3p^54s^2\ ^2P$ resonances to both be ~2meV and ~1meV respectively.

between this and the value of Lyon et al is due to coupling to two electron excitations near the 3p→3d transition. In terms of width, our deconvolved profile gives ~0.09eV which compares to Lyon et al's value of ~0.1eV and to the theoretical widths of Miecznik et al (1990) and Ivanov and West (1993) of 0.05eV and 0.06eV, respectively. In figure 3.16(c), we again see that structure seen in the photoion data is also present in the DLP measurements. For the photoion peak at ~34eV, Ivanov and West (1993) have suggested a $3p^5 3d4p$ assignment. Instead of the single peak observed by Lyon et al (1987), we observe up to six peaks (see table 3.1). The three photoion peaks centred at ~35.25eV appear in DLP measurements to each consist of two to three sharp and rather strong lines. Mansfield and Newsom (1977) calculated an energy of 40.6eV for the $3p^5 4p^2$ level of Ca^+ which after subtraction of the Ca^+ ionisation potential of 6.11eV, gives 35.5eV. Ivanov and West's (1993) calculation for $3p^5 4p^2$ configurations, which they believe accurate due to these configurations being free of correlations since there is no d shell excitation, also gives energies of ~35.5eV. A $3p^5 4p^2$ label for this structure is thus compelling. The photoion structure between 36 and 36.5eV can again be seen, through DLP measurements, to consist of multiple peaks (see table 3.1) which through oscillator strength comparisons with Lyon et al's data, Ivanov and West have designated a $3p^5 4s5s$ label.

In figure 3.16(d), we see a strong pair of lines in the photoion spectrum, the lines being at 37.55 and 37.66eV. Miecznik et al (1990) assigned them to $3p^5 4s4d\ ^2P$ levels but further calculations by Ivanov and West (1993) suggested that the lower energy $3p^5 4s4d\ ^2P_{3/2}$ component should be very weak. They further argued that the large separation between the observed peaks (~0.1eV) was too large to be considered as due to spin-orbit splitting, especially in view of its apparent absence for the $3p^5 4s3d$ resonance. It was thus their conclusion that the line at 37.55eV, whilst probably associated with the 3p→4d transition, is not due to spin-orbit splitting but more likely a two electron transition enhanced by interaction with the main 3p→4d line at 37.66eV. With the DLP measurements, we can now reveal that the peak at ~37.66eV is in fact comprised of two lines which we tentatively assign to the $3p^5 4s4d\ ^2P_{3/2,1/2}$ resonances, their spin-orbit splitting being ~0.03eV (see table 3.1). Although in figure 3.16(d) we only show the optically thick deconvolution of this energy region, where the lines at 37.64 and 37.67eV

have peak cross sections of 1022 and 948MB, the optically thin deconvolution results in peak cross sections for these same lines of 1057 and 952MB respectively. This is further evidence that, measured under both opacity regimes, the $3p^54s4d\ ^2P$ lines are consistent being unaffected by saturation and therefore a suitable choice for the normalisation procedure described earlier. The remaining photoion structure at ~39.1eV and 39.6eV is also seen in the DLP data. Ivanov and West (1993) have assigned these to $3p^54s6s$ and $3p^54s5d$ configurations respectively.

Finally, in figure 3.16(e), we see many sharp features in the DLP data which are believed to be the many $3p^54snd$ series members running to the four possible $3p^54s$ thresholds i.e. $^3P_{2,1,0}$ and $^1P_1$. The two distinct peaks seen by Lyon et al at ~40.1eV and ~40.6eV have been assigned, by Ivanov and West, to $3p^54s6d$ and $3p^54s7d$ transitions, respectively. However, we have found, through the use of experimentally measured 3p ionisation thresholds for Ca^+ (see Ivanov and West 1993) and through the use of the Rydberg formula

$$E_n = I_p - Z^2R/(n-\delta)^2 \qquad [3.1]$$

where n is the principal quantum number, δ the quantum defect, Z the atomic number, I_p the ionisation potential (in eV), E_n the transition energy and R the Rydberg constant for the element in question (R_{Ca} = 13.605478eV), that the DLP measured lines at 33.2, 37.67, 39.56, 40.61, 41.09 and 41.33eV form a smooth series running to the $3p^54s\ ^3P_0$ threshold at 42.3eV. We therefore assign these lines to members of the $3p^54snd\ ^2P_{1/2}$ series where n = 3-8.

Although we have made progress in terms of obtaining more detailed and highly resolved spectra and achieved some measure of success in the extraction of, what we believe to be, more accurate cross sections, a full interpretation of this complex region of Ca^+ is not yet within our grasp. Indeed, the rich multielectron structure and manifold Rydberg series require more accurate theoretical predictions if they are to be identified with any certainty. We have seen, in the above discussion, that much of the structure can be interpreted in broad strokes as arising from Ca^+ ground state transitions. However, the anomalous structure between ~28.6 and 32eV does not, even loosely, conform to a Ca^+ ground state origin. It thus seems appropriate that in the next section we investigate this energy region in more detail and through rigorous exploitation of the DLP system's

capabilities and comparison with recent literature, present some evidence that this anomalous structure is due to excited states.

3.3 The Calcium isonuclear sequence in the region of 3p excitation : Ca^0, Ca^+ and Ca^{2+}.

In our search for an assignment to the structure found in the DLP Ca^+ spectrum between ~28.6 and 32eV, we begin by ensuring that our Ca^+ spectrum is free from ion stage impurities. To do this, we must look at the first three members of the calcium isonuclear sequence. Any cross contamination should then be immediately obvious.

3.3.1 Spatio-temporal studies.

In order to establish the best experimental parameters for the clear separation of successive ion stages, we have constructed spatio-temporal maps. We begin by choosing known lines which are representative of each ion stage. We then track their presence as a function of ΔX and ΔT (see section 2.2), keeping the power density on target constant. By measuring the integrated area under the profile of each line, we can then construct a three dimensional map of the ion stage to which it belongs which when inter-compared with other maps allows one to choose the best experimental parameters for each ion stage such that its presence in the plasma as a function of inter-laser time delay (ΔT) and target proximity to the optic axis (ΔX), is optimised.

For neutral calcium, we have chosen to track the $3p^54s^23d\ ^1P$ resonance at 31.4eV due to its appreciable intensity and the fact that neither Ca^+ nor Ca^{2+} exhibit ground state transitions at this energy. For similar reasons, the $3p^54s3d\ ^2P$ resonance at 33.2eV was used for Ca^+ and the $3p^53d\ ^1P$ resonance at ~34.6eV for Ca^{2+}. The relative proximity of these resonances was also a consideration in their choosing as if, for example, both the Ca^+ and Ca^0 3d resonances can be captured within one CEMA setting then the relative ion stage contribution to each spectrum can be monitored in realtime, experimental conditions are assured of being identical for each of the lines and experiment run-time is significantly reduced.

For Ca^0 and Ca^+, a CEMA setting of 28" permitted the capture of both their respective resonances simultaneously. A total of 14 ΔX settings were implemented i.e. 0.25, 0.5, 0.75, 1.0, 1.5, 2.0, 2.5, 3.0, 3.5, 4.0, 4.5, 5.0, 6.0 and 7.0mm and at each of these a total of 19 ΔT settings were used i.e. 25, 50, 75, 100, 150, 200, 250, 300, 400, 500, 600, 800, 1000, 1200, 1400, 1600, 1800, 2000 and 2400ns. The integrated area under the resonance profile of interest could then be calculated for each ΔX, ΔT pair and the resulting 14x19 matrix interpolated and smoothed to produce the map. It may be noticed that both ΔX and ΔT values were not incremented in constant steps. This is because very soon after plasma initiation (10s of ns), the more energetic ions will recombine to form the longer lived neutral atoms. Hence, the Ca^+ resonance will dominate initially but will soon fade in favour of the neutral resonance. We therefore require a greater density of points for smaller ΔX and ΔT should we wish to monitor the rapidly changing plasma, and consequently spectra, successfully. For each ΔX, ΔT pair a spectrum was recorded which comprised of 3 shots, an I_0 spectrum only being required after every 5 Is. A 200mJ

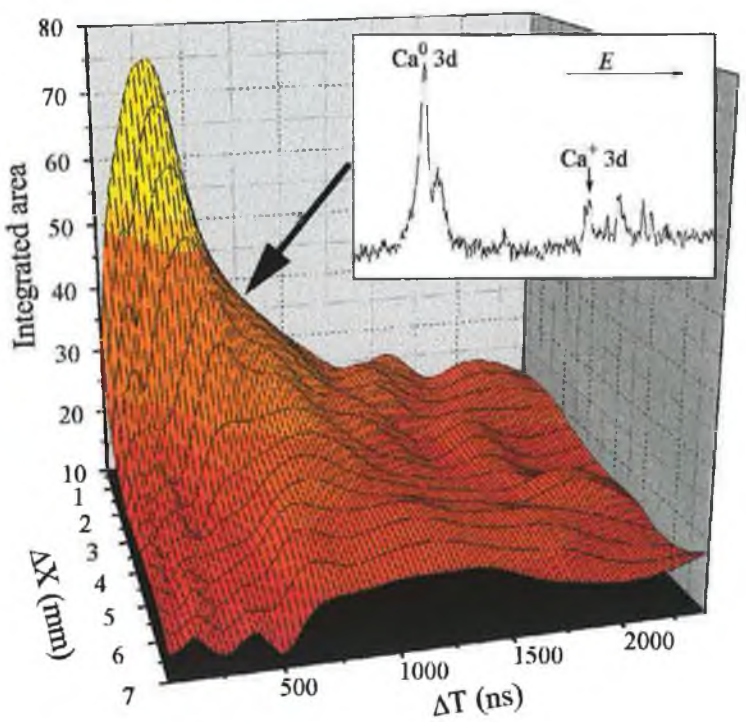

Figure 3.17 : The temporal and spatial evolution of Ca^0. The inset shows the spectrum obtained at the optimum experimental conditions i.e. ΔX = 0.05mm and ΔT = 800ns.

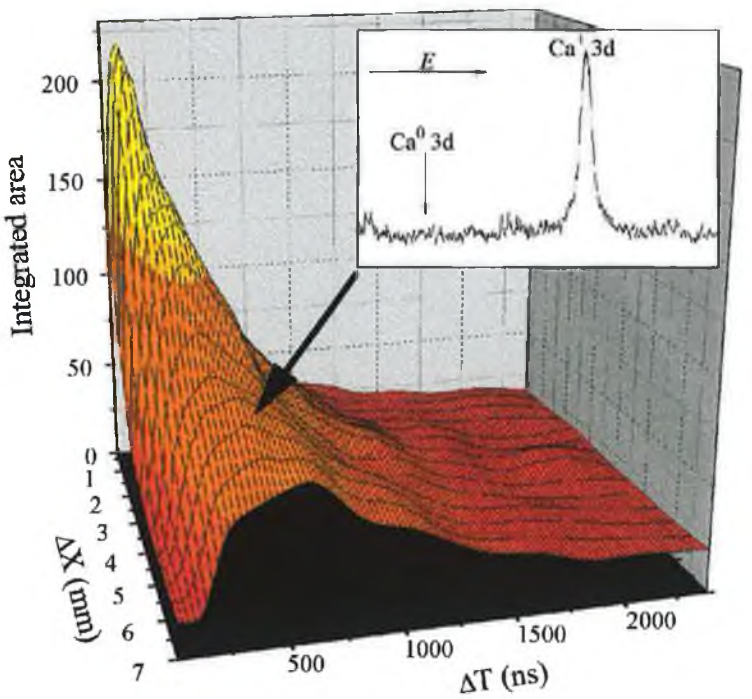

Figure 3.18 : The temporal and spatial evolution of Ca^{+}. The inset shows the spectrum obtained at the optimum experimental conditions i.e. ΔX = 6mm and ΔT = 500ns.

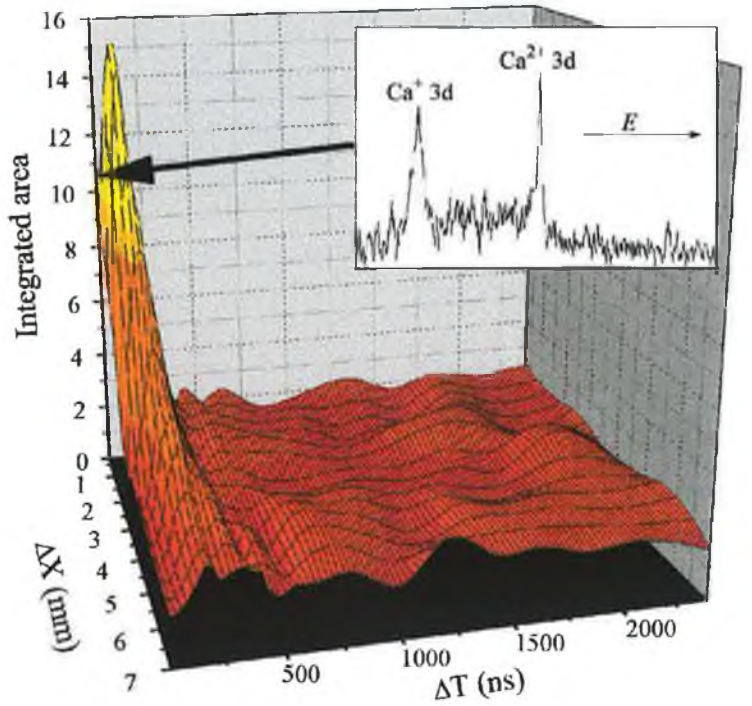

Figure 3.19 : The temporal and spatial evolution of Ca^{2+}. The inset shows the spectrum obtained at the optimum experimental conditions i.e. ΔX = 0.3mm and ΔT = 20ns.

Nd:YAG laser was line focussed via a cylindrical lens (f~10cm) to form our absorbing calcium plasma. The background tungsten plasma was created using a second Nd:YAG (~760mJ) focussed via a spherical lens (f~10cm).

For Ca^{2+}, a CEMA setting of 27" was required. This also allowed the simultaneous recording of the change in strength of the Ca^{+} 3d resonance. Much the same procedure was followed for Ca^{2+} except that owing to the more energetic and short-lived nature of Ca^{2+} ions, a greater number of ΔT settings were used with emphasis placed on obtaining a greater density of points at shorter time delays (ΔT). Hence, the matrix was 14x21 in dimension. The resultant spatio-temporal maps for Ca^{0}, Ca^{+} and Ca^{2+} are shown in figures 3.17, 3.18 and 3.19 respectively. Comparison of figures 3.17, 3.18 and 3.19 reveals that the population of each species peaks at different stages of the plasma expansion.¶ Thus, for ΔX = 0.05mm‡ and ΔT = 800ns, the dominant ion stage in the plasma is Ca^{0}, for ΔX = 6mm and ΔT = 500ns, the dominant ion stage is Ca^{+} and for ΔX = 0.3mm and ΔT = 20ns, the population of Ca^{2+} ions is optimised. It is interesting to note that the evolution of each species is independent of the incident laser energy used to create the target plasma. This is shown in figure 3.20 where we show a superposition of two Ca^{+} spatio-temporal maps. The green and blue maps refer to calcium plasmas created by a Nd:YAG of energy = 750mJ and energy = 200mJ respectively. Both were taken by tracking the Ca^{+} 3d resonance across the range of ΔX and ΔT parameters discussed above. Both maps are seen to have almost identical profiles, the rate of Ca^{+} population decay with increasing ΔX and ΔT the same. However, as one can see, for any given pair of ΔX and ΔT parameters, the blue map indicates a much lower Ca^{+} population as the population referred to in the green map was initially larger than that referred to in the blue. Although not shown here we have made similar observations for Ca^{0} and Ca^{2+}. These maps are therefore only meaningful for the determination of relative species populations

---

¶ The vertical scales are not directly comparable as each transition has a different oscillator strength.

‡ ΔX = 50μm only has meaning when the method by which ΔX = 0 was determined is given. In this work ΔX = 0 was taken to correspond to the point at which the continuum background just started to drop as a result of the target beginning to block the spectrometer's view of the source. It should also be noted that the micrometer screw controlling ΔX had an accuracy of 10μm.

provided the same laser energy is used in the generation of each map.

In the insets of figures 3.17, 3.18 and 3.19, we show the observed spectrum for each set of optimum experimental parameters. We see that it was not possible to completely eliminate the presence of Ca^+ from the Ca^0 spectrum, some small trace of the Ca^+ 3d resonance remaining. For Ca^+, the optimum conditions achieved excellent ion stage separation with not even the merest hint of the Ca^0 resonance apparent. With the Ca^{2+} spectrum, the presence of the ubiquitous Ca^+ ions could not be fully avoided. As the use of a cylindrical lens for the calcium plasma produced insufficient densities of Ca^{2+} ions, a spherical lens (f~10cm) was later installed which facilitated better results. The optimum conditions for a clean Ca^{2+} photoabsorption spectrum with the spherical lens in place were $\Delta X = 0.8$mm and $\Delta T = 45$ns. However, the use of the spherical lens to achieve

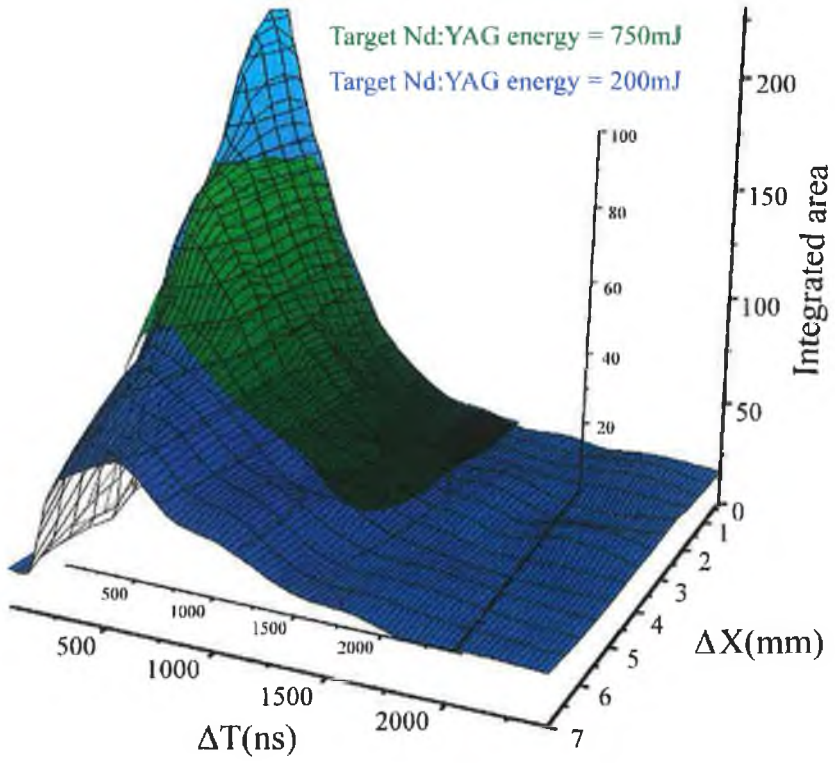

Figure 3.20 : The spatio-temporal evolution of Ca^+ where the green plot was mapped using a 750mJ Nd:YAG to create the calcium plasma and the blue plot mapped using a 200mJ Nd:YAG. The same range of ΔX and ΔT values were used in both cases. The green map is superimposed on the blue to illustrate the profile and thus, population decay, similarities. Note that during the interval between the taking of these two plots, mechanical slippage (see section 2.2) has led to the Ca^+ 3d resonance appearing across different pixels despite being at the same CEMA setting. Hence, the disparity in integrated area scales.

a higher power density on target coupled with the target's close proximity to the optic axis meant that calcium emission from the plasma core was also imaged. To counteract this, the target Nd:YAG was reduced in energy from 201mJ to ~90mJ, the emission count falling to zero but Ca^{2+} populations remaining strong.

The resulting spectra, obtained with the aid of our spatio-temporal maps, are shown in figure 3.21 where (a) shows the Ca^{0} photoabsorption spectrum, (b) the Ca^{+} photoabsorption spectrum, (c) the Ca^{2+} photoabsorption spectrum having used a cylindrical lens to generate the calcium plasma and (d) the Ca^{2+} photoabsorption spectrum, this time the result of using a spherical lens for our absorbing plasma. The experimental parameters for all four spectra were as described above. Each spectrum was obtained by using six CEMA settings along the Rowland circle (25.9→29.4") with a large overlap, due to the 0.7" increment, ensuring that absorption levels were seen to be consistent from setting to setting. At each CEMA setting, the spectrum obtained was the average result of a total of nine independent spectra, each the accumulation of five I and I_0 scans. It is clear that the Ca^{+} spectrum in figure 3.21(b) is free from cross contamination due to other ion stages. This is verified by the complete absence of the Ca^{0} 3d resonance at 31.4eV and the fact that although there is a feature in the Ca^{+} spectrum at 34.6eV, it is highly unlikely that it is due to the Ca^{2+} 3d resonance, the Ca^{2+} ions long since decayed at the ΔX and ΔT parameters required for Ca^{+}. With cross contamination of ion species now clearly not responsible for the anomalous features between 29and 32eV, we are left with only two alternatives. Either the features are the result of Ca^{0} or Ca^{+} excited state transitions or they are due to impurities in our calcium target material. The latter of these possibilities was explored by obtaining a typical purity analysis for the calcium ingot used, this having been purchased from Johnson Matthey PLC. The suppliers report a calcium metal purity of 99%, the remaining 1% predominantly due to nitrogen with trace amounts of manganese (0.0208%), silicon (0.0023%), copper (0.001%), Iron (0.0171%), magnesium (0.37%) and aluminium (0.175%), also being present. With such negligible quantities of foreign material present in our sample, it is very unlikely that transitions arising from these materials are present in our spectra. This is further supported by the absence in our Ca^{+} spectrum of any of the strong transitions in N, Mg and Al, listed in Kelly's tables (1987).

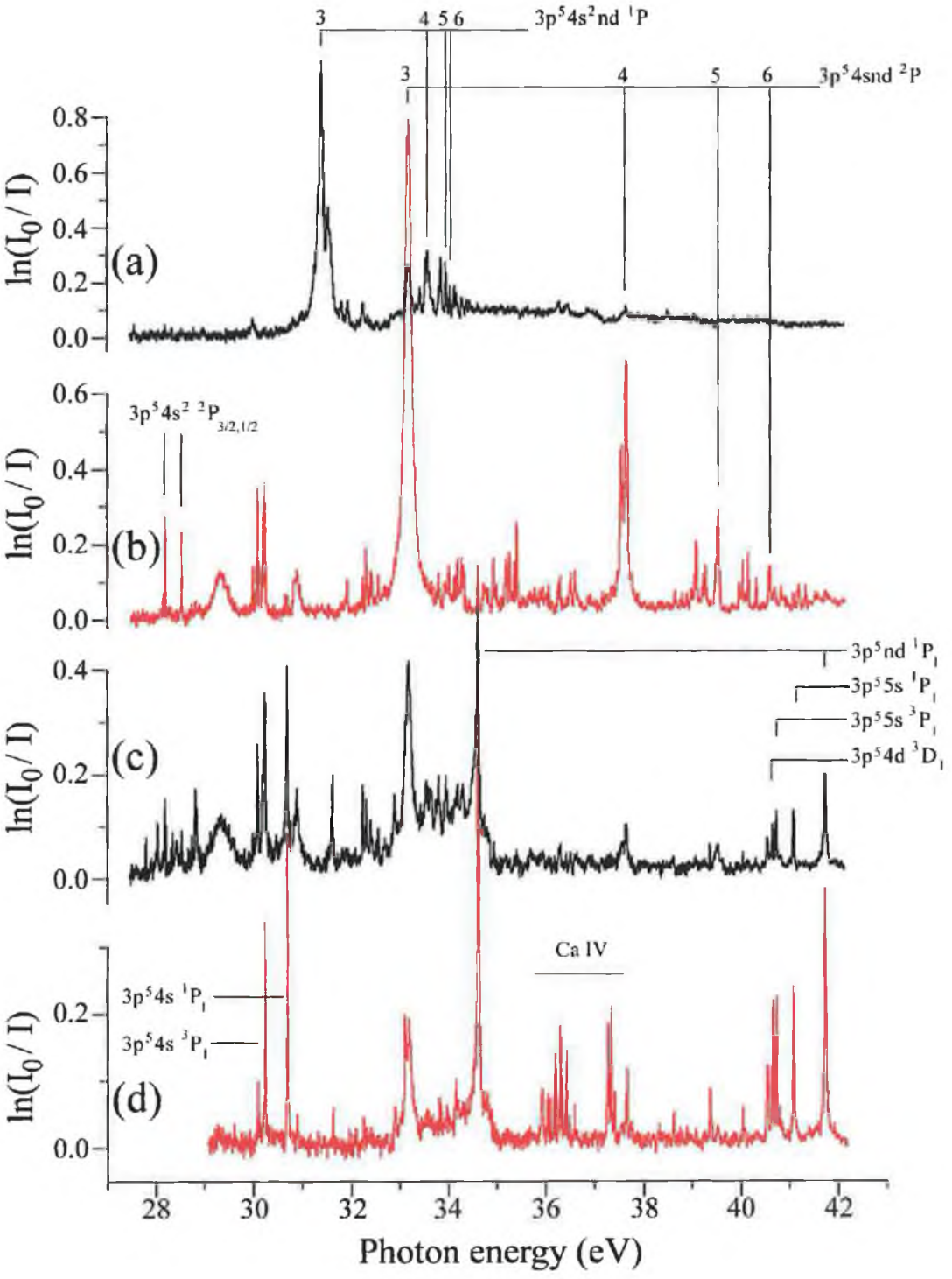

Figure 3.21 : The first three members of the Ca isonuclear sequence in photoabsorption where (a) is Ca^0 (ΔX=0.05mm, ΔT=800ns, cylindrical lens), (b) is Ca^+ (ΔX=6mm, ΔT=500ns, cylindrical lens), (c) is Ca^{2+} (ΔX=0.3mm, ΔT=20ns, cylindrical lens) and (d) is Ca^{2+} (ΔX=0.8mm, ΔT=45ns, spherical lens). Note that the identification of Ca IV resonances has been done using the tables of Kelly (1987).

3.3.2. Evidence for metastable Ca^+ $3p^63d$ transitions

As mentioned in section 3.1.2, Gottwald et al (1997) have recently interpreted structure in their electron-ion coincidence spectra as arising from the excited $3p^63d$ states of Ca^+. Knowing the Ca^+ 3d states to lie 1.7eV above the Ca^+ 4s ground state (Moore 1949), they interpreted a strong resonance at ~31.8eV as being the $3p^63d \rightarrow 3p^53d4s\ ^2P$ transition by simply subtracting 1.7eV from the known energy of the $3p^64s \rightarrow 3p^53d4s\ ^2P$ 'giant' resonance at 33.2eV. Similarly, peaks at 32.4eV and ~32.7eV were assigned to $3p^63d \rightarrow 3p^53d4s\ ^2D$ and ^2F transitions. However, it has recently been revealed in a private communication (Gottwald 1998), that the data presented in their 1997 paper suffered from energy calibration uncertainties, both relative and absolute, of ~±0.1eV. They now believe, after a recent energy recalibration, that the strong peak in their data, originally placed at 31.8eV, actually lies at 31.6eV. This gives further support to their $3p^53d4s\ ^2P$ designation and means better agreement with our DLP results. Indeed, comparing our data with the extended and revised (but as yet unpublished) spectrum from Gottwald, in figure 3.22, we see immediate agreement, not only for the line at 31.6eV, which we see as two lines at 31.6 and 31.63eV, but also for structures observed by Gottwald at ~28.2, ~29, ~30.2, ~30.9, ~32.4 and ~32.7eV.

Owing to the hot and dense nature of laser produced plasmas, it is not unexpected that, through various collisional and recombination processes, excited state atoms and ions are present in non-negligible quantities (Mosnier et al 1994). Moreover, with lifetimes of the order of 1 second (in the absence of collisions) (see section 3.1.2.), we might expect Ca^+ 3d states to be particularly prevalent. With regard to DLP experimentation, empirical evidence suggests that excited state atoms and ions are present under similar conditions to those favouring the presence of the next highest ion stage. We would therefore expect excited Ca^+ 3d transitions to reveal themselves under DLP conditions suited to capturing Ca^{2+} transitions and accordingly figure 3.22 (b) and to a lesser extent (c), having both been taken under conditions promoting Ca^{2+} transitions, are the spectra to which we mostly refer when drawing comparisons with the data of Gottwald (figure 3.22(d)).

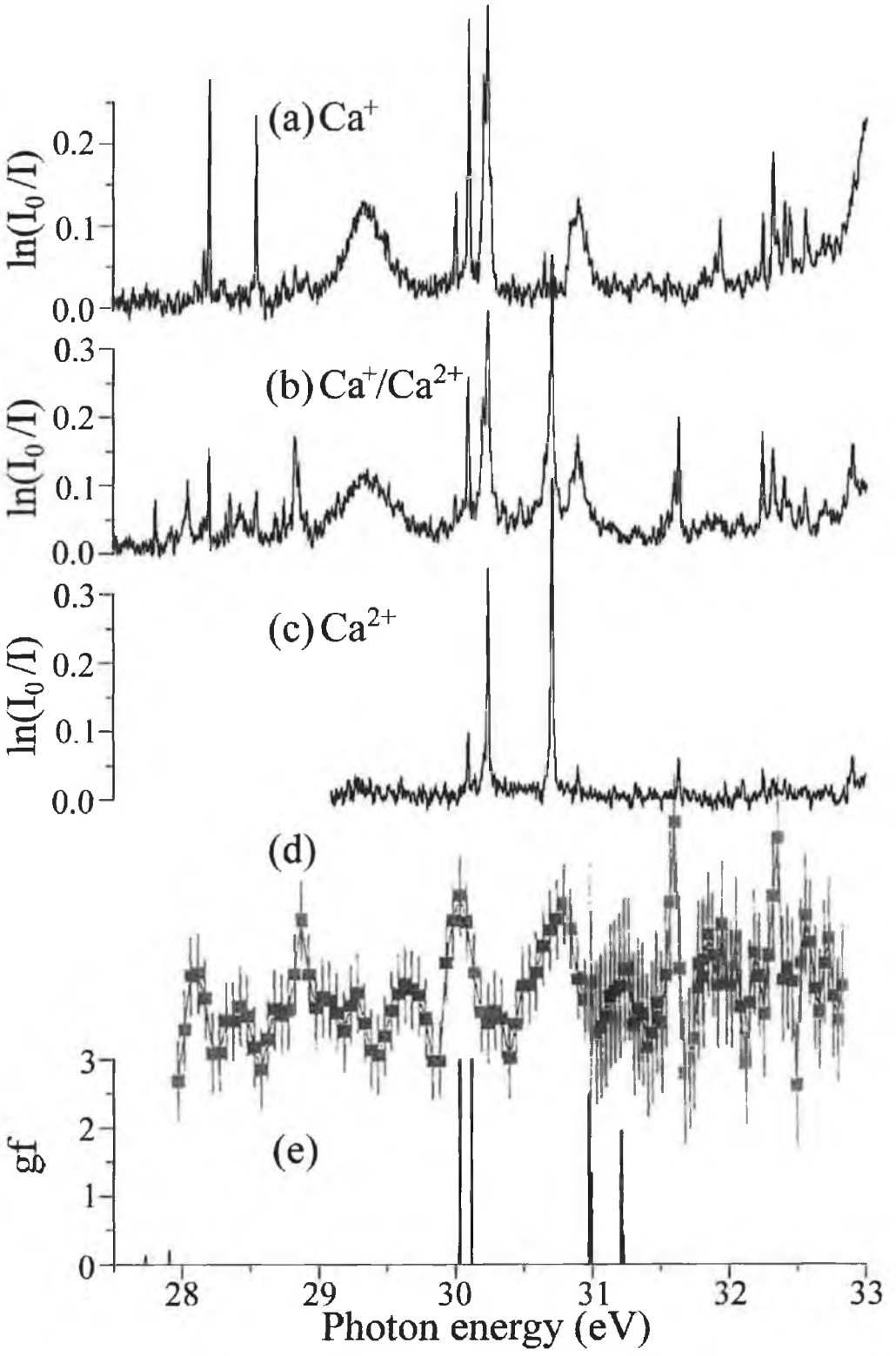

Figure 3.22 : The region of suspected Ca^0 and Ca^+ excited state transitions where (a), (b) and (c) are the DLP spectra as seen in figure 3.21 (b), (c) and (d) respectively, (d) is the Ca^+ 3d spectrum of Gottwald (1998) and (e) the $3p^63d \rightarrow 3p^53d^2$ predictions of Hansen and Quinet (1996).

In table 3.2, we show, in red, the measured energies of features to which we have attributed a Ca^+ $3p^63d$ origin. We also indicate the figure from which the measurement was taken and draw comparison with the Ca^+ 3d features of Gottwald (1998) and the predicted $3p^63d \rightarrow 3p^53d^2$ transitions of Hansen and Quinet (1996). For the line at 28.35eV, we infer a $3p^53d^2$ assignment by subtracting 1.7eV from the limit proposed by Mansfield and Newsom (1977). The pair of lines at ~28.83eV are also assigned to $3p^53d^2$, again by subtracting the 1.7eV difference between 4s and 3d initial states, but this time from the Ivanov and West (1993) assigned Ca^+ $3p^53d^2$ $^2P_{1/2}$ transition at 30.31eV. Our measured energies for this feature are also in agreement with the strong peak observed by Gottwald (1998). At 30.1eV, we see a sharp peak in both figures 3.22 (b) and (c) to which we also propose a Ca^+ $3d^53d^2$ designation as it is in agreement with the broad structure observed by Gottwald (1998) at ~30.2eV and the strong $3p^53d^2$ (^3F) ^2F predictions of Hansen and Quinet (1996) in the 30 to 30.1eV region. It may be noticed that we also list a feature observed in figure 3.22(a) at 30.11eV which we have associated with Ca^+4s. The experimental parameters corresponding to figure 3.22(a) are ΔT = 500ns and ΔX = 6mm. Therefore, it is highly unlikely that the suspected Ca^+ excited state transition at 30.1eV, seen for a much shorter ΔX and ΔT in figures 3.22 (b) and (c), could be so intense in figure 3.22 (a). We therefore suggest that the Ca^+ excited state feature (seen in figures 3.22 (b) and (c)) has been replaced by another line (in figure 3.22 (a)), of the same energy but which is of Ca^+4s origin. Further support for this is obtained by examining a time evolution of features in the 28.5 to 32eV region. In figure 3.23, we have plotted spectra taken at a CEMA setting of 29" having kept ΔX constant and having used a variety of ΔT values which ranged from 25ns to 1000ns. Colour has been used to help track the evolution of each species where features of Ca^+3p^64s, Ca^+3p^63d, Ca^03p^64s3d and $Ca^{2+}3p^6$ origin are marked in green, red, blue and yellow, respectively. As only one significant $Ca^03p^64s^2$ feature exists in this region ($3p^54s^23d$ ^1P @ 31.4eV), this species was not assigned a colour. In cases where features originating from one or more species are thought to be overlapped, a coloured dot signifies the species of lesser presence.

Using the spectra in both figure 3.22 and 3.23, we see that features at 30.11 and 30.27eV are, at earlier times, composed of a superposition of features from both Ca^+ and Ca^{0*}

Photon energy (DLP) (eV) *	Figure 3.22	Assignment	Gottwald et al (1998) (eV)	Hansen and Quinet (1996) (eV)
28.04	b	?		
28.20	a,b	Ca^+	28.2	
28.35	b	Ca^{+*} $3p^53d^2$ †		
28.55	a,b	Ca^+		
28.83	b	Ca^{+*} $3p^53d^2$ ¶		
28.86	b	Ca^{+*} $3p^53d^2$ ¶	29	
29.34	a,b	Ca^{0*} $3p^5(3d^3\ ^3D_2)\ ^1P_1$ § $3p^5(4p^2\ ^1D)(^2P)3d\ ^3D_1$ § $3p^5(3d^2\ ^1S)(^2P)4s\ ^1P_1$ § $3p^54s^24d\ ^3P_1$ § $3p^5(3d^3\ ^4P)\ ^3D_1$ §		
30.01	a,b	Ca^+		
30.10	b,c	Ca^{+*} $3p^53d^2\ (^3F)\ ^2F_{5/2}$ #		30.03
30.11	a,b	Ca^+		
30.21	b,c	Ca^{+*} $3p^53d^2(^3F)\ ^2F_{7/2}$ ‡#¶	30.2	30.12
30.22	a,b	Ca^{0*}		
30.25	b,c	Ca^{2+}		
30.25	a,b	Ca^{0*} $3p^5(4p^2\ ^1D)(^2D)4s\ ^3D_1$§		
30.27	a	Ca^+		
30.48	b	Ca^{+*}		
30.66	b,c	Ca^{+*} $3p^53d^2(^3F)\ ^2D$ ‡#¶		30.97
30.71	b,c	Ca^{2+}		
30.90	b,c	Ca^{+*} $3p^53d^2\ (^3P)\ ^2P$ ‡#	30.9	31.21
30.90	a	Ca^{0*} $3p^5(4p^2\ ^1S)\ (^2P)4s\ ^1P_1$ § $3p^5(3d^2\ ^1S)5s$ §		
31.60	b	Ca^{+*} $3p^54s3d\ ^2P$ ‡$	31.6	
31.63	b,c	Ca^{+*} $3p^54s3d\ ^2P$ ‡$		
31.90	a	Ca^+		
31.94	a	Ca^+		
32.25	b,c	Ca^{+*}		
32.25	a	Ca^+		
32.32	a	Ca^+		
32.32	b	Ca^{+*} $3p^53d4p$ ¶‡		
32.36	a	Ca^+		
32.40	b	Ca^{+*} $3p^53d4s\ ^2D$ ‡$	32.4	
32.41	a	Ca^+		
32.44	a	Ca^+		
32.45	a	Ca^+		
32.52	b	Ca^{+*} ‡		
32.56	b	Ca^{+*} ‡		
32.56	a	Ca^+		
32.71	b	Ca^{+*} $3p^53d4s\ ^2F$ ‡$	32.7	
32.88	b	Ca^{+*} ‡		
32.90	b,c	Ca^{+*} ‡		

* ±0.02eV
† from Mansfield and Newsom (1977) Ca^0 limit (-1.7eV)
¶ from Ivanov and West (1993) Ca^* assignment (-1.7eV)
‡ adding 1.7eV yields the energy of a Ca^+ line
§ from Mansfield and Newsom (1977) Ca^0 assignment (-2.52eV (^3D) or -2.71eV (^1D))
# assigned using Hansen and Quinet's predictions
$ assigned from Gottwald at al (1997)

Table 3.2 : Ca^0 $3p^64s3d$ and Ca^+ $3p^63d$ excited state transitions between 28 and 33eV. See text for further details.

and/or Ca^{+*}. This is particularly clear in figure 3.23 for spectra taken for ΔT's up to and including 300ns but for ΔT's $\geq$ 350ns, these two features become almost entirely due to $Ca^{+}4s$. The evidence for this comes from (a) the relative weakness of the once dominating Ca^{0*} features (indicated in blue) at ~29.34 and 30.9eV (to be discussed in the next section), (b) the fact that these two features have maintained relative intensity with the known $Ca^{+}4s$ transition at 28.55eV and (c) the fact that no Ca^{+} excited state features are in evidence elsewhere in the spectra. Hansen and Quinet (1996) predict strong $3p^53d^2$ transitions at 30.03 and 30.12eV. As mentioned earlier, our measurements suggest that there is a feature at 30.1eV which is of $3p^53d^2$ origin. Assuming Hansen and Quinet's spin orbit splittings to be correct and assuming the line at 30.1eV to be their $3p^63d\ ^2D \rightarrow 3p^53d^2\ (^3F)\ ^2F_{5/2}$ transition, we should therefore expect the spin orbit $^2F_{7/2}$ partner to lie at an energy of 30.19eV (30.1 + 0.09eV) and indeed we see a feature at 30.21eV which through the time evolution of figure 3.23 and Ivanov and West's Ca^{+} assignments, we are confident is of $Ca^{+}3p^63d \rightarrow 3p^53d^2$ origin. We have thus assigned the lines at 30.1 and 30.21eV according to Hansen and Quinet's designations (see table 3.2). In relation to the line at 30.25eV (see table 3.2), we see from figures 3.22 and 3.23 how at very early times, this line is the $Ca^{2+}\ 3p^54s\ ^3P_1$ transition but as Ca^{2+} ions recombine quickly, the fact that this line is still present at much later times indicates that the Ca^{2+} line has been replaced by a Ca^{0} excited state transition. The lines at 30.48 and 30.66eV have been identified with the aid of Ivanov and West's Ca^{+} assignments as $Ca^{+}3p^63d \rightarrow 3p^53d^2$ transitions. In figure 3.22 (b) and (c), the less energetic of the two is just discernible as a shoulder on the $Ca^{2+}\ 3p^54s\ ^1P_1$ line at 30.71eV but it becomes more distinct in figure 3.22(a) where due to the large ΔX and ΔT parameters used for this spectrum, the Ca^{2+} ions and their associated transitions have disappeared. Indeed, they are even more apparent in figure 3.23 where in further support of their $Ca^{+}3d$ assignment, they evolve in synchronisation with the other supposed $Ca^{+}3d$ features, fading into the background noise level at a ΔT of around 250ns. Another $Ca^{+}3d$ line is thought to lie at an energy of 30.9eV. The evidence for this comes from a distinct peak seen in figure 3.22 (c) which we know is not of Ca^{2+} origin. Indeed, by adding 1.7eV to the energy of this line we get 32.6eV and at this energy we have measured a Ca^{+} line (see table 3.1) which lends further support to our argument. In figure 3.22 (b) and (c), the $Ca^{+}3d$ line at 30.9eV is still present but now

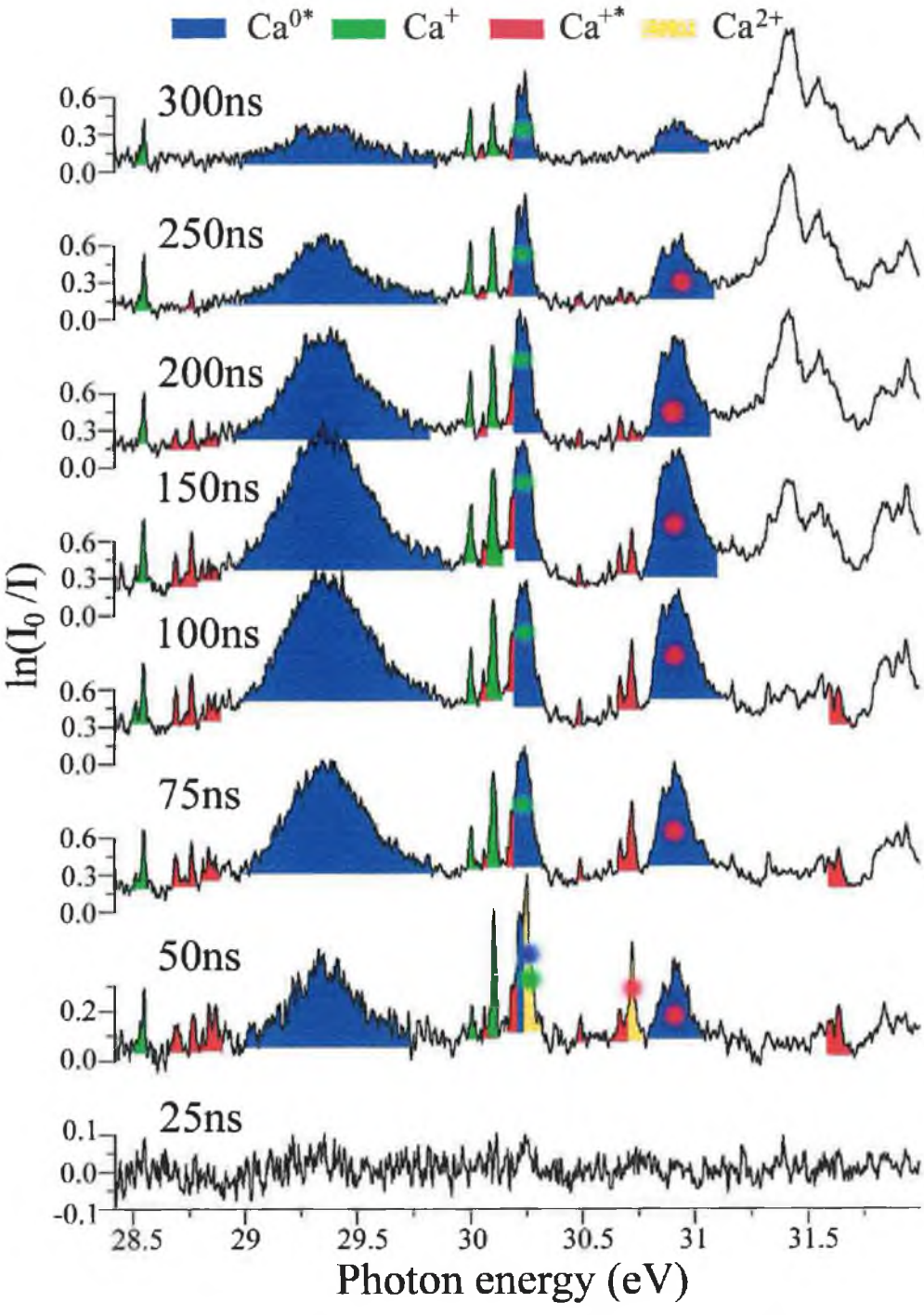

Figure 3.23 : A time evolution of Calcium photoabsorption spectra in the 28 - 32eV energy region where ΔX = 0.5mm and ΔT has been varied as indicated. Each feature has been associated with its proposed species of origin where $Ca^{+}3p^{6}4s$, $Ca^{+}3p^{6}3d$, $Ca^{0}3p^{6}4s3d$ and $Ca^{2+}3p^{6}$ transitions are indicated by green, red, blue and yellow respectively. In cases where a feature is a superposition of lines from more than one species, coloured circles indicate the minority species. Note the presence of the Ca^{0} $3p^{6}4s^{2} \rightarrow 3p^{5}4s^{2}3d$ transition(uncoloured) at 31.4eV from ΔT = 150ns onwards.

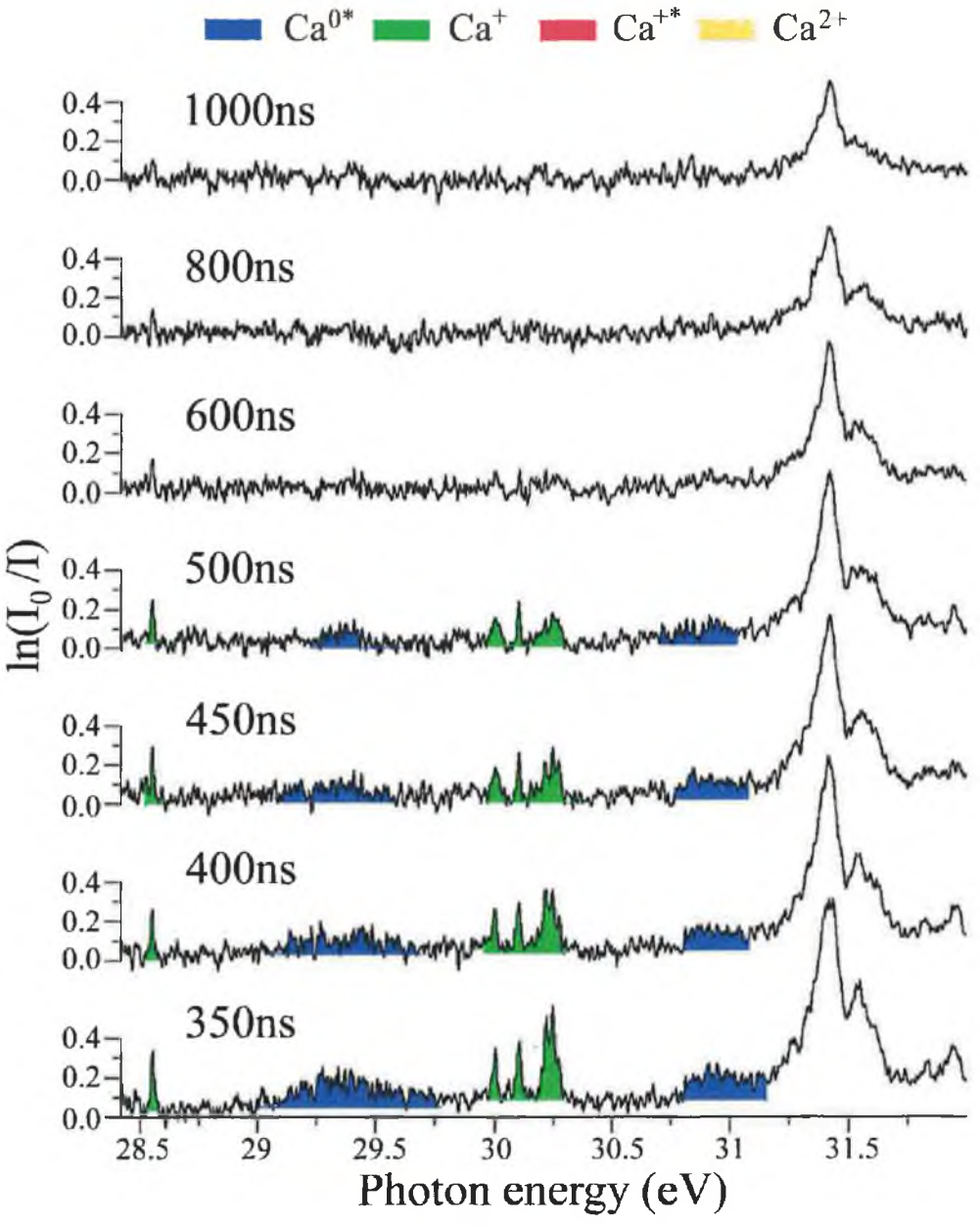

Figure 3.23 (continued).

completely overwhelmed by a broad $Ca^0 3p^6 4s3d$ structure (see next section). Attempting to distinguish this $Ca^+ 3d$ line in figure 3.23, we see that it is not possible as the experimental parameters used for these spectra did not sufficiently subdue the onset of Ca^0 excited state transitions. Using the theoretical calculations of Hansen and Quinet (1996) which predict a strong pair of lines separated by 0.24eV at ~31eV, we see that if

we take our measured $3p^53d^2$ line at 30.66eV and add 0.24eV, we get 30.9eV. Thus, according to Hansen and Quinet (1996) our measured lines at 30.66 and 30.9eV are the $3p^63d\ ^2D \rightarrow 3p^53d^2(^3F)\ ^2D$ and $3p^63d\ ^2D \rightarrow 3p^53d^2(^3P)\ ^2P$ transitions respectively (see table 3.2). The remaining Ca^+3d features highlighted in table 3.2 have been located by similar energy level considerations as those described above and have been assigned in accordance with the data of Gottwald (1997) and through the use of the Ca^+ assignments of Ivanov and West (1993). Finally, although an assignment was not possible in every case, we are confident that the features in figure 3.22(b) with measured energies from 31.6 to 32.9eV are also of Ca^+ 3d origin as they cannot be associated with Ca^{2+} transitions and through relative intensity and experimental parameter considerations also cannot be of Ca^+ 4s origin.

3.3.3. Evidence for transitions from $Ca^0\ 3p^64s3d$ levels

3.3.3.1 Experimental evidence

Revisiting figure 3.22, we see that the broad feature observed by DLP photoabsorption at ~29.3eV, has no equivalent in the data of Gottwald (1998). Indeed, if we re-examine figure 3.15 (a), we see that it is also not recorded in the Ca^+ photoion data of Lyon et al (1987). A similar absence of equivalent features in the data of Gottwald and Lyon et al for broad structures observed in our DLP results at ~30.2 and ~30.9eV has led us to believe that all three are the result of transitions from the same species. This conclusion is further supported in figure 3.23 where we see their relative intensities remain constant as the presence of this species ebbs and flows within the plasma as a function of time. By process of elimination, we see from a comparison of figure 3.22 (b) and (c) that these features are not of Ca^{2+} origin. Nor do they arise from Ca^+3p^63d transitions as they clearly remain appreciable in intensity long after the other Ca^+3d transitions have disappeared from the spectra (see figure 3.23). It is also apparent that they cannot be associated with Ca^+4s transitions as they are absent from the data of Lyon et al and from figure 3.23, their intensities do not scale as a function of time with the known Ca^+4s line at 28.55eV. A ground state neutral calcium association is also not possible as they are absent in the neutral calcium spectrum of figure 3.21. It is therefore reasonable to

conclude that the broad DLP features at 29.3, 30.2 and 30.9eV are the result of transitions from excited neutral calcium states, the most likely being the metastable $3p^64s3d\ ^3D$ and ^1D levels as they lie only 2.52eV and 2.71eV respectively (Moore 1949) above the $3p^64s^2$ ground state. Indeed, any neutral excited state features should be present for similar experimental conditions as those favouring the next highest ion stage i.e. Ca^+ 4s. We can see from figure 3.23, that this is the case, our broad features remaining strong in the spectra over the same ΔT range as the Ca^+4s transitions (marked in green). With our time and space DLP measurements indicating the presence of Ca^0 $3p^64s3d$ excited state transitions, we have subtracted the 2.52eV difference between these states and the $Ca^03p^64s^2$ ground state from the strongest $Ca^03p^64s^2$ transitions observed and assigned by Mansfield and Newsom (1977). Doing this, we have found a strong correlation, the levels to which transitions occur from the Ca^0 ground state also appearing to be the most likely for transitions from the Ca^03p^64s3d initial states. We list our assignments in blue in table 3.2. The very broad structure observed by DLP photoabsorption and centred at ~29.34eV, we now believe to be the result of a blend of strong transitions from Ca^03p^64s3d to $3p^53d^3$, $3p^54p^23d$, $3p^53d^24s$ and $3p^54s^24d$ levels (see table 3.2), strong transitions to these levels from the Ca^0 $3p^64s^2$ ground state having been recorded by Mansfield and Newsom for energies ranging from 31.2672 to 31.9667eV. Similarly, the feature we have measured at 30.25eV is thought to correspond to a moderately strong $3p^64s^2 \rightarrow 3p^5(4p^2\ ^1D)\ (^2D)\ 4s\ ^3D_1$ transition seen by Mansfield and Newsom at 32.761eV i.e. 30.25 - 2.52 = 30.24eV. The third broad structure measured by DLP photoabsorption and thought to be due to neutral excited states is centred at ~ 30.9eV. Mansfield and Newsom (1977) have recorded nine ground state transitions between 33.3094 and 33.6028eV. Of these only three have been identified but as the transitions at 33.5658 and 33.6028eV, assigned to $3p^54p^24s$ and $3p^53d^25s$ transitions, were very strong, we believe the major proportion of oscillator strength in our feature at 30.9eV is attributable to $Ca^03p^64s3d \rightarrow 3p^5\ (4p^2\ ^1S)\ (^2P)\ 4s\ ^1P_1$ (33.5658 - 2.71 (^1D) = 30.86eV) and $Ca^03p^64s3d \rightarrow 3p^5\ (3d^2\ ^1S)\ 5s$ transitions (see table 3.2).

3.3.3.2 Calculational evidence

To further corroborate our assignments, we have used the Cowan suite of codes to calculate the energies and oscillator strengths of transitions from the $Ca^0 3p^6 4s3d$ excited states. The expansions used for even and odd configurations are shown in table 3.3 and as can be seen we have included as many configurations as possible for both the initial and final states so that both valence and core correlations would be taken into account.

Ca^0	
Even configurations	**Odd configurations**
$3p^6 4s^2$	$3p^6 4s4p$
$3p^6 4s3d$	$3p^6 3d4p$
$3p^6 4s4d$	$3p^6 4s5p$
$3p^6 4s5s$	$3p^5 4s^2 3d$
$3p^6 4s6s$	$3p^5 4s^2 4d$
$3p^6 4p^2$	$3p^5 4s^2 5d$
$3p^5 4s^2 4p$	$3p^5 4s^2 6d$
$3p^5 4s^2 5p$	$3p^5 4s^2 7d$
$3p^5 4s^2 6p$	$3p^5 4s^2 5s$
$3p^5 3d^2 4p$	$3p^5 4s^2 6s$
$3p^5 3d^2 5p$	$3p^5 4s^2 7s$
$3p^5 3d^2 6p$	$3p^5 4s^2 8s$
$3p^5 4p5s^2$	$3p^5 3d^2 4d$
$3p^5 4p6s^2$	$3p^5 3d^2 5d$
$3p^5 4p^3$	$3p^5 3d^2 6d$
	$3p^5 4s3d^2$
	$3p^5 5s3d^2$
	$3p^5 6s3d^2$
	$3p^5 3d4p^2$
	$3p^5 4s4p^2$
	$3p^5 3d^3$

Table 3.3 : The expansions for the even and odd configurations in the calculation of gf values for transitions from the $3p^6 4s3d$ excited states of neutral calcium.

As has been pointed out by Hansen and Quinet (1996) in performing calculations for 3d metastables in Ca^+, core correlations are expected to be especially important due to the sensitivity of the 3d orbital to its surroundings. Unfortunately, no f orbitals could be included in the calculations due to computational limitations. As a result, core correlations could not be fully accounted for, especially for configurations with 3d character, and thus, our predictions show the $Ca^0 3p^6 4s3d$ transitions with the larger probabilties (gf ~3-4) to lie some 3-4 eV above where we propose they reside

Transition	λ(Å)	E(eV)	gf
$3p^6 4s3d\ (^2D)\ ^3D_1 \rightarrow 3p^5 4s^2 3d\ (^2P)\ ^3D_1$	501.895	24.70	0.099
$\rightarrow 3p^5 4s3d^2\ (^1D)\ ^3F_2$	472.492	26.24	0.116
$\rightarrow 3p^5 3d4p^2\ (^1S)\ ^3F_2$	407.338	30.44	0.143
$\rightarrow 3p^5 3d4p^2\ (^1D)\ ^3F_2$	405.397	30.58	0.719
$\rightarrow 3p^5 3d^2 5d\ (^1G)\ ^3F_2$	404.402	30.66	0.224
$\rightarrow 3p^5 3d^2 5d\ (^1D)\ ^3F_2$	400.955	30.92	0.254
$\rightarrow 3p^5 4s^2 4d\ (^2P)\ ^3F_2$	400.582	30.95	0.173
$\rightarrow 3p^5 3d^3\ (^2D)\ ^3F_2$	398.844	31.09	0.274
$\rightarrow 3p^5 5s3d^2\ (^3P)\ ^3D_2$	398.649	31.10	0.099
$\rightarrow 3p^5 3d^3\ (^2D)\ ^1D_2$	398.384	31.12	0.200
$\rightarrow 3p^5 3d^3\ (^2D)\ ^1D_2$	397.845	31.16	0.262
$\rightarrow 3p^5 3d^3\ (^2D)\ ^1D_2$	397.407	31.20	0.178
$\rightarrow 3p^5 3d^2 4d\ (^1G)\ ^1D_2$	394.452	31.43	0.129
$\rightarrow 3p^5 4s^2 5d\ (^2P)\ ^3P_2$	394.216	31.45	0.303
$\rightarrow 3p^5 3d^2 4d\ (^3P)\ ^3D_2$	394.141	31.46	0.381
$\rightarrow 3p^5 4s4p^2\ (^3P)\ ^3P_0$	382.567	32.41	0.141
$\rightarrow 3p^5 3d4p^2\ (^1D)\ ^1S_0$	373.801	33.17	0.235
$\rightarrow 3p^5 4s4p^2\ (^3P)\ ^3S_1$	373.525	33.19	0.102
$\rightarrow 3p^5 4s3d^2\ (^3P)\ ^3P_0$	371.833	33.34	1.047
$\rightarrow 3p^5 4s3d^2\ (^3P)\ ^3P_1$	371.825	33.34	0.334
$\rightarrow 3p^5 3d^2 5d\ (^1S)\ ^1P_1$	366.293	33.85	0.184
$\rightarrow 3p^5 3d^2 5d\ (^1S)\ ^3F_2$	366.03	33.87	0.182
$\rightarrow 3p^5 4s3d^2\ (^3F)\ ^3D_2$	365.823	33.89	1.102
$\rightarrow 3p^5 4s3d^2\ (^3F)\ ^3D_1$	365.705	33.90	3.467
$\rightarrow 3p^5 3d^2 5d\ (^1S)\ ^3P_1$	365.309	33.94	0.429
$\rightarrow 3p^5 3d^3\ (^2F)\ ^3D_1$	361.607	34.29	0.148

Table 3.4 : The calculated wavelengths, transition energies and oscillator strengths (gf) for the $3p^6 4s3d\ ^3D_1$ transitions of neutral calcium. Only gf values ≥ 0.1 are shown..

in our measurements. Following the arguments put forward by Hansen and Quinet (1996), we have used a 15% scaling on the electrostatic integrals. A representative sample of our results showing only $3p^6 4s3d\ ^3D_1$ transitions is shown in table 3.4. Many strong transitions are predicted but of particular interest is the fact that the most probable transitions involve the levels which, through the data and assignments of Mansfield and Newsom (1977), we have inferred to be responsible for our suspected $Ca^0 3p^6 4s3d$ structure at 29.3, 30.25 and 30.9eV. Despite, as Hansen and Quinet (1996) have pointed out, that if the energies are incorrectly determined, there is a non-negligible probability that the f-values are also inaccurate, the results shown in table 3.4 are judged to further support our assignments, albeit tentative, for the Ca^0 excited state transitions shown in table 3.2.

Conclusions

In this chapter, we have provided an up-to-date survey of XUV studies on the first three members of the calcium isonuclear sequence i.e. Ca^0, Ca^+ and Ca^{2+}, with particular attention having been paid to the 3p region of excitation. We have been particularly keen to emphasise the effect of 3d wavefunction collapse and its ramifications both to experimental and theoretical investigations. Applying the Dual laser plasma technique to calcium in the 3p region, we have exploited the DLP system's high resolution capability and resolved many new Ca^+ features and through comparison with previous work in this region we have also been successful in extracting, what we consider to be more accurate absolute cross sections. Through careful attention to both instrumental effects and plasma opacity and by using the DLP system's inherent ability to separate ion stages, we have tentatively measured and assigned excited state transitions for both neutral ($3p^64s3d$) and singly ionised ($3p^63d$) calcium. In total, we have associated 18 features with the Ca^+3p^63d excited state and 4 features with the Ca^03p^64s3d excited state. Many of these excited state transitions have been observed for the first time.

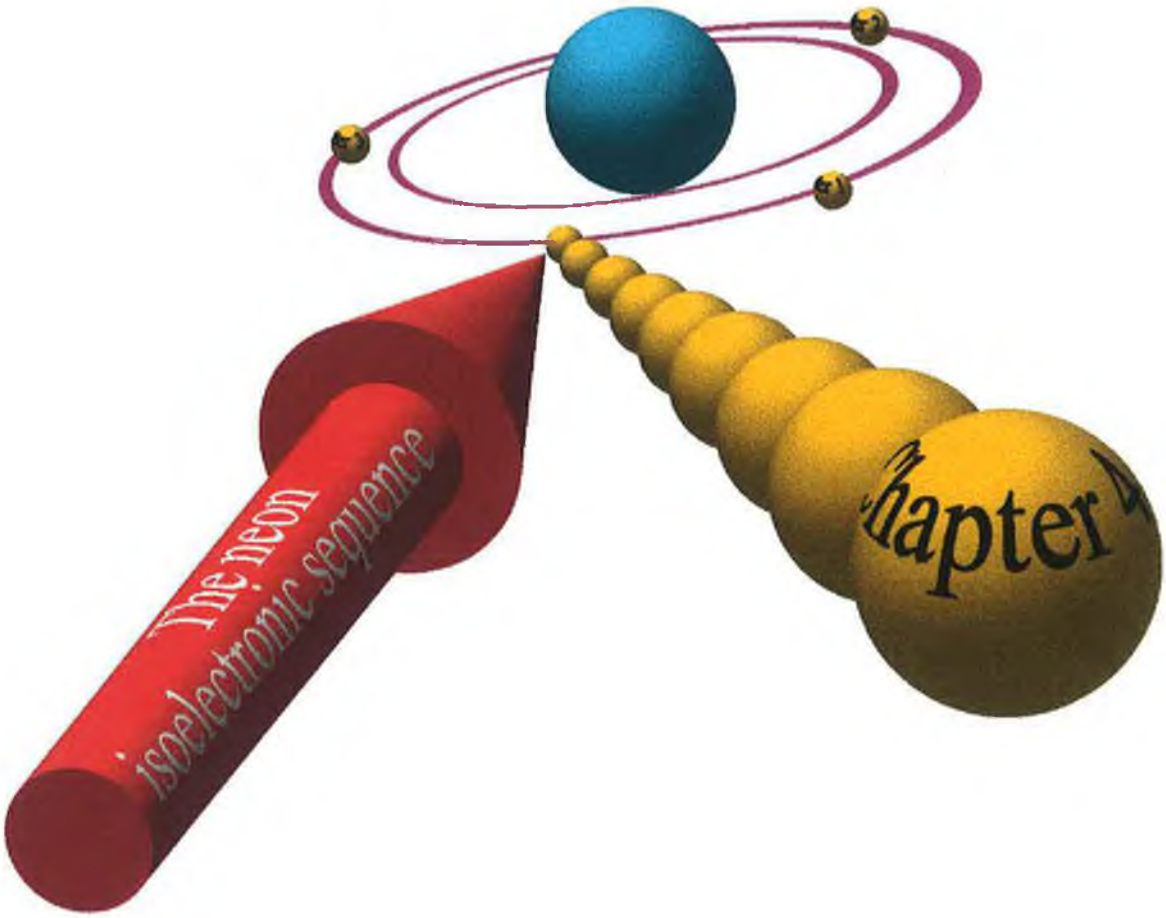
Chapter 4
The neon isoelectronic sequence

Introduction

Photoionisation of the neon isoelectronic sequence is of fundamental importance as it deals with the response to ionising radiation of the simplest noble gas structure with multiple shells ($1s^2 2s^2 2p^6$). It is also of particular interest owing to the significant cosmic abundance of Ne, Na^+, Mg^{2+}, Al^{3+}, Si^{4+}, S^{6+}, Ar^{8+}, Ca^{10+} and Fe^{16+} (Hibbert and Scott 1994, Shull 1993) and thus, there is a constant demand in astrophysics for the greater provision of atomic data concerning these elements particularly with regard to energy levels, wavelengths and f-values (Morton 1993). From a fundamental point of view, the study of positive ions in Isoelectronic, Isonuclear and Isoionic sequences provides excellent insight into the dynamic interplay between many-body electron-electron correlations, electron-nucleus interactions and relativistic effects. Furthermore, the neon Isoelectronic sequence has in recent times become the subject of intense experimental activity due to its members possessing an almost unique suitability for X-ray laser systems based on electron-collisional pumping (see Appendix 1). Fuelled by such motivations, we have devoted this chapter to an experimental study of the first five members of the neon sequence. Our primary interest has been the experimentally neglected $2s^2 2p^6 \rightarrow 2s2p^6np\ ^1P_1$ series but we also present measurements on the discrete $2s^2 2p^6 \rightarrow 2s^2 2p^5 ns$, nd series of each member. Our experimental measurements are supported by Hartree-Fock calculations which were performed using the Cowan suite of atomic codes. We present new measurements for some of the higher $2s^2 2p^5 ns$, nd series members and, in the first systematic experimental study of the 2s region in Ne-like ions, present Fano parameters for the low lying members of the $2s2p^6np\ ^1P_1$ series which, in the case of Na^+, Mg^{2+},Al^{3+} and Si^{4+}, have not previously been recorded. Through our measurements, we present evidence to suggest that the Si^{4+} $2s2p^6 3p\ ^1P_1$ resonance profile appears asymmetric as a result of 'forced autoionisation'. We also study the photoionisation cross section of neon sequence members near threshold and show that the behaviour for Si^{4+} is anomalous due to the movement of the $2s2p^6np$ inner shell resonances below threshold with increasing atomic number, Z.

4.1 Background

4.1.1 Ne^0 in the region of 2s excitation

Experimental studies

In 1967, Codling et al measured, with 12meV resolution, the VUV absorption spectrum of neutral neon in the 44 to 64eV spectral range. In this landmark study, Codling et al used a 3m grazing incidence spectrograph and synchrotron light as a background source to clearly resolve a strong series of $2s^22p^6\ {}^1S_0 \rightarrow 2s2p^6(^2S)np\ {}^1P_1$ (n=3-12) one electron asymmetric resonances. They were also successful in the identification of rich structure involving series arising from two electron excitation of the 2p subshell. Prior to this, none of these resonances had been observed as previous studies had concentrated on the shape of the continuous background (Ederer and Tomboulian 1964). More recently, Aleksandrov et al (1983) used photoabsorption measurements to derive the oscillator strength, radiative lifetime and linewidth of a variety of lines in the 16-62eV region including the n=3-6 members of the inner-shell $2s2p^6np\ {}^1P$ series. Chan et al (1992) captured low resolution (ΔE ~1eV) and high resolution (ΔE = 0.098eV) electron energy loss spectra for neon in the 16-250eV region and calculated both the photoionisation cross section over the entire region and the absolute oscillator strength for many discrete transitions including the $2s2p^6np$ (n=3-6) and $2s^22p^43lnl'$ autoionising resonances. Photoion techniques have also been applied to the 2s region of neutral neon. In 1992, as part of a performance rating on the newly installed SX700/II grazing incidence plane grating monochromator at BESSY, Domke et al were able to resolve some 14 members (n=3-17) of the $2s2p^6np\ {}^1P$ series. Quantitatively fitting their Rydberg series results, a monochromator resolution of 5.5meV at $h\nu$ = 48eV was determined. However, in the most detailed survey of the neon 2s region to date, Schulz et al (1996) bettered the resolution achieved by Domke and co-workers, quoting a resolution of ~3meV in the 45-53eV photon energy range. With this superior resolving capability, they were successful in the measurement of $2s2p^6np\ {}^1P$ series members up to n=20. They also turned their attention to the rich and overlapping doubly excited $2s^22p^43snp$ and $2s^22p^43pnl$ (l=s,d)

series, successfully identifying many higher members which were previously unresolved.

Indeed, interest in these doubly excited resonances has provoked a number of recent photoelectron investigations as the simultaneous excitation of two atomic electrons by a single photon reveals higher-order, inter-electron correlation effects and provides a more stringent testing ground for the accuracy of existing theoretical and computational methods. Wills et al (1990) investigated the selective decay of these levels into energetically accessible ionic states in the 50-60eV range, a two dimensional scanning technique allowing either photoelectron spectra (fixed photon energy) or constant ionic state (CIS) spectra (fixed binding energy) to easily be produced. In so doing, they were able to observe behaviour not usually observable unless most of the constituent ion states are well resolved. More recent photoelectron studies employed up to three time of flight (TOF) spectrometers to angularly resolve the outgoing electrons from the decay of the $2s2p^6np$ (n=3-5) autoionising resonances and the $2p^4(^3P)3s(^2P)3p\ ^1P$ doubly excited resonance (Langer et al 1997). Using the third generation synchrotron light source at the Advanced Light Source (ALS) in Berkeley, to achieve both higher resolution (18meV) and higher photon flux, Langer et al (1997) were successful in measuring both the partial cross sections and the angular distribution parameter (β) of these resonances. Their results showed that as predicted by Fano (1961, 1965), the resonance cross sections show no strong n dependence of the q and ρ parameters and that the width Γ varies as the quantum defect theory predicts (see section 1.3).

While it has been shown that for the Ne $2s2p^6np\ ^1P$ configuration, LS coupling is dominant (Codling et al 1967), early indications, through the observation of fine structure splittings, were that for the doubly excited $2p^4(^3P)3s(^2P_{1/2,3/2})nl$ resonances, LS coupling did not hold. Schulz et al (1996), with higher resolution than previous experiments, could resolve the fine structure splitting with even greater detail and concluded that in contrast to low-lying Rydberg series members, highly excited Rydberg states are better characterised by either jj or jK coupling. In a very recent study, Wills et al (1998) followed up on these initial observations of Codling et al and Schulz et al and used two-dimensional photoelectron spectra (2DPES) to conclusively demonstrate the breakdown of LS coupling for, in particular, the $2p^43pns,nd$ doubly excited resonances

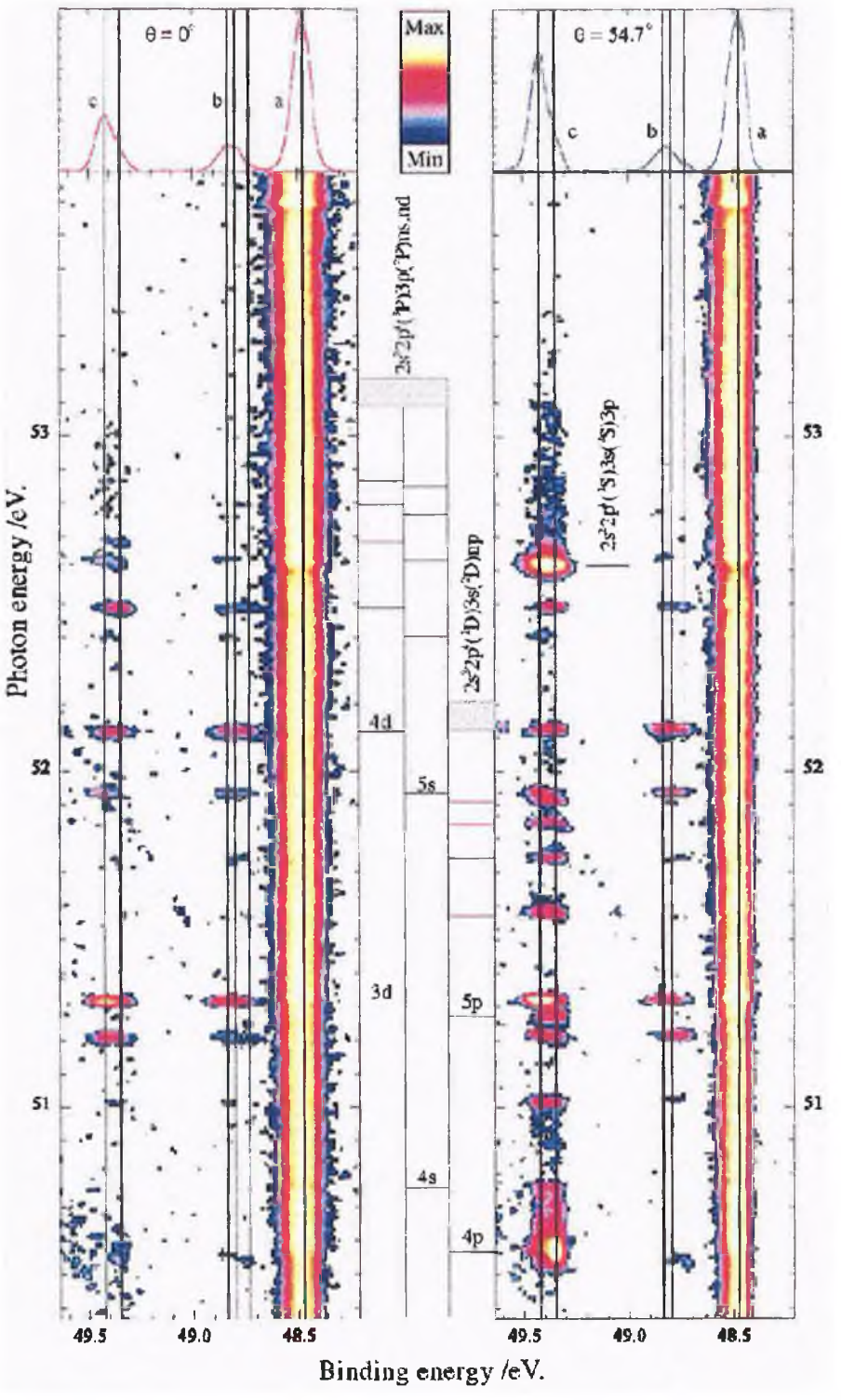

Figure 4.1 : Photoelectron yield for neon as a function of photon energy and binding energy at 0° and 54.7°. The upper graphs show the spectrum at 51.3eV photon energy, and the vertical bars indicate the positions of the (a)$2s2p^6(^2S)$, (b)$2s^22p^4(^3P)3s(^4P)$, and (c)$2s^22p^4(^3P)3s(^2P)$ fine structure levels (after Wills et al 1998).

of neon. With a photon energy resolution of 20meV at 57eV, a significant improvement over resolutions of the order of ~100meV as seen in previous experiments (Wills et al 1990) was evident. An example of their 2DPES spectra is shown in figure 4.1. The 2D nature of these spectra is particularly useful for the observation of LS coupling breakdown for two reasons.

Firstly, it can be shown that parity unfavoured contributions to the differential cross section of a resonance vanish at $\theta = 0°$, where θ is the angle between the photoelectron momentum vector and the photon polarisation axis (Wills et al 1998, Dill and Fano 1972). Thus, as in this case, when two time of flight (TOF) electron energy analysers are positioned at $\theta = 0°$ and $\theta = 54.7°$ (the magic angle), one can easily determine if a resonance is indicative of LS coupling breakdown by simply looking to see if there is a signal, at its corresponding photon energy, for $\theta = 0°$. This can be seen in figure 4.1 where if we look along the vertical lines (c), corresponding to the $2p^43s\ ^2P$ satellites at a binding energy of 49.4eV, it can be seen that several resonances appear at both angles while others disappear in the 0° spectrum. As a specific example, we see that the $2p^4(^3P)3p(^2P)3d$ resonance at a photon energy of 51.3eV shows a photoelectron yield that is almost equally as strong at 0° as it is at 54.7°, whereas, the $2p^4(^1D)3s(^2D)4p$ resonance at 50.6eV disappears almost completely in the 0° spectrum. Since both these transitions are parity unfavoured in LS coupling, the appearance of any signal at 0° is an immediate indication of LS coupling breakdown.

Secondly, evidence for LS coupling breakdown can be obtained by looking at the photoelectron intensity of spin-orbit partners. For example, if we again look along the two vertical lines (c) corresponding to the $2p^43s\ ^2P_{3/2}$ and $2p^43s\ ^2P_{1/2}$ satellites (at 49.35eV and 49.42eV binding energies), it can clearly be seen that the ratio is not equal to 2 as it should be when LS coupling is in effect. Using both of these indicators for LS coupling breakdown, Wills et al (1998) observed many resonances to exhibit LS forbidden behaviour and concluded, through the observation of these spin orbit effects, that even for low lying resonances in a system as light as neon, it is not safe to assume the validity of LS coupling.

Theoretical studies

On the theoretical front, studies of the resonant and non-resonant structure of neutral neon in the vicinity of the ^2S threshold have been given impetus periodically by resolution improvements in experimental investigations. The Random Phase Approximation with Exchange (RPAE) (Amusia et al 1971), Multiconfiguration close coupling methods (Luke 1973) and the R-Matrix method (Burke and Taylor 1975) had all been applied within a decade of Codling et al's experimental work. Only the latter calculations (Luke 1973, Burke and Taylor 1975) considered the resonant structure of the $2s2p^6np\ ^1P_1$ transitions, seeing careful study of these resonances as a more sensitive test of theory. Methodologies such as the Relativistic Random Phase Approximation (RRPA) have also been used (Johnson et al 1980) which have been found to agree well with experiment (Johnson and Cheng 1979). More recently, the photoionisation cross section of neon has been studied by application of the Relativistic Time Dependent Local Density Approximation (RTDLDA) method (Parpia et al 1984) and via a modified TDLDA calculation (Stener et al 1995) which supported the correct coulombic asymptotic behaviour to allow accurate prediction of the $2s2p^6np\ ^1P$ resonance series. Finally, perhaps the most detailed of recent calculations have been performed by Schulz et al (1996) who, having improved upon recent R-Matrix calculations (Hibbert and Scott 1994), have used a combination of the R-Matrix method, Multichannel quantum defect theory and the recoupling frame transformation to accurately predict the many overlapping two electron ($2s^22p^43snp$, $2s^22p^43pnl$ [l=s,d]) and single electron ($2s2p^6np\ ^1P_1$) excitations within a 10eV band centred at the ^2S threshold.

4.1.2. Na^+ in the regions of 2s and 2p excitation

In contrast to the wealth of activity involving neutral neon, its nearest relatives in the isoelectronic sequence have been all but neglected. The first observation of singly ionised sodium was by Lucatorto and McIlrath (1976), when, in a resonant laser-driven ionisation experiment, they employed a BRV vacuum spark as continuum source coupled with a 3m grazing incidence spectrograph to photographically record the XUV spectrum of Na^+ in the 30-84eV region. The discrete members of the Na^+ $2p^6 \rightarrow 2p^5ns,nd$

series up to n=13 were reported as were the first six members of the $2s2p^6np\ ^1P_1$ autoionising series. Lucatorto and McIlrath also derived a value for the photoionisation cross section (5.5MB) at energies just beyond the $2p^5\ ^2P_{3/2,1/2}$ thresholds where the onset of the continuum could be clearly seen. Most recently, Dorn et al (1995) used high resolution electron spectroscopy to study Auger decay from many sodium states not accessible from the ground state. Using a relatively new technique, they combined laser excitation and electron impact to excite and ionise the 3p and 4d levels of neutral sodium and accurately inferred energies for the $2s2p^6np\ ^1P$ and ^3P levels of Na^+ for n=3-5. Theoretically, Zatsarinny (1995) calculated positions and widths for the $2s2p^6ns,np,nd$(n=3-7) states of Na^+ using the Hartree-Fock approximation with the additional inclusion of inner-core and core-polarisation correlation. Nienhaus et al (1997) recently extended these calculations to include the n=8-12 members and Dorn et al (1997), through experimental and theoretical Auger and autoionisation spectra obtained via electron impact on laser excited sodium atoms, investigated the decay dynamics arising from the $2s2p^6nl$ (n=3-8, l=0-2) states of Na^+. Kupliauskiene (1998) performed term-dependent Hartree-fock calculations for the Na^+ $2s2p^6np$(n=3,4) $^{1,3}P$, ns(n=3-5) $^{1,3}S$, nd(n=3-5)$^{1,3}D$ states and obtained good agreement with the experimental values of Dorn et al (1995) for the np members. Lamoureux and Radojevic (1982) applied RPAE methods to Na^+ as part of a systematic look at the first five members of the neon isoelectronic sequence. However, only the $2p^6\ ^1S \rightarrow 2p^5ns,nd\ ^1P$ discrete transition series and the continuum beyond their $^2P_{3/2,1/2}$ limits were treated. Transitions arising from a hole in the 2s subshell were neglected but Lamoureux and Radojevic's calculated cross section at threshold (~6.4MB) was in close agreement with Lucatorto and McIlrath's (1976) experimental determination (5.5 ± 2.5MB).

4.1.3. Mg^{2+} in the regions of 2s and 2p excitation

The first analysis of the 2p region of Mg^{2+} was performed by Söderqvist (1934) where within the 51-83eV energy region, the $2p^5ns$ and $2p^5nd$ series were measured up to n=6 and n=8 respectively. More recently, Lundström (1973) returned to this region in Mg^{2+} and, with a quoted accuracy of ~0.001eV from a 5m grazing incidence spectrograph,

measured the $2p^5ns,nd$ for ns members up to n=6 and nd members up to n=9. In 1974, Esteva and Mehlman, applying a dual BRV spark technique, studied the 2s region of Mg^{2+} excitation and reported the first experimental evidence of levels with inner shell excitation leading to autoionisation in the case of a doubly ionised atom. These strongly asymmetric resonances between 97 and 120eV constituted the first clear observation of the $2s2p^6np\ ^1P_1$ series in Mg^{2+}. Energies corresponding to the first six members of the series were determined. Subsequently, Kastner et al (1977) pursued the isoelectronic sequence, and in particular the $2s2p^6np\ ^1P_1$ series, into the realm of the heavier ions. Attempting to negotiate Mg^{2+} to S^{6+} via a high voltage spark arrangement, only Mg^{2+} and Al^{3+} proved successful. Si^{4+}, P^{5+} and S^{6+} proved too difficult to produce in sufficient quantities to clearly manifest absorption features. Kastner et al's measurements for the Mg^{2+} inner shell series agreed well with those of Esteva and Mehlman, although their spectra were far from unambiguous as the nature of the experimental technique employed led to the unavoidable presence of many emission lines, in both first and second orders, which served to obscure the true absorption spectra. Indeed, in none of these studies of the $2s2p^6np\ ^1P$ series in Mg^{2+}, was any attempt made to characterise the asymmetric resonances in terms of the usual Beutler-Fano criteria (Fano 1961, Fano and Cooper 1965) i.e. Γ, q and ρ^2 (see section 1.3).

4.1.4. Al^{3+} in the regions of 2s and 2p excitation

As with Mg^{2+}, the first investigations of the 2p region of Al^{3+} were performed by Söderqvist (1934) measuring $2p^6 \rightarrow 2p^54d$, 5s, 5d, 6d transitions. Ferner (1948) also recorded $2p^6 \rightarrow 2p^54d$, 5s, 5d transitions. Subsequently, Kaufman et al (1974) extended the analysis in measuring the energies of $2p^6 \rightarrow 2p^53s$, 3d, 4s transitions. In 1971, the Al^{3+} $2p^6 \rightarrow 2p^54d$ transitions became the focus of considerable attention when Jaegle et al (1971) interpreted intensity anomalies observed in the emission from the 4d $^1P_1$, $^3D_1$ and $^3P_1$ lines as being due to the $^3P_1$ line at 117.41Å (105.6eV) showing stimulated emission, the population inversion in favour of this state being manifested by negative absorption. In subsequent publications, this group argued that the autoionising inner shell

$2p^6 \rightarrow 2s2p^6np$ transitions play a prominent role in the population inversion, the main processes being (Carillon et al 1972),

$$Al^{4+}(2s^22p^5\ ^2P) + e^- \rightarrow Al^{3+}(2s2p^6np\ ^3P)$$

$$Al^{3+}(2s2p^6np\ ^3P) + e^- \rightarrow Al^{3+}(2s^22p^5n'd\ ^3P) + e^-$$

$$Al^{3+}(2s^22p^5n'd\ ^3P) \rightarrow Al^{3+}(2s^22p^6\ ^1S) + h\nu$$

$$Al^{3+}(2s^22p^6\ ^1S) + h\nu' \rightarrow Al^{3+}(2s^22p^5n''d\ ^1P, ^3D)$$

$$Al^{3+}(2s^22p^6\ ^1S) + h\nu'' \rightarrow Al^{3+}(2s2p^6np\ ^1P, ^3P)$$

In the course of their study, the first two members of the $2s2p^6np\ ^1P$ series and the first three members of the $2s2p^6np\ ^3P$ series were measured (Carillon et al 1972). However, accurate energy determinations were not possible due to their absorption spectra being partially obscured by several emission lines. Continuing their investigations into a possible lasing action on the $Al^{3+}\ 2p^54d\ ^3P_1 \rightarrow 2p^6\ ^1S_0$ transition at 117.41Å, Jaegle et al (1974) reported a measured gain in a dual laser plasma experiment of 17%, estimating the gain coefficient to be of the order of $10cm^{-1}$. Furthermore, in the course of their work on Al^{3+}, the group added to Söderqvist's earlier identifications by measuring energies for $2p^6\ ^1S_0 \rightarrow 2p^5nd\ ^3P_1, ^3D_1, ^1P_1$ transitions up to n=7 (Jamelot et al 1972). With regard to lasing in Al^{3+} plasmas, Valero (1974) disputed such conclusions through a series of laser generated Al^{3+} plasma experiments. He concluded that the intensity anomalies, previously interpreted as evidence for stimulated emission, were in fact due to $2p^6\ ^1S \rightarrow 2p^5nd\ ^1P$ and ^3D transitions being strongly absorbed in the 'cooler' regions of the plasma, while the radiation from the $2p^6\ ^1S \rightarrow 2p^5nd\ ^3P$ transitions, which possess much smaller transition probabilities, is not strongly absorbed. The net result is, therefore, a relative increase in the intensity of the lines having lower transition probabilities.

As mentioned earlier, Kastner et al (1977), in a systematic study of the low Z members of the neon isoelectronic sequence, recorded members of the $2s2p^6np\ ^1P$ series up to n=8, this being a significant extension to the work of Carillon et al (1972). Kastner et al concluded that the n=3 and 4 members of this series had been incorrectly assigned to the n=3 and 4 members of the $2s2p^6np\ ^3P$ series by Carillon et al (1972). Kastner et al further reported the n=3 and 4 members of the $2s2p^6np\ ^3P$ series as lying ~0.2eV lower than that reported by Carillon et al. The unwanted presence of strong aluminium emission in the absorption spectra of both Carillon et al (1972) and Kastner et al (1977) is obviously the

cause of the disagreement as to the position of the $2s2p^6np\ ^3P$ series members. As we shall see in section 4.4.2, we have seen no evidence in our absorption spectra for the presence of these intercombination transitions, which our calculations indicate are far weaker than those belonging to the $2s2p^6np\ ^1P$ series.

4.1.5. Si^{4+} in the regions of 2s and 2p excitation

The 2p region of Si^{4+} was first investigated through emission measurements by Ferner (1942) where the $2p^6 \rightarrow 2p^5nd$ (n=4-6) transitions were identified. More recently, as part of an analysis of the Si^{4+} $2p^53s$, 3p, 3d and 4s configurations, where ~90 new lines were identified, Brillet (1976) measured the $2p^6 \rightarrow 2p^53s$,3d and 4s transitions between 105 and 138eV. In a follow up study, Brillet and Artru (1976) extended their analysis of Si^{4+} levels by identifying ~120 more new lines arising from $2p^54p$, 4d, 4f, 5f and 5g configurations. From these new measurements, Brillet and Artru were able to recalculate the Si^{4+} $2p^5$ $^2P_{3/2,1/2}$ limits for which they deduced energies of 166.77eV and 167.4eV respectively. Experimental observations of the discrete principal series of Si^{4+} being sparse, they are even more so for the 2s region with the only experimental data prior to this work being the photographic photoabsorption spectra of Brilly (1990).

4.1.6 Neon isoelectronic sequence studies

Despite the lack of experimental data on the 2s region for members of the neon isoelectronic sequence beyond Na^+, there have been a number of recent theoretical studies of the sequence and the trends found therein. Hibbert et al (1998), in a contribution to the ongoing Opacity project (Seaton 1987), have used the non-relativistic R-Matrix method to calculate the photoionisation cross section of the first five members of the sequence ($Ne^0 \rightarrow Si^{4+}$) with a sufficiently fine photon energy mesh to manifest the resonant $2s2p^6np\ ^1P_1$ series. Chakraborty et al (1999), in a combined study of the sequence using RRPA calculations (up to Z=100) and the DLP experimental results of this work (Z=1-5), have reported measurements and calculations on both the near threshold ($^2P_{3/2,1/2}$) photoionisation cross section and the energy position of $2s2p^6np\ ^1P$

resonances. They have observed a dramatic near threshold anomaly at Si^{4+} whereby the cross section is reduced substantially as a consequence of the inner shell resonances moving below threshold with increasing Z. This anomalous behaviour in the progression of the sequence shall be dealt with in more detail in section 4.5.4.

Clearly, there is a lack of experimental data concerning the 2s subshell autoionising transitions in neon isoelectronic sequence members beyond Na^+. In the following sections we present the first systematic photoabsorption spectra of the $2s^22p^5ns$, nd and $2s2p^6np$ series for Ne^0 through to Si^{4+}. The experimental data is supported both through the theoretical calculations of Chakraborty et al (1999) and through our own independent Hartree-Fock configuration interaction (HFCI) calculations (Cowan 1981), enabling confident assignments and commentary on the prevailing coupling schemes.

4.2. Measurement of the $2p \rightarrow nd,ns$ ($n \geq 3$) Rydberg series : $Na^+ \rightarrow Si^{4+}$

Although our primary objective was the observation of the $2s2p^6np\ ^1P_1$ series for each of the first five members of the neon isoelectronic series, it was deemed prudent to first record the $2p^5ns$, nd series running up to threshold. The motivations for this were : (a) to use these 'well known' $2p^5ns$, nd transitions to optimise our experimental conditions i.e. ΔX, ΔT, and incident target irradiance, so that upon moving to CEMA settings corresponding to the 2s region, ion stage purity would be assured, (b), to independently establish each isoelectronic member's $^2P_{3/2,1/2}$ limits and (c), to test the resolving power of the instrument by measurement of the higher series members as they approach their $^2P_{3/2,1/2}$ limits. Figure 4.2 (a)-(d) shows the $2p^6 \rightarrow 2p^5ns,nd$ series of Na^+ to Si^{4+} respectively. The corresponding series for Ne^0 was omitted as it lay beyond the range of our instrument. All spectra were recorded using the DLP system detailed in chapter 2.

Figure 4.2 (a) shows how excellent isolation of Na^+ ions in the plasma plume was achieved by employing a ΔT of 50ns and a ΔX of 0.5mm. A laser energy of 115mJ was directed via a cylindrical lens (f=11cm) and sharply focused on target, forming a rich Na^+ absorbing column, 10mm in length. Indeed, a high level of absorption was produced to facilitate measurement of the ns, nd members up to n=9 as at lower Na^+ column densities these higher members would not survive obscuration by background

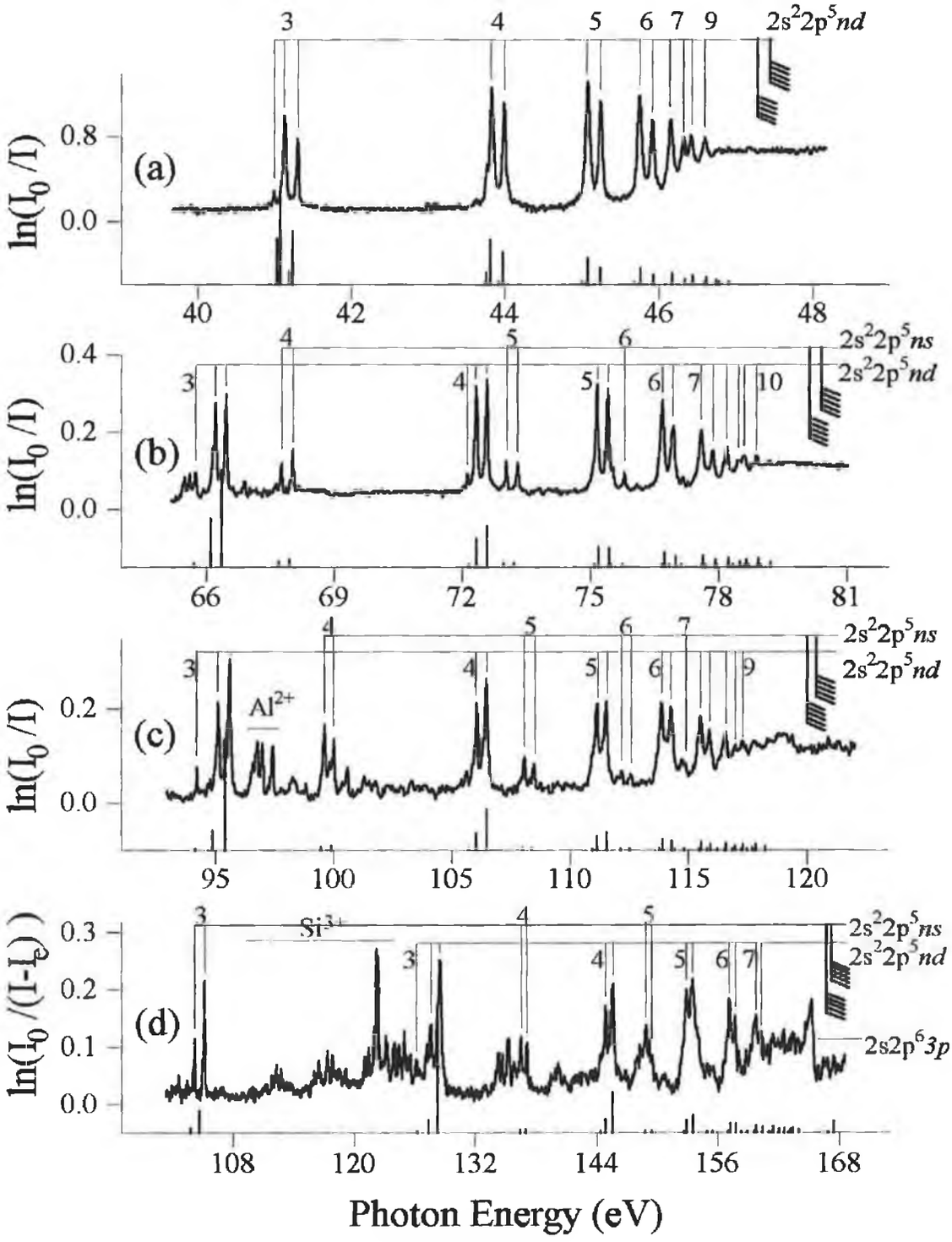

Figure 4.2 : The 2p photoabsorption spectra of (a) Na^+, (b) Mg^{2+}, (c) Al^{3+} and (d) Si^{4+} (see text for details). Configuration interaction Hartree-Fock calculations performed via the Cowan suite of codes are represented by stick plots in each figure.

noise. Furthermore, an increased signal to noise ratio meant less laser shots were required to achieve a clear, unambiguous spectrum. In total, three CEMA settings along the Rowland circle were used to record the $2p^5ns$, nd series i.e. 25.4, 24.7 and 24", the 0.7" increment ensuring a generous overlap of spectra, allowing absorption levels from setting to setting to be monitored and thus kept consistent. A further advantage in recording the same features at different CEMA settings is that average peak energies may be extracted reducing the likelihood of energy measurement errors due to the limited number of pixels across any individual peak. Figure 4.2 (a) is the average result of only 10 shots, the quantity $\ln(I_0/I)$ having been computed to generate the required photoabsorption data as described in section 2.2.6.

Figure 4.2 (b) shows the $2p^5ns$, nd series for Mg^{2+}. The more energetic and faster Mg^{2+} ions were captured with a ΔT of 40ns and a ΔX of 0.4mm. Again, a cylindrical lens (f=11cm) was sharply focused on target and the incident laser beam with an energy of 184mJ was apertured, before reaching the lens (see figure 2.3, section 2.2.3), to produce an absorbing column 1.5mm in length. The resultant absorption of ~28% (at peak) proved sufficient to enable measurement up to n=10 of the series while circumventing the onset of saturation. An excellent signal to noise ratio was obtained by taking the average result of a total of five independent spectra, each the accumulation of ten I and I_0 scans. The CEMA settings over which this spectrum was recorded were 20.9, 20.2 and 19.5".

Moving to Al^{3+} in figure 4.2 (c), we again see the distinct $2p^5ns$, nd series running to threshold. Intuitively, with increasing ionisation, there is a need to introduce more energy to the system and move closer to the target surface to capture the short-lived, highly ionised species shortly after generation. Thus, a ΔT of 15ns and a ΔX of 0.25mm combined with an incident laser energy of 128mJ, focused sharply via a spherical lens (f=11cm), enabled the recording of a reasonably pure Al^{3+} absorption spectrum. It was not possible to completely isolate the Al^{3+} ions and thus, some transitions from the $Al^{2+}2p^53snd$, ns series are clearly visible, albeit weak, between 95 and 100eV. The spectrum was the average of ten independent spectra, each the accumulation of five I and I_0 scans and corresponds to CEMA settings of 19.1, 18.4, 17.7 and 17".

Finally, figure 4.2 (d) shows the Si^{4+} photoabsorption spectrum in the 2p region of excitation. An increased laser energy (240mJ) coupled with sharp focusing via a spherical lens (f=11cm) and a ΔT and ΔX of 20ns and 0.1mm, respectively, were required to produce a sufficient density of Si^{4+} ions to record an absorption spectrum. However, the necessarily high laser irradiances and sharp focusing conditions meant that an unwanted by-product was an unavoidable and strong emission signal from the target silicon plasma. This was compensated for by way of a modified version of Beer's law (Jannitti et al 1988) where the emission signal $I_e(\lambda)$ was simply subtracted from the absorption signal $I(\lambda)$ before applying the usual $\ln(I_0/I)$ transformation. While this process enabled the $2p^5ns$, nd series to be clearly observed, the spectrum was not without contamination by transitions from the $Si^{3+}2p^53snd$, ns series between 108 and 142eV. Figure 4.2(d) comprises the average of ten independent spectra, each the accumulation of ten I_0, I and I_e scans and corresponds to CEMA settings of 18.1, 17.4, 16.7, 16 and 15.3".

4.3 Measurement of the 2s → np (n≥3) inner shell autoionising series : $Ne^0 \rightarrow Si^{4+}$

Figure 4.3 (a)-(c) and figure 4.4 (a)-(b) show the $2s2p^6np\ ^1P_1$ series in Ne^0 through to Si^{4+}. Figure 4.3 (a) shows the series in neutral neon, which is known to overlap with the weaker fine structure attributable to double excitation from the 2p subshell. In order to reveal the higher series members, a neon gas pressure of 0.19mbar was maintained in the target chamber. The I_0 and I signals were respectively recorded in the absence and presence of the neon gas. The neon absorbing column length was ~25cm. This corresponded to the distance between the plasma source on the tungsten rod and the nexus point (i.e. the GCA) to the next chamber of our differentially pumped system. To minimise noise levels, the average of fifteen independent spectra, each the accumulation of ten I_0 and I scans, was required. The entire series was captured at a single CEMA setting on the Rowland circle i.e. 24". The $Na^+\ 2s^22p^6 \rightarrow 2s2p^6np\ ^1P_1$ series displayed in figure 4.3 (b) was recorded with the same experimental parameters as those used for its kindred $2s^22p^6 \rightarrow 2s^22p^5ns$, nd series, shown in figure 4.2(a), except that here, an absorbing column 1.5mm in length was used. This shorter column length reduced

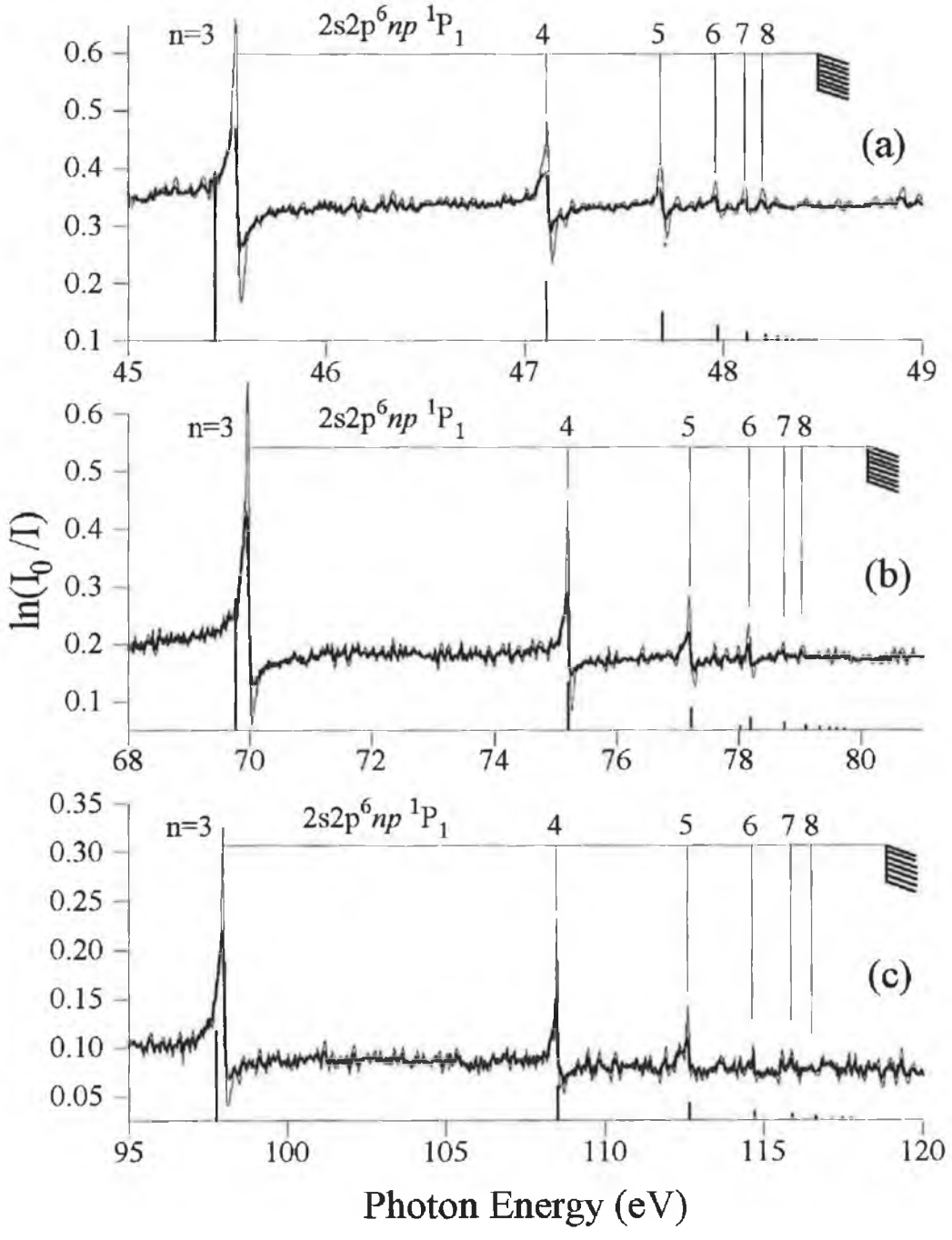

Figure 4.3 : The 2s photoabsorption spectra of (a) Ne^0, (b) Na^+ and (c) Mg^{2+}. The unrestored DLP data is shown in bold. Data after deconvolution with a 4 pixel FWHM Lorentzian instrument function is represented by the lighter curves. Configuration interaction Hartree-Fock calculations performed via the Cowan suite of codes are represented by stick plots in each figure. See text for further details.

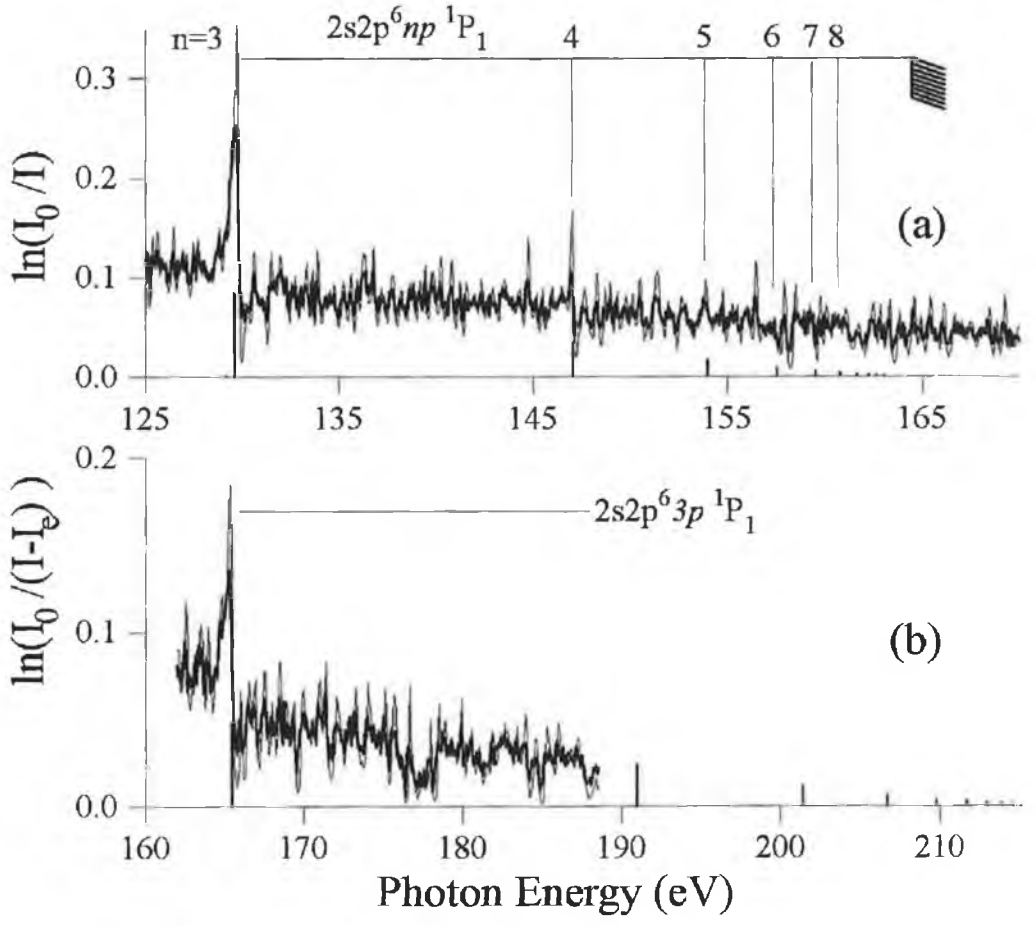

Figure 4.4 : The 2s photoabsorption spectra of (a) Al^{3+} and (b)Si^{4+}. The unrestored DLP data is shown in bold. Data after deconvolution with a 4 pixel FWHM lorentzian instrument function is represented by the lighter curves. Configuration interaction Hartree-Fock calculation performed via the Cowan suite of codes are represented by stick plots in each figure. See text for further details.

absorption levels thereby avoiding saturation, a critical factor in the accurate measurement of any profile. With less signal, noise reduction was essential and so, an average of fifty shots, five sets of ten I and I_0s, were taken. The np series of Na^+ was recorded at CEMA settings of 20.1 and 20.8". The remaining figure 4.3(c) and figures 4.4 (a) and (b), which show the $2s^22p^6 \rightarrow 2s2p^6np\ ^1P_1$ series for Mg^{2+}, Al^{3+} and Si^{4+} respectively, were recorded with identical experimental conditions to those described for their corresponding $2s^22p^6 \rightarrow 2s^22p^5ns$, nd series in figure 4.2. Unfortunately, in the case of Si^{4+}, members of the series greater than n=3 lay beyond the range of our

instrument. The CEMA settings used were 18.8, 18.1 and 17.4" for Mg^{2+}, 17, 16.3 and 15.6" for Al^{3+} and 16 and 15.3" for Si^{4+}.

As discussed in section 2.3.4. of chapter 2, we have reason to believe that stray light is present in our system for energies above 100eV. Thus, in accordance with the treatment prescribed in section 2.3.4, we have used the proportion of stray light (p) curve of figure 2.12 in conjunction with equation [2.11] to correct the neon isoelectronic sequence spectra for the contribution of this stray light. This procedure was carried out for the spectra shown in figures 4.2, 4.3 and 4.4 where energies exceed 100eV. In section 2.3.4, we also noted that the effect of stray light on absorption spectra may be minimised by adhering to optically thin regimes. Thus, in our measurements for the neon isoelectronic sequence, we have consistently kept absorption levels to a minimum,

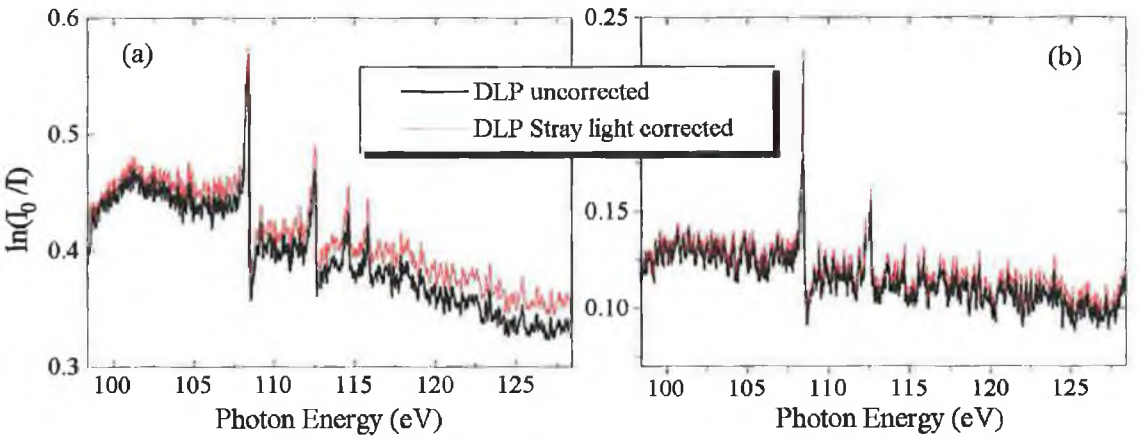

Figure 4.5 : The effect of stray light on Mg^{2+} photoabsorption spectra where (a) is an 'optically thick' spectrum taken for ΔX = 0.4mm, ΔT = 40ns and an absorbing column length = 10mm and (b) is an 'optically thin' spectrum for ΔX = 0.4mm, ΔT = 40ns and an absorbing column length = 1.5mm. Both spectra were taken at a single CEMA setting i.e. 17.4". See text for further details.

thereby both avoiding saturation and reducing the influence of stray light. Figure 4.5 (a) and (b) illustrate the effect of stray light on different absorption levels for the case of Mg^{2+} in the energy region between 100 and 130eV where it is clear that stray light is not as influential for the lower absorption levels which may be referred to as 'optically thin'. Figure 4.6 further illustrates the consequences of absorption levels being too high and therefore subject to saturation, where (a) and (b) show the measured and deconvolved profile, respectively, of the Mg^{2+} $2s2p^63p$ ^1P resonance for different absorption levels. In

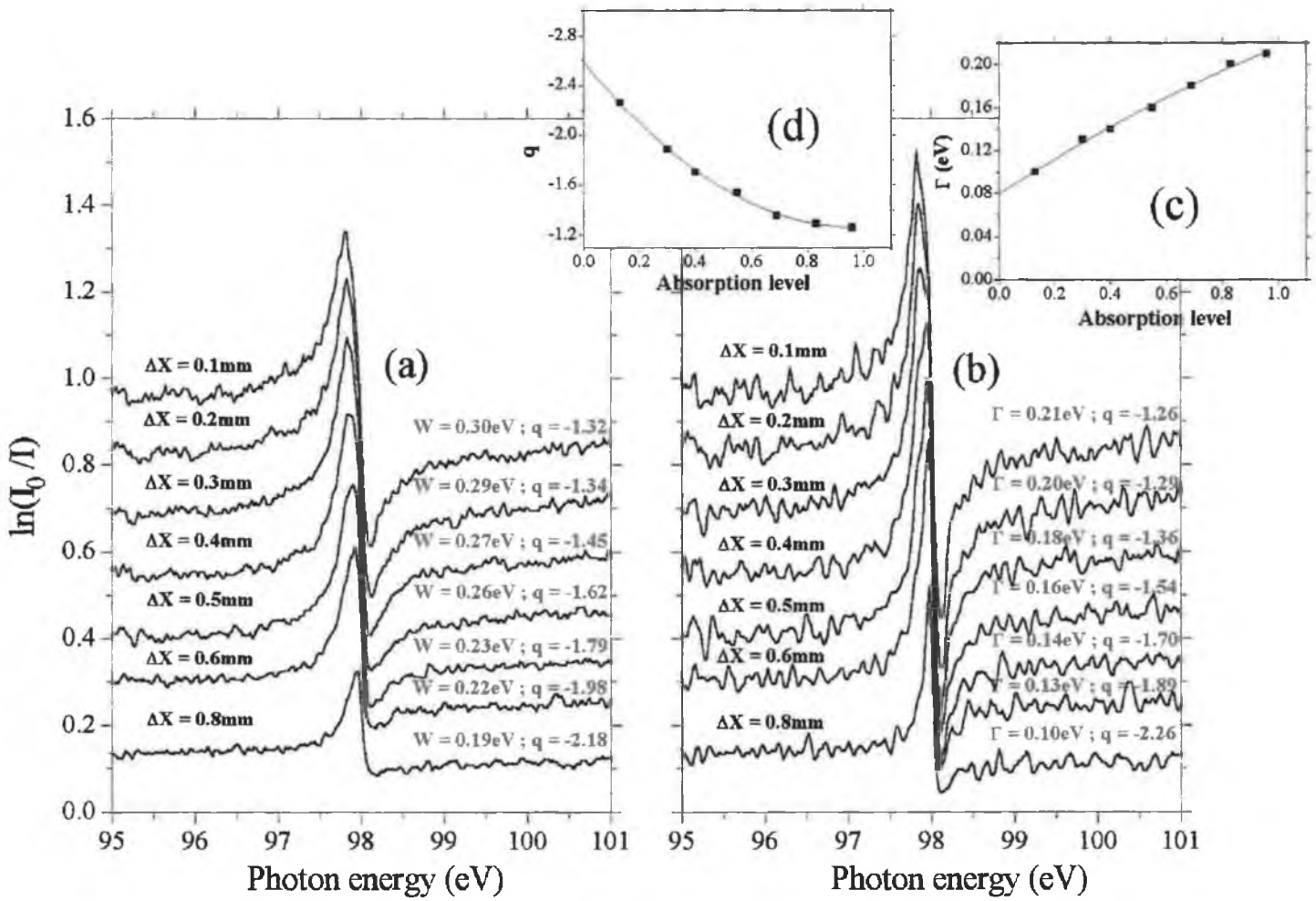

Figure 4.6 : The effect of saturation on the profile of the Mg^{2+} $2s2p^63p$ ^1P resonance where (a) and (b) show the measured and deconvolved profiles respectively. The absorption levels have been varied by changing the value of ΔX, ΔT remaining constant at 40ns. In (c) and (d), respectively, the widths and q values from (b) are shown as a function of non-resonant absorption level. See text for further details.

(b), with the instrumental function now removed, it can be seen that the width (Γ) and profile index (q) are very sensitive to absorption levels, the more accurate results being for low levels of absorption where saturation is avoided and as we saw from figure 4.5, the effects of stray light are minimised. In figures 4.6(c) and (d), we have plotted the width (Γ) and q value of the profiles shown in (b) against the average non-resonant absorption level on the low energy side of the resonance. Figure 4.6(c) shows how the profile width decreases with absorption level almost linearly. In figure 4.6(d), we see that the q value also changes dramatically with absorption level, increasing almost linearly below an absorption level of ~0.5. The intercept values of Γ=0.08eV and q~-2.6 can clearly never be obtained but it is interesting to note that by systematically reducing opacity and measuring the resulting profile width and q value, best estimates may be obtained by extrapolation. This could be done for future measurements of any asymmetric resonance. Figure 4.6(c) and (d) further emphasise the necessity of minimising absorption levels (until noise becomes prohibitive), if accurate asymmetric resonance profile parameters are to be obtained.

In figures 4.3 and 4.4, we also show the deconvolution of each spectrum with a 4 pixel FWHM Lorentzian profile which we have found to best approximate our instrument function (see section 2.3.5). As for the calcium spectra in chapter 3, section 3.2.2, all deconvolutions were carried out using a maximum likelihood routine and were performed in 'pixel space' so as to account for the monotonic increase, with increasing energy, in linear dispersion from the grating. A total of twenty iterations were carried out for each deconvolution ensuring that convergence was reached while at the same time preventing excessive noise amplification. Typical results from this process are a gain in resolution of a factor of 2. To complete figures 4.2, 4.3 and 4.4, we have performed calculations for each member of the isoelectronic sequence which we show in the form of stick plots. These calculations were performed using the Cowan suite of codes (see section 2.4) and were scaled by suitable factors to achieve the closest agreement with experiment in terms of energy position, weighted oscillator strength (gf) and term splitting. It has been noted (Hansen and Quinet 1996) that correlation effects are far more important than the effects of scaling, as scaling only serves to 'fine tune' the results. For this reason configuration interaction calculations were employed and both

the $2s^22p^6 \rightarrow 2s^22p^5ns$, nd series and the $2s^22p^6 \rightarrow 2s2p^6np$ series were run in unison together with any other basis states thought to make a non-negligible contribution to the term mixing. The most important configurations included in our expansion were :

$2s^22p^6 \rightarrow 2s^22p^5ns$, nd(n=3-10) + $2s2p^6np$(n=3-10) + $2p^43snp$(n=3-10) + $2p^43pns$(n=3-10)

The $2s^22p^6 \rightarrow 2p^43pnd$ series was not included in our expansion as the PC version of the codes which we utilised was unable to process the large eigenvalue and eigenvector matrices associated with two open p shells and one open d shell. This was despite altering the PC code's matrix capacity so that it could handle larger matrices than both the VAX and UNIX versions of the code. However, the calculations indicate that the exclusion of the $2p^43pnd$ series affects the absolute but not the relative energy positions.
Initially, no scaling was applied to the Hartree-Fock parameters, which resulted in members of the $2s^22p^6 \rightarrow 2s^22p^5ns$ series being predicted to lie too close to the (n-1)d members running alongside. As the scaling was increased, this situation was rectified, with the ns series members moving to higher energies relative to the nd series members, which remained largely unaffected. Best agreement with experiment was obtained with the Coulomb integrals F^k, G^k and R^k reduced by 25%. This conformed to recommendations by Cowan (Cowan 1981) of between 20 and 30% for neutral and lowly ionised atoms. It was also consistent with previous calculations on Mg-like ions (Costello et al 1992, Sayyad et al 1995). The spin orbit integral (ζ) was not reduced as it was found that the ab initio value of this energy parameter sufficed for each member of the neon isoelectronic sequence studied here.
Finally, it must be emphasised that extreme care was taken in the energy calibration of each spectrum in order to obtain accurate and independent energy measurements of members belonging to ns, nd and np series. Both aluminium and magnesium emission lines were employed (see section 2.2.6 and figure 2.5) to calibrate the Ne^0, Na^+, Mg^{2+} and Al^{3+} absorption spectra. For the Si^{4+} absorption spectra, the unavoidable emission from the silicon target (remarked on in the last section) became useful; the emission lines used for calibration in conjunction with those from an aluminium target. For CEMA settings corresponding to regions of sparse line density in both aluminium and magnesium

emission spectra e.g. 22.9 → 20.8" (230 → 190Å), oxygen emission lines, accessed via single shots to fresh aluminium and magnesium target areas where a thin oxide layer was present, were also utilised.

4.4 Sequence trends

4.4.1. 2p → nd, ns (n ≥ 3) Rydberg series : $Na^+ \rightarrow Si^{4+}$

In tables 4.1, 4.2, 4.3 and 4.4, we compare calculated and measured transition energies for the 2p → nd, ns (n ≥ 3) series of Na^+, Mg^{2+}, Al^{3+} and Si^{4+} respectively. The measured energies correspond to the spectra shown in figure 4.2. Transition energies listed in Kelly's compilation of known atomic and ionic spectrum lines below 2000Å (Kelly 1987) are also shown. Although referenced to Kelly, the energies of these lines were originally measured and documented by those authors discussed in sections 4.12 to 4.15 i.e. Na^+ (Lucatorto and McIlrath 1976), Mg^{2+} (Lundström 1973), Al^{3+} (Söderqvist 1934, Ferner 1948, Kaufman et al 1974), Si^{4+} (Ferner 1942, Brillet 1976). Our scaled calculations correlate well with experiment, the term splitting energy difference being in agreement to better than 7meV in most cases. However, it was a feature of the predicted energies that for each element under investigation, the results were displaced from the actual measured energies by a constant amount. For the ns, nd series, an underestimation of transition energies was evident and the computed values required a shift to higher energies, to aid experimental assignment, of 0.71, 0.65, 0.59 and 0.57eV for Na^+, Mg^{2+}, Al^{3+} and Si^{4+} respectively. The stick plots representing our calculations in figure 4.2 have been shifted in energy by these amounts to coincide with observed features whereas the calculated energies of these transitions are unshifted in the listings of tables 4.1 to 4.4. Despite the underestimation, the code predicted configuration centre of gravity energies (E_{av}) well within the tolerances indicated by Cowan (1981). Absolute energies were predicted with an accuracy ranging from ~2% for Na^+ to ~0.5% for Si^{4+}. It can also be seen that for Na^+, Mg^{2+}, Al^{3+} and Si^{4+}, the predicted interval between succeeding members in both the ns and nd series improves in accuracy with increasing n, as the systems become more hydrogenic due to screening by the core. Further verification of

Transition	E_{calc} (eV)	E_{obs} (eV) §	E(eV) (Kelly 1987)	E(eV) (Lucatorto and McIlrath 1976)	gf_{calc}†	n^*
$2s^22p^6(^1S_0)\rightarrow$						
$3d[3/2,3/2]_1$	40.23	40.99	40.99	-	20	-
$4s[3/2,1/2]_1$	40.32	-	-	-	647	-
$3d[3/2,5/2]_1$	40.36	41.13	41.13	-	1208	2.98
$4s[1/2,1/2]_1$	40.48	-	-	-	182	-
$3d[1/2,3/2]_1$	40.52	41.30	41.31	-	759	2.98
$5s[3/2,1/2]_1$	43.06	43.77	$43.77^{\#(4d)}$	-	168	3.94
$4d[3/2,5/2]_1$	43.11	43.83	43.84	-	640	3.98
$5s[1/2,1/2]_1$	43.21	-	43.86	-	40	-
$4d[1/2,3/2]_1$	43.27	44.00	44.00	-	455	3.97
$6s[3/2,1/2]_1$	44.29	-	-	-	53	-
$5d[3/2,3/2]_1$	44.34	-	45.05	45.05	32	-
$5d[3/2,5/2]_1$	44.37	45.08	45.09	45.08	376	4.98
$6s[1/2,1/2]_1$	44.45	-	45.10	-	18	-
$5d[1/2,3/2]_1$	44.53	45.25	45.25	45.25	240	4.98
$7s[3/2,1/2]_1$	44.96	-	-	-	29	-
$6d[3/2,5/2]_1$	45.05	45.75	$45.76^{\#(7s)}$	45.76	238	5.98
$7s[1/2,1/2]_1$	45.13	-	-	-	11	-
$6d[1/2,3/2]_1$	45.21	45.92	$45.92^{\#(7s)}$	45.93	139	5.98
$8s[3/2,1/2]_1$	45.37	-	-	-	17	-
$7d[3/2,5/2]_1$	45.46	46.16	-	46.11	160	6.98
$8s[1/2,1/2]_1$	45.53	-	-	-	7	-
$7d[1/2,3/2]_1$	45.62	46.32	-	46.33	85	6.97
$8d[3/2,5/2]_1$	45.72	46.42	-	46.43	125	7.96
$9s[3/2,1/2]_1$	45.73	-	-	-	2	-
$8d[1/2,3/2]_1$	45.89	-	-	46.60	37	-
$9s[1/2,1/2]_1$	45.90	-	-	-	17	-
$9d[3/2,5/2]_1$	45.91	46.60	-	46.60	104	8.96
$9d[1/2,3/2]_1$	46.07	-	-	-	50	-
$2s^22p^5\ ^2P_{3/2}$ *limit*	46.58	47.28	-	47.29		
$2s^22p^5\ ^2P_{1/2}$ *limit*	46.75	47.44	-	47.46		

§ ±0.02eV
† gf values have been multiplied by 10^4.
# Assignment (shown in parenthesis) differs from this work

Table 4.1 : The experimental and calculated transition energies for Na^+ $2p \rightarrow nd$, $(n+1)s$ $[n\geq3]$. The energies listed by Kelly (1987) which were taken from the unpublished work of Crooker (1966) are also shown, as are the measured energies of Lucatorto and McIlrath (1976).

the code's suitability for the description of these systems is evidenced by the calculated gf values associated with each transition whereby they are clearly seen to mimic the experimental trend. As can be seen in tables 4.1 to 4.4, a jj designation has been adopted

Transition	E_{calc} (eV)	E_{obs} (eV)§	E(eV) (Kelly 1987)	gf_{calc}†	n^*
$2s^22p^6(^1S_0)\rightarrow$					
$3d[3/2,3/2]_1$	65.05	65.75	65.76	40	-
$3d[3/2,5/2]_1$	65.45	66.22	66.23	1950	2.97
$3d[1/2,3/2]_1$	65.71	66.46	66.48	4018	2.97
$4s[3/2,1/2]_1$	67.03	67.75	67.76	143	3.15
$4s[1/2,1/2]_1$	67.29	68.02	68.03	222	3.15
$4d[3/2,3/2]_1$	71.50	72.13	72.13	30	-
$4d[3/2,5/2]_1$	71.68	72.34	72.34	1127	3.97
$4d[1/2,3/2]_1$	71.94	72.58	72.59	1626	3.96
$5s[3/2,1/2]_1$	72.32	73.04	73.04	49	4.16
$5s[1/2,1/2]_1$	72.58	73.30	73.30	57	4.16
$5d[3/2,5/2]_1$	74.53	75.16	75.17	764	4.97
$5d[1/2,3/2]_1$	74.78	75.41	75.42	721	4.96
$6s[3/2,1/2]_1$	74.82	-	75.54	25	-
$6s[1/2,1/2]_1$	75.08	75.80	75.80	24	5.16
$6d[3/2,5/2]_1$	76.07	76.68	76.70	526	5.97
$7s[3/2,1/2]_1$	76.19	-	-	29	-
$6d[1/2,3/2]_1$	76.33	76.94	76.96	360	5.96
$7s[1/2,1/2]_1$	76.46	77.17	-	13	6.17
$7d[3/2,5/2]_1$	76.99	77.60	77.62	380	6.97
$8s[3/2,1/2]_1$	77.03	-	-	5	-
$7d[1/2,3/2]_1$	77.26	77.87	77.88	217	6.98
$8s[1/2,1/2]_1$	77.30	-	-	8	-
$8d[3/2,5/2]_1$	77.59	78.20	78.21	277	7.98
$9s[3/2,1/2]_1$	77.69	-	-	9	-
$8d[1/2,3/2]_1$	77.86	78.47	78.48	133	7.99
$9s[1/2,1/2]_1$	77.96	-	-	12	-
$9d[3/2,5/2]_1$	78.00	78.60	78.62	221	8.98
$9d[1/2,3/2]_1$	78.26	-	-	36	-
$10d[3/2,5/2]_1$	78.29	78.89	-	249	9.96
$2s^22p^5\ ^2P_{3/2}$ limit	79.53	80.12	80.14		
$2s^22p^5\ ^2P_{1/2}$ limit	79.79	80.38	80.40		

§ ±0.05eV
† gf values have been multiplied by 10^4.

Table 4.2 : The experimental and calculated transition energies for Mg^{2+} 2p → nd, (n+1)s [n≥3]. The energies listed by Kelly (1987) are also shown.

for labelling the Rydberg series members; the eigenvector matrices support this choice. Tables 4.5 to 4.8 show the calculated jj and LS energy level data for each ns, nd Rydberg member up to n=9 for Na^+ and n=10 for Mg^{2+}, Al^{3+} and Si^{4+}. In each case, only the four largest jj and LS eigenvector percentage purities are shown. It is clear that the $2p^5ns$

Transition	E_{calc} (eV)	E_{obs} (eV)§	E(eV) (Kelly 1987)	E(eV) (Jamelot et al 1972)	gf_{calc}†	n^*
$2s^22p^6(^1S_0)\rightarrow$						
$3d[3/2,3/2]_1$	93.53	94.21	94.18	94.18	37	-
$3d[3/2,5/2]_1$	94.28	95.12	95.09	95.07	1406	2.96
$3d[1/2,3/2]_1$	94.80	95.59	95.57	95.57	8260	2.96
$4s[3/2,1/2]_1$	98.87	99.61	99.55	-	175	3.27
$4s[1/2,1/2]_1$	99.27	100.00	99.96	-	236	3.27
$4d[3/2,3/2]_1$	105.10	-	105.64	105.60	30	-
$4d[3/2,5/2]_1$	105.44	106.02	106.04	106.04	1200	3.95
$4d[1/2,3/2]_1$	105.86	106.44	106.46	106.46	2985	3.95
$5s[3/2,1/2]_1$	107.38	108.06	108.06	-	72	4.27
$5s[1/2,1/2]_1$	107.79	108.47	108.46	-	63	4.27
$5d[3/2,5/2]_1$	110.54	111.14	111.11	111.11	975	4.96
$5d[1/2,3/2]_1$	110.93	111.53	111.50	111.50	1247	4.96
$6s[3/2,1/2]_1$	111.50	112.20	-	-	29	5.29
$6s[1/2,1/2]_1$	111.91	112.59	-	-	27	5.29
$6d[3/2,5/2]_1$	113.28	113.87	113.85	113.84	719	5.96
$6d[1/2,3/2]_1$	113.68	114.27	114.24	114.25	634	5.97
$7s[3/2,1/2]_1$	113.80	-	-	-	3	-
$7s[1/2,1/2]_1$	114.21	114.90	-	-	15	6.30
$7d[3/2,5/2]_1$	114.93	115.51	-	115.48	531	6.97
$8s[3/2,1/2]_1$	115.21	-	-	-	27	-
$7d[1/2,3/2]_1$	115.33	115.91	-	115.89	336	6.98
$8s[1/2,1/2]_1$	115.63	-	-	-	9	-
$8d[3/2,5/2]_1$	115.99	116.57	-	-	405	7.98
$9s[3/2,1/2]_1$	116.25	-	-	-	13	-
$8d[1/2,3/2]_1$	116.40	116.97	-	-	211	7.99
$9s[1/2,1/2]_1$	116.67	-	-	-	23	-
$9d[3/2,5/2]_1$	116.72	117.27	-	-	321	8.94
$9d[1/2,3/2]_1$	117.13	-	-	-	119	-
$10d[3/2,5/2]_1$	117.24	-	-	-	328	-
$10d[1/2,3/2]_1$	117.65	-	-	-	148	-
$2s^22p^5\ ^2P_{3/2}$ *limit*	119.45	119.99	119.96	119.97		
$2s^22p^5\ ^2P_{1/2}$ *limit*	119.84	120.38	120.34	120.35		

§ ±0.09eV
† gf values have been multiplied by 10^4.

Table 4.3 : The experimental and calculated transition energies for Al^{3+} $2p \rightarrow nd$, $(n+1)s$ $[n\geq3]$. The energies listed by Kelly (1987) and also those measured by Jamelot et al (1972) are shown for further comparison.

configurations exhibit jj purities close to 100% for Na^+ through to Si^{4+}. Only the $2p^55s[3/2,1/2]_1$ term for Na^+ exhibited a purity of less than 50% making unique labelling difficult and suggesting strong mixing with the $2p^54d[3/2,3/2]_1$ term. On examination of

Transition	E_{calc} (eV)	E_{obs} (eV)§	E(eV) (Kelly 1987)	gf_{calc}†	n^*
$2s^22p^6(^1S_0)\rightarrow$					
$3s[3/2,1/2]_1$	103.28	104.25	104.22	37	2.33
$3s[1/2,1/2]_1$	104.10	105.21	105.20	213	2.34
$3d[3/2,3/2]_1$	125.68	126.23	126.24	4	-
$3d[3/2,5/2]_1$	126.82	127.64	127.63	121	2.95
$3d[1/2,3/2]_1$	127.75	128.53	128.56	1186	2.97
$4s[3/2,1/2]_1$	135.83	136.49	136.47	20	3.35
$4s[1/2,1/2]_1$	136.42	137.09	137.08	23	3.36
$4d[3/2,5/2]_1$	144.33	144.90	144.88	129	3.95
$4d[1/2,3/2]_1$	144.99	145.56	145.57	407	3.96
$5s[3/2,1/2]_1$	148.22	148.87	-	8	4.37
$5s[1/2,1/2]_1$	148.82	149.43	-	7	4.37
$5d[3/2,5/2]_1$	152.32	152.88	152.86	115	4.96
$5d[1/2,3/2]_1$	152.91	153.46	153.43	164	4.97
$6s[3/2,1/2]_1$	154.30	-	-	4	-
$6s[1/2,1/2]_1$	154.91	-	-	3	-
$6d[3/2,5/2]_1$	156.62	157.11	157.14	87	5.95
$6d[1/2,3/2]_1$	157.21	157.69	157.72	80	5.97
$7s[3/2,1/2]_1$	157.74	-	-	2	-
$7s[1/2,1/2]_1$	158.35	-	-	2	-
$7d[3/2,5/2]_1$	159.20	159.68	-	65	6.95
$7d[1/2,3/2]_1$	159.79	160.17	-	47	6.95
$8s[3/2,1/2]_1$	159.87	-	-	-	-
$8s[1/2,1/2]_1$	160.48	-	-	1	-
$8d[3/2,5/2]_1$	160.87	-	-	50	-
$9s[3/2,1/2]_1$	161.38	-	-	3	-
$8d[1/2,3/2]_1$	161.46	-	-	26	-
$9d[3/2,5/2]_1$	162.00	-	-	30	-
$9s[1/2,1/2]_1$	162.02	-	-	12	-
$9d[1/2,3/2]_1$	162.61	-	-	17	-
$10d[3/2,5/2]_1$	162.82	-	-	40	-
$10d[1/2,3/2]_1$	163.43	-	-	19	-
$2s^22p^5\,^2P_{3/2}$ *limit*	166.27	166.73	166.77		
$2s^22p^5\,^2P_{1/2}$ *limit*	166.83	167.22	167.40		

§ ±0.17eV
† gf values have been multiplied by 10^3.

Table 4.4 : The experimental and calculated transition energies for Si^{4+} $2p \rightarrow nd$, ns [$n \geq 3$]. The energies listed by Kelly (1987) are also shown.

the $2p^5nd$ members, we see a jj designation to be the most convincing for the $nd[1/2,3/2]_1$ terms, with purities, more often than not, in excess of 90%. Their fine structure partners, the $nd[3/2,5/2]_1$ terms, are less dominant in leading eigenvector

Config./term	E_{calc}	E_{obs}	*jj* purity / *LS* purity
3d[3/2,3/2]$_1$	**40.23**	**40.99**	**57%[3/2,3/2]$_1$ - 32%[3/2,5/2]$_1$ - 5%4s[3/2,1/2]$_1$ + 4%3d[1/2,3/2]$_1$** **88%3d(^{3}P) - 6%4s(^{3}P) - 3%3d(^{3}P) - 2%3d(^{1}P)**
4s[3/2,1/2]$_1$	**40.32**	**-**	**85%[3/2,1/2]$_1$ - 11%3d[3/2,5/2]$_1$ + 4%[1/2,1/2]$_1$ + 0%3d[3/2,3/2]$_1$** **47%4s(^{3}P) + 41%4s(^{1}P) - 6%3d(^{1}P) + 5%3d(^{3}P)**
3d[3/2,5/2]$_1$	**40.36**	**41.13**	**55%[3/2,5/2]$_1$ + 40%[3/2,3/2]$_1$ +4%4s[3/2,1/2]$_1$ + 2%4s[1/2,1/2]$_1$** **56%3d(^{1}P) - 38%3d(^{3}D) + 5%4s(^{3}P) + 1%4s(^{1}P)**
4s[1/2,1/2]$_1$	**40.48**	**-**	**-92%[1/2,1/2]$_1$ + 6%[3/2,1/2]$_1$ +1%3d[3/2,5/2]$_1$ - 1%3d[1/2,3/2]$_1$** **56%4s(^{1}P) - 42%4s(^{3}P) - 1%3d(^{3}P) - 1%3d(^{3}D)**
3d[1/2,3/2]$_1$	**40.52**	**41.30**	**95%[1/2,3/2]$_1$ - 3%[3/2,3/2]$_1$ + 1%[3/2,5/2]$_1$ + 1%4s[3/2,1/2]$_1$** **58%3d(^{3}D) + 36%3d(^{1}P) + 5%3d(^{3}P) + 1%4s(^{1}P)**
5s[3/2,1/2]$_1$	**43.06**	**43.77**	**38%[3/2,1/2]$_1$ + 36%4d[3/2,3/2]$_1$ -25%4d[3/2,5/2]$_1$ + 0%4d[1/2,3/2]$_1$** **55%4d(^{3}P) + 26%5s(^{1}P) + 13%5s(^{3}P) - 4%4d(^{1}P)**
4d[3/2,5/2]$_1$	**43.11**	**43.83**	**64%[3/2,5/2]$_1$ + 35%[3/2,3/2]$_1$ + 1%5s[3/2,1/2]$_1$ + 0%5s[1/2,1/2]$_1$** **56%4d(^{1}P) - 43%4d(^{3}D) + 1%5s(^{3}P) + 0%5s(^{1}P)**
5s[1/2,1/2]$_1$	**43.21**	**-**	**98%[1/2,1/2]$_1$ -1%[3/2,1/2]$_1$ -1%4d[3/2,5/2]$_1$ + 0%4d[3/2,3/2]$_1$** **57%5s(^{3}P) - 42%5s(^{1}P) + 1%4d(^{3}P) - 0%4d(^{1}P)**
4d[1/2,3/2]$_1$	**43.27**	**44.00**	**98%[1/2,3/2]$_1$ +1%[3/2,5/2]$_1$ - 0%[3/2,3/2]$_1$ + 0%5s[3/2,1/2]$_1$** **51%4d(^{3}D) + 40%4d(^{1}P) + 9%4d(^{3}P) + 0%5s(^{1}P)**
6s[3/2,1/2]$_1$	**44.29**	**-**	**99%[3/2,1/2]$_1$ -1%5d[3/2,3/2]$_1$ + 0%[1/2,1/2]$_1$ - 0%3p6s[4/3,1/3]$_1$** **61%6s(^{1}P) + 38%6s(^{3}P) - 1%5d(^{3}P) + 0%5d(^{3}D)**
5d[3/2,3/2]$_1$	**44.34**	**-**	**67%[3/2,3/2]$_1$ -31%[3/2,5/2]$_1$ +1%6s[3/2,1/2]$_1$ +0%[1/2,3/2]$_1$** **87%5d(^{3}P) - 9%5d(^{3}D) - 3%5d(^{1}P) + 1%6s(^{1}P)**
5d[3/2,5/2]$_1$	**44.37**	**45.08**	**68%[3/2,5/2]$_1$ + 32%[3/2,3/2]$_1$ + 0%6s[3/2,1/2]$_1$ + 0%6s[1/2,1/2]$_1$** **58%5d(^{1}P) - 41%5d(^{3}D) - 0%5d(^{3}P) + 0%6s(^{3}P)**
6s[1/2,1/2]$_1$	**44.45**	**-**	**99%[1/2,1/2]$_1$ - 0%5d[3/2,5/2]$_1$ - 0%[3/2,1/2]$_1$ + 0%5d[3/2,3/2]$_1$** **62%6s(^{3}P) - 38%6s(^{1}P) + 0%5d(^{3}P) - 0%5d(^{1}P)**
5d[1/2,3/2]$_1$	**44.53**	**45.25**	**99%[1/2,3/2]$_1$ + 0%[3/2,5/2]$_1$ - 0%[3/2,3/2]$_1$ + 0%6s[3/2,1/2]$_1$** **50%5d(^{3}D) + 38%5d(^{1}P) + 12%5d(^{3}P) + 0%6d(^{1}P)**
7s[3/2,1/2]$_1$	**44.96**	**-**	**100%[3/2,1/2]$_1$ - 0%6d[3/2,3/2]$_1$ - 0%3p7s[4/3,1/3]$_1$ + 0%[1/2,1/2]$_1$** **64%7s(^{1}P) + 36%7s(^{3}P) - 0%3p7s(^{3}P) - 0%6d(^{3}P)**
6d[3/2,5/2]$_1$	**45.05**	**45.75**	**70%[3/2,5/2]$_1$ + 30%[3/2,3/2]$_1$ + 0%7s[1/2,1/2]$_1$ - 0%[1/2,3/2]$_1$** **60%6d(^{1}P) - 39%6d(^{3}D) - 1%6d(^{3}P) + 0%7s(^{3}P)**
7s[1/2,1/2]$_1$	**45.13**	**-**	**99%[1/2,1/2]$_1$ - 0%6d[3/2,5/2]$_1$ - 0%[3/2,1/2]$_1$ - 0%3p7s[2/3,1/3]$_1$** **64%7s(^{3}P) - 36%7s(^{1}P) + 0%6d(^{3}P) - 0%3p7s(^{3}P)**
6d[1/2,3/2]$_1$	**45.21**	**45.92**	**100%[1/2,3/2]$_1$ + 0%[3/2,5/2]$_1$ - 0%7d[3/2,5/2]$_1$ - 0%[3/2,3/2]$_1$** **50%6d(^{3}D) + 36%6d(^{1}P) + 14%6d(^{3}P) - 0%7d(^{1}P)**
8s[3/2,1/2]$_1$	**45.37**	**-**	**100%[3/2,1/2]$_1$ - 0%3p8s[4/3,1/3]$_1$ - 0%7d[3/2,3/2]$_1$ - 0%3p8s[2/3,1/3]$_1$** **65%8s(^{1}P) + 35%8s(^{3}P) - 0%3p8s(^{1}P) - 0%3p8s(^{3}P)**
7d[3/2,5/2]$_1$	**45.46**	**46.16**	**72%[3/2,5/2]$_1$ + 28%[3/2,3/2]$_1$ - 0%8d[3/2,5/2]$_1$ + 0%6d[3/2,5/2]$_1$** **61%7d(^{1}P) - 38%7d(^{3}D) - 1%7d(^{3}P) + 0%6d(^{1}P)**
8s[1/2,1/2]$_1$	**45.53**	**-**	**100%[1/2,1/2]$_1$ - 0%7d[3/2,5/2]$_1$ - 0%3p8s[2/3,1/3]$_1$ +0%3p8s[4/3,1/3]$_1$** **65%8s(^{3}P) - 35%8s(^{1}P) - 0%3p8s(^{3}P) + 0%7d(^{3}P)**
7d[1/2,3/2]$_1$	**45.62**	**46.32**	**100%[1/2,3/2]$_1$ - 0%8d[3/2,5/2]$_1$ + 0%[3/2,5/2]$_1$ + 0%8d[3/2,3/2]$_1$** **50%7d(^{3}D) + 35%7d(^{1}P) + 15%7d(^{3}P) - 0%8d(^{1}P)**
8d[3/2.5/2]$_1$	**45.72**	**46.42**	**73%[3/2.5/2]$_1$ + 24%[3/2,3/2]$_1$ - 3%9s[3/2.1/2]$_1$ + 0%7d[1/2,3/2]$_1$** **61%8d(^{1}P) - 35%8d(^{3}D) - 2%9s(^{1}P) - 1%8d(^{3}P)**
9s[3/2,1/2]$_1$	**45.73**	**-**	**97%[3/2,1/2]$_1$ + 2%8d[3/2,3/2]$_1$ + 1%8d[3/2,5/2]$_1$ + 0%7d[1/2,3/2]$_1$** **63%9s(^{1}P) + 33%9s(^{3}P) - 2%8d(^{3}D) + 1%8d(^{1}P)**
8d[1/2,3/2]$_1$	**45.89**	**-**	**92%[1/2,3/2]$_1$ - 5%9d[3/2,5/2]$_1$ + 2%9d[3/2,3/2]$_1$ - 1%9s[1/2,1/2]$_1$** **46%8d(^{3}D) + 32%8d(^{1}P) + 14%8d(^{3}P) + 5%9d(^{3}P)**
9s[1/2,1/2]$_1$	**45.90**	**-**	**87%[1/2,1/2]$_1$ -5%9d[3/2,3/2]$_1$ + 4%9d[3/2,5/2]$_1$ + 3%8d[1/2,3/2]$_1$** **57%9s(^{3}P) - 30%9s(^{1}P) - 7%9d(^{3}P) + 1%8d(^{3}D)**
9d[3/2,5/2]$_1$	**45.91**	**46.60**	**75%[3/2,5/2]$_1$ + 18%[3/2,3/2]$_1$ - 5%10s[3/2,1/2]$_1$ + 1%8d[1/2,3/2]$_1$** **60%9d(^{1}P) - 31%9d(^{3}D) - 3%10s(^{1}P) - 3%9d(^{3}P)**
9d[1/2,3/2]$_1$	**46.07**	**-**	**100%[1/2,3/2]$_1$ + 0%10d[3/2,5/2]$_1$ - 0%10d[3/2,3/2]$_1$ - 0%10d[1/2,3/2]$_1$** **50%9d(^{3}D) + 34%9d(^{1}P) + 16%9d(^{3}P) - 0%10d(^{3}P)**

Table 4.5 : Experimental and calculated energy level data (in eV) for Na^+ 2p → nd, (n+1)s [n≥3].

Config./term	E_{calc}	E_{obs}	*jj* purity / *LS* purity
$3d[3/2,3/2]_1$	65.05	65.75	62%$[3/2,3/2]_1$ - 31%$[3/2,5/2]_1$ + 6%$[1/2,3/2]_1$ + 0%4s$[1/2,1/2]_1$ 97%3d(^{3}P) - 2%3d(^{3}D) - 1%3d(^{1}P) - 0%4s(^{3}P)
$3d[3/2,5/2]_1$	65.45	66.22	-55%$[3/2,5/2]_1$ - 37%$[3/2,3/2]_1$ + 8%$[1/2,3/2]_1$ + 0%4d$[3/2,5/2]_1$ 67%3d(^{3}D) - 33%3d(^{1}P) + 1%3d(^{3}P) + 0%4d(^{1}P)
$3d[1/2,3/2]_1$	65.71	66.46	86%$[1/2,3/2]_1$ + 14%$[3/2,5/2]_1$ + 0%4s$[3/2,1/2]_1$ + 0%$[3/2,3/2]_1$ 66%3d(^{1}P) + 31%3d(^{3}D) + 2%3d(^{3}P) - 0%4s(^{1}P)
$4s[3/2,1/2]_1$	67.03	67.75	93%$[3/2,1/2]_1$ + 6%$[1/2,1/2]_1$ + 0%3d$[1/2,3/2]_1$ + 0%3d$[3/2,3/2]_1$ 58%4s(^{1}P) + 41%4s(^{1}P) + 0%3d(^{1}P) + 0%3d(^{1}P)
$4s[1/2,1/2]_1$	67.29	68.02	-93%$[1/2,1/2]_1$ + 6%$[3/2,1/2]_1$ + 0%3d$[3/2,5/2]_1$ + 0%3p4s$[2/3,1/3]_1$ 58%4s(^{1}P) - 41%4s(^{3}P) - 0%3p4s(^{1}P) + 0%3d(^{1}P)
$4d[3/2,3/2]_1$	71.50	72.13	69%$[3/2,3/2]_1$ - 28%$[3/2,5/2]_1$ + 3%$[1/2,3/2]_1$ + 0%5s$[1/2,1/2]_1$ 93%4d(^{3}P) - 6%4d(^{3}D) - 1%4d(^{1}P) - 0%5s(^{3}P)
$4d[3/2,5/2]_1$	71.68	72.34	-64%$[3/2,5/2]_1$ - 31%$[3/2,3/2]_1$ + 5%$[1/2,3/2]_1$ + 0%5d$[3/2,5/2]_1$ 58%4d(^{3}D) - 40%4d(^{1}P) + 2%4d(^{3}P) + 0%5d(^{1}P)
$4d[1/2,3/2]_1$	71.94	72.58	92%$[1/2,3/2]_1$ + 7%$[3/2,5/2]_1$ + 0%5s$[3/2,1/2]_1$ + 0%5d$[3/2,5/2]_1$ 58%4d(^{1}P) + 36%4d(^{3}D) + 6%4d(^{3}P) - 0%5s(^{3}P)
$5s[3/2,1/2]_1$	72.32	73.04	98%$[3/2,1/2]_1$ + 1%$[1/2,1/2]_1$ + 0%4d$[1/2,3/2]_1$ + 0%4d$[3/2,3/2]_1$ 56%5s(^{1}P) + 43%5s(^{3}P) + 0%4d(^{1}P) + 0%4d(^{3}P)
$5s[1/2,1/2]_1$	72.58	73.30	99%$[1/2,1/2]_1$ - 1%$[3/2,1/2]_1$ + 0%4d$[3/2,5/2]_1$ + 0%3p5s$[2/3,1/3]_1$ 56%5s(^{3}P) - 43%5s(^{1}P) - 0%4d(^{1}P) - 0%3p5s(^{3}P)
$5d[3/2,5/2]_1$	74.53	75.16	71%$[3/2,5/2]_1$ + 26%$[3/2,3/2]_1$ - 2%$[1/2,3/2]_1$ + 0%6s$[3/2,1/2]_1$ 50%5d(^{1}P) - 48%5d(^{3}D) - 2%5d(^{3}P) - 0%6s(^{1}P)
$5d[1/2,3/2]_1$	74.78	75.41	81%$[1/2,3/2]_1$ - 17%6s$[3/2,1/2]_1$ + 2%$[3/2,5/2]_1$ + 0%6d$[3/2,5/2]_1$ 39%5d(^{1}P) + 37%5d(^{3}D) - 11%6s(^{1}P) + 7%5d(^{3}P)
$6s[3/2,1/2]_1$	74.82	-	83%$[3/2,1/2]_1$ + 16%5d$[1/2,3/2]_1$ + 1%5d$[3/2,5/2]_1$ + 0%$[1/2,1/2]_1$ 51%6s(^{1}P) + 32%6s(^{3}P) + 9%5d(^{1}P) + 6%5d(^{3}D)
$6s[1/2,1/2]_1$	75.08	75.80	99%$[1/2,1/2]_1$ + 0%$[3/2,1/2]_1$ + 0%5d$[3/2,5/2]_1$ + 0%3p6s$[2/3,1/3]_1$ 61%6s(^{3}P) - 38%6s(^{1}P) - 0%3p6s(^{3}P) - 0%5d(^{1}P)
$6d[3/2,5/2]_1$	76.07	76.68	75%$[3/2,5/2]_1$ + 24%$[3/2,3/2]_1$ - 1%$[1/2,3/2]_1$ + 0%7s$[3/2,1/2]_1$ 56%6d(^{1}P) - 41%6d(^{3}D) - 2%6d(^{3}P) - 0%7s(^{1}P)
$7s[3/2,1/2]_1$	76.19	-	99%$[3/2,1/2]_1$ + 0%6d$[1/2,3/2]_1$ + 0%6d$[3/2,3/2]_1$ + 0%$[1/2,1/2]_1$ 63%7s(^{1}P) + 36%7s(^{3}P) - 0%6d(^{3}D) - 0%3p7s(^{1}P)
$6d[1/2,3/2]_1$	76.33	76.94	98%$[1/2,3/2]_1$ + 1%$[3/2,5/2]_1$ + 0%7s$[3/2,1/2]_1$+0%7d$[3/2,5/2]_1$ 45%6d(^{3}D) + 42%6d(^{1}P) + 12%6d(^{3}P) + 0%7s(^{3}P)
$7s[1/2,1/2]_1$	76.46	77.17	100%$[1/2,1/2]_1$ + 0%$[3/2,1/2]_1$ + 0%6d$[3/2,5/2]_1$ + 0%3p7s$[2/3,1/3]_1$ 64%7s(^{3}P) - 36%7s(^{1}P) - 0%3p7s(^{3}P) + 0%6d(^{1}P)
$7d[3/2,5/2]_1$	76.99	77.60	76%$[3/2,5/2]_1$ + 21%$[3/2,3/2]_1$ - 1%8s$[3/2,1/2]_1$ + 0%$[1/2,3/2]_1$ 58%7d(^{1}P) - 37%7d(^{3}D) - 3%7d(^{3}P) - 1%8s(^{1}P)
$8s[3/2,1/2]_1$	77.03	-	98%$[3/2,1/2]_1$ + 1%7d$[3/2,3/2]_1$ + 1%7d$[3/2,5/2]_1$ + 0%7d$[1/2,3/2]_1$ 64%8s(^{1}P) + 35%8s(^{3}P) - 1%7d(^{3}D) + 1%7d(^{1}P)
$7d[1/2,3/2]_1$	77.26	77.87	99%$[1/2,3/2]_1$ + 0%$[3/2,5/2]_1$ + 0%8d$[3/2,5/2]_1$ + 0%8s$[3/2,1/2]_1$ 47%7d(^{3}D) + 39%7d(^{1}P) + 13%7d(^{3}P) - 0%8d(^{1}P)
$8s[1/2,1/2]_1$	77.30	-	100%$[1/2,1/2]_1$ + 0%3p8s$[2/3,1/3]_1$ + 0%8d$[3/2,5/2]_1$ + 0%7d$[3/2,5/2]_1$ 65%8s(^{3}P) - 35%8s(^{1}P) - 0%3p8s(^{3}P) + 0%7d(^{1}P)
$8d[3/2,5/2]_1$	77.59	78.20	78%$[3/2,5/2]_1$ + 21%$[3/2,3/2]_1$ + 0%$[1/2,3/2]_1$ + 0%7d$[1/2,3/2]_1$ 61%8d(^{1}P) - 36%8d(^{3}D) - 3%8d(^{3}P) + 0%7d(^{1}P)
$9s[3/2,1/2]_1$	77.69	-	100%$[3/2,1/2]_1$ + 0%8d$[3/2,3/2]_1$ + 0%8d$[1/2,3/2]_1$ + 0%8d$[3/2,5/2]_1$ 65%9s(^{1}P) + 35%9s(^{3}P) - 0%8d(^{3}D) + 0%8s(^{1}P)
$8d[1/2,3/2]_1$	77.86	78.47	99%$[1/2,3/2]_1$ - 1%9d$[3/2,5/2]_1$ + 0%$[3/2,5/2]_1$ + 0%10d$[3/2,5/2]_1$ 48%8d(^{3}D) + 37%8d(^{1}P) + 14%8d(^{3}P) - 1%9d(^{1}P)
$9s[1/2,1/2]_1$	77.96	-	98%$[1/2,1/2]_1$ + 1%9d$[3/2,5/2]_1$ - 1%9d$[3/2,3/2]_1$ + 0%10s$[3/2,1/2]_1$ 64%9s(^{3}P) - 34%9s(^{1}P) - 2%9d(^{3}P) + 0%9d(^{1}P)
$9d[3/2,5/2]_1$	78.00	78.60	80%$[3/2,5/2]_1$ + 18%$[3/2,3/2]_1$ + 0%8d$[1/2,3/2]_1$ + 0%9s$[1/2,1/2]_1$ 62%9d(^{1}P) - 33%9d(^{3}D) - 4%9d(^{3}P) + 1%8d(^{1}P)
$9d[1/2,3/2]_1$	78.26	-	82%$[1/2,3/2]_1$ - 14%10d$[3/2,5/2]_1$ + 3%10d$[3/2,3/2]_1$ + 0%$[3/2,5/2]_1$ 41%9d(^{3}D) + 29%9d(^{1}P) + 12%9d(^{3}P) + 11%10d(^{3}P)
$10d[3/2,5/2]_1$	78.29	78.89	77%$[3/2,5/2]_1$ + 14%$[3/2,3/2]_1$ + 9%9d$[1/2,3/2]_1$ + 0%10s$[1/2,1/2]_1$ 57%10d(^{1}P) - 28%10d(^{3}D) - 5%10d(^{3}P) + 4%9d(^{1}P)

Table 4.6 : Experimental and calculated energy level data (in eV) for Mg^{2+} 2p → nd,(n+1)s [n≥3].

Config./term	E_{calc}	E_{obs}	*jj* purity / *LS* purity
$3d[3/2,3/2]_1$	93.53	94.21	63%$[3/2,3/2]_1$ - 30%$[3/2,5/2]_1$ + 7%$[1/2,3/2]_1$ + 0%$2s3p[1/2,1/2]_1$ 98%$3d(^3P)$ - 2%$3d(^3D)$ - 0%$3d(^1P)$ + 0%$2s3p(^3P)$
$3d[3/2,5/2]_1$	94.28	95.12	-41%$[3/2,5/2]_1$ - 36%$[3/2,3/2]_1$ + 22%$[1/2,3/2]_1$ + 0%$4d[3/2,5/2]_1$ 84%$3d(^3D)$ - 15%$3d(^1P)$ + 1%$3d(^3P)$ + 0%$4d(^1P)$
$3d[1/2,3/2]_1$	94.80	95.59	70%$[1/2,3/2]_1$ + 29%$[3/2,5/2]_1$ + 1%$[3/2,3/2]_1$ - 0%$4d[3/2,5/2]_1$ 85%$3d(^1P)$ + 14%$3d(^3D)$ + 1%$3d(^3P)$ - 0%$4d(^1P)$
$4s[3/2,1/2]_1$	98.87	99.61	95%$[3/2,1/2]_1$ + 5%$[1/2,1/2]_1$ - 0%$3p4s[4/3,1/3]_1$ + 0%$3d[1/2,3/2]_1$ 56%$4s(^3P)$ + 44%$4s(^1P)$ + 0%$3p4s(^3P)$ + 0%$3p4s(^1P)$
$4s[1/2,1/2]_1$	99.27	100.00	-95%$[1/2,1/2]_1$ + 5%$[3/2,1/2]_1$ + 0%$3d[3/2,5/2]_1$ + 0%$3p4s[2/3,1/3]_1$ 56%$4s(^1P)$ - 44%$4s(^3P)$ + 0%$3p4s(^1P)$ + 0%$3p4s(^3P)$
$4d[3/2,3/2]_1$	105.10	-	70%$[3/2,3/2]_1$ - 27%$[3/2,5/2]_1$ + 3%$[1/2,3/2]_1$ - 0%$5s[1/2,1/2]_1$ 93%$4d(^3P)$ - 6%$4d(^3D)$ - 1%$4d(^1P)$ + 0%$3d(^3P)$
$4d[3/2,5/2]_1$	105.44	106.02	-58%$[3/2,5/2]_1$ - 30%$[3/2,3/2]_1$ + 12%$[1/2,3/2]_1$ + 0%$5d[3/2,5/2]_1$ 69%$4d(^3D)$ - 28%$4d(^1P)$ + 3%$4d(^3P)$ + 0%$5d(^1P)$
$4d[1/2,3/2]_1$	105.86	106.44	85%$[1/2,3/2]_1$ + 15%$[3/2,5/2]_1$ + 0%$[3/2,3/2]_1$ - 0%$5d[3/2,5/2]_1$ 70%$4d(^1P)$ + 25%$4d(^3D)$ + 4%$4d(^3P)$ - 0%$5d(^1P)$
$5s[3/2,1/2]_1$	107.38	108.06	99%$[3/2,1/2]_1$ + 1%$[1/2,1/2]_1$ + 0%$4d[1/2,3/2]_1$ - 0%$3p5s[4/3,1/3]_1$ 57%$5s(^1P)$ + 43%$5s(^3P)$ + 0%$4d(^1P)$ + 0%$3p5s(^1P)$
$5s[1/2,1/2]_1$	107.79	108.47	99%$[1/2,1/2]_1$ - 1%$[3/2,1/2]_1$ - 0%$4d[3/2,5/2]_1$ - 0%$3p5s[2/3,1/3]_1$ 57%$5s(^3P)$ - 43%$5s(^1P)$ + 0%$3p5s(^3P)$ + 0%$3p5s(^1P)$
$5d[3/2,5/2]_1$	110.54	111.14	-70%$[3/2,5/2]_1$ - 25%$[3/2,3/2]_1$ + 5%$[1/2,3/2]_1$ + 0%$6d[3/2,5/2]_1$ 54%$5d(^3D)$ - 43%$5d(^1P)$ + 3%$5d(^3P)$ + 0%$6d(^1P)$
$5d[1/2,3/2]_1$	110.93	111.53	94%$[1/2,3/2]_1$ + 5%$[3/2,5/2]_1$ - 0%$6s[3/2,1/2]_1$ - 0%$6d[3/2,5/2]_1$ 55%$5d(^1P)$ + 36%$5d(^3D)$ + 8%$5d(^3P)$ - 0%$6d(^1P)$
$6s[3/2,1/2]_1$	111.50	112.20	99%$[3/2,1/2]_1$ + 0%$[1/2,1/2]_1$ + 0%$5d[1/2,3/2]_1$ - 0%$3p6s[4/3,1/3]_1$ 62%$6s(^1P)$ + 38%$6s(^3P)$ + 0%$5d(^1P)$ - 0%$3p6s(^1P)$
$6s[1/2,1/2]_1$	111.91	112.59	100%$[1/2,1/2]_1$ - 0%$[3/2,1/2]_1$ - 0%$5d[3/2,5/2]_1$ - 0%$3p6s[2/3,1/3]_1$ 62%$6s(^3P)$ - 38%$6s(^1P)$ - 0%$3p6s(^3P)$ + 0%$3p6s(^1P)$
$6d[3/2,5/2]_1$	113.28	113.87	75%$[3/2,5/2]_1$ + 22%$[3/2,3/2]_1$ - 2%$[1/2,3/2]_1$ - 0%$7d[3/2,5/2]_1$ 51%$6d(^1P)$ - 45%$6d(^3D)$ - 3%$6d(^3P)$ + 0%$5d(^1P)$
$6d[1/2,3/2]_1$	113.68	114.27	96%$[1/2,3/2]_1$ + 2%$[3/2,5/2]_1$ - 2%$7s[3/2,1/2]_1$ - 0%$7d[3/2,5/2]_1$ 46%$6d(^1P)$ + 42%$6d(^3D)$ + 10%$6d(^3P)$ - 1%$7s(^1P)$
$7s[3/2,1/2]_1$	113.80	-	98%$[3/2,1/2]_1$ + 2%$6d[1/2,3/2]_1$ + 0%$6d[3/2,5/2]_1$ + 0%$[1/2,1/2]_1$ 63%$7s(^1P)$ + 36%$7s(^3P)$ + 1%$6d(^1P)$ + 0%$6d(^3D)$
$7s[1/2,1/2]_1$	114.21	114.90	100%$[1/2,1/2]_1$ - 0%$[3/2,1/2]_1$ + 0%$7d[3/2,5/2]_1$ - 0%$3p7s[2/3,1/3]_1$ 64%$7s(^3P)$ - 36%$7s(^1P)$ - 0%$3p7s(^3P)$ + 0%$7d(^1P)$
$7d[3/2,5/2]_1$	114.93	115.51	78%$[3/2,5/2]_1$ + 20%$[3/2,3/2]_1$ - 1%$[1/2,3/2]_1$ - 0%$8d[3/2,5/2]_1$ 56%$7d(^1P)$ - 40%$7d(^3D)$ - 4%$7d(^3P)$ + 0%$6d(^1P)$
$8s[3/2,1/2]_1$	115.21	-	99%$[3/2,1/2]_1$ - 1%$7d[1/2,3/2]_1$ + 0%$7d[3/2,3/2]_1$ - 0%$3p8s[4/3,1/3]_1$ 64%$8s(^1P)$ + 35%$8s(^3P)$ - 1%$7d(^3D)$ - 0%$7d(^1P)$
$7d[1/2,3/2]_1$	115.33	115.91	98%$[1/2,3/2]_1$ + 1%$[3/2,5/2]_1$ + 1%$8s[3/2,1/2]_1$ - 0%$8d[3/2,5/2]_1$ 45%$7d(^3D)$ + 42%$7d(^1P)$ + 12%$7d(^3P)$ + 0%$8s(^1P)$
$8s[1/2,1/2]_1$	115.63	-	100%$[1/2,1/2]_1$ + 0%$8d[3/2,5/2]_1$ - 0%$3p8s[2/3,1/3]_1$ - 0%$[3/2,1/2]_1$ 65%$8s(^3P)$ - 35%$8s(^1P)$ - 0%$8d(^3P)$ - 0%$3p8s(^3P)$
$8d[3/2,5/2]_1$	115.99	116.57	80%$[3/2,5/2]_1$ + 19%$[3/2,3/2]_1$ - 0%$[1/2,3/2]_1$ - 0%$9d[3/2,5/2]_1$ 59%$8d(^1P)$ - 36%$8d(^3D)$ - 4%$8d(^3P)$ + 0%$7d(^1P)$
$9s[3/2,1/2]_1$	116.25	-	100%$[3/2,1/2]_1$ - 0%$8d[1/2,3/2]_1$ + 0%$8d[3/2,3/2]_1$ + 0%$8d[3/2,5/2]_1$ 65%$9s(^1P)$ + 34%$9s(^3P)$ - 0%$8d(^3D)$ + 0%$8d(^3P)$
$8d[1/2,3/2]_1$	116.40	116.97	98%$[1/2,3/2]_1$ - 1%$9d[3/2,5/2]_1$ + 0%$[3/2,5/2]_1$ + 0%$9s[3/2,1/2]_1$ 47%$8d(^3D)$ + 39%$8d(^1P)$ + 14%$8d(^3P)$ - 1%$9d(^1P)$
$9s[1/2,1/2]_1$	116.67	-	76%$[1/2,1/2]_1$ - 15%$9d[3/2,3/2]_1$ + 9%$9d[3/2,5/2]_1$ + 0%$8d[1/2,3/2]_1$ 50%$9s(^3P)$ - 27%$9s(^1P)$ - 20%$9d(^3P)$ + 2%$9d(^3D)$
$9d[3/2,5/2]_1$	116.72	117.27	80%$[3/2,5/2]_1$ + 17%$[3/2,3/2]_1$ - 2%$9s[1/2,1/2]_1$ + 0%$8d[1/2,3/2]_1$ 60%$9d(^1P)$ - 33%$9d(^3D)$ - 5%$9d(^3P)$ - 1%$9s(^3P)$
$9d[1/2,3/2]_1$	117.13	-	96%$[1/2,3/2]_1$ - 3%$10d[3/2,5/2]_1$ + 0%$[3/2,5/2]_1$ - 0%$10d[1/2,3/2]_1$ 47%$9d(^3D)$ + 36%$9d(^1P)$ + 14%$9d(^3P)$ - 2%$10d(^1P)$
$10d[3/2,5/2]_1$	117.24	-	81%$[3/2,5/2]_1$ + 16%$[3/2,3/2]_1$ + 2%$9d[1/2,3/2]_1$ + 0%$10s[1/2,1/2]_1$ 60%$10d(^1P)$ - 32%$10d(^3D)$ - 5%$10d(^3P)$ + 2%$9d(^1P)$
$10d[1/2,3/2]_1$	117.65	-	100%$[1/2,3/2]_1$ + 0%$[3/2,5/2]_1$ + 0%$9d[1/2,3/2]_1$ + 0%$9d[3/2,5/2]_1$ 48%$10d(^3D)$ + 37%$10d(^1P)$ + 15%$10d(^3P)$ + 0%$9d(^1P)$

Table 4.7 : Experimental and calculated energy level data (in eV) for Al^{3+} $2p \rightarrow nd,(n+1)s$ [$n \geq 3$].

Config./term	E_{calc}	E_{obs}	*jj* purity / *LS* purity
$3s[3/2,1/2]_1$	103.28	104.25	72%[3/2,1/2]1 + 28%[1/2,1/2]1 - 0%2s3p[1/2,1/2]1 - 0%3d[3/2,3/2]1 85%3s(^{3}P) + 15%3s(^{1}P) - 0%2s3p(^{3}P) + 0%3s3p(^{3}P)
$3s[1/2,1/2]_1$	104.10	105.21	-72%[1/2,1/2]1 + 28%[3/2,1/2]1 - 0%3d[3/2,5/2]1 - 0%2s3p[1/2,3/2]1 85%3s(^{1}P) - 15%3s(^{3}P) + 0%3s3p(^{1}P) + 0%3p3s(^{1}P)
$3d[3/2,3/2]_1$	125.68	126.23	63%[3/2,3/2]$_1$ - 29%[3/2,5/2]$_1$ + 8%[1/2,3/2]$_1$ + 0%2s3p[1/2,1/2]$_1$ 98%3d(^{3}P) - 2%3d(^{3}D) - 0%3d(^{1}P) + 0%2s3p(^{3}P)
$3d[3/2,5/2]_1$	126.82	127.64	-36%[3/2,5/2]$_1$ - 35%[3/2,3/2]$_1$ + 29%[1/2,3/2]$_1$ + 0%4d[3/2,5/2]$_1$ 89%3d(^{3}D) - 9%3d(^{1}P) + 1%3d(^{3}P) + 0%4d(^{1}P)
$3d[1/2,3/2]_1$	127.75	128.53	63%[1/2,3/2]$_1$ + 35%[3/2,5/2]$_1$ + 2%[3/2,3/2]$_1$ - 0%4d[3/2,5/2]$_1$ 90%3d(^{1}P) + 9%3d(^{3}D) + 1%3d(^{3}P) - 0%4d(^{1}P)
$4s[3/2,1/2]_1$	135.83	136.49	96%[3/2,1/2]$_1$ + 4%[1/2,1/2]$_1$ - 0%3p4s[4/3,1/3]$_1$ + 0%3d[1/2,3/2]$_1$ 53%4s(^{3}P) + 47%4s(^{1}P) + 0%3p4s(^{3}P) + 0%3p4s(^{1}P)
$4s[1/2,1/2]_1$	136.42	137.09	-96%[1/2,1/2]$_1$ + 4%[3/2,1/2]$_1$ - 0%4d[3/2,5/2]$_1$ + 0%3p4s[2/3,1/3]$_1$ 53%4s(^{1}P) - 47%4s(^{3}P) + 0%3p4s(^{1}P) + 0%4d(^{1}P)
$4d[3/2,5/2]_1$	144.33	144.90	-56%[3/2,5/2]$_1$ - 28%[3/2,3/2]$_1$ + 16%[1/2,3/2]$_1$ - 0%5d[3/2,5/2]$_1$ 73%4d(^{3}D) - 24%4d(^{1}P) + 3%4d(^{3}P) + 0%5d(^{1}P)
$4d[1/2,3/2]_1$	144.99	145.56	81%[1/2,3/2]$_1$ + 18%[3/2,5/2]$_1$ + 0%[3/2,3/2]$_1$ - 0%5d[3/2,5/2]$_1$ 75%4d(^{1}P) + 21%4d(^{3}D) + 3%4d(^{3}P) - 0%5d(^{1}P)
$5s[3/2,1/2]_1$	148.22	148.87	99%[3/2,1/2]$_1$ + 1%[1/2,1/2]$_1$ + 0%4d[1/2,3/2]$_1$ - 0%3p5s[4/3,1/3]$_1$ 58%5s(^{1}P) + 42%5s(^{3}P) + 0%4d(^{1}P) + 0%3p5s(^{1}P)
$5s[1/2,1/2]_1$	148.82	149.43	99%[1/2,1/2]$_1$ - 1%[3/2,1/2]$_1$ + 0%5d[3/2,5/2]$_1$ - 0%3p5s[2/3,1/3]$_1$ 58%5s(^{3}P) - 42%5s(^{1}P) + 0%3p5s(^{3}P) + 0%5d(^{1}P)
$5d[3/2,5/2]_1$	152.32	152.88	-70%[3/2,5/2]$_1$ - 24%[3/2,3/2]$_1$ + 6%[1/2,3/2]$_1$ + 0%6d[3/2,5/2]$_1$ 56%5d(^{3}D) - 40%5d(^{1}P) + 4%5d(^{3}P) + 0%6d(^{1}P)
$5d[1/2,3/2]_1$	152.91	153.46	92%[1/2,3/2]$_1$ + 7%[3/2,5/2]$_1$ - 0%6d[3/2,5/2]$_1$ + 0%4d[3/2,5/2]$_1$ 58%5d(^{1}P) + 34%5d(^{3}D) + 7%5d(^{3}P) - 0%6d(^{1}P)
$6s[3/2,1/2]_1$	154.30	-	100%[3/2,1/2]$_1$ + 0%[1/2,1/2]$_1$ + 0%5d[1/2,3/2]$_1$ - 0%3p6s[4/3,1/3]$_1$ 62%6s(^{1}P) + 38%6s(^{3}P) + 0%5d(^{1}P) + 0%3p6s(^{1}P)
$6s[1/2,1/2]_1$	154.91	-	100%[1/2,1/2]$_1$ - 0%[3/2,1/2]$_1$ + 0%6d[3/2,5/2]$_1$ - 0%3p6s[2/3,1/3]$_1$ 62%6s(^{3}P) - 38%6s(^{1}P) + 0%3p6s(^{3}P) + 0%6d(^{1}P)
$6d[3/2,5/2]_1$	156.62	157.11	76%[3/2,5/2]$_1$ + 21%[3/2,3/2]$_1$ - 2%[1/2,3/2]$_1$ - 0%7d[3/2,5/2]$_1$ 50%6d(^{1}P) - 45%6d(^{3}D) - 4%6d(^{3}P) + 0%5d(^{1}P)
$6d[1/2,3/2]_1$	157.21	157.69	97%[1/2,3/2]$_1$ + 2%[3/2,5/2]$_1$ - 0%7s[3/2,1/2]$_1$ - 0%7d[3/2,5/2]$_1$ 48%6d(^{1}P) + 41%6d(^{3}D) + 10%6d(^{3}P) - 0%7d(^{1}P)
$7s[3/2,1/2]_1$	157.74	-	100%[3/2,1/2]$_1$ + 0%6d[1/2,3/2]$_1$ + 0%[1/2,1/2]$_1$ - 0%3p7s[4/3,1/3]$_1$ 64%7s(^{1}P) + 36%7s(^{3}P) + 0%6d(^{1}P) + 0%3p7s(^{1}P)
$7s[1/2,1/2]_1$	158.35	-	100%[1/2,1/2]$_1$ + 0%7d[3/2,5/2]$_1$ - 0%[3/2,1/2]$_1$ - 0%3p7s[2/3,1/3]$_1$ 64%7s(^{1}P) - 36%7s(^{1}P) + 0%7d(^{1}P) + 0%7d(^{3}P)
$7d[3/2,5/2]_1$	159.20	159.68	79%[3/2,5/2]$_1$ + 20%[3/2,3/2]$_1$ - 1%[1/2,3/2]$_1$ - 0%8d[3/2,5/2]$_1$ 56%7d(^{1}P) - 40%7d(^{3}D) - 4%7d(^{3}P) + 0%6d(^{1}P)
$7d[1/2,3/2]_1$	159.79	160.17	94%[1/2,3/2]$_1$ - 4%8s[3/2,1/2]$_1$ + 1%[3/2,5/2]$_1$ - 0%8d[3/2,5/2]$_1$ 43%7d(^{1}D) + 40%7d(^{1}P) + 12%7d(^{3}P) - 3%8s(^{1}P)
$8s[3/2,1/2]_1$	159.87	-	96%[3/2,1/2]$_1$ + 4%7d[1/2,3/2]$_1$ + 0%7d[3/2,5/2]$_1$ - 0%8d[3/2,5/2]$_1$ 62%8s(^{1}P) + 34%8s(^{3}P) + 2%7d(^{1}P) + 1%7d(^{3}D)
$8s[1/2,1/2]_1$	160.48	-	100%[1/2,1/2]$_1$ + 0%8d[3/2,5/2]$_1$ - 0%[3/2,1/2]$_1$ - 0%3p8s[2/3,1/3]$_1$ 65%8s(^{3}P) - 35%8s(^{1}P) - 0%8d(^{3}P) + 0%8d(^{1}P)
$8d[3/2,5/2]_1$	160.87	-	80%[3/2,5/2]$_1$ + 18%[3/2,3/2]$_1$ - 0%[1/2,3/2]$_1$ - 0%9d[3/2,5/2]$_1$ 59%8d(^{1}P) - 36%8d(^{3}D) - 4%8d(^{3}P) + 0%7d(^{1}P)
$9s[3/2,1/2]_1$	161.38	-	98%[3/2,1/2]$_1$ - 2%8d[1/2,3/2]$_1$ - 0%2s3p[1/2,1/2]$_1$ + 0%8d[3/2,3/2]$_1$ 64%9s(^{1}P) + 34%9s(^{3}P) - 1%8d(^{3}D) - 1%8d(^{1}P)
$8d[1/2,3/2]_1$	161.46	-	97%[1/2,3/2]$_1$ + 2%9s[3/2,1/2]$_1$ - 1%9d[3/2,5/2]$_1$ + 0%[3/2,5/2]$_1$ 45%8d(^{3}D) + 39%8d(^{1}P) + 13%8d(^{3}P) + 1%9s(^{1}P)
$9d[3/2,5/2]_1$	162.00	-	47%[3/2,5/2]$_1$ + 36%9s[1/2,1/2]$_1$ + 16%[3/2,3/2]$_1$ + 0%8d[1/2,3/2]$_1$ 38%9d(^{1}P) - 25%9d(^{3}D) + 24%9s(^{3}P) - 12%9s(^{1}P)
$9s[1/2,1/2]_1$	162.02	-	62%[1/2,1/2]$_1$ - 33%9d[3/2,5/2]$_1$ - 3%9d[3/2,3/2]$_1$ - 0%8d[1/2,3/2]$_1$ 40%9s(^{3}P) - 22%9d(^{1}P) - 22%9s(^{1}P) + 11%9d(^{3}D)
$9d[1/2,3/2]_1$	162.61	-	97%[1/2,3/2]$_1$ - 2%10d[3/2,5/2]$_1$ + 0%[3/2,5/2]$_1$ + 0%10s[3/2,1/2]$_1$ 47%9d(^{3}D) + 37%9d(^{1}P) + 14%9d(^{3}P) - 2%10d(^{1}P)
$10d[3/2,5/2]_1$	162.82	-	81%[3/2,5/2]$_1$ + 16%[3/2,3/2]$_1$ + 2%9d[1/2,3/2]$_1$ + 0%9d[3/2,5/2]$_1$ 61%10d(^{1}P) - 32%10d(^{3}D) - 5%10d(^{3}P) + 1%9d(^{1}P)
$10d[1/2,3/2]_1$	163.43	-	100%[1/2,3/2]$_1$ + 0%[3/2,5/2]$_1$ + 0%9d[1/2,3/2]$_1$ + 0%9d[3/2,5/2]$_1$ 48%10d(^{3}D) + 37%10d(^{1}P) + 15%10d(^{3}P) + 0%9d(^{1}P)

Table 4.8 : Experimental and calculated energy level data (in eV) for Si^{4+} 2p → nd, ns [n≥3].

status with purities usually in excess of 70% but always above 50%. An exception to this is the $2p^5 3d[3/2,5/2]_1$ term for Al^{3+} which possesses a leading eigenvector purity of only 41% as it is strongly mixed with the $3d[3/2,3/2]_1$ and $3d[1/2,3/2]_1$ terms. The same term for Si^{4+} has similar characteristics, again mixing strongly with the $3d[3/2,3/2]_1$ and $3d[1/2,3/2]_1$ terms. The Si^{4+} $2p^5 9d[3/2,5/2]_1$ term also displays a jj purity below 50%, strong mixing with the $2p^5 9s[1/2,1/2]_1$ term being responsible in this case. Generally speaking, the leading jj eigenvector purity increased in dominance as the sequence progressed from Na^+ to Si^{4+}. This is to be expected as with increasing Z and ionic charge, jj coupling becomes more dominant over LS coupling due to an increase in spin-orbit interactions (Z^4 dependence) relative to Coulombic interactions (Z dependence). Although LS purities were often above 50%, the coupling scheme was deemed unsuitable for designation of the Rydberg series as, with increasing n, strong mixing led to severe competition for leading eigenvector status. In fact, a switch in dominance was seen to occur whereby the leading eigenvectors of the nd series flipped from $nd^3D \rightarrow nd^1P$ and vice versa. This occurred for Mg^{2+}, Al^{3+} and Si^{4+} between n=5 and 7 but was not mirrored in Na^+, LS coupling being better suited to singly ionised sodium's lower atomic number and ionic charge. Obviously, a coherent Rydberg series could therefore not be unambiguously assigned within an LS framework.

Referring back to tables 4.1, 4.2, 4.3 and 4.4, we see that for Na^+, our measured energies are in excellent agreement with those listed by Kelly (1987). For the most part, agreement is within the limits of our experimental error. Although Kelly did not use Lucatorto and McIlrath's (1976) published energies for the nd series ($n \geq 5$), they are listed here for further comparison. It has been noted previously (Lamoureux and Radojevic 1982, Hibbert and Scott 1994) that for Na^+ some of the $2p^5ns$ and $2p^5nd$ terms lie very close in energy. This close proximity meant that within the limits of our experimental resolution, we were unable to measure any members of the $2p^6 \rightarrow 2p^5ns$ series as they were blended into the stronger overlapping $2p^6 \rightarrow 2p^5nd$ series. The existence of small shoulders on the lower energy sides of the $2p^6 \rightarrow 2p^5nd$ transitions coupled with the calculated gf values for both the $2p^5ns$ and $2p^5nd$ series allows some degree of confidence in labelling all of the strong features as belonging to the $2p^6 \rightarrow 2p^5nd$ series. We note that through quantum defect considerations, our assignments for the transitions

at 45.75 and 45.92eV are to the $2p^6 \rightarrow 2p^5 6d$ lines. This agrees with Lucatorto and McIlrath's designation but conflicts with that of Kelly, who favoured a $2p^5 7s$ label. Indeed, using our assignments and the Rydberg formula given by equation [3.1], where we have calculated the Rydberg constant for sodium (R_{Na}) to be 13.60522eV¶, the inferred $2s^2 2p^5\ ^2P_{3/2}$ and $^2P_{1/2}$ series limits were 47.28 ± 0.02eV and 47.44 ± 0.02eV respectively. These compare with those of Moore (1949) at 47.30 and 47.47eV and those given by Lucatorto and McIlrath at 47.29 and 47.46eV.

For Mg^{2+} (see table 4.2), we have measured the nd series up to n=10 and again agreement with Kelly's listed energies, to within our experimental error, is evident. The ns series from n=4 to 6 can now clearly be discerned (see figure 4.2) but beyond n=6, this weaker series becomes obscured by the overlapping higher members of the nd series. For Mg^{2+}, the $2s^2 2p^5\ ^2P_{3/2}$ and $^2P_{1/2}$ limits were again inferred via equation [3.1] (R_{Mg} = 13.605555eV), to lie at 80.12 ± 0.05eV and 80.38 ± 0.05eV respectively. These compare favourably with those given by Moore (1949) at 80.14 and 80.42eV. For Al^{3+} (see table 4.3), we have measured the lower members of both series in agreement with the previous literature values (Kelly 1987, Jamelot et al 1972) and we have extended the series by resolving six new lines corresponding to the n=6 and 7 members of the ns series and to the n=8 and 9 members of the nd series. The measurements have yielded values (via equation 3.1, R_{Al} = 13.605444eV) of 119.99 ± 0.09eV and 120.38 ± 0.09eV for the $2s^2 2p^5\ ^2P_{3/2}$ and $^2P_{1/2}$ limits respectively. These limits have been stated by Moore (1949) as being located at 119.99 and 120.42eV. Finally, in table 4.4, we list energies for the ns, nd series of Si^{4+}, once again drawing comparison with those listed by Kelly (1987). For the first time we present new energy measurements for the 5s and 7d line pairs. Values for the $2s^2 2p^5\ ^2P_{3/2}$ and $^2P_{1/2}$ limits of 166.73 ± 0.17eV and 167.22 ± 0.17eV have been calculated (R_{Si} = 13.605399eV) which compare with those given by Moore of 166.77 and 167.40eV. The energy difference (ΔE) between our measured limits is 0.49eV. This compares with our calculated ΔE of 0.56eV and the ΔE between the limits inferred

---

¶ We have calculated the Rydberg constants for all five members of the neon isoelectronic sequence studied here using the mass and abundance of the isotopes listed in the CRC handbook of chemistry and physics (Lide 1993).

from Kelly's (1987) listed transition energies of 0.63eV. Finally, to further corroborate our results, we have carried out a quantum defect analysis for each member of the isoelectronic sequence and have found the effective principal quantum number ($n^* = n - \delta$) to vary smoothly along both the $2p \rightarrow ns$ and $2p \rightarrow nd$ series.

4.4.2. $2s \rightarrow np$ ($n \geq 3$) inner shell autoionising series : $Ne^0 \rightarrow Si^{4+}$

In tables 4.9 to 4.13, we compare our measured data for the $2s2p^6np\ ^1P_1$ series, in Ne^0 through to Si^{4+}, with a variety of relevant theoretical and experimental measurements found in the literature. As mentioned in section 4.1.1, the majority of investigations on the neon isoelectronic sequence have concerned neutral neon and parameters relating to its $2s2p^6np\ ^1P_1$ series are now well established. The wealth of data currently available on Ne^0 therefore allowed us to assess our instrument's capability to accurately measure this narrow autoionising series. We have deconvolved our $2s2p^6np\ ^1P_1$ series spectra for Ne^0 through to Si^{4+} (see figures 4.3 and 4.4) with a 4 pixel FWHM Lorentzian instrument function and all DLP experimental data shown in tables 4.9 to 4.13 relate to the deconvolved resonances. The data presented in the tables describes the asymmetric nature of the $2s2p^6np\ ^1P_1$ resonances, indicative of the interaction of an excited state with an underlying direct photoionisation continuum, in terms of the parameters first formulated by Fano (1961) (see chapter 1, section 1.3). We have fitted each resonance using equation [1.42] in order to extract the relevant centre energy (ε_0), width (Γ) and profile index (q). Each resonance was fitted using a variety of different data point windows and different CEMA settings, the average for each parameter being our final result. Only Γs and qs for those members of the $2s2p^6np\ ^1P_1$ series which had sufficient strength to be fitted without the undue influence of noise are listed in the tables. Noise levels were not so critical for centre energy measurements. These measurements were therefore extended to higher series members.

We have used the profile parameters of the $Ne^0\ 2s2p^63p\ ^1P$ resonance, measured by Codling et al (1967), to obtain our instrument function (see section 2.3.5, method (b)). We should therefore expect that deconvolving our measurement of this resonance should return a profile which possesses the same parameters as those measured by Codling et

al. However, from table 4.9 it can be seen that we get Γ = 19meV instead of 13meV. This is because the neon sequence spectra were deconvolved in pixel space (to save on processing time) which means that our deconvolved resonance profile is subject to the spatial resolution constraints of our detector. The plate factor at the energy position corresponding to the 3p resonance (45.55eV) is 6meV. It is therefore not possible to measure a width (Γ) of 13meV which would correspond to only two pixels.

Although the Ne^0 $2s2p^6np\ ^1P$ resonances are too narrow for us to measure, this is not the case for the series in Na^+ to Si^{4+}. The 3p members for Na^+ to Si^{4+} are greater than three pixels in width (after deconvolution) and are not subject to spatial resolution constraints. The 3p parameters given in tables 4.10 to 4.13 are therefore expected to be accurate. However, series members with n>3 *are* limited by the detector's spatial resolution and for this reason errors for their Γ and q parameters could not be established. For all $2s2p^63p\ ^1P$ resonances, errors for the Γ and q parameters were determined by deconvolving the same resonances with upper and lower limits for the instrument function i.e. 3 pixel FWHM and 5 pixel FWHM Lorentzians. The errors on all energy measurements were equal to three times the plate factor at the energy of interest.

Ne⁰ : For Ne^0 (see table 4.9), we have measured the resonance energies of the first six members of the $2s^2 \rightarrow 2s2p^6np\ ^1P_1$ series. However, only the first three were strong enough to allow Γ and q parameters to be extracted. Recent high resolution experiments (Schulz et al 1996, Langer et al 1997) have now established a consensus with the original measurements of Codling et al (1967) in that the 3p member has a width (Γ) of ~13meV and a q value of ~-1.6. We have measured the 3p member to possess a Γ of 19meV and a q value of -1.5. Although, for the reasons given above, our neon Γ measurements are incorrect, the measured q values for the $2s2p^6np\ ^1P$ series still conform to those of Codling et al's and verify Fano's assertion that, within a series, the q value should be approximately constant (see section 1.3, equation [1.55]).

By using a quantum defect analysis i.e. using equation [3.1], both the $2s2p^6\ ^2S_{1/2}$ series limit and the effective principal quantum numbers were ascertained. The series limit was found to be 48.48eV which agrees well with that of both Schulz et al at 48.46eV and Codling et al at 48.48eV. Taking the width of the $2s2p^63p\ ^1P$ member (Γ_{3p}) to be 13meV, we should expect from Fano's criterion (Fano and Cooper 1965), which states that within

n	E_{exp}	E_{calc}	E (Chan et al 1992)	E (Schulz et al 1996)	E (Codling et al 1967)	E (Stener et al 1995)†	E (Hibbert and Scott 1994)†
3	45.55(±0.02)	47.25	45.55	45.54	45.55	46.25	47.55
4	47.12(±0.02)	48.91	47.13	47.12	47.12	47.40	49.08
5	47.69(±0.02)	49.50	47.68	47.70	47.69	47.81	49.63
6	47.97(±0.02)	49.78	47.98	47.97	47.97	-	49.90
7	48.12(±0.02)	49.93	-	48.12	48.12	-	50.05
8	48.21(±0.02)	50.02	-	48.21	48.21	-	-
$2s2p^6(^2S_{1/2})$ *limit*	48.48(±0.02)	50.29	48.48	48.46	48.48	-	50.41

n	Γ_{exp}¶	Γ (Codling et al 1967)	Γ (Langer et al 1997)	Γ (Langer et al 1997)†	Γ (Stener et al 1995)†	Γ (Schulz et al 1996)†	Γ (Hibbert and Scott 1994)†
3	0.019	0.0130	0.0132	0.0186	0.0139	0.0349	0.0230
4	0.016	0.0045	0.0057	0.0043	0.0039	0.0067	0.0080
5	0.021	0.0020	0.0036	0.0018	0.0016	0.0025	0.0040
6	-	-			-	0.0013	0.0017
7	-	-			-	0.0007	0.0009
8	-	-			-	0.0005	-

n	q_{exp}¶	q (Codling et al 1967)	q (Langer et al 1997)	q (Langer et al 1997)†	q (Stener et al 1995)†	q (Hibbert and Scott 1994)†	n^*_{exp}	n^* (Schulz et al 1996)
3	-1.5	-1.6	-1.6	-1.6	-3.7	-2.0	2.16	2.16
4	-1.5	-1.6	-1.5	-1.9	-4.0	-2.9	3.17	3.17
5	-1.6	-1.6	-1.5	-1.9	-4.1	-1.2	4.16	4.18
6	-	-			-	-2.6	5.16	5.17
7	-	-			-	-1.9	6.15	6.16
8	-	-			-	-	7.07	7.16

† Theoretical values

¶ Errors not given due to Γ and q values being incorrect as a result of an insufficient number of pixels across the resonance.

Table 4.9 : Experimental and theoretical values of Fano parameters for Ne^0 2s → np (n=3-8) autoionising transitions. All energies and widths are given in eV. DLP experimental values are denoted with the subscript (exp). Hartree-Fock calculations are denoted with the subscript (calc).

the confines of a single autoionising Rydberg series, the width of each member should vary as the inverse cube of its effective principal quantum number (n*) (see section 1.3, equation [1.56]), that Γ_{4p} and Γ_{5p} are equal to ~4meV and ~2meV respectively. Codling et al's measured Γ_{4p} and Γ_{5p} of 4.5meV and 2meV therefore verify Fano's theory. The large discrepancy between these values and the DLP values (Γ_{4p} = 16meV and Γ_{5p} = 21meV after deconvolution) further demonstrates the spatial resolution constraints of the DLP detector. Recent theoretical calculations on the widths of the series members tend to confirm the original experimental values of Codling et al (1967) with both Stener et al (1995) and Langer et al (1997) in excellent agreement with each other while Hibbert (1994, 1998) overestimates the Ne^0 $2s2p^6np\ ^1P_1$ widths by an average of ~46%. Agreement on q values is somewhat less apparent. Stener et al (1995) predict values which remain relatively constant between -3.7 and -4.0, almost a factor of 2.5 larger than seen experimentally. They attribute this discrepancy to the limitations of experimental resolution. However, the q values obtained in R-Matrix calculations by Hibbert (1994, 1998) of an average of -2.0 for n = 3-7 and by Langer et al (1997) of $-1.6 \leq q \leq -1.9$ for n = 3-5, favour the experimental values.

As a last remark on Ne^0, it must be noted that within the vicinity of the $2s2p^6np\ ^1P_1$ series, a number of double excitation series from the $2p^43snp$ and $2p^43pns$, nd configurations have been revealed in great detail, first by Codling et al (1967) with 12meV resolution and more recently by Schulz et al (1996) with 3meV resolution and by Wills et al (1998) with 20meV resolution (see section 4.1.1). Their presence is not thought to perturb the $2s2p^6np\ ^1P_1$ series to any great extent, a fact re-enforced by our own Hartree-Fock calculations which we will discuss later. Many members of these complex intertwining double excitation series have now been untangled and clearly resolved. In figure 4.7, we demonstrate the extent to which the region is now known by showing the data of Schulz et al (1996) which we compare with our DLP data for the same region. Although visible in the DLP data, the doubly excited resonances are broadened and smeared and thus, have not been treated here. We have, however, measured the energy position of the strongest double excitation, which is common to both the $2s^22p^6 \rightarrow 2p^43s(^2P)3p$ and the $2s^22p^6 \rightarrow 2p^43p(^2P)3s$ transitions and is clearly visible at 44.98 ± 0.02eV (see figure 4.7(a)).

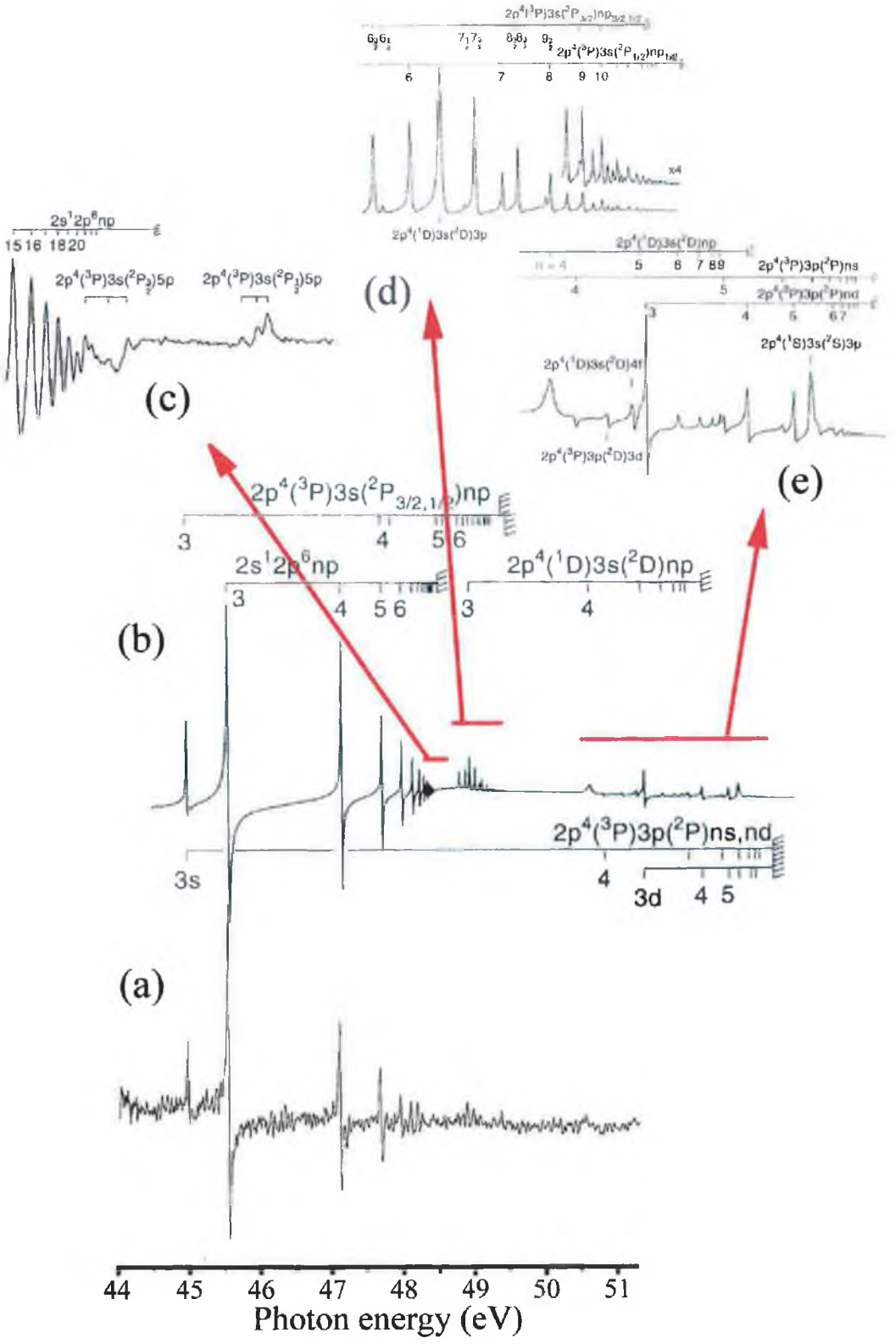

Figure 4.7 : The 2s region of Ne^0 as recorded by DLP photoabsorption in (a) and by high resolution photoion techniques in (b), (c), (d) and (e) (after Schulz et al 1996). (c) shows the region from 48.4 to 48.6eV, (d) the region from 48.72 to 49.46eV and (e) the region from 50.3 to 53.2eV.

Na⁺ : For Na^+ (see table 4.10), we have measured the resonance energies of the first five members of its $2s2p^6np\ ^1P_1$ series. The energy measurements compare well (within 0.04eV) with the experimental values of Lucatorto and McIlrath (1976) and also with the values of Dorn et al (1995). Theoretical predictions by Zatsarinny (1995) also show excellent agreement for the first five members with the recent predictions of Kupliauskiene (1998) exhibiting a slight overestimation. Employing a quantum defect analysis, a $2s2p^6\ ^2S_{1/2}$ limit of 80.11 ± 0.06eV was determined. Lucatorto and McIlrath have stated a value for the same limit of 80.09eV. As with Ne^0, the higher members (n > 5) were weak in strength and showed significant contamination due to noise. Γ and q parameters could therefore only be extracted for n = 3-5. As we have seen for Ne^0, the q values for the Na^+ 2s → np series also remain relatively static as the Rydberg series progresses, this time at an average value of ~-2.1 which indicates that coupling of the resonances to the underlying continua is not as strong as in the case of Ne^0. It is also apparent that as for Ne^0, the spatial resolution of our detector is responsible for a lower limit on the width measurements (0.04eV), this performance limitation quickly arising at just n = 4. The DLP Γ_{4p} and Γ_{5p} measurements (after deconvolution) are therefore clearly overestimated due to an insufficient number of pixels across the resonances. From Fano's theory, we again apply an inverse cube relationship between each series member's n* value and its width and infer from a measured Γ_{3p} of 0.05eV that Γ_{4p} should be ~0.017eV and Γ_{5p} ~ 0.008eV. Theoretical width calculations by Zatsarinny (1995) support our findings, excellent agreement with our measured Γ_{3p} and inferred Γ_{4p} and Γ_{5p} values being apparent. Zatsarinny also concludes that the decay widths of the $2s2p^6 \rightarrow 2s2p^6np\ ^1P_1$ members are dominated by the εd channel, its contribution being almost two orders of magnitude greater than that of the εs channel. Theoretical Γ and q values for the Na^+ 2s → np series have also been calculated by Hibbert (1998). As with Ne^0, Hibbert's predictions for the series q values, with an average value of -2.1, are in close agreement with those measured here. The width of the 3p member is again overestimated, this time by ~42%. Assuming, as was the case for his Ne^0 calculations, a similar overestimate of 42% for the higher Rydberg members, actual values of ~0.018eV and ~0.007eV for Γ_{4p} and Γ_{5p} would be expected. These values are in close agreement with Zatsarinny's results and also with those predicted here via application of Fano's

n	E_{exp}	E_{calc}	E (Lucatorto and McIlrath 1976)	E (Dorn et al 1995)	E (Zatsarinny 1995)†	E (Kupliauskiene 1998) †	E (Hibbert 1998) †
3	69.96(±0.04)	71.57	69.95	69.97	69.95	70.73	71.95
4	75.20(±0.05)	77.01	75.18	75.21	75.20	76.02	77.08
5	77.19(±0.05)	79.03	77.17	77.18	77.20	-	79.05
6	78.17(±0.05)	80.01	78.14	-	78.18	-	80.02
7	78.74(±0.05)	80.57	78.70	-	78.73	-	80.57
8	-	80.91	79.03	-	-	-	-
$2s2p^6(^2S_{1/2})$ *Limit*	80.11(±0.06)	81.95	80.09	-	80.11	-	81.94

n	Γ_{exp}	Γ (Zatsarinny 1995)†	Γ (Hibbert 1998) †	q_{exp}	q (Hibbert 1998) †	n^* (Lucatorto and McIlrath 1976)	n^*_{exp}
3	0.05(±0.01)	0.054	0.086	-2.0(±0.1)	-1.9	2.32	2.32
4	0.04¶	0.017	0.031	-2.1¶	-2.0	3.33	3.33
5	0.04¶	0.007	0.012	-2.2¶	-2.2	4.32	4.32
6	-	0.004	0.009	-	-2.1	5.28	5.29
7	-	0.002	0.005	-	-2.3	6.24	6.30

† Theoretical values

¶ Errors not given due to Γ and q values being incorrect as a result of an insufficient number of pixels across the resonance.

Table 4.10 : Experimental and theoretical values of Fano parameters for Na^+ 2s → np (n=3-8) autoionising transitions. All energies and widths are given in eV. DLP experimental values are denoted with the subscript (exp). Hartree-Fock calculations are denoted with the subscript (calc).

formula to our DLP Γ_{3p} measurement.

Mg²⁺ : Table 4.11 shows our measurements of the $2s^22p^6 \rightarrow 2s2p^6np\ ^1P_1$ series for Mg^{2+}. Here, the trend continues in that the resonance energies of the first five members could be measured but only the n = 3-5 members were sufficient in strength for meaningful Fano parameter extraction. The measured energies compare well with those of Esteva and Mehlman (1974) and also those of Kastner et al (1977).

n	E_{exp}	E_{calc}	E (Esteva and Mehlman 1974)	E (Kastner et al 1977)	E (Hibbert 1998) †
3	97.98(±0.07)	99.55	98.01	98.02	99.92
4	108.46(±0.09)	110.28	108.45	108.44	110.25
5	112.60(±0.09)	114.44	112.55	112.59	114.35
6	114.68(±0.09)	116.51	114.72	-	116.40
7	115.87(±0.10)	117.69	115.96	115.82	117.56
8	-	118.43	116.64	-	-
$2s2p^6(^2S_{1/2})$ Limit	118.86(±0.10)	120.68	118.65	118.77	120.55

n	Γ_{exp}	Γ (Hibbert 1998) †	q_{exp}	q (Hibbert 1998) †	n^* (Kastner et al 1977)	n^*
3	0.10(±0.01)	0.203	-2.1(±0.1)	-2.2	2.43	2.42
4	0.07¶	0.070	-2.8¶	-2.3	3.44	3.43
5	0.08¶	0.026	-2.9¶	-2.6	4.45	4.42
6	-	0.021	-	-1.9	5.50	5.41
7	-	0.008	-	-5.2	6.44	6.40

† Theoretical values

¶ Errors not given due to Γ and q values being incorrect as a result of an insufficient number of pixels across the resonance.

Table 4.11 : Experimental and theoretical values of Fano parameters for Mg^{2+} 2s → np (n=3-8) autoionising transitions. All energies and widths are given in eV. DLP experimental values are denoted with the subscript (exp). Hartree-Fock calculations are denoted with the subscript (calc).

Our inferred $2s2p^6\ ^2S_{1/2}$ limit lies at 118.86 ± 0.10eV which compares with Esteva and Mehlman's value of 118.65eV and Kastner et al's value of 118.77eV. Unfortunately, only Hibbert's recent theoretical calculations (Hibbert 1998) allow a comparative assessment of the Γ and q measurements reported here. For Ne^0, Hibbert overestimated Γ_{3p} by ~46%. Γ_{4p} and Γ_{5p} were also overestimated by ~46%. For Na^+, Hibbert's prediction for Γ_{3p} was again too broad, this time by ~42%. Again, this overestimate was replicated for Γ_{4p} and Γ_{5p}. For Mg^{2+}, we see that Hibbert's prediction for Γ_{3p} is ~50% broader than that observed via the DLP technique employed here. We therefore suggest that Hibbert's Γ_{4p}

and Γ_{5p} values are overestimated and should be closer to 0.035eV and 0.013eV respectively. Applying Fano's formula relating a resonance's n* value to its width, we obtain, using the DLP Γ_{3p} measurement of 0.10eV, widths for Γ_{4p} and Γ_{5p} of 0.035eV and 0.016eV respectively. As with Ne^0 and Na^+, the widths of the Mg^{2+} 2s $\rightarrow$ np series members could not be accurately determined beyond n=3, this being due, as mentioned earlier, to spatial resolution limitations. The derived widths are therefore more likely to represent the actual values than the measured values of 0.07eV and 0.08eV shown in table 4.11. The measured q values, however, are in good agreement with theoretical estimates (Hibbert 1998) but are slightly higher with an average value of -2.6 compared to the theoretical average over the first three members of -2.4.

Al^{3+} : With Al^{3+} (see table 4.12), we have only been successful in determining the resonance energies of the first two members of the $2s^22p^6 \rightarrow 2s2p^6np\ ^1P_1$ series. Our measured energies agree well with those of Kastner et al (1977) and are slightly lower than those reported by Carillon et al (1972).

We see no evidence for the presence of $2s2p^6np\ ^3P$ series members which according to our calculations possess oscillator strengths a factor of ~500 weaker than equivalent members of the $2s2p^6np\ ^1P$ series. They would therefore be totally submerged in our background noise levels. The n=3 and n=4 members of the triplet series are predicted to lie 0.44 and 0.14eV, respectively, below the n=3 and 4 members of the singlet series The measured separation between ^1P and ^3P members for n=3 and 4 were reported as 1.43eV and 0.39eV by Carillon et al (1972) and 0.16 and 0.17eV by Kastner et al (1977). The large discrepancy between each set of measurements and between the measurements and our calculations casts further doubt as to the validity of both Kastner et al's and Carillon et al's $2s2p^6np\ ^3P$ observations.

From our measurements of the $2s2p^6np\ ^1P$ series, Γ and q values have been determined and compared with the theoretical calculations of Hibbert (1998). As with the preceding three members of the isoelectronic sequence, Hibbert overestimates Γ_{3p} for the Al^{3+} $2s^22p^6 \rightarrow 2s2p^63p\ ^1P_1$ resonance, this time by ~20%. Assuming the calculated Γ_{4p} value to also be too broad by ~20%, we expect a more accurate estimate to be 0.069eV. This compares with a derived value from the DLP Γ_{3p} measurement, of 0.075eV. In light of the agreement, we conclude that 0.075eV is more indicative of the true width associated

n	E_{exp}	E_{calc}	E (Carillon et al 1972)	E (Kastner et al 1977)	E (Hibbert 1998) †
3	129.76(±0.12)	131.30	131.23	129.75	131.65
4	147.01(±0.14)	148.76	147.35	146.94	148.61
5	-	155.72	-	153.87	155.49
6	-	159.23	-	157.36	158.95
7	-	161.25	-	159.38	160.94
8	-	162.52	-	160.64	-
$2s2p^6(^2S_{1/2})$ *limit*	-	166.43	-	164.48	166.15

n	Γ_{exp}	Γ (Hibbert 1998) †	q_{exp}	q (Hibbert 1998) †	*n** (Kastner et al 1977)	*n**§
3	0.21(±0.02)	0.263	-2.0(±0.1)	-2.2	2.50	2.50
4	0.10¶	0.086	-1.9¶	-3.1	3.52	3.53
5	-	0.042	-	-3.2	4.53	-
6	-	0.023	-	-3.0	5.53	-
7	-	0.014	-	-2.3	6.54	-

† Theoretical values

§ Obtained by using Kastner et al's value for the $2s2p^6\ ^2S_{1/2}$ limit.

¶ Errors not given due to Γ and q values being incorrect as a result of an insufficient number of pixels across the resonance.

Table 4.12 : Experimental and theoretical values of Fano parameters for Al^{3+} 2s → np (n=3-8) autoionising transitions. All energies and widths are given in eV. DLP experimental values are denoted with the subscript (exp). Hartree-Fock calculations are denoted with the subscript (calc).

with the Al^{3+} $2s^22p^6 \rightarrow 2s2p^64p\ ^1P_1$ resonance, than our detector limited measured width of 0.10eV. Continuing to compare our measurements to the calculations of Hibbert, we find agreement on the value of q_{3p}, both being ~-2.0. However, q_{4p} does not correlate as well, the experimental value being considerably lower.

Si^{4+} : For Si^{4+} (see table 4.13), we could only measure the 3p member of the $2s^22p^6 \rightarrow 2s2p^6np\ ^1P_1$ series as subsequent members were too weak to be drawn out of the considerable noise levels present at the upper energy extremes of our measuring

capability. A comparison of our experimental values with the theoretical data of Hibbert (1998) would suggest that Hibbert's Γ_{3p} value is overestimated by ~33% and on

n	E_{exp}	E_{calc}	E (Hibbert 1998)†	Γ_{exp}¶	Γ (Hibbert 1998)†	q_{exp}¶	q (Hibbert 1998)†
3	165.39(±0.17)	166.89	167.02	0.3	0.45	-1.6	-2.7
4	-	192.45	192.06	-	0.15	-	-2.9
5	-	202.86	202.39	-	0.06	-	-6.4
6	-	208.15	207.64	-	0.04	-	-2.1
7	-	211.22	210.68	-	0.03	-	-2.4
8	-	213.15	-	-	-	-	-
$2s2p^6(^2S_{1/2})$ limit	-	219.15	218.66				

† Theoretical values

¶ Errors are not given as the degree of resonance profile asymmetry is dependent on experimental conditions (see section 4.5)

Table 4.13 : Experimental and theoretical values of Fano parameters for Si^{4+} 2s → np (n=3-8) autoionising transitions. All energies and widths are given in eV. DLP experimental values are denoted with the subscript (exp). Hartree-Fock calculations are denoted with the subscript (calc).

the basis of the arguments presented above, we would expect a similar overestimate for the Γ_{4p} value. Hence, a more probable value for Γ_{4p} than that given by Hibbert, would be 0.10eV. Unfortunately, as we have no experimental energy value for the 4p member and thus no n* value, we are unable to use our experimental data, as we have done with the other sequence members, to infer a value for Γ_{4p}.

Summary of observations on inner shell resonances for $Na^+ \rightarrow Si^{4+}$: Comparison with calculations : To summarise, our measured values of Γ and q for the $2s2p^63p\ ^1P$ resonance in Na^+ to Si^{4+}, which we consider accurate, are shown in table 4.14. We also show the theoretical Γ and q values predicted by Hibbert (1998) and in the case of Na^+, the Γ value calculated by Zatsarinny (1995). The lack of experimental data previous to this work is clear.

Ion	Γ_{exp}	$\Gamma_{Zatsarinny\ (1995)}$	$\Gamma_{Hibbert\ (1998)}$	q_{exp}	$q_{Hibbert\ (1998)}$
Na^{+}	0.05±0.01	0.054	0.086	-2.0±0.1	-1.9
Mg^{2+}	0.10±0.01	-	0.203	-2.1±0.1	-2.2
Al^{3+}	0.21±0.02	-	0.263	-2.0±0.1	-2.2
Si^{4+}	0.3	-	0.45	-1.6	-2.7

Table 4.14 : A Summary of the measured Γ and q values for the 2s2p⁶3p ¹P resonance in Na⁺ to Si⁴⁺. The values are compared with the theoretical calculations of Hibbert (1998) and Zatsarinny (1995). No errors are given for the Si⁴⁺ values as this resonance is forced to autoionise by a lowering of the ionisation potential and therefore Γ and q for this resonance vary with experimental conditions.

We now briefly discuss the output of Hartree-Fock calculations we have performed for the $2s2p^6np\ ^1P_1$ series, details of which have been given in section 4.3. Eigenvector purities for $2s2p^6np\ ^1P_1$ series of Ne^0, Na^+, Mg^{2+}, Al^{3+} and Si^{4+} have been calculated under both jj and LS coupling schemes and are shown in tables 4.15 to 4.19. As with the calculations for the $2s^22p^5ns$, nd series, only the four largest percentage purities are given. It is quite clear that in contrast to the valence excitation series, LS coupling is now

Config./term	E_{calc}	E_{exp}	gf_{calc}†	*LS* purity / *jj* purity
$2s^22p^6(^1S_0)\rightarrow$				
$2s2p^63p\ ^1P_1$	47.25	45.55	144	94%3p(^{1}P) + 1%3s5p(^{1}P) - 1%3s3p(^{1}P) - 1%3p3s(^{1}P) 63%3p[1/2,3/2]$_1$ + 31%3p[1/2,1/2]$_1$
$2s2p^64p\ ^1P_1$	48.91	47.12	52	97%4p(^{1}P) - 3%3s4p(^{1}P) + 0%3p(^{1}P) + 0%5p(^{1}P) 65%4p[1/2,3/2]$_1$ + 32%4p[1/2,1/2]$_1$
$2s2p^65p\ ^1P_1$	49.50	47.69	25	97%5p(^{1}P) - 3%3s5p(^{1}P) - 1%3p4s(^{1}P) + 0%3p4s(^{1}P) 66%5p[1/2,3/2]$_1$ + 31%5p[1/2,1/2]$_1$
$2s2p^66p\ ^1P_1$	49.78	47.97	13	97%6p(^{1}P) - 2%3s6p(^{1}P) + 0%7p(^{1}P) + 0%5p(^{1}P) 66%6p[1/2,3/2]$_1$ + 32%6p[1/2,1/2]$_1$
$2s2p^67p\ ^1P_1$	49.93	48.12	8	98%7p(^{1}P) - 2%3s7p(^{1}P) + 0%8p(^{1}P) + 0%6p(^{1}P) 66%7p[1/2,3/2]$_1$ + 32%7p[1/2,1/2]$_1$
$2s2p^68p\ ^1P_1$	50.02	48.21	5	98%8p(^{1}P) - 2%3s8p(^{1}P) + 0%9p(^{1}P) + 0%7p(^{1}P) 66%8p[1/2,3/2]$_1$ + 32%8p[1/2,1/2]$_1$
$2s2p^69p\ ^1P_1$	50.08	-	3	98%9p(^{1}P) - 2%3s9p(^{1}P) + 0%10p(^{1}P) + 0%8p(^{1}P) 66%9p[1/2,3/2]$_1$ + 32%9p[1/2,1/2]$_1$
$2s2p^610p\ ^1P_1$	50.12	-	2	98%10p(^{1}P) - 2%3s10p(^{1}P) + 0%11p(^{1}P) + 0%9p(^{1}P) 65%10p[1/2,3/2]$_1$ + 33%10p[1/2,1/2]$_1$

† gf values have been multiplied by 10^3.

Table 4.15 : Experimental and calculated energy level data (in eV) for the Ne⁰ 2s2p⁶np[n≥3] series.

Config./term	E_{calc}	E_{exp}	gf_{calc}†	*LS* purity / *jj* purity
$2s^22p^6(^1S_0)\rightarrow$				
$2s2p^63p\ ^1P_1$	71.57	69.96	518	100%3p(^{1}P) - 0%3s3p(^{1}P) - 0%3p3s(^{1}P) + 0%3d(^{1}P) 68%3p[1/2,3/2]$_1$ + 32%3p[1/2,1/2]$_1$
$2s2p^64p\ ^1P_1$	77.01	75.20	187	100%4p(^{1}P) - 0%3s4p(^{1}P) + 0%4p(^{3}P) + 0%3p(^{1}P) 68%4p[1/2,3/2]$_1$ + 31%4p[1/2,1/2]$_1$
$2s2p^65p\ ^1P_1$	79.03	77.19	88	100%5p(^{1}P) - 0%3s5p(^{1}P) + 0%5p(^{3}P) + 0%6p(^{1}P) 68%5p[1/2,3/2]$_1$ + 31%5p[1/2,1/2]$_1$
$2s2p^66p\ ^1P_1$	80.01	78.17	49	100%6p(^{1}P) - 0%3s6p(^{1}P) + 0%6p(^{3}P) + 0%7p(^{1}P) 68%6p[1/2,3/2]$_1$ + 31%6p[1/2,1/2]$_1$
$2s2p^67p\ ^1P_1$	80.57	78.74	30	100%7p(^{1}P) - 0%3s7p(^{1}P) + 0%7p(^{3}P) + 0%8p(^{1}P) 68%7p[1/2,3/2]$_1$ + 31%7p[1/2,1/2]$_1$
$2s2p^68p\ ^1P_1$	80.91	-	19	100%8p(^{1}P) - 0%3s8p(^{1}P) + 0%8p(^{3}P) + 0%9p(^{1}P) 68%8p[1/2,3/2]$_1$ + 31%8p[1/2,1/2]$_1$
$2s2p^69p\ ^1P_1$	81.14	-	13	100%9p(^{1}P) - 0%3s9p(^{1}P) + 0%9p(^{3}P) + 0%10p(^{1}P) 68%9p[1/2,3/2]$_1$ + 31%9p[1/2,1/2]$_1$
$2s2p^610p\ ^1P_1$	81.29	-	10	100%10p(^{1}P) - 0%3s10p(^{1}P) + 0%10p(^{3}P) + 0%11p(^{1}P) 68%10p[1/2,3/2]$_1$ + 31%10p[1/2,1/2]$_1$

† gf values have been multiplied by 10^4.

Table 4.16 : Experimental and calculated energy level data (in eV) for the Na^+ $2s2p^6np[n\geq3]$ series.

Config./term	E_{calc}	E_{exp}	gf_{calc}†	*LS* purity / *jj* purity
$2s^22p^6(^1S_0)\rightarrow$				
$2s2p^63p\ ^1P_1$	99.55	97.98	85	100%3p(^{1}P) - 0%2p^{5}3d(^{1}P) - 0%3s3p(^{1}P) - 0%3p3s(^{1}P) 69%3p[1/2,3/2]$_1$ + 31%3p[1/2,1/2]$_1$
$2s2p^64p\ ^1P_1$	110.28	108.46	32	100%4p(^{1}P) - 0%3s4p(^{1}P) - 0%4p(^{3}P) + 0%3p(^{1}P) 70%4p[1/2,3/2]$_1$ + 30%4p[1/2,1/2]$_1$
$2s2p^65p\ ^1P_1$	114.44	112.60	15	100%5p(^{1}P) - 0%3s5p(^{1}P) - 0%5p(^{3}P) + 0%6p(^{1}P) 70%5p[1/2,3/2]$_1$ + 30%5p[1/2,1/2]$_1$
$2s2p^66p\ ^1P_1$	116.51	114.68	9	100%6p(^{1}P) - 0%6p(^{3}P) - 0%3s6p(^{1}P) + 0%7p(^{1}P) 70%6p[1/2,3/2]$_1$ + 30%6p[1/2,1/2]$_1$
$2s2p^67p\ ^1P_1$	117.69	115.87	5	100%7p(^{1}P) - 0%3s7p(^{1}P) - 0%7p(^{3}P) + 0%8p(^{1}P) 70%7p[1/2,3/2]$_1$ + 30%7p[1/2,1/2]$_1$
$2s2p^68p\ ^1P_1$	118.43	-	3	100%8p(^{1}P) - 0%8p(^{3}P) - 0%3s8p(^{1}P) + 0%9p(^{1}P) 70%8p[1/2,3/2]$_1$ + 30%8p[1/2,1/2]$_1$
$2s2p^69p\ ^1P_1$	118.91	-	2	100%9p(^{1}P) - 0%3s9p(^{1}P) - 0%9p(^{3}P) + 0%10p(^{1}P) 70%9p[1/2,3/2]$_1$ + 30%9p[1/2,1/2]$_1$
$2s2p^610p\ ^1P_1$	119.26	-	2	100%10p(^{1}P) - 0%3s10p(^{1}P) - 0%10p(^{3}P) + 0%11p(^{1}P) 70%10p[1/2,3/2]$_1$ + 30%10p[1/2,1/2]$_1$

† gf values have been multiplied by 10^3.

Table 4.17 : Experimental and calculated energy level data (in eV) for the Mg^{2+} $2s2p^6np[n\geq3]$ series.

Config./term	E_{calc}	E_{exp}	gf_{calc}†	*LS* purity / *jj* purity
$2s^22p^6(^1S_0)\rightarrow$				
$2s2p^63p\ ^1P_1$	131.30	129.76	108	99%3p(^{1}P) - 0%3p(^{3}P) - 0%2p^{5}3d(^{1}P) - 0%4d(^{1}P) 70%3p[1/2,3/2]$_1$ + 29%3p[1/2,1/2]$_1$
$2s2p^64p\ ^1P_1$	148.76	147.01	44	100%4p(^{1}P) - 0%4p(^{3}P) - 0%3s4p(^{1}P) + 0%3p(^{1}P) 71%4p[1/2,3/2]$_1$ + 29%4p[1/2,1/2]$_1$
$2s2p^65p\ ^1P_1$	155.72	-	21	100%5p(^{1}P) - 0%5p(^{3}P) - 0%3s5p(^{1}P) + 0%4p(^{1}P) 71%5p[1/2,3/2]$_1$ + 29%5p[1/2,1/2]$_1$
$2s2p^66p\ ^1P_1$	159.23	-	12	100%6p(^{1}P) - 0%6p(^{3}P) - 0%3s6p(^{1}P) + 0%7p(^{1}P) 71%6p[1/2,3/2]$_1$ + 29%6p[1/2,1/2]$_1$
$2s2p^67p\ ^1P_1$	161.25	-	7	100%7p(^{1}P) - 0%7p(^{3}P) - 0%3s7p(^{1}P) + 0%8p(^{1}P) 71%7p[1/2,3/2]$_1$ + 29%7p[1/2,1/2]$_1$
$2s2p^68p\ ^1P_1$	162.52	-	5	100%8p(^{1}P) - 0%8p(^{3}P) - 0%3s8p(^{1}P) + 0%9p(^{1}P) 71%8p[1/2,3/2]$_1$ + 29%8p[1/2,1/2]$_1$
$2s2p^69p\ ^1P_1$	163.36	-	3	100%9p(^{1}P) - 0%9p(^{3}P) - 0%3s9p(^{1}P) + 0%10p(^{1}P) 71%9p[1/2,3/2]$_1$ + 29%9p[1/2,1/2]$_1$
$2s2p^610p\ ^1P_1$	163.96	-	2	100%10p(^{1}P) - 0%10p(^{3}P) - 0%3s10p(^{1}P) + 0%11p(^{1}P) 71%10p[1/2,3/2]$_1$ + 29%10p[1/2,1/2]$_1$

† gf values have been multiplied by 10^3.

Table 4.18 : Experimental and calculated energy level data (in eV) for the Al^{3+} $2s2p^6np[n\geq3]$ series.

Config./term	E_{calc}	E_{exp}	gf_{calc}†	*LS* purity / *jj* purity
$2s^22p^6(^1S_0)\rightarrow$				
$2s2p^63p\ ^1P_1$	166.89	165.39	107	99%3p(^{1}P) - 0%3p(^{3}P) - 0%2p^{5}3d(^{1}P) - 0%2p^{5}4d(^{1}P) 71%3p[1/2,3/2]$_1$ + 28%3p[1/2,1/2]$_1$
$2s2p^64p\ ^1P_1$	192.45	-	54	99%4p(^{1}P) - 1%4p(^{3}P) + 0%3s4p(^{1}P) + 0%2p^{5}4d(^{1}P) 73%4p[1/2,3/2]$_1$ + 27%4p[1/2,1/2]$_1$
$2s2p^65p\ ^1P_1$	202.86	-	26	99%5p(^{1}P) - 1%5p(^{3}P) + 0%3s5p(^{1}P) + 0%4p(^{1}P) 73%5p[1/2,3/2]$_1$ + 27%5p[1/2,1/2]$_1$
$2s2p^66p\ ^1P_1$	208.15	-	15	99%6p(^{1}P) - 1%6p(^{3}P) + 0%3s6p(^{1}P) + 0%7p(^{1}P) 73%6p[1/2,3/2]$_1$ + 27%6p[1/2,1/2]$_1$
$2s2p^67p\ ^1P_1$	211.22	-	9	99%7p(^{1}P) - 1%7p(^{3}P) + 0%3s7p(^{1}P) + 0%8p(^{1}P) 73%7p[1/2,3/2]$_1$ + 27%7p[1/2,1/2]$_1$
$2s2p^68p\ ^1P_1$	213.15	-	6	99%8p(^{1}P) - 1%8p(^{3}P) + 0%3s8p(^{1}P) + 0%9p(^{1}P) 73%8p[1/2,3/2]$_1$ + 27%8p[1/2,1/2]$_1$
$2s2p^69p\ ^1P_1$	214.44	-	4	99%9p(^{1}P) - 1%9p(^{3}P) + 0%3s9p(^{1}P) + 0%10p(^{1}P) 73%9p[1/2,3/2]$_1$ + 27%9p[1/2,1/2]$_1$
$2s2p^610p\ ^1P_1$	215.36	-	3	99%10p(^{1}P) - 1%10p(^{3}P) + 0%3s10p(^{1}P) + 0%11p(^{1}P) 73%10p[1/2,3/2]$_1$ + 27%10p[1/2,1/2]$_1$

† gf values have been multiplied by 10^3.

Table 4.19 : Experimental and calculated energy level data (in eV) for the Si^{4+} $2s2p^6np[n\geq3]$ series.

overwhelmingly dominant with purities for $2s2p^6np\ ^1P_1$ series members, for Ne^0 to Si^{4+}, in excess of 97%. This clearly indicates that in each of the first five isoelectronic members, the series is unperturbed, the only possible exception being Ne^0 where mixing with the overlapping double excitations is evident but relatively insignificant. The computed gf values for the series are distinctly seen to mimic experimental observations,

members above n=6 dropping in oscillator strength such that their presence in the experimental data is, at best, faint. As for the 2p → ns, nd valence excitations, the computed $2s^22p^6 \rightarrow 2s2p^6np\ ^1P_1$ transitions required a shift to enable direct comparison with their experimental counterparts. The computed energies were overestimated and shifts of -1.81, -1.81, -1.79, -1.72 and -1.45eV were applied for Ne^0, Na^+, Mg^{2+}, Al^{3+} and Si^{4+} respectively, in order that experimental features be unambiguously identified (see figures 4.3 and 4.4). In contrast to the shifted computational data shown in figures 4.3 and 4.4, the energies listed in tables 4.9 to 4.13 and 4.15 to 4.19 are unshifted. As with calculations for the 2p → ns, nd series, the predicted energy interval between the higher members of the 2s → np series became more accurate with increasing n, as with an increase in n, the system becomes more Coulombic in nature.

4.5 Behaviour of the $2s2p^63p\ ^1P$ resonance near the $Si^{4+}\ ^2P_{3/2,1/2}$ limits.

4.5.1 Experimental evidence for 'forced autoionisation'.

It has been noted previously (Kastner et al 1977) that the $2s2p^6np$ series encroaches upon the $2s^22p^5\ ^2P_{3/2,1/2}$ limits of the $2s^22p^5ns$, nd series as the neon isoelectronic sequence is progressed. Kastner et al, using measurements on the $2s2p^6np$ series of Mg^{2+} and Al^{3+} and the results of earlier studies by Codling et al (1967) and Lucatorto and McIlrath (1976), on Ne^0 and Na^+, portrayed the situation clearly in a plot which we have revised in figure 4.8. In figure 4.8, we have plotted our recent measurements for the $2s2p^6np$ series and the $2s^22p^5$ limits together with measurements available in Kelly's tables (Kelly 1987) for equivalent transitions and limits of heavier ions not investigated here. The evolution of the 3p member toward the $2s^22p^5$ boundary is clearly evidenced. Our measurements show the Si^{4+} $2s2p^63p$ resonance to be centred at 165.4eV whereas the $2s^22p^5\ ^2P_{3/2}$ and $^2P_{1/2}$ limits are at 166.7eV and 167.2eV respectively. With the $2s2p^63p$ resonance below the limits by 1.3eV, it should not be in a position to interact with the underlying continuum, yet its profile clearly indicates an asymmetry

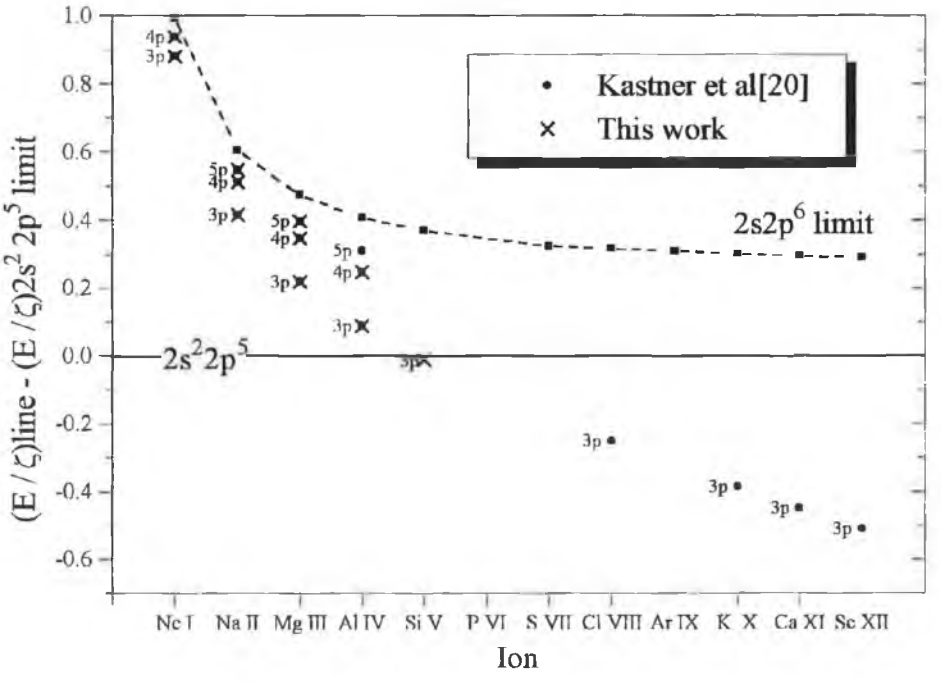

Figure 4.8 : The $2s^22p^6\ {}^1S_0 \rightarrow 2s2p^6np\ {}^1P_1$ Rydberg series relative to $2s^22p^5$ and $2s2p^6$ limits for members of the neon isoelectronic sequence. E is the transition energy in atomic units and ζ is the spectral number.

characteristic of autoionisation (see figure 4.4). The cause of this phenomenon we attribute to forced autoionisation (see section 1.3, chapter 1) whereby micro electric fields generated in the silicon plasma give rise to a Stark continuum which depresses the ionisation limit relative to that of totally free silicon ions. The $2s2p^63p$ resonance is thus able to interact with the 'Pseudo' continuum giving rise to its profile asymmetry.

As mentioned in chapter 1, section 1.3, the phenomenon of forced autoionisation was first observed by Garton et al (1962) in the absorption spectrum of shock heated barium. Since then, due to the advent of the tunable laser and increasing interest in atomic Rydberg states, there has been a renewed interest in forced autoionisation. Since 1980, the original suggestion of Garton et al has been verfied through a series of thorough and controlled experiments (Sandner et al 1981, Cole et al 1980, Gallagher et al 1983, Blondel et al 1983, Sandner et al 1986) where in addition to its fundamental importance, forced autoionisation has also been used as a spectroscopic tool to measure the small and often difficult to detect energy shifts of Rydberg levels in the presence of a weak perturbing level. This has been demonstrated particularly well by Gallagher et al (1983) where by

application of an electric field (>2kV/cm) to depress the Ba^+ 6s limit to an energy below that of the 5d7d state, which perturbs the 6sng Rydberg series, the 5d7d state becomes much more apparent as it now interacts with a continuum, not a series of discrete states. Thus, the strength of this extremely weak resonance's configuration interaction could be measured as it is proportional to the width of the forced autoionisation resonance. More recently, forced autoionisation through the application of electric fields has been used to study molecular systems e.g. H_2 (Glab and Qin 1993) and Li_2 (Mahon et al 1990) and alternative forms of the phenomenon, such as laser-induced autoionisation, have been documented. One such example of laser-induced autoionisation is the perturbed Ba 6snd Rydberg series, the perturber being the 5d7d state. By increasing the intensity of a subpicosecond pulsed laser tuned to the Ba $5d7d(^1D_2) \rightarrow 6p7d$ transition at $\lambda = 620nm$, it has been shown (Vrijen et al 1995) that the lifetime of the perturbing $5d7d(^1D_2)$ state decreases. At a certain intensity, the lifetime becomes so short that the photoionisation rate of the Rydberg states becomes limited by the rate of population transfer between the Rydberg states and the perturber i.e. the configuration interaction. At that point the perturber state is strongly coupled to the continuum and the Rydberg states become an autoionising Rydberg series.

4.5.2 *Calculations for the lowering of the ionisation potential*

While we have not measured the electron density or the electron temperature in our silicon plasma, more evidence to support a case of forced autoionisation for the Si^{4+} $2s2p^63p$ member can be obtained through estimates of these quantities. For example, a calculation to justify the occurrence of forced autoionisation can be made by considering the electron density within our silicon plasma. Using the Rydberg formula (equation [3.1]) and taking $I_p(^2P_{3/2}) = 166.7eV$, $R_{Si} = 13.605399eV$ and $\delta = 0.05$, we see that the Si^{4+} $2s2p^63p$ member lies at an energy position that corresponds to the n=16 member of the $2s^22p^5nd\ [3/2,5/2]_1$ series. Using the Inglis-Teller relationship, which relates the electron density to the principal quantum number (n_{max}) of the last discernible line in a Rydberg series (Cooper 1966) i.e.

$$\log n_e = 23.26 - 7.5 \log n_{max} + 4.5 \log Z \qquad [4.1]$$

where n_e is in cm^{-3} and Z-1 is the net charge of the atom, we thus get an electron density of $2x10^{17}cm^{-3}$ for $n_{max} = 16$. The relationship given by Unsöld (1995) can then be used to relate this electron density to a lowering of the ionisation energy whereby (in SI units)

$$\Delta X_{Z-1} = 1.7022x10^{31} Z^{2/3} \frac{e^2}{r_e} \text{ (eV)} \qquad [4.2]$$

with $$r_e = \left(\frac{4}{3}\pi n_e\right)^{-1/3}$$

where e is the electron charge and Z for $Si^{4+} = 4$. Thus, for $n_e = 2x10^{17}cm^{-3}$, we get ΔX = 1.0eV. Clearly, as the $^2P_{3/2}$ ionisation limit must be lowered by at least 1.3eV, in order that the $2s2p^63p$ resonance appears autoionising, we can infer that the electron density within our silicon plasma must be > $2x10^{17}cm^{-3}$.

Revising our calculations in considering only the maximum visible member of the $2s^22p^5nd$ series from our Si^{4+} photoabsorption spectrum, we find that $n_{max} = 7$. We now obtain through the Inglis-Teller relationship, an electron density $n_e = 1.2x10^{20}cm^{-3}$ which by equation [4.2] above implies a lowering of the ionisation limit by 8.8eV. Even though an electron density of $1.2x10^{20}cm^{-3}$ is a factor of 8 times less than the critical density for a Nd:YAG laser (λ = 1.064μm) which via equation [1.11] is ~$1x10^{21}cm^{-3}$, it results in ionisation limit depression which is clearly too large. By considering the visible members of the $2s^22p^5nd$ series for the five isoelectronic sequence members studied here, we see that the highest member visible corresponded to n = 10. Repeating the above treatment with $n_{max} = 10$ would therefore give $n_e = 3x10^{18}cm^{-3}$ and ΔX = 2.6eV. The above qualitative discussion illustrates that with the typical electron densities known to pertain in laser produced plasmas, a lowering of the ionisation limit would not be unexpected and thus forced autoionisation as an explanation for the asymmetry of the $2s2p^63p$ resonance is compelling.

4.5.3 Variation of the Si^{4+} $2s^22p^6 \rightarrow 2s2p^63p\ ^1P_1$ resonance profile with experimental conditions.

In section 4.1.5, we mentioned that Brilly (1990) had recorded this Si^{4+} 2p threshold region photographically. Brilly observed that the n=3 member seemed to change profile as the experimental conditions, and in particular the amount by which the target lens

was defocussed, were varied. We have attempted to repeat this observation, defocussing the target lens by up to 10mm. Figure 4.9 shows our recorded spectra where (a) to (e) show the effect of progressive defocussing on the $2s2p^63p$ resonance profile. Each spectrum was the average result of a total of four spectra, each the accumulation of ten I, I_0 and I_e scans. As before, we have subtracted the target silicon plasma emission from the I signal before performing the $\ln(I_0/I)$ transformation. All experimental conditions were identical to those used for earlier Si^{4+} spectra (see sections 4.2 and 4.3) with the exception of target lens focussing, the amount by which the lens was defocussed for each spectrum being indicated. The spectra were taken at a single CEMA setting i.e. 15.5".

From figure 4.9, we can see that with increased defocussing of the lens used to create the silicon plasma, the $2s2p^63p$ profile becomes more asymmetric. To rule out the profile change being the result of contamination of the absorption spectra with unwanted emission from the silicon plasma, we have plotted in figure 4.10 (a) to (e), the silicon emission signal which was present for each of the spectra in figure 4.9 (a) to (e), this, as previously explained, having necessarily been subtracted from the I signal to produce the desired absorption spectra. As is evident from figure 4.10, the emission from the silicon target plasma falls off rapidly with increased defocusing but more importantly, it is clear that there are no emission lines in the region of the $2s2p^63p$ resonance, regardless of experimental conditions. This assures us that the profile change as a function of focussing conditions is not an artefact. A complete explanation for the change in behaviour would require a complete theoretical calculation, taking into account the relevant atomic physics in the presence of the plasma fields. This would be a very challenging calculation. However, it is intriguing to suggest possible scenarios.

For example, we would expect that sharp focusing conditions would produce a hotter and denser silicon plasma with more intense electric fields. The depression of the ionisation limit from its zero field value would therefore be greater. The continuum cross section is usually at a maximum at or near threshold and falls off from this maximum with increasing energy. If the ionisation limit has been depressed to energies considerably lower than that corresponding to the $2s2p^63p$ resonance, the continuum cross section maximum is also well below the 3p resonance. This means that the 3p

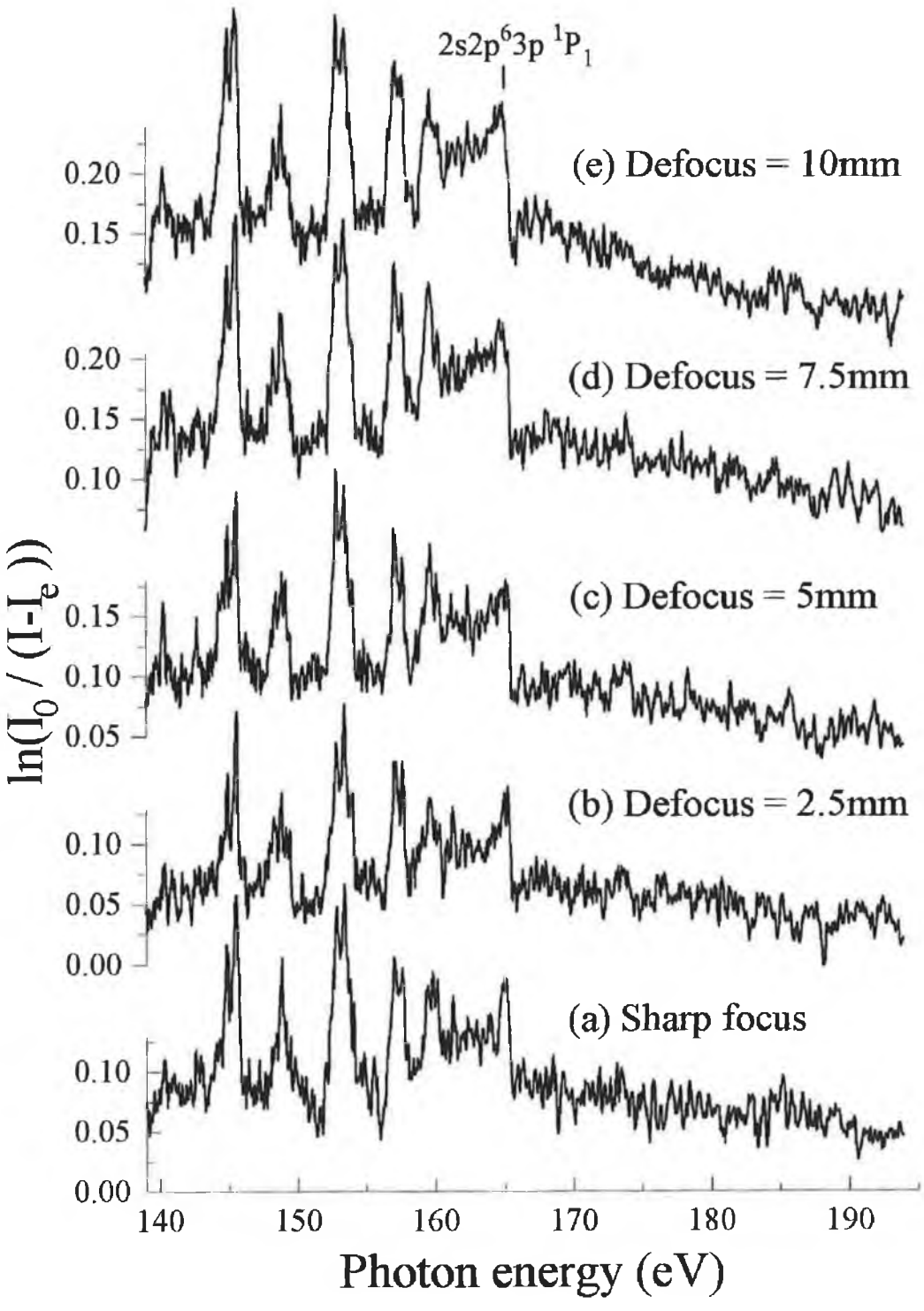

Figure 4.9 : The change in profile of the Si^{4+} $2s^22p^6 \rightarrow 2s2p^63p\ ^1P_1$ resonance with increased defocussing of the lens used to create the silicon plasma. See text for details.

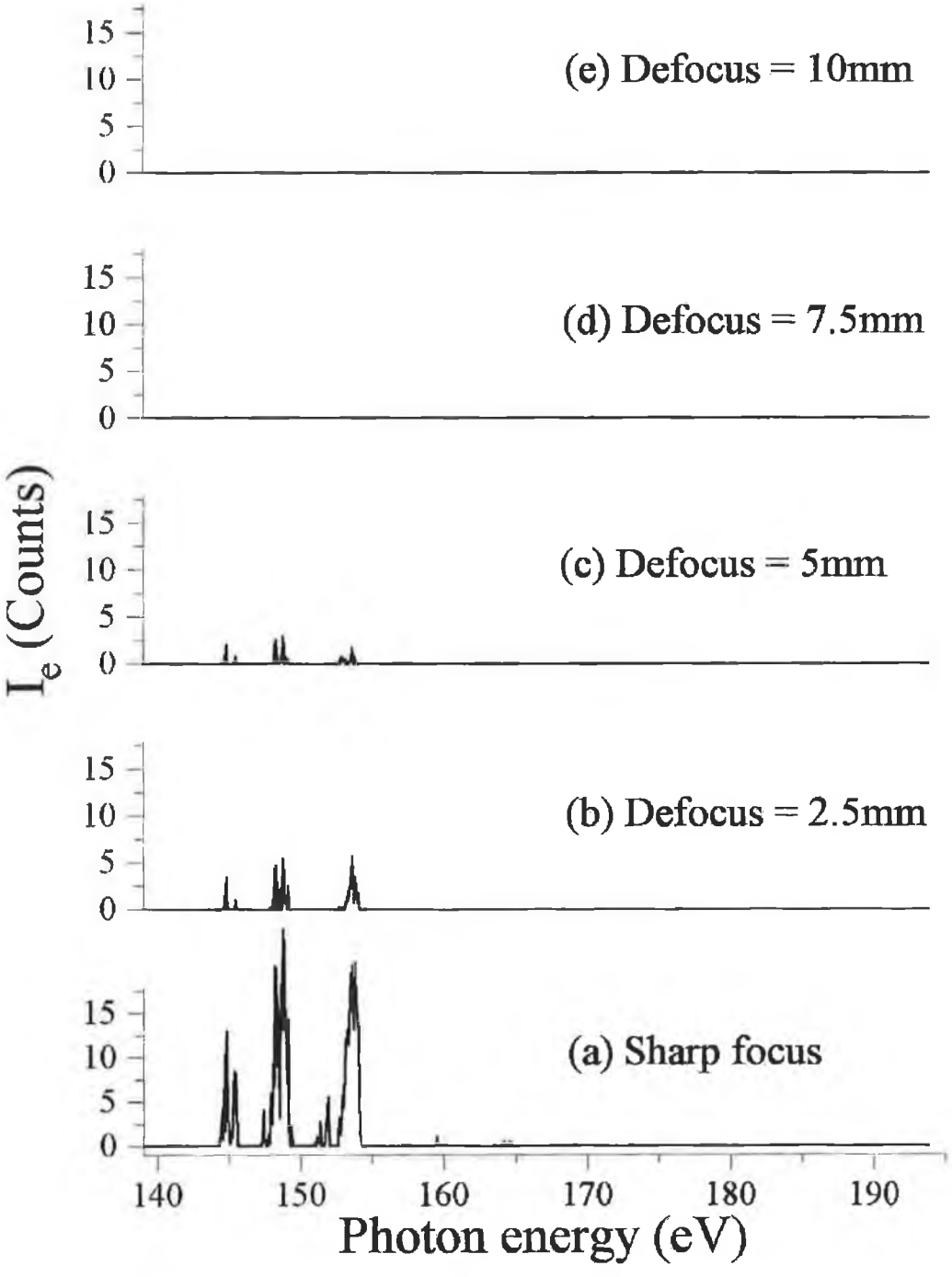

Figure 4.10 : The silicon plasma emission as a function of target lens defocussing. The spectra were taken with identical experimental conditions to those which produced the corresponding spectra in figure 4.9.

resonance interacts with a weaker part of the decreasing continuum tail. The result of this weak interaction i.e. less coupling of the resonance to the underlying continuum, is therefore a 3p resonance profile which is more symmetric. With progressive defocusing, the ionisation limit is not lowered by as much. The maximum in continuum cross section therefore moves to higher energies and moves closer to the 3p resonance. The resonance can now interact with a stronger part of the continuum and its profile becomes more asymmetric as a result. If this theory is correct then continued defocusing of the target lens will eventually result in a plasma in which the electric fields are not strong enough to depress the limit to an energy below the resonance. At this point, the resonance profile should become symmetric again.

Further experimentation and theoretical support would be needed to obtain reliable physical insight into the basic physics involved. However, it seems clear that forced autoionisation is the basic phenomenon required for the appearance of the feature with the detailed behaviour dependent on the exact plasma conditions.

4.6 Anomalous threshold cross section behaviour in the neon isoelectronic sequence

Recently, in the first combined theoretical and experimental investigation of photoionisation along the neon isoelectronic sequence, it has been shown that the near-threshold behaviour of the cross section for Si^{4+} differs dramatically from that of the nearby ions in the sequence. Our DLP measurements (see figures 4.2, 4.3 and 4.4) have been compared with calculations that have been performed, by an international consortium of researchers, using the Relativistic Random Phase Approximation (RRPA) (Johnson and Cheng 1979, Johnson et al 1980). This has resulted in a collaboration where both our experimental results and the results from these calculations have been combined in a joint publication (Chakraborty et al 1999).

The RRPA method has been shown to agree well with experiment for neon (Johnson and Cheng 1979) but calculations using this method are expected to become even more accurate as the isoelectronic sequence is progressed. This is because multi-electron interactions, which arise from the part of the Hamiltonian being approximated, become less important with increasing stages of ionisation. The calculations were carried out for all members of the neon isoelectronic sequence up to Z = 100 and, for each member, the seven relativistic single excitation channels arising from the 2s and 2p subshells i.e. $2s \rightarrow \varepsilon p_{1/2}$, $\varepsilon p_{3/2}$; $2p_{1/2} \rightarrow \varepsilon s_{1/2}$, $\varepsilon d_{3/2}$; $2p_{3/2} \rightarrow \varepsilon s_{1/2}$, $\varepsilon d_{3/2}$, $\varepsilon d_{5/2}$, were included. The 1s channels were shown (by test calculations) to have a negligible effect on the behaviour of the near threshold cross section and were therefore excluded.

The results of the calculations for the photoionisation cross section at the $2s^22p^5\ ^2P_{1/2}$ threshold are shown in table 4.20 (column 3) and in figure 4.11 (square points). The most striking feature of the results is the smooth evolution of the cross section along the sequence with the exception of Si^{4+}, where the cross section is smaller by more than an order of magnitude. Figure 4.11 (solid line) and table 4.20 (column 2) also show the calculated results with the coupling between 2s and 2p channels excluded. An appreciable difference from the full RRPA result is evident. Without the coupling, the threshold 2p cross section for Si^{4+} is consistent with that of its neighbours, the neighbouring threshold cross sections remaining essentially unchanged. It can therefore

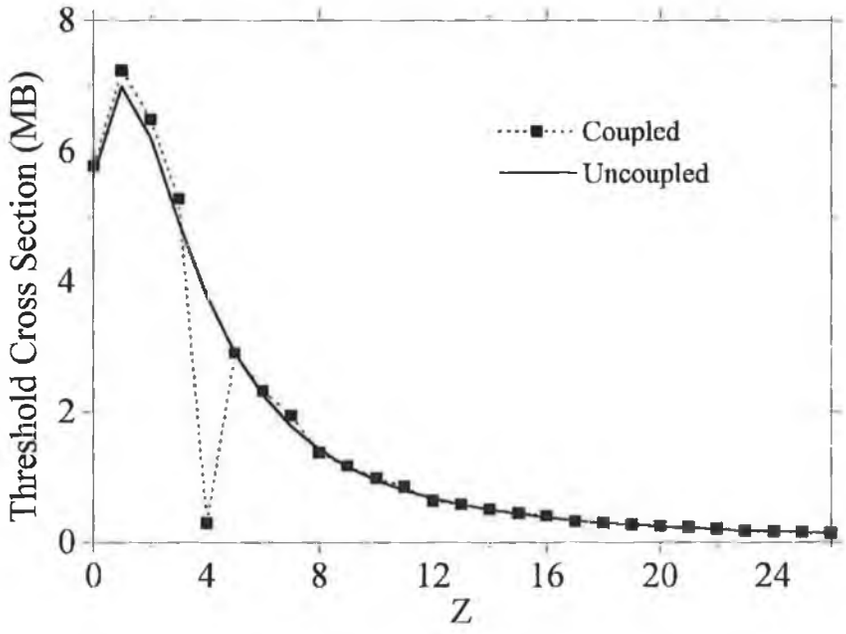

Figure 4.11 : Calculated photoionisation cross section (MB) at the $^2P_{1/2}$ threshold Vs initial state charge, Z, for the neon isoelectronic sequence. Results are given with and without the inclusion of the coupling between the 2s and 2p channels (after Chakraborty et al 1999).

Ion	5 Channel	7 Channel
Ne	5.61	5.77
Na^+	6.98	7.24
Mg^{2+}	6.21	6.49
Al^{3+}	4.93	5.27
Si^{4+}	3.79	0.30
P^{5+}	2.91	2.90

Table 4.20 : Calculated photoionisation cross section (MB) at the $^2P_{1/2}$ threshold for the first six members of the neon isoelectronic sequence with (7 channel) and without (5 channel) coupling between the 2p and 2s ionisation channels (after Chakraborty et al 1999).

be concluded that the anomalous threshold behaviour for Si^{4+} is related to the coupling between 2s and 2p channels.

To illustrate this more clearly, the calculated cross section in the $^2P_{1/2}$ threshold region for photoionisation of Ne^0, Na^+, Mg^{2+}, Al^{3+}, Si^{4+} and P^{5+} is shown in figure 4.12. For Na^+, the remnants of the $2p \rightarrow \varepsilon d$ delayed maximum, seen in neutral neon, is responsible for the slightly increasing cross section at threshold, most of the rise now below the threshold in the discrete region. Mg^{2+} shows a cross section which is almost flat with a

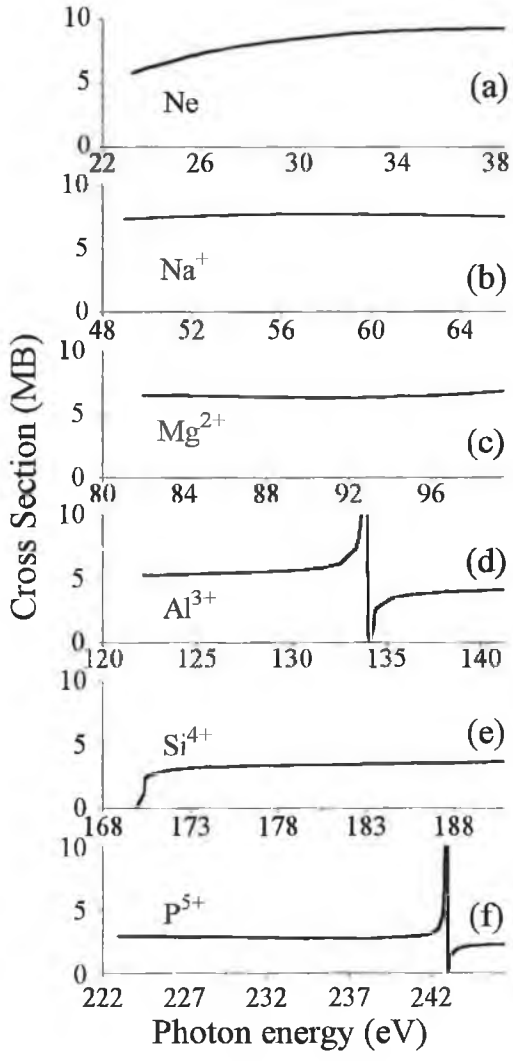

Figure 4.12 : Calculated near-threshold photoionisation cross sections for (a) Ne, (b) Na^+, (c) Mg^{2+}, (d) Al^{3+}, (e) Si^{4+} and (f) P^{5+}. Note that the full height of the Al^{3+} resonance peak is not shown (after Chakraborty et al 1999).

slight increase well above threshold. The threshold cross section of Al^{3+} is again flat but the cross section becomes dominated at higher energies by the inner shell 2s → 3p resonance which has moved down to within ~13eV of the threshold. For Si^{4+}, the 3p resonance is predicted to almost coincide in energy with the ionisation limit and this changes the threshold cross section dramatically. Finally, for P^{5+}, the 2s → 3p resonance has moved to an energy well below that of the ionisation limit, resulting in the threshold cross section returning to 'normal'. However, the 2s → 4p resonance can now be seen to approach the threshold region. Indeed, the movement of successive resonances through

the ionisation limit continues as the sequence progresses. Figure 4.12 thus shows clearly how the anomalous threshold cross section is linked to the movement, with increasing Z along the sequence, of inner shell 2s → np resonances into the discrete region below the 2p thresholds.

In any isoelectronic sequence, the 2s and 2p thresholds become degenerate as $Z \rightarrow \infty$. Hence, the downward movement of inner shell resonances with respect to outer shell thresholds occurs for all sequences for which the outermost subshell is other than $l = 0$. As this constitutes the majority of the periodic table, it is evident that the movement, with increasing Z, of an inner shell resonance into the close proximity of an outer threshold and the resultant dramatic modification of the near threshold cross section, is a general phenomenon.

To illustrate the accuracy of the calculations, we show for Na^+, in figure 4.13, a comparison between the calculated photoionisation cross section above threshold and

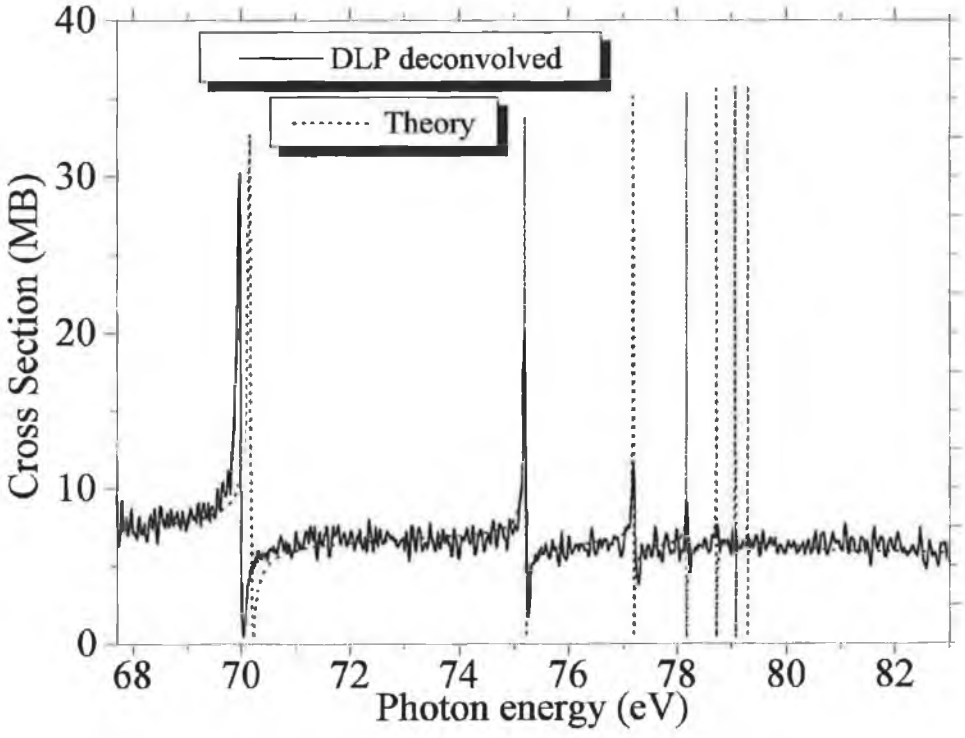

Figure 4.13 : Comparison between the (deconvolved) DLP relative total photoabsorption cross section of Na^+, in the region of the np inner-shell resonances, with the Calculated (RRPA) photoionisation cross section (after Chakraborty et al 1999). The experimental result is normalised to the theory in the background, non-resonant region.

the measured DLP deconvolved photoabsorption spectrum. The calculated data was shifted by -3.8eV in order to match the energy of the second resonance with that of the experiment. In general, good agreement between the two in terms of resonance positions and profiles is evident. The limited experimental spectral resolution does however reduce the contrast for the higher resonances.

In figure 4.14, we show the DLP measured results in the threshold energy region of Na^+, Mg^{2+}, Al^{3+} and Si^{4+}. Figure 4.14 is a close up of the DLP spectra shown in figure 4.2. For Na^+ to Al^{3+}, the valence $2p \rightarrow ns$, nd transitions are seen to run to their series limits (as indicated) with a smooth continuation in the value of the cross section across the limit. With Si^{4+}, however, the behaviour is notably different. The near threshold cross section is now dominated by the inner shell $2s \rightarrow 3p$ resonance (at 165.4eV) which has moved down to just below the ionisation limits (166.7 and 167.2eV respectively) (see section 4.5.1). The experimental results thus confirm the presence of the $2s \rightarrow 3p$ resonance just below the ionisation limit, and support the theoretical calculations which indicate an anomalous near threshold cross section behaviour for Si^{4+}. Furthermore, they out point the importance of including inner shell resonances in future calculations of photoionisation cross sections as failure to do so may lead to misleading results.

Conclusions

In the first systematic experimental study of the first five members of the neon isoelectronic sequence, we have measured transitions in both the 2p and 2s regions of excitation of Ne, Na^+, Mg^{2+}, Al^{3+} and Si^{4+}. Energy positions for some higher $2s^22p^6 \rightarrow 2s^22p^5ns$, nd series members, not previously documented, have been determined with the aid of quantum defect analyses and configuration interaction Hartree-Fock calculations. The measurements have yielded independent energy positions for the $^2P_{3/2,1/2}$ thresholds in each sequence member which are generally in good agreement with the literature. We have also measured the $2s^22p^6 \rightarrow 2s2p^6np\ ^1P_1$ series for these Ne-like ions and have experimentally determined, for the first time, the Fano parameters of low lying members in the cases of Na^+, Mg^{2+}, Al^{3+} and Si^{4+}. The fact that the Si^{4+} $2s2p^63p\ ^1P_1$ member lies some 1.3eV below the Si^{4+} $^2P_{3/2}$ threshold but possesses an asymmetric

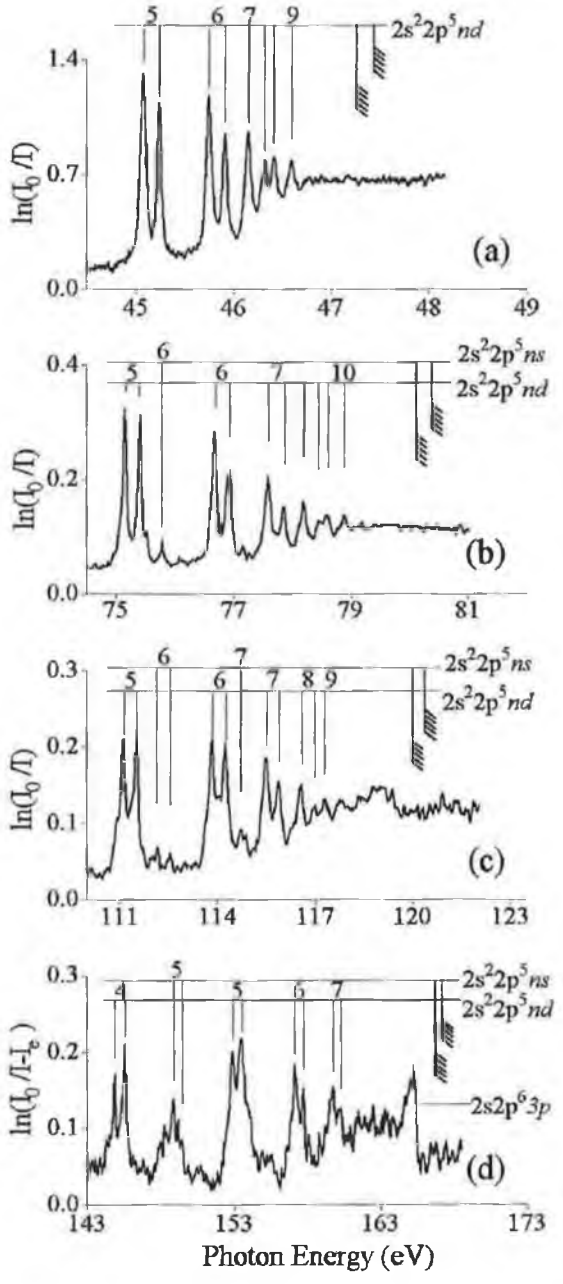

Figure 4.14 : The DLP photoabsorption spectra for (a) Na^{+}, (b) Mg^{2+}, (c) Al^{3+} and (d) Si^{4+} with many of the $2s^22p^5nl$ absorption features identified. The $2s^22p^5\ ^2P_{3/2,1/2}$ thresholds are indicated in bold. Note the changes in energy scales along the sequence.

profile strongly suggests forced autoionisation. To our knowledge, this is the first time that this phenomenon has been observed in a laser produced plasma. Finally, we have

been able to study in detail the behaviour of the near threshold photoionisation cross section. We have shown that the behaviour for Si^{4+} is anomalous due to the movement of the $2s \rightarrow 3p$ inner shell resonance into the immediate vicinity of the 2p thresholds. Furthermore, the movement of inner shell resonances below threshold in isoelectronic sequences, with increasing Z, and the resultant near threshold cross section modification is expected to be a general phenomenon.


Conclusions
and
suggestions
for
future work

A number of experimental investigations have been outlined which characterise and assess the DLP system's performance capabilities with regard to the accurate measurement of photoabsorption spectra. It has been shown that system resolving power varies from ~900 at 177eV to ~3,000 at 28eV, the resolving power being optimised when a feature of interest is imaged between pixels 500 and 600 of the photodiode array. Spatial gain variation across the detector has been shown to have negligible consequence for the measurement of absorption spectra. Higher order contributions have been seen to be <1% and stray light seen to be only important for energies >100eV where at the upper energy extremes of our measuring capability (190eV), it reaches a maximum of ~10%. A procedure for correcting any absorption spectrum for this unwanted signal has been described. The system's instrument function has been determined to be Lorentzian in profile with FWHM equivalent to 4 PDA pixels. It has also been shown that saturation may be avoided by adhering to what may be described as optically thin plasma regimes. Generally speaking, the lower the absorption level, the better, provided signal to noise ratios can be maintained at acceptable levels.

Embracing the above, the first three members of the calcium isonuclear sequence have been studied. By creating spatio-temporal maps which show how the prominence of different calcium species in the plasma varies as a function of experimental parameters, a high level of Ca^{0}, Ca^{+} and Ca^{2+} spectral purity was obtained. Inter-comparing these spectra, observing how the spectra change as a function of time only, using independent Hartree-Fock calculations and using the data from other experimental studies, has brought about the identification of 18 features arising from the $Ca^{+}3p^{6}3d$ excited state and 4 features arising from the $Ca^{0}3p^{6}4s3d$ excited state. This is the first time that transitions from these states have been experimentally observed. Our high resolution investigations have also revealed many broad Ca^{+} ground state features to in fact be comprised of multiple peaks. These have been identified where possible. For Ca^{+}, we have correlated both high resolution optically thick and optically thin photoabsorption spectra with previous lower resolution photoion spectra and revealed the landscape of the Ca^{+} 3p region to differ substantially from that previously supposed. In particular, the peak cross sections of $Ca^{+}3p^{5}4snd\ ^{2}P$ transitions have been revealed to be larger than

previously thought but most dramatically, the results show the $3p^5 4s^2\ ^2P$ transitions to possess peak cross sections a factor of 5 times greater than previously reported.

In the first systematic experimental study of the neon isoelectronic sequence (Z = 1-5), transitions in both the 2p and 2s region of excitation have been measured. The quality of all spectra was optimised by correcting for stray light contributions and paying special attention to plasma opacity. Some higher members of the $2s^2 2p^6 \rightarrow 2s^2 2p^5 ns,nd$ series, not previously resolved, have been identified with the aid of quantum defect analyses and Hartree-Fock calculations. Independent $^2P_{3/2,1/2}$ thresholds have also been established. We have measured the $2s^2 2p^6 \rightarrow 2s 2p^6 np\ ^1P$ inner shell series for Ne^0 through to Si^{4+} and for the first time extracted Fano parameters for low lying members in Na^+, Mg^{2+}, Al^{3+} and Si^{4+}. Given that the $2s 2p^6 3p\ ^1P_1$ resonance of Si^{4+} has been measured to lie 1.3eV below the $^2P_{3/2,1/2}$ limits but is asymmetric in profile, we have concluded that the resonance is strongly suggestive of forced autoionisation. We believe that this is the first observation of such a phenomenon in a laser produced plasma.

We have shown that the cross section for Si^{4+} at threshold is anomalous in contrast to its neighbours. The anomaly has been shown to be the direct result of inner shell resonances moving below threshold with increasing Z along the sequence. Relativistic Random Phase Approximation (RRPA) calculations for the near threshold photoionisation cross section for the neon isoelectronic sequence up to Z=100 support this conclusion. The calculations further indicate that this is a general phenomenon in isoelectronic sequences provided the outermost subshell is other than l=0, which strongly suggests that interpolation or extrapolation of photoionisation or recombination cross sections along sequences should be viewed with extreme caution unless inner shell transitions have been accurately accounted for.

With regard to the DLP system's performance, a number of improvements could be implemented. As the ultimate resolving power is limited by the spatial resolution of the detector, an obvious improvement would be an increase in the number of pixels. Manufacturers such as EG&G Reticon now supply photodiode linear arrays with as many as 8192 pixels. Other developments in PDA technology such as linear arrays with two layers of pixels would also be of great benefit. As one layer is positioned behind and

is shifted laterally with respect to the other, the overlap of the two greatly reduces the uncertainty inherent in a single layer PDA as to which pixel genuinely corresponds to the peak of a particular absorption or emission line. Two dimensional CCD arrays are now falling in cost so that their implementation in imaging systems is becoming more widespread. A 2D detector brings about the ability to spatially resolve the plasma which allows plasma density gradients and the velocity of the plasma species to be determined. An obvious advantage to plasma diagnostics, this variety of detector would also find much use in spectroscopic studies. These 2D detectors are available with typical pixel matrices of 512 x 512 or 1024 x 1024.

Perhaps the most significant limitation associated with the DLP photoabsorption technique is that reliable plasma densities and consequently, absolute cross sections, are difficult to establish. One method of plasma density determination would involve the merging of a 1m normal incidence spectrometer (recently commissioned in DCU) with the 2.2m grazing incidence spectrometer used throughout this work. A second focussing optic, such as an off axis parabolic mirror modified with a hole through its centre, could act as a beamsplitter allowing light from the source plasma to be imaged simultaneously in two different energy regions i.e. visible and VUV. As the cross sections of many valence transitions (corresponding to the visible energy region) are well known for many atoms and ions, the density of the absorbing plasma could be accurately determined allowing spectral features observed simultaneously in the VUV to be put on an absolute cross sectional scale.

With regard to the calcium results presented in chapter 3, the introduction of a third laser to resonantly pump the $Ca^0 3p^6 4s^2 \rightarrow 3p^6 4s3d\ ^3D, ^1D$ and $Ca^+ 3p^6 4s \rightarrow 3p^6 3d\ ^2D$ transitions would put our Ca^0 and Ca^+ excited state assignments beyond all doubt. Laser dyes are available which show maximum lasing at energies corresponding to the appropriate resonant transitions i.e. 2.52eV(492nm), 2.71eV (458nm) and 1.7eV(730nm) respectively. These are, respectively, Coumarin 487, Coumarin 460 and LDS730. Of course, the implementation of a third laser would require a target chamber re-design.

The improved cross sections for Ca^+ given in chapter 3 have a peak cross section error estimated at ~±20%. Although this is quite large, the difference in the relative intensity between Ca^+ features in the 3p region, when compared with lower resolution

measurements, is considerable. The Ca^+ 3p region would therefore be a worthy candidate for investigation with third generation synchrotrons where with the extremely high resolution photoion detection techniques now available, the accuracy of our absolute cross section determinations could be tested.

A full interpretation of both the Ca^+4s spectrum and the excited state spectra of Ca^+3d and $Ca^0 4s3d$ will remain prohibitively difficult unless subjected to more rigorous theoretical investigations. Although more complex theoretical methodologies, such as R-Matrix and RRPA would be more likely to provide a detailed interpretation, the Hartree-Fock based suite of codes by Cowan could be used for term-dependent calculations. Given, as we have found, the calculational difficulties in adequately accounting for 3d wavefunction collapse to accurately predict transitions between levels with 3d character, term-dependent calculations could be used to extract Slater intergrals suitable for specific term wavefunctions. This would thus lead to better results than those obtained using Centre-of-Gravity wavefunctions.

In investigating the first five members of the neon isoelectronic sequence, the DLP system has been pushed to the limits. An extension of the sequence investigations to higher members is not possible as the 2s region of higher members lies beyond our measuring range. However, other systems, capable of measuring to higher energies could be used to confirm the predicted anomalous near threshold cross sections for other sequence members as higher $2s2p^6np\ ^1P$ resonances successively move down to cross the $^2P_{3/2,1/2}$ thresholds. With the recent advances in highly charged ion source technology, it will soon be possible to measure Mg^{2+}, Al^{3+} and Si^{4+} with extremely high resolution photoion and photoelectron spectroscopic techniques. Confirmation of forced autoionisation for the $Si^{4+}\ 2s2p^63p\ ^1P$ resonance should then be possible.


References

Al Moussalami S., Bizau J-M., Rouvellou B., Cubaynes D., Journel L., Wuilleumier F.J., Obert J., Putaux J.C., Morgan T.J. and Richter M., Phys. Rev. Lett., 76, 24, 4496-4499, 1996.

Aleksandrov Yu. M., Gruzdev P.F., Kozlov M.G., Loginov A.V., Makhov V.N., Fedorchuk R.V. and Yakimenko M.N., Opt. Spectrosc. (USSR), 54, 1, 4-7, 1983.

Alton G.D. and Smithe D.N., Rev. Sci. Instrum., 65, 4, 775-787, 1994.

Alton G.D., Meyer F.W., Liu Y., Beene J.R. and Tucker D., Rev. Sci. Instrum., 69, 6, 2305-2312, 1998.

Altun Z. and Kelly H.P., Phys. Rev. A, 31, 6, 3711-3717, 1985.

Amusia M. Ya., Cherepkov N.A. and Chernysheva L.V., Zh. Eksp. Teor. Fiz., 60, 160 (Sov. Phys. - JETP, 33, p90), 1971.

Anderson J., Ap. J., 59, 76, 1924.

Arbes F., Gudjons T., Kurth F., Werth G., Marin F. and Inguscio M., Z. Phys. D, 25, 295-298, 1993.

Baier S., Fiedler W., Müller B.R., Schulze M., Zimmermann P., Meyer M., Pahler M., Prescher Th., von Raven E., Richter M., Rüder J. and Sonntag B., J. Phys. B: At. Mol. Opt. Phys., 25, 923-930, 1992.

Ballofet G, Romand J and Vodar C, C. R. Acad. Sci., 252, 4139, 1961.

Balmer J., Lewis C.L.S., Corbett R.E., Robertson E., Saadat S., O'Neill D., Kilkenny J.D., Back C.A. and Lee R.W., Phys. Rev. A, 40, 1, 330-340, 1989.

Basov N. G. et al, Sov. Phys.-Tech. Phys., 13, 1581, 1969.

Bates, D.R., Kingston A.E. and McWhirter R.W.P., Proc. Roy. Soc. A., 267, 297-312, 1962.(Part I)

Bates, D.R., Kingston A.E. and McWhirter R.W.P., Proc. Roy. Soc. A., 270, 155-167, 1962.(Part II)

Becker U., Szostak D., Kerkhoff H.G., Kupsch M., Langer B., Wehlitz R., Yagishita A. and Hayaishi T., Phys. Rev. A., 39, 8, 3902-3911, 1989.

Bekefi G., Deutsch C. and Yaakobi B., *Principles of Laser Plasmas*, Ed: Bekefi G., John Wiley and Sons, 1976.

Beutler H.G., J. Opt. Soc. Am., 35, 311, 1945.

Beyer H-J., West J.B., Ross K.J., Ueda K., Kabachnik N.M., Hamdy H. and Kleinpoppen H., J. Phys. B: At. Mol. Opt. Phys., 28, L47-L52, 1995.

Bizau J.M., Gérard P., Wuilleumier F.J. and Wendin G., Phys. Rev. A, 36, 3, 1220-1248, 1987.

Bizau J-M., Cubaynes D., Gérard P. and Wuilleumier F.J., Phys. Rev. A., 40, 6, 3002-3025, 1989.

Bizau J-M., Cubaynes D., Richter M., Wuilleumier F., Obert J. and Putaux J.C., Rev. Sci. Instrum., 63, 1, 1389-1392, 1992.

Bizau J-M., Cubaynes D., Richter M., Wuilleumier F.J., Obert J., Putaux J.C., Morgan T.J., Källne E., Sorensen S. and Damany A., Phys. Rev. Lett., 67, 5, 576-579, 1991.

Blondel C., Champeau R-J. and Delsart C., Phys. Rev. A, 27, 1, 583-586, 1983.

Boland B.C., Irons F.E. and McWhirter R.W.P., J. Phys. B (Proc. Phys. Soc.), 2, 1, 1180-1191, 1968.

Borgström A., Ark. Fys., 38, 243, 1968.

Borgström A., Phys. Scr., 3, 157, 1971.

Bowen I.S., Phys. Rev., 31, 497, 1928.

Bransden B.H. and Joachain C.J., *Physics of Atoms and Molecules*, Longman scientific and technical, 1990.

Bridges J.M., Cromer C.L. and McIlrath T.J., Appl. Opt., 25, 2208-2214, 1986.

Brillet W-U. L. and Artru M-C., Phys. Scr., 14, 285-289, 1976.

Brillet W-U. L., Phys. Scr., 13, 289-292, 1976.

Brilly J., Ph.D. Thesis, Dublin City University, 1990.

Bruch R., Paul G., Andrä J. and Lipsky L., Phys. Rev. A, 12, 1808, 1975.

Burke P.G. and Taylor K.T., J. Phys. B: At. Mol. Phys., 8, 16, 2620-2639, 1975.

Burke P.G., Kingston A.E. and Thompson A., J. Phys. B: At. Mol. Phys., 16, L385, 1983.

Carillon A., Jaégle P. and Dhez P., Phys. Rev. Lett. 25, 140, 1970.

Carillon A., Jamelot G., Sureau A. and Jaegle P., Phys. Lett., 38A, 2, 91-92, 1972.

Carroll P.K. and Costello J.T., Phys. Rev. Lett., 57, 1581, 1986.

Carroll P.K. and Kennedy E.T., Contemp. Phys., 22, 61-96, 1981.

Carroll P.K. and Kennedy E.T., Phys. Rev. Lett., 38, 1068, 1977.

Carroll P.K. and O'Sullivan G., Phys. Rev. A, 25, 275, 1982.

Carroll P.K., Kennedy E. T. and O'Sullivan G., Appl. Opt., 19, 1454-1462, 1980.

Carroll P.K., Kennedy E.T. and O'Sullivan G., IEEE. J. Quant. Electron., QE-19, 1807, 1983.

Carroll P.K., Kennedy E.T. and O'Sullivan G., Opt. Lett., 2, 72, 1978.

Chakraborty H.S., Gray A., Costello J.T., Deshmukh P.C., Haque G.N., Kennedy E.T., Manson S.T. and Mosnier J-P., *Accepted in* Phys. Rev. Lett. (*To be published*), 1999.

Chan W.F., Cooper G., Guo X. and Brion C.E., Phys. Rev. A, 45, 3, 1420-1433, 1992.

Codling K., Madden R.P. and Ederer D.L., Phys. Rev., 155, 1, 26-37, 1967.

Cohen-Tannoudji C., Diu B. and Laloë F., *Quantum Mechanics : Volumes I and II*, John Wiley and sons, 1977.

Cole B.E., Cooper J.W. and Saloman E.B., Phys. Rev. Lett., 45, 11, 887-890, 1980.

Colombant D. and Tonon G.F., J. Appl. Phys., 44, 8, 3524-3537, 1973.

Cooper J., Rep. Prog. Phys., 29, 1, 35-130, 1966.

Corney A., *Atomic and Laser Spectroscopy*, Clarendon Press, Oxford, 1977.

Costello J. T., Mosnier J-P. and Kennedy E.T., Physica Scripta, T34, p77-92, 1991.

Costello J.T., Evans D., Hopkins R.B., Kennedy E.T., Kiernan L., Mansfield M.W.D., Mosnier J-P., Sayyad M.H. and Sonntag B.F., J. Phys. B: At. Mol. Opt. Phys., 25, 5055-5068, 1992.

Costello J.T., Kennedy E.T., Mosnier J-P. and Sayyad M.H., J. Phys. B : At. Mol. Opt. Phys., 31, 677-688, 1998a.

Costello J.T., Kennedy E.T., Mosnier J-P., Sayyad M.H. and McGuinness C., J. Phys. B : At. Mol. Opt. Phys., 31, L547, 1998b.

Costello J.T., Mosnier J-P, Kennedy E.T, Carroll P.K. and O'Sullivan G, Phys. Scr., T34, 77-92, 1991.

Cowan R.D., J. Opt. Soc. Am., 58, 6, 808, 1968.

Cowan R.D., *The Theory of Atomic Structure and Spectra*, Berkeley, CA : University of California Press, 1981.

Crooker A.M., *Unpublished information*, 1966.

Davidson S.J., Foster J.M., Smith C.C., Warburton K.A. and Rose S.J., Appl. Phys. Lett., 52, 10, 847-849, 1988.

Dill D. and Fano U., Phys. Rev. Lett., 29, 1203, 1972.

Dimitrijevic M.S. and Sahal-Bréchot S., Astron. Astrophys. Suppl. Ser. 119, 369, 1996.(available at ftp://adc.gsfc.nasa.gov/pub/adc/archives/journal_tables/A+AS/119/369).

Doerfert J., Träbert E., Wolf A., Schwalm D. and Uwira O., Phys. Rev. Lett., 78, 23, 4355-4358, 1997.

Domke M., Mandel T., Puschmann A., Xue C., Shirley A., Kaindl G., Petersen H. and Kuske P., Rev. Sci. Instr., 63, 1, 80-89, 1992a.

Domke M., Remmers G. and Kaindl G., Phys. Rev. Lett., 69, 8, 1171-1174, 1992b.

Domke M., Schulz K., Remmers G., Gutiérrez A., Kaindl G. and Wintgen D., Phys. Rev. A, 51, 6, R4309-R4312, 1995.

Domke M., Schulz K., Remmers G., Kaindl G. and Wintgen D., Phys. Rev. A, 53, 3, 1424-1438, 1996.

Domke M., Xue C., Puschmann A., Mandel T., Hudson E., Shirley D.A., Kaindl G., Greene C.H., Sadeghpour H.R. and Petersen H., Phys. Rev. Lett., 66, 10, 1306-1309, 1991.

Dorn A., Nienhaus J., Wetzstein M., Winnewisser C., Eichmann U., Sandner W. and Mehlhorn W., J. Phys. B: At. Mol. Opt. Phys., 28, L225-L231, 1995.

Dorn A., Zatsarinny O. and Mehlhorn W., J. Phys. B: At. Mol. Opt. Phys., 30, 2975-2997, 1997.

Eckart M.J., Scofield J.H. and Hazi A.U., J. de Physique, C1, 361, 1988.

Ederer D.L. and Tomboulian D.H., Phys. Rev., 133, 6A, A1525-A1532, 1964.

Ehler A. W. and Weisller G.L., Appl. Phys. Lett., 8, 89, 1966.

Ekefors E., Z. Phys., 71, 53, 1931.

Elton R.C., Lee T.N. and McLean E.A., J. de Physique, C9, 359, 1987.

Elton R.C., *X-Ray Lasers*, Academic Press, 1990.

Esteva J.M. and Mehlman G., Ap. J., 193, 747-753, 1974.

Fano U. and Cooper J.W., Phys. Rev., 137, 5A, A1364-A1379, 1965.

Fano U., Phys. Rev., 124, 6, 1866-1878, 1961.

Fauquignon C. and Floux F., Phys. Fluids, 13, 2, 386-391, 1970.

Ferner E., Ark. Mat. Astron. Fysik, 28A, 4, 21, 1942.

Ferner E., Ark. Mat. Astron. Fysik, 36A, 1, 65, 1948.

Galanti M. and Peacock N. J., J. Phys. B, 8, 2427, 1975.

Gallagher T.F., Gounand F., Kachru R., Tran N.H. and Pillet P., Phys. Rev. A, 27, 5, 2485-2492, 1983.

Garton W.R.S. and Codling K., Proc. Phys. Soc. Lon., 75, 87, 1960.

Garton W.R.S., *Autoionisation : Astrophysical, Theoretical and Laboratory Experimental Aspects*, Ed : Temkin A., Mono Book Corp., Baltimore, 1966.

Garton W.R.S., Parkinson W.H. and Reeves E.M., Proc. Phys. Soc. Lon., 80, 860, 1962.

Glab W.L. and Qin K., Phys. Rev. A, 48, 6, 4492-4499, 1993.

Gohil P., Kaufman V. and McIlrath T.J., Appl. Opt., 25, 2039, 1986.

Gottwald A., Anger S., Bizau J-M., Rosenthal D. and Richter M., Phys. Rev. A, 55, 5, 3941-3944, 1997.

Gottwald A., *Private communication,* 1998.

Griem H.R., *Spectral Line Broadening by Plasmas,* Academic Press, 1974.

Gudjons T., Hilbert B., Seibert P. and Werth G., Europhys. Lett., 33, 8, 595-598, 1996.

Gullikson E.M., Denham P., Mrowka S. and Underwood J.H., Phys. Rev. B, 49, 23, 16283, 1994.

Hagemann H-J., Gudat W. and Kunz C., DESY SR-74/7 Internal Report, 1974.

Hamdy H., Beyer H-J., West J.B. and Kleinpoppen H., J. Phys. B: At. Mol. Opt. Phys., 24, 4957-4972, 1991.

Hansen J.E. and Quinet P., J. Elec. Spect. Relat. Phenom., 79, 307-310, 1996.

Hansen J.E., J. Phys. B: At. Mol. Phys., 8, 17, 2759-2770, 1975.

Henke B.L., Gullikson E.M. and Davis J.C., *X-ray interactions: photoabsorption, scattering, transmission and reflection at E = 50 - 30,000eV, Z = 1-92,* Atomic data and Nuclear data tables, 54 (No. 2), p181-342, 1993.

Hibbert A. and Scott M.P., J. Phys. B: At. Mol. Opt. Phys., 27, 1315-1323, 1994.

Hibbert A., *Private communication,* 1998.

Hopkins B., M.Sc. Thesis, Dublin City University, 1992.

Hora H., *Plasmas at High Temperature and Density - Applications and Implications of Laser-Plasma Interaction*, Springer-Verlag, 1991.

Hughes I., Phys. World, 8, 43, 1995.

Hughes T.P., *Plasmas and Laser Light*, Adam Hilger Ltd., 1975.

Irons F.E., McWhirter R.W.P. and Peacock N.J., J. Phys. B: At. Mol. Phys., 5, 1975-1987, 1972.

Ivanov V.K. and West J.B., J. Phys. B: At. Mol. Opt. Phys., 26, 2099-2113, 1993.

Jaegle P., Carillon A., Dhez P., Jamelot G., Sureau A. and Cukier M., Phys. Lett., 36A, 3, 167-168, 1971.

Jaegle P., Jamelot G., Carillon A., Sureau A. and Dhez P., Phys. Rev. Lett., 33, 18, 1070-1073, 1974.

Jamelot G., Sureau A. and Jaegle P., Phys. Lett., 41A, 2, 153-154, 1972.

Jannitti E., Mazzoni M., Nicolosi P., Tondello G. and Yong-Chang W., J. Opt. Soc. Am., B2, 1078, 1985.

Jannitti E., Nicolosi P. and Tondello G., Opt. Commun., 50, 225, 1984b.

Jannitti E., Nicolosi P. and Tondello G., Phys. Lett., A131, 186, 1988.

Jannitti E., Nicolosi P. and Tondello G., Physica Scripta, 36, 93, 1987b.

Jannitti E., Nicolosi P. and Tondello G., Physica Scripta, 41, 458, 1990.

Jannitti E., Nicolosi P. and Tondello G., Physica, 124C, 139, 1984a.

Jannitti E., Nicolosi P. and Tondello G., SPIE Vol. 911, *X-Ray and VUV interaction databases, calculations and measurements,* 157-165, 1988.

Jannitti E., Nicolosi P., Tondello G., Yongzhen Z. and Mazzoni M., Opt. Commun., 63, 37, 1987a.

Jannitti E., Pinzhong F. and Tondello G., Physica Scripta, 33, 434, 1986.

Jauhiainen J., Ausmees A., Kivimäki A., Osborne S.J., Naves de Brito A., Aksela S., Svensson S. and Aksela H., J. Elec. Spect. Rel. Phen., 69, 181-187, 1994.

Johnson W.R. and Cheng K.T., Phys. Rev. A, 20, 978, 1979.

Johnson W.R., Lin C.D., Cheng K.T. and Lee C.M., Phys. Scr., 21, 409, 1980.

Johnston T. W. and Dawson J.M., Phys. Fluids, 16, 5, 722, 1973.

Kalachnikov M.P., Nickles P.V., Schnurer M., Sandner W., Shlyaptsev V.N., Danson C., Neely D., Wolfrum E., Zhang J., Behjat A., Demir A., Tallents G.J., Warwick P.J. and Lewis C.L.S., Phys. Rev. A, 57, 6, 4778-4783, 1998.

Kastner S.O., Crooker A.M., Behring W.E. and Cohen L., Phys. Rev. A, 16, 2, 577-582, 1977.

Kaufman V, Artru M-C. and Brillet W-U. L., J. Opt. Soc. Am., 64, 2, 197-201, 1974.

Keane C.J., Ceglio N.M., MacGowan B.J., Matthews D.L., Nilson D.G., Trebes J.E., Whelan D.A., J. Phys. B: At. Mol. Opt. Phys., 22, 3343-3362, 1989.

Kelly R.L., *Atomic and Ionic Spectrum Lines below 2000 Angstroms*, Part I (H-Cr), Part II (Mn-Kr) and Part III (Finding List), J. Phys. Chem. Ref. Data, Vol. 16 (Supp. No. 1), 1987.

Kennedy E.T., Costello J.T. and Mosnier J-P., J. Elec. Spect. Relat. Phenom., 79, 283-288, 1996.

Kennedy E.T., Costello J.T., Gray A., McGuinness C., Mosnier J-P. and van Kampen P., J. Elec. Spect. Relat. Phenom., 101-103, 161-166, 1999.

Kennedy E.T., Costello J.T., Mosnier J-P., Cafolla A.A., Collins M., Kiernan L., Köble U., Sayyad M.H., Shaw M., Sonntag B.F. and Barchewitz R., Opt. Eng., 33, 12, 3984-3992, 1994.

Key M.H., Lewis C.L.S., Lunney J.G., Moore A., Hall T.A. and Evans R.G., Phys. Rev. Lett., 41, 21, 1467-1470, 1978.

Khan M.A. and Al-Kuhaili M.F., J. Phys. B: At. Mol. Opt. Phys., 26, 393-402, 1993.

Khan M.A., Connerade J-P. and Rafique M., J. Phys. B: At. Mol. Opt. Phys., 27, L563-L569, 1994b.

Khan M.A., Gondal M.A. and Rais M.H., J. Phys. B: At. Mol. Opt. Phys., 27, 2889-2904, 1994a.

Khan M.A., Khawaja E.E. and Al-Juwair H.A., J. Phys. B: At. Mol. Opt. Phys., 23, L533-L539, 1990.

Khan M.A., Qureshi R.A. and Gondal M.A., Chem. Phys. Lett., 264, 273-278, 1997.

Kiernan L., Ph.D. Thesis, Dublin City University, 1994.

Kiernan L.M., Costello J.T., Kennedy E.T., Mosnier J-P. and Sonntag B.F., J. Phys. B : At. Mol. Opt. Phys., 30, 4801-4812, 1997.

Kiernan L.M., Kennedy E.T., Mosnier J-P. and Costello J.T., Phys. Rev. Lett., 72, 15, 2359-2362, 1994.

Kirkbright G.F. and Sargent M., *Atomic Absorption and Fluorescence Spectroscopy*, Academic Press, 1974.

Knoop M., Vedel M. and Vedel F., Phys. Rev. A, 52, 5, 3763-3769, 1995.

Köble U., Costello J.T., Mosnier J-P., Kennedy E.T. and Martins M., J. Phys. B : At. Mol. Opt. Phys., 28, 181-190, 1995a.

Köble U., Kiernan L., Costello J.T., Mosnier J-P. and Kennedy E.T., Phys. Rev. Lett., 74, 12, 2188-2191, 1995b.

Kupliauskiene A., J. Phys. B: At. Mol. Opt. Phys., 31, 2885-2896, 1998.

Lamoureux M. and Radojevic V., J. Phys. B: At. Mol. Phys., 15, 1341-1351, 1982.

Langer B., Berrah N., Wehlitz R., Gorczyca T.W., Bozek J. and Farhat A., J. Phys. B: At. Mol. Opt. Phys., 30, 593-607, 1997.

Langer B., Berrah N., Wehlitz R., Gorczyca T.W., Bozek J. and Farhat A., J. Phys. B: At. Mol. Opt. Phys., 30, 593-607, 1997.

Lassettre E.N. and Silverman S., J. Chem. Phys., 40, 1265, 1964.

Lee T.N., McLean E.A. and Elton R.C., Phys. Rev. Lett., 39, 1185, 1987.

Lee T.N., McLean E.A., Stamper J.A., Griem H.R. and Manka C.K., Bull. Am. Phys. Soc., 33, 1920, 1988.

Lerner J.M. and Thevenon A., *The Optics of Spectroscopy - A Tutorial V2.0*, Jobin-Yvon Optical Systems, Instruments S.A. Ltd., 1988.

Li Y., Pretzler G. and Fill E.E., Phys. Rev. A, 52, 5, R3433-R3435, 1995.

Liaw S-S., Phys. Rev. A, 51, 3, R1723-R1726, 1995.

Lide D.R., *CRC Handbook of Chemistry and Physics, 74th Edition*, CRC Press, 1993.

Lin J.Y., Tallents G.J., Smith R., MacPhee A.G., Wolfrum E., Zhang J., Eker G., Keenan R., Lewis C.L.S., Neely D., O'Rourke R.M.N., Pert G.J., Pestehe S.J. and Wark J.S., J. Appl. Phys., 85, 2, 672-675, 1999.

Lochte-Holtgreven W., *Plasma Diagnostics*, AIP Press, New York, 1995.

Lucatorto T.B. and McIlrath T.J., Phys. Rev. Lett., 37, 7, 428-431, 1976.

Lucatorto T.B., McIlrath T.J. and Roberts J.R., J. Opt. Soc. Am., 18, 2505, 1979.

Lucatorto T.B., McIlrath T.J., Sugar J. and Younger S.M., Phys. Rev. Lett., 47, 1124, 1981.

Luke T.M., J. Phys. B: At. Mol. Phys., 6, 30-41, 1973.

Lundström T., Phys. Scr., 7, 62-64, 1973.

Lyon I.C., Peart B. and Dolder K., J. Phys. B: At. Mol. Phys., 20, 1925-1932, 1987b.

Lyon I.C., Peart B., Dolder K and West J.B., J. Phys. B: At. Mol. Phys., 20, 1471-1477, 1987a.

Lyon I.C., Peart B., West J.B. and Dolder K., J. Phys. B: At. Mol. Phys., 19, 4137-4147, 1986.

MacGowan B.J. et al, J. Appl. Phys., 61, 5243, 1987.

Mack J.E., Stehn J.R. and Edlén B., J. Opt. Soc. Am., 22, 245, 1932.

Madden R.P. and Codling K., Ap. J., 141, 364, 1965.

Madden R.P. and Codling K., *Autoionisation : Astrophysical, Theoretical and Laboratory Experimental Aspects*, Ed : Temkin A., Mono Book Corp., Baltimore, 1966.

Mahon C.R., Janik G.R. and Gallagher T.F., Phys. Rev. A, 41, 3746, 1990.

Mannervik S., Short R.T., Sonnek D., Träbert E., Möller G., Lodwig Y., Heckmann P.H., Blanke J.H. and Brand K., Phys. Rev. A, 39, 3964, 1989.

Mansfield M.W.D. and Newsom G.H., Proc. R. Soc. Lond. A, 357, 77-102, 1977.

Mansfield M.W.D. and Ottley T.W., Proc. R. Soc. Lond. A, 365, 413-424, 1979.

Mansfield M.W.D. in '*Giant resonances in atoms, molecules and solids*', eds. Connerade J.P., Esteva J.M. and Karnatak, NATO ASI series : series B: physics vol. 151, Plenum press, New York, 1987.

Mansfield M.W.D., Proc. R. Soc. Lond. A, 346, 555-563, 1975.

Mansfield M.W.D., Proc. R. Soc. Lond. A, 348, 143-151, 1976.

Martinson I. Rep. Prog. Phys., 52, 157-225, 1989.

Matthews D.L. et al, J. de Physique, C6, 1, 1986.

McGuinness C., Ph.D. Thesis, University College Dublin, 1996.

McIlrath T.J. and Carlsten J.L., J. Phys. B: At. Mol. Phys., 6, 697-708, 1973.

McWhirter R.W.P., *Plasma Diagnostic Techniques*, Ed: Huddlestone R.H. and Leonard S.L., Academic Press, 1965.

Meighan O., Dardis L., Kennedy E.T., Morgan T.J., Mosnier J-P., van Kampen P. and Costello J.T., J. Phys. B: At. Mol. Opt. Phys., 32, 13, L285-90, 1999

Menzel A., Frigo S.P., Whitfield S.B., Caldwell C.D. and Krause M.O., Phys. Rev. A, 54, 3, 2080-2090, 1996.

Menzel A., Frigo S.P., Whitfield S.B., Caldwell C.D., Krause M.O., Tang J-Z., Shimamura I., Phys. Rev. Lett., 75, 8, 1479-1482, 1995.

Meyer M., von Raven E., Richter M., Sonntag B. and Hansen J.E., J. Elec. Spect. Relat. Phenom., 51, 407-416, 1990.

Meyer M., von Raven E., Sonntag B. and Hansen J.E., Phys. Rev. A, 49, 3685-3703, 1994.

Miecznik G., Berrington K.A., Burke P.G. and Hibbert A., J. Phys. B: At. Mol. Opt. Phys., 23, 3305-3314, 1990.

Mitchell A.C.G. and Zemansky M.W., *Resonance Radiation and Excited Atoms*, Cambridge University Press, 1971 (1st Pub. 1934).

Moloney C., M.Sc. Thesis, Dublin City University, 1998.

Moore C.E., *Atomic Energy Levels Vol. 1*, NBS Circular No. 467 (Washington, DC: US Govt. Printing Office), 1949.

Morgenstern R., *Hollow atoms, Atomic Physics 15*, eds. Linden Van den Heuvell H.B., Walraven J.T.M., Reynolds M.W., World Scientific, Singapore, 97-112, 1997.

Morton D.C., Phys. Scr., T47, 183-185, 1993.

Mosnier J-P., Costello J.T., Kennedy E.T., Kiernan L. and Sayyad M.H., Phys. Rev. A, 49, 2, 755-761, 1994.

Nakamura M., Sasanuma M., Sato S., Watanabe M., Yamashita H., Iguchi Y., Ejiri A., Nakai S., Yamaguchi S., Sagawa T., Nakai Y. and Oshio T., Phys. Rev. Lett., 21, 18, 1303-1305, 1968.

Namioka T., J. Opt. Soc. Am., 49, 446, 1959.

Nienhaus J., Zatsarinny O.I., Dorn A. and Mehlhorn W., J. Phys. B: At. Mol. Opt. Phys., 30, 3611-3626, 1997.

Nilsen J., Zhang J., MacPhee A.G., Lin J., Barbee Jr. T.W., Danson C., Da Silva L.B., Key M.H., Lewis C.L.S., Neely D., O'Rourke R.M.N., Pert G.J., Smith R., Tallents G.J., Wark J.S. and Wolfrum E., Phys. Rev. A, 56, 4, 3161-3165, 1997.

Obst B., Benten W., von dem Borne A., Costello J., Dardis L., Gerth Ch., Glatzel P., Gray A., Hansen J.E., Meighan O., Kennedy E., McGuinness C., Sonntag B., Verweyen A., Wernet Ph. and Zimmermann P., J. Elec. Spect. Relat. Phenom., 101-103, 39-42, 1999.

O'Neill D., Lewis C.L.S., Neely D., Davidson S.J., Rose S.J. and Lee R.W., Phys. Rev. A, 44, 4, 2641-2648, 1991.

Orth F. B., Ueda K., McIlrath T.J. and Ginter M.L., Appl. Opt., 25, 2215, 1986.

O'Sullivan G., J. Phys. B, 16, 3291, 1983.

O'Sullivan G., McGuinness C., Costello J.T., Kennedy E.T. and Weinmann B., Phys. Rev. A, 25, 3211, 1996.

Parpia F.A., Johnson W.R. and Radojevic V., Phys. Rev. A, 29, 6, 3173-3180, 1984.

Peart B. and Dolder K.T., J. Phys. B: At. Mol. Phys., 8, 56-62, 1975.

Peart B. and Lyon I.C., J. Phys. B: At. Mol. Phys., 20, L673-L675, 1987b.

Peart B., Lyon I.C. and Dolder K., J. Phys. B: At. Mol. Phys., 20, 5403-5410, 1987a.

Pejcev V., Ottley T.W., Rassi D. and Ross K.J., J. Phys. B : At. Mol. Phys., 10, 12, 2389-2398, 1977.

Pejcev V., Ottley T.W., Rassi D. and Ross K.J., J. Phys. B: At. Mol. Phys., 11, 3, 531-539, 1978.

Perkampus H-H., *UV-VIS Spectroscopy and its Applications*, Springer-Verlag, 1992.

Pindzola M.S., Bottcher C. and Griffin D.C., J. Phys. B: At. Mol. Phys., 20, 3535, 1987.

Powell F.R., Vedder P.W., Lindblom J.F. and Powell S.F., Opt. Eng., 29, 6, 614, 1990.

Puell H., Z. Naturforsch, 25a, 1807-1815, 1970.

Quinet P. and Hansen J.E., J. Phys. B: At. Mol. Opt. Phys., 28, L213-L220, 1995.

Rae A.I.M., *Quantum Mechanics : 2nd Edition*, Adam Hilger, 1990.

Ready J.F., *Effects of High-Power Laser Radiation*, Academic Press, 1971.

Ready J.F., J. Appl. Phys., 36, 462, 1965.

Ritter G. and Eichmann U., J. Phys. B: At. Mol. Opt. Phys., 30, L141-L146, 1997.

Ross K.J., West J.B. and Beyer H-J., J. Phys. B: At. Mol. Opt. Phys., 30, L735-L740, 1997.

Rost J.M., Schulz K., Domke M. and Kaindl G., J. Phys. B: At. Mol. Opt. Phys., 30, 4663-4694, 1997.

Samson J.A.R., *Techniques of Vacuum Ultraviolet Spectroscopy*, John Wiley and Sons, 1967.

Sandner W., Safinya K.A. and Gallagher T.F., Phys. Rev. A, 24, 1647, 1981.

Sandner W., Safinya K.A. and Gallagher T.F., Phys. Rev. A, 33, 2, 1008-1019, 1986.

Sato Y., Hayaishi T., Itikawa Y., Itoh Y., Murakami J., Nagata T., Sasaki T., Sonntag B., Yagishita A. and Yoshino M., J. Phys. B: At. Mol. Phys., 18, 225-231, 1985.

Sayyad M.H., Kennedy E.T., Kiernan L., Mosnier J-P. and Costello J.T., J. Phys. B : At. Mol. Opt. Phys., 28, 1715, 1995.

Sayyad M.H., Ph.D. Thesis, Dublin City University, 1994.

Schlapp M., Pardo R.C., Vondrasek R.C., Szczech J., Billquist P.J., Vieregg J., Xie Z.Q., Lyneis C.M. and Harkewicz R., Rev. Sci. Instrum., 69, 2, Part 2 ,631-633, 1998.

Schmidt V., Rep. Prog. Phys., 55, 1483-1659, 1992.

Schulz K., Domke M., Puttner R., Gutiérrez A., Kaindl G., Miecznik G. and Greene C., Phys. Rev. A, 54, 4, 3095-3112, 1996.

Schulz K., Kaindl G., Domke M., Bozek J.D., Heimann P.A., Schlachter A.S. and Rost J.M., Phys. Rev. Lett., 77, 15, 3086-3089, 1996.

Seaton M.J., J. Phys. B : At. Mol. Opt. Phys., 21, 3033, 1988.

Seaton M.J., J. Phys. B: At. Mol. Opt. Phys., 20, 6363-6378, 1987.

Shaw M., M.Sc. Thesis, Dublin City University, 1996.

Shenstone A.S., Phys. Rev., 38, 873, 1931.

Shore B.W., J. Opt. Soc. Am., 57, 7, 881-884, 1967b

Shore B.W., Rev. Mod. Phys., 39, 2, 439-462, 1967a

Shull J.M., Phys. Scr., T47, 165-170, 1993.

Söderqvist J., Nova Acta Reg. Soc. Sci. Uppsala [IV], 9, 7, 1934.

Sonntag B. and Zimmermann P., Rep. Prog. Phys., 911-987, 1992.

Sonntag B.F., Cromer C.L., Bridges J.M., McIlrath T.J. and Lucatorto T.B., Am. Inst. Phys. Conf. Ser. No. 147 (New York: AIP), 412-422, 1986.

Spectron Laser Systems, *Pulsed Nd:YAG SL400/800 systems owners manual,* 1991.

Stener M., Decleva P. and Lisini A., J. Phys. B: At. Mol. Opt. Phys., 28, 4973-4999, 1995.

Sugar J. and Corliss C., '*Atomic Energy Levels of the Iron-Period Elements: Potassium through Nickel*', J. Phys. Chem. Ref. Data, Vol. 14, Suppl. 2, 1985.

Ueda K., West J.B., Kabachnik N.M., Sato Y., Ross K.J., Beyer H-J., Hamdy H. and Kleinpoppen H., Phys. Rev. A, 54, 1, 490-495, 1996.

Ueda K., West J.B., Ross K.J., Hamdy H., Beyer H-J. and Kleinpoppen H., Phys. Rev. A, 48, 2, R863-R866, 1993.

Ueda K., West J.B., Ross K.J., Kabachnik N.M., Beyer H-J., Hamdy H. and Kleinpoppen H., J. Phys. B: At. Mol. Opt. Phys., 30, 2093-2108, 1997.

Unsöld in *Plasma Diagnostics* Ed : Lochte-Holtgreven W., AIP Press, New York, 1995.

Vaeck N., Godefroid M. and Froese Fischer C., Phys. Rev. A, 46, 7, 3704-3716, 1992.

Valero F. P. J., App. Phys. Lett., 25, 1, 64-66, 1974.

van Kampen P., Kiernan L., Costello J.T., Kennedy E.T., van der Mullen J.A.M. and O'Sullivan G., J. Phys. B: At. Mol. Opt. Phys., 28, 4771-4779, 1995.

van Kampen P., O'Sullivan G., Ivanov V.K., Ipatov A.N., Costello J.T. and Kennedy E.T., Phys. Rev. Lett., 78, 16, 3082-3085, 1997.

Verner D.A., Barthel P.D. and Tytler D., Astron. Astrophys. Suppl. Ser. 108, 287, 1994.(available at ftp://adc.gsfc.nasa.gov/pub/adc/archives/journal_tables/A+AS/108/287).

Vrijen R.B., Hoogenraad J.H. and Noordam L.D., Phys. Rev. A, 52, 3, 2279-2287, 1995.

Wedowski M., Godehusen K., Weisbarth F., Zimmermann P., Martins M., Dohrmann Th., von dem Borne A., Sonntag B. and Grum-Grzhimailo A.N., Phys. Rev. A, 55, 3, 1922-1936, 1997.

Wernet Ph., Glatzel P., Verweyen A., Sonntag B., Obst B., Benten W., Gerth Ch., Zimmermann P., Gray A. and Costello J., J. Phys. B: At. Mol. Opt. Phys., 31, L289-L296, 1998.

West J.B., Ueda K., Kabachnik N.M., Ross K.J., Beyer H-J. and Kleinpoppen H., Phys. Rev. A, 53, 1, R9-R11, 1996.

Whitty W., Costello J.T., Kennedy E.T., Moloney C. and Mosnier J-P., Appl. Surf. Sci., 127-129, p686-691, 1998.

Whitty W., Ph.D. Thesis, Dublin City University, 1998.

Wills A.A., Cafolla A.A., Svensson A. and Comer J., J. Phys. B: At. Mol. Opt. Phys., 23, 2013-2028, 1990.

Wills A.A., Gorczyca T.W., Berrah N., Langer B., Felfli Z., Kukk E., Bozek J.D., Nayandin O. and Alshehri M., Phys. Rev. Lett., 80, 23, 5085-5088, 1998.

Wuilleumier F.J., Bizau J-M., Cubaynes D., Rouvellou B. and Journel L., Nucl. Instr. and Meth. in Phys. Res. B, 87, 190-197, 1994.

Xie Z.Q., Rev. Sci. Instrum., 69, 2, Part 2, 625-630, 1998.

Zatsarinny O.I., J. Phys. B: At. Mol. Opt. Phys., 28, 4759-4769, 1995.

Zhang J., MacPhee A.G., Lin J., Wolfrum E., Smith R., Danson C., Key M.H., Lewis C.L.S., Neely D., Nilsen J., Pert G.J., Tallents G.J. and Wark J.S., Science, 276, 1097-1100, 1997a.

Zhang J., MacPhee A.G., Nilsen J., Lin J., Barbee Jr. T.W., Danson C., Key M.H., Lewis C.L.S., Neely D., O'Rourke R.M.N., Pert G.J., Smith R., Tallents G.J., Wark J.S. and Wolfrum E., Phys. Rev. Lett., 78, 20, 3856-3859, 1997b.

Zhang J., Warwick P.J., Wolfrum E., Key M.H., Danson C., Demir A., Healy S., Kalantar D.H., Kim N.S., Lewis C.L.S., Lin J., MacPhee A.G., Neely D., Nilsen J., Pert G.J., Smith R., Tallents G.J. and Wark J.S., Phys. Rev. A, 54, 6, R4653-R4656, 1996.


Appendix 1
Ne-like ion lasers

Isoelectronic sequences, and in particular the neon sequence, are of considerable interest due to their suitability for laser systems based on electron-collisional pumping. In its simplest form, the system involves $2p \rightarrow 3p$ valence electron excitation, where the 2p level is the ground state $1s^2 2s^2 2p^6$ configuration. The 3p level is quite metastable against direct spontaneous dipole decay to the ground state and as the $2p \rightarrow 3p$ excitation rate is comparable to that for the $2p \rightarrow 3s$ or $2p \rightarrow 3d$ dipole rates, lasing can then occur on a $\Delta n=0$ transition from the 3p to the 3s levels, the 3s state then rapidly depopulating back to 2p. Theoretically, any 2p isoelectronic sequence can be used but neon ($2p^6$) has proven the most successful due to the greater stability of the species in a transient plasma, which is associated with the higher ionisation potential of the closed shell configuration. Most X-ray laser schemes require electron densities of the order of $10^{20} cm^{-3}$ for which it has been found that driving lasers with wavelengths ~1μm e.g. Nd:Glass, are most useful. Typically, drive laser pulse widths in the picosecond regime with energies in the 0.1-5kJ range are transversely focussed onto a slab or foil target of interest. The resulting line plasma within which lasing occurs is thus well suited for axial measurements of the laser gain through monitoring the emission and is also suited to cavity installation. A typical experimental set-up employing multiple aligned line focussed high power laser beams is shown in figure A1.1. With regard to neon like ion lasers, the primary energy levels involved in X-ray laser production are shown in figure A1.2. Although there are ten 3p levels and four 3s levels, lasing has only been detected on the six transitions shown in figure A1.2, of which the largest gain e.g. Se^{24+}=4-5cm^{-1} has been measured on the two transitions B and C shown in bold. To date, many species of the neon isoelectronic sequence have been seen to lase on the 3p-3s transitions, higher atomic number target elements yielding shorter lasing wavelengths. A sample of species and their associated lasing wavelengths on the transitions labelled in figure A1.2 are shown in table A1.1 (Elton 1990). More recently, significant advances have been made in the field, lasing now having been obtained with significant gain for neon like species with atomic numbers as low as Scandium(Z=21), Calcium(Z=20), Potassium(Z=19) and Chlorine(Z=17) (Li et al 1995). Lasing in these low Z species has been made possible

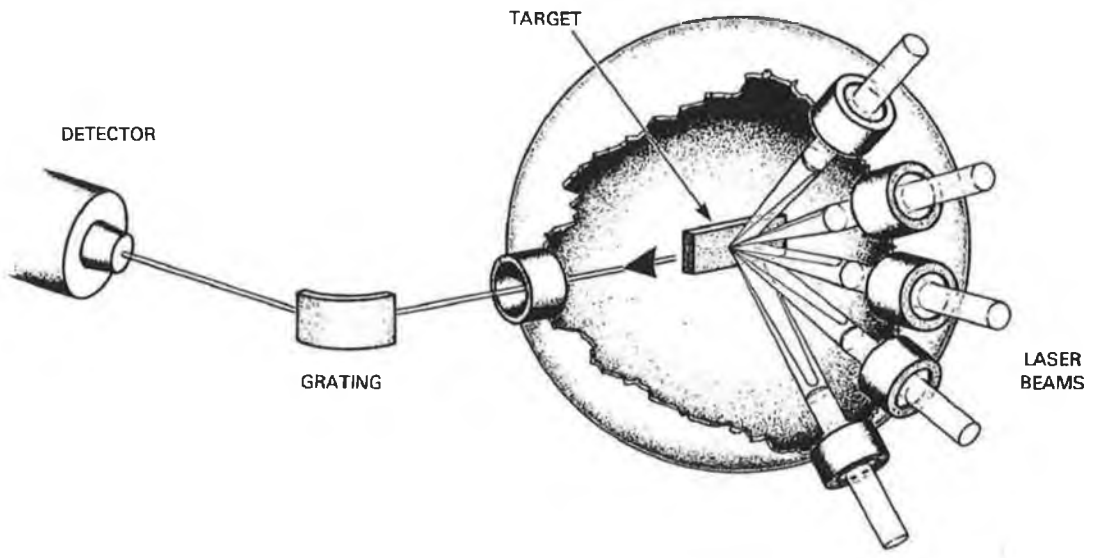

Figure A1.1 : Schematic of an X-ray laser pumped transversely by multiple aligned line-focused high power laser beams (after Elton 1990).

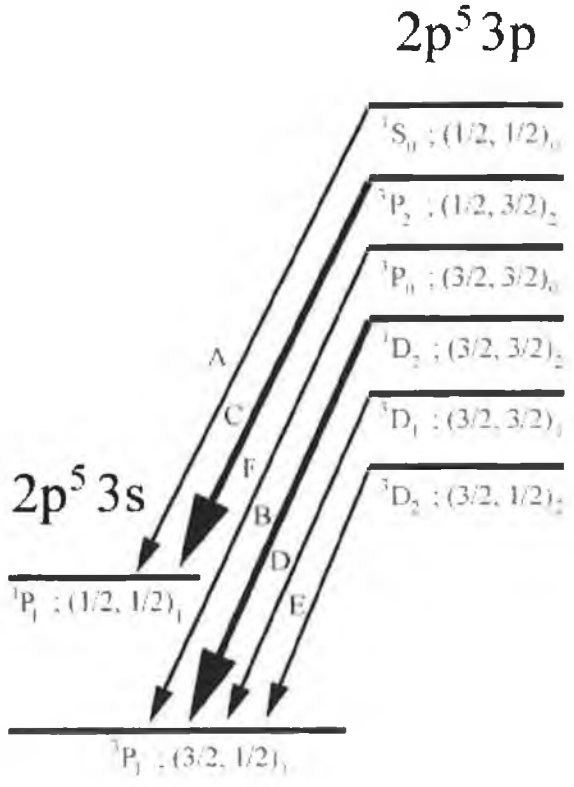

Figure A1.2 : Six neon-like ion laser transitions observed for Z≥29. Energy levels are labelled in both LS and jj notation. The 'B' and 'C' transitions produce the largest measured gain and are shown in bold (after Elton 1990).

Transition	A	B	C	D	E	F	Reference
Species							
Cu^{19+}	221.11	279.31	284.67				Lee et al (1987)
Zn^{20+}	212.17	262.32	267.23				Lee et al (1988)
Ga^{21+}		246.70	251.11				Lee et al (1988)
Ge^{22+}	196.06	232.24	236.26	247.32	286.46		Elton et al (1987)
As^{23+}		218.84	222.56				Lee et al (1988)
Se^{24+}	182.43	206.38	209.78	220.28	262.94	169.29	Keane et al (1989), Eckart et al (1988)
	182.44	206.35	209.73				Lee et al (1988)
Sr^{28+}	159.80	164.10	166.50				Keane et al (1989)
Y^{29+}		155.00	157.10	165.00	218.00		Keane et al (1989), Matthews et al (1986)
Mo^{32+}	141.60	131.00	132.70	139.40		106.4	MacGowan et al (1987), Keane et al (1989)

Table A1.1 : The measured wavelengths (Å) of 3p→3s lasing lines in Ne-like systems. The transition letters refer to those labelled in figure A1.2 (after Elton 1990).

through the application of novel techniques to achieve the lower electron densities required in order that the density gradients are not too steep for laser propagation. One such technique involves the use of a low-intensity prepulse to generate the laser medium which is heated several nanoseconds later by the main pulse. The success of this prepulse technique is primarily due to the prepulse being very efficient in making a larger and more uniform plasma allowing better propagation of the laser beam along the gain region. Success in demonstrating laser action in many neon like species having now been achieved, efforts are now focussed on improving the X-ray laser efficiency and reducing the systems in size and cost to make them more accessible to users without access to large scale facilities. One such improvement has been in achieving 'saturated operation', where the maximum power possible for a given volume of an excited plasma is extracted by stimulated emission. This saturation also tends to produce an output energy which is consistent with little variation from shot to shot, this being a requisite for potential applications in interferometry of dense plasmas relevant to inertial confinement fusion and laboratory astrophysics and also in holography and microscopy of biological specimens (Zhang et al 1997a). Despite the enormous optical energies

required to achieve saturation i.e. a gain-length product of 15, saturated operation has been demonstrated in many species including Ne-like Ti (Kalachnikov et al 1998) and Ne-like Ge (Zhang et al 1996) and also in Ni-like Ag (Nilsen et al 1997, Zhang et al 1997b) and Ni-like Sm (Zhang et al 1997a, Lin et al 1999), which at 73Å is currently the shortest wavelength saturated X-ray laser to date.